Laser Spectroscopy in Scattering Media for Biological and Medical Applications

Linda Persson

Doctoral Thesis
2007

Lund University

LASER SPECTROSCOPY IN SCATTERING MEDIA FOR BIOLOGICAL AND MEDICAL APPLICATIONS

© 2007 Linda Persson
All rights reserved
Printed in Sweden by Media-Tryck, Lund, 2007

Division of Atomic Physics
Department of Physics
Faculty of Engineering, LTH
Lund University
P.O. Box 118
SE–221 00 Lund
Sweden

http://www.atom.fysik.lth.se

ISSN: 0281-2762
Lund Reports on Atomic Physics, LRAP-385

ISBN: 978-91-628-7274-8

An attempt to improve the health and environment for mankind

ABSTRACT

Tunable diode laser absorption spectroscopy can be utilised for gas detection in biological and medical applications. The common approach is to analyse transmitted light according to the Beer-Lambertian law. Normally, the light has a well-defined path length through the gas sample since it can be assumed that it has negligible scattering properties. Samples which, by contrast, have strong scattering properties, meaning that light is extensively scattered, are investigated in this work. In such materials, the light travels an undefined path through the sample. Thus, light propagation in scattering media must be understood. The aim of this work has been to combine knowledge from two fields, namely, tunable diode laser absorption spectroscopy and light propagation in scattering media, in order to extract information of gas contents within porous samples for biological and medical applications.

Porous materials containing free gas are common in our everyday environment. Examples are wood and other construction materials, and fruit and many other food stuffs. The human paranasal sinuses located within the human skull are air-filled cavities surrounded by strongly scattering tissue. Thus, light transport through the cavities becomes complicated. Measurements of molecular oxygen at 760 nm and water vapour at 935 nm were successfully performed within the sinuses on volunteers, using tunable diode laser absorption spectroscopy combined with wavelength modulation techniques. To fully understand the signals recorded, measurements on phantoms, representing human sinuses, and Monte Carlo simulations, were first carried out.

Gas measurements based on the same technique have also been demonstrated in pharmaceutical tablets to investigate the potential for extracting information on the porosity of the tablets. This is of importance since the porosity is directly related to the drug delivery time to the body after administration.

To understand the drying process of wood, the same type of measurements were carried out on samples of wood. The results showed that it is possible to extract additional information on the drying process, not provided by the commercial techniques available.

In horticultural produce different gases have a significant role in the respiration process. Promising gas measurements have been performed on fruit, in particular apples, to study the potential of developing a system based on tunable diode lasers to measure the gas content within the product when different packaging techniques are employed.

From the experience with the setups and the various measurements performed in the laboratory, a mobile system based on two pigtailed diode lasers was developed, making measurements outside the laboratory possible. Based on the previous promising results, a clinical trial at the Lund University Hospital in cooperation with the Ear, Nose and Throat Clinic, the Radiology Clinic, and the Oncology Clinic has been initiated to investigate the human sinuses in healthy and diseased sinuses. Preliminary results are presented in this thesis.

POPULÄRVETENSKAPLIG SAMMANFATTNING

Spektroskopi är den vetenskapsgren som används för att studera samspelet mellan strålning/ljus och materia för tillämpningar i både diagnostiska och terapeutiska syften. Då ljus sänds in i ett prov sätts olika fysikaliska processer igång. I denna avhandling studeras företrädesvis en process som kallas för absorption. Vid absorptionsspektroskopi är våglängden av ljuset, som sänds in i provet, noga avstämd för att motsvara en övergång mellan två energinivåer hos atomen eller molekylen som ska studeras. Detta möjliggör en specifik absorption av ljuset, vilket innebär att energin hos ljuset övergår till atomen eller molekylen. I princip kan koncentrationen av en absorbator, t.ex. en gas, bestämmas genom att mäta intensiteten av ljuset efter det att ljuset passerat provet, dvs det så kallade transmitterade ljuset. Denna intensitet jämförs sedan till intensiteten av ljuset innan det passerat provet. Då prov med försumbara spridningsegenskaper undersöks, dvs då det insända ljusets väg i provet är densamma som provets tjocklek, kan mängden ljus som absorberats direkt relateras till koncentrationen av den absorberande gasen.

Det finns många naturliga och syntetiska material som är porösa med gasfyllda kaviteter (hålrum). Dessa material har en kraftig spridning av ljuset. Detta innebär då att ljus som sänds in inte kommer att ta den kortaste sträckan genom provet motsvarande materialets tjocklek, utan spridas inuti provet. Detta resulterar i att den sträcka som ljuset färdats i materialet kan vara många gånger längre än materialets dimensioner. Detta betyder i sin tur att det inte går att direkt relatera mängden absorberat ljus till den absorberande gasens koncentration. Under dessa förutsättningar måste det tas hänsyn till hur ljuset utbreder sig i spridande material.

Målet med denna avhandling har i huvudsak varit att undersöka möjligheten att använda diodlaserspektroskopi för att studera gaskoncentrationer i spridande material för biologiska och medicinska tillämpningar. Metoden har fått namnet GASMAS vilket står för GAs in Scattering Media Absorption Spectroscopy. Som ljuskälla har lågenergetiska diodlasrar använts med noggrant valda våglängder för att överensstämma med energiövergångar i olika gaser av intresse. Eftersom ljuset sprids är det möjligt att studera både bakåtspritt ljus och ljus som transmitterats genom provet. I denna avhandling har båda dessa aspekter utnyttjats. Bakåtspridning är för en del tillämpningar det enda som kan utnyttjas, eftersom baksidan av provet inte är tillgänglig. Metoden våglängdsmoduleringsspektroskopi har tillämpats för att öka känsligheten hos tekniken. Den innebär att svaga absorptioner kan observeras genom att det insända ljuset märks med en modulationsfrekvens. Detektionen av ljuset sker sedan vid samma frekvens. Eftersom endast ljus med den givna frekvensen detekteras, undertrycks allt brus med andra frekvenser och en ökad känslighet erhålls.

En biologisk tillämpning av metoden, som använts i denna avhandling, är studien av ansiktsskelettets bihålor, vilka finns hos vuxna och äldre barn, bl.a. i överkäkarna och bakom pannan. Bihålorna har förbindelse med näshålan via smala gångar. I icke-infekterade bihålor kan luft, vätska och slem fritt passera. Varje år får ungefär 3% av Sveriges befolkning diagnosen bihåleinflammation. Oftast är diagnosen endast baserad på patientens sjukdomshistoria och onödig ordinering av antibiotika förekommer. För en mer säker diagnos måste en skikt-röntgen (CT-undersökning) av skallen utföras, vilket är kostsamt och inte heller helt ofarligt för patienten.

I denna avhandling har vi undersökt möjligheten att använda GASMAS-metoden, beskriven ovan, för att på ett icke-invasivt sätt, och utan användning av joniserande strålning, karakterisera bihålorna. Laserljuset appliceras via fibrer på hudytan eller mot gomtaket, beroende på vilken bihåla som undersöks. Ljuset detekteras sedan med känsliga detektorer som placerats externt på hudytan. Våglängden av ljuset som sänds in är noggrant avstämd så att information av syrgas- och vattenångeinnehållet i bihålorna kan erhållas. Tekniken gör det även möjligt att undersöka kommunikationen mellan näshålan och bihålorna genom att kvävgas spolas in i näshålan samtidigt som det kontinuerligt mäts hur gassammansättningen förändras i bihålorna. Hos en frisk patient registreras en minskning av syrekoncentrationen, då bihålan fylls med kvävgas. Hos en sjuk patient, däremot, blockerar svullnaden av slemhinnorna passagen mellan kaviteterna. Lovande resultat har erhållits från studier på frivilliga testpersoner och dessa resultat presenteras i denna avhandling. En klinisk studie har påbörjats tillsammans med Öron- Näs- Halskliniken, Röntgenkliniken samt Onkologiska kliniken i Lund. Under denna studie genomgår patienterna en planerad CT-undersökning av skallen och direkt efter görs lasermätningar. Detta ger en möjlighet att direkt jämföra de båda teknikerna. Preliminära resultat från denna studie diskuteras i avhandlingen.

Läkemedel i form av tabletter används idag i stor utsträckning som medicinering för att bota eller lindra symptom av sjukdomar. Det är viktigt att varje tablett av samma sort ger samma dos till kroppen efter det att den intagits av patienten. Tablettens löslighet är relaterad till dess porositet. GASMAS-metoden diskuterad ovan har använts för att undersöka om syrgaskoncentrationen inuti dessa ljusspridande tabletter kan användas för att studera porositet. Resultaten av dessa undersökningar diskuteras i avhandlingen.

Samma icke-invasiva metod har används för att undersöka gaskoncentrationer i livsmedel. Förpackningsmetoder för livsmedel syftar till att stänga ute syrgas. Frukter är mycket känsliga för gaser. En för hög syrgaskoncentration påskyndar mognadsprocessen och en för låg koncentrationen kan åstadkomma jäsning. Detta innebär att det finns en optimal syrgaskoncentration som ger produkterna optimal hållbarhet. Olika förpackningstekniker har utvecklats för att reglera mängden syre i livsmedel. I dessa sammanhang är det viktigt att, på ett ickeförstörande sätt, kunna uppskatta syrgaskoncentrationen. I denna avhandling har gasmätningar utförts på matprodukter, exempelvis äpplen. Möjligheten att använda sig av diodlaserspektroskopi inom förpackningsindustrin har demonstrerats genom att studera gasutbyte genom olika förpackningsmaterial, exempelvis plast.

Mätningar har även utförts under torkningsprocessen av trä. Den årliga världsproduktionen av virke är ungefär 3 miljarder m^3. Ungefär hälften av detta virke används inom byggnadsindustrin där det är mycket viktigt att träet då är torrt för att undvika mögel och fukt i byggnader som uppförs. I denna avhandling har diodlaserspektroskopimetoden använts för att studera möjligheten att följa torkningsprocessen. Förändringen av syrgas och vattenångekoncentrationen har mätts under förloppet och lovande resultat har erhållits gällande metodens användbarhet i detta syfte.

LIST OF PUBLICATIONS

This thesis is based on the following papers, which will be referred to by their Roman numerals in the text.

I **On the potential of human sinus cavity diagnostics using diode laser gas spectroscopy**
L. Persson, K. Svanberg, and S. Svanberg.
Applied Physics B **82**, 313–318 (2006).

II **Non-intrusive optical study of gas and its exchange in human maxillary sinuses**
L. Persson, M. Andersson, T. Svensson,
M. Cassel-Engquist, K. Svanberg, and S. Svanberg.
Proceeding of SPIE-OSA Biomedical Optics **6628**,
Art. ID: 662804 (2007).

III **Gas monitoring in human sinuses using tunable diode laser spectroscopy**
L. Persson, M. Andersson, M. Cassel-Engquist,
K. Svanberg, and S. Svanberg.
Journal of Biomedical Optics **12**, Art. ID: 053001 (2007).

IV **Simultaneous detection of molecular oxygen and water vapour in the tissue optical window using tunable diode laser spectroscopy**
L. Persson, M. Andersson, M. Cassel-Engquist,
K. Svanberg, and S. Svanberg.
Submitted, (2007).

V **Diode laser absorption spectroscopy for studies of gas exchange in fruits**
L. Persson, H. Gao, M. Sjöholm, and S. Svanberg.
Optics and Lasers in Engineering **44**, 687–698 (2006).

VI **Studies of gas exchange in fruits using laser spectroscopic techniques**
L. Persson, B. Anderson, M. Andersson, M. Sjöholm, and S. Svanberg.
Proceedings of FRUITIC 05, Information and Technology for Sustainable Fruit and Vegetable Production, 543–551, Montpellier (September 2005).

VII **Noninvasive characterization of pharmaceutical solids by diode laser oxygen spectroscopy**
T. Svensson, L. Persson, M. Andersson, S. Svanberg, S. Andersson-Engels, J. Johansson, and S. Folestad.
Applied Spectroscopy **61**, 784–786 (2007).

VIII **Spectroscopic studies of wood-drying processes**
M. Andersson, L. Persson, M. Sjöholm, and S. Svanberg.
Optics Express **14**, 3641–3653 (2006).

IX **Fluorescence monitoring of a topically applied liposomal Temoporfin formulation and photodynamic therapy of non-pigmented skin malignancies**
N. Bendsoe, L. Persson, A. Johansson, J. Axelsson, J. Svensson, S. Gräfe, T. Trebst, S. Andersson-Engels, S. Svanberg, and K. Svanberg.
Journal of Environmental Pathology, Toxicology and Oncology **26**, 117–126 (2007).

X **Monte Carlo simulations related to gas-based optical diagnosis of human sinusitis**
L. Persson, E. Kristensson, L. Simonsson, and S. Svanberg.
Journal of Biomedical Optics **12**, Art. ID: 053002 (2007).

XI **Approach to optical interference fringes reduction in diode laser absorption spectroscopy**
L. Persson, F. Andersson, M. Andersson, and S. Svanberg.
Applied Physics B **87**, 523–530 (2007).

XII **Flexible lock-in detection system based on synchronized computer plug-in boards applied in sensitive gas spectroscopy**
M. Andersson, L. Persson, T. Svensson, and S. Svanberg.
Submitted, (2007).

XIII **Temporal correlation scheme for spectroscopic gas analysis using multimode diode lasers**
G. Somesfalean, M. Sjöholm, L. Persson, H. Gao,
T. Svensson and S. Svanberg.
Applied Physics Letters **86**, Art. ID: 184102 (2005).

XIV **Laser spectroscopy of gas in scattering media at scales ranging from kilometers to millimeters**
M. Andersson, R. Grönlund, L. Persson, M. Sjöholm,
K. Svanberg and S. Svanberg.
Laser Physics **17**, 893–902 (2007).

ABBREVIATIONS

CA	Controlled atmosphere storage
CT	Computer tomography
DAS	Direct absorption spectroscopy
DBR	Distributed Bragg reflector
DFB	Distributed feedback
FSP	Fiber saturation point
GASMAS	Gas in scattering media absorption spectroscopy
HWHM	Half width at half maximum
IR	Infrared
MAP	Modified atmosphere packaging
MIR	Mid infrared
MRI	Magnetic resonance imaging
MC	Monte Carlo
NIR	Near infrared
NMR	Nuclear magnetic resonance
PDT	Photodynamic therapy
PET	Positron emission tomography
QCL	Quantum cascade laser
RAM	Residual amplitude modulation
RTE	Radiative transport equation
SNR	Signal to noise ratio
SPECT	Single photon emission computerised tomography
TDLS	Tunable diode laser spectroscopy
UV	Ultraviolet
WMS	Wavelength modulation spectroscopy

CONTENTS

Papers

Chapter 1

Introduction

Spectroscopy elucidates the interaction between electromagnetic radiation and matter. Researchers have for decades used spectroscopic methods to gain information about matter in various applications, for instance, in the environmental, biological, and medical fields. The principle is based on the fact that every atom and molecule has its own specific way of interacting with light. This is the case since each atom and molecule has a different set of energy levels. These sets of energy levels can be considered as fingerprints for each atom and molecule. Resonance transitions can occur between different levels by absorption or emission of light, providing highly specific spectroscopic features. Thus, it is possible, by illuminating a sample with electromagnetic radiation and analysing the radiation after interaction, to gain information of various kinds.

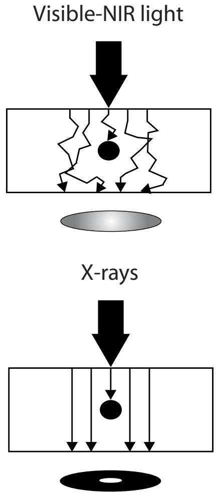

Figure 1.1. *When electromagnetic radiation in the visible region to the NIR region illuminates tissue the radiation becomes multiply scattered, resulting in a blurry image. By contrast, a clear image is obtained when radiation in the X-ray region is used.*

Light propagation in scattering media, such as human tissue, has for a long time been an interesting topic for research related to medical applications. In contrast to illumination with electromagnetic radiation in the X-ray region, electromagnetic radiation from the visible region to the near infrared (NIR) region will not propagate straight through the tissue as it is illuminated. In this case light becomes multiply scattered within the tissue. Thus the path length of the light within the sample will be many times longer than the dimension of the sample; see Figure 1.1. Scattering leads to image blurring. The most common techniques used at hospitals today to provide images of human tissue are X-ray radiography including computed tomography (CT), magnetic resonance imaging (MRI), single photon emission computerised tomography (SPECT) and positron emission tomography (PET). However, optical investigation can supply additional information to these methods.

Spectroscopy is commonly used to investigate gas compositions for a variety of applications. The system usually consists of three main components; a light source, the sample containing the gas to be investigated and a detector. The basic principle is to illuminate the sample with the light source and to detect the transmitted light. Depending on the species in the sample, some specific frequencies might be absorbed and an attenuation of the transmitted light will be detected. By contrast to the case explained above with scattering samples, the light will propagate straight through the gas in this type of measurements; see Figure 1.2.

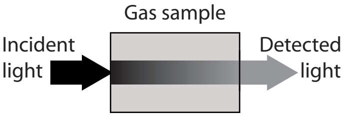

Figure 1.2. *Basic principle of gas absorption spectroscopy. The incident light will propagate straight through the sample containing the gas. If the frequency of the light corresponds to an energy transition it will become attenuated in relation to the concentration of the absorbing gas and the sample dimension.*

Our environment consists of many materials which are both scattering and contain free gas. How optical gas absorption spectroscopy can be used to investigate these media is practically an unexplored area. The basic ideas behind gas absorption spectroscopy cannot be directly applied since the light will become multiply scattered. Here knowledge of light propagation in scattering media has to be considered. This has been the main issue in most of the work presented in this thesis; gas absorption spectroscopy in scattering media.

Outline of the thesis

The outline of this thesis is as follows. In Chapter 2 scattering matter containing free gas will be discussed in which measurements of different gas species and gas exchange have a significant role. The following chapter gives a short review of light interaction with matter. Chapter 4 starts with a discussion of the basic principles of laser light, followed by a brief presentation of the light source commonly used in this work, namely, the tunable semiconductor laser. The final part of this chapter introduces the basic principle of the main technique used, namely, gas absorption spectroscopy. In Chapter 5 a short presentation of the possibilities to model light propagation in scattering media is provided. In the final chapter, some gas measurements in the applications discussed in Chapter 2, using the technique denoted GASMAS (GAs in Scattering Media Absorption Spectroscopy), are presented.

CHAPTER 2

GAS EXCHANGE IN BIOLOGICAL AND MEDICAL CONTEXTS

Gas exchange of various kinds can in some way be considered as the key to life. The major part of this thesis has involved measurements of gas contents and exchange in biological and medical processes by using diode laser absorption spectroscopy. This chapter will not describe exhaustively all applications in which gas exchange occurs or where it is of importance to investigate the gas content in biological and medical contexts. Instead some background knowledge will be given to the applications studied in this thesis.

The major part of the medical applications investigated in this work has involved the human sinuses. To start with, a brief overview will be given of the different air-filled cavities within the human skull, such as the nasal cavity, the oral cavity, the paranasal sinuses, and the mastoid bone. The gas content within these cavities can in some cases be directly related to health status. In Section 6.2.1, measurements of molecular oxygen and water vapour within the paranasal sinuses and the mastoid bone, based on diode lasers, will be discussed (Papers **I** – **IV**).

Further, a short presentation of the processes in the respiration within living tissue will be given. By controlling the concentration of different gases during the storage of horticulture produce, the shelf-time can be extended. Discussions of one method to measure the gas concentration in packaging of produce will be presented in the last chapter of this thesis, in Section 6.2.2 (Papers **V** and **VI**).

For pharmaceutical tablets gas concentration measurements can be of importance when the release time of the drug after administration is to be investigated. This is, for example, related to the particle size of the active substance and the porosity of the tablets. A brief description of pharmaceutical tablets will be given in this chapter and measurements of the gas contents of tablets will be discussed in Section 6.2.3 (Paper **VII**).

In the final section of this chapter, a brief discussion of the drying process of wood will be presented. The concentration of oxygen and water vapour can during the drying process be related to the moisture content of the wood. In Section 6.2.4 measurements of these gases in wood will be discussed (Paper **VIII**).

2.1 Cavities in the human skull

The human skull contains hollow cavities, which are connected to each other through ventilation channels. In a healthy individual, these cavities are air-filled and air transport occurs, while in an unhealthy state some of these cavities may be filled with pus, liquid, and swollen mucosa. In this section, the nasal cavity, the oral cavity, the paranasal cavities, also called sinuses, and the mastoids will be discussed. In the section about the paranasal cavities an unhealthy condition called sinusitis, implying that either an infection or an inflammation is present in the cavities, will also be mentioned. Most of the material in this section basically follows that presented in Refs 1–3.

2.1.1 The nasal cavity

The nasal cavity is a large space located behind the outer part of the nose in the middle of the face. One of the functions of the nasal cavity is to clean, heat and humidify the air as it is inhaled. It is also involved in olfaction with the olfactory nerve for the sense of smell.

The hard and semihard part of the nasal cavity consists of cartilage in the front and of bone in the back. It is divided into two halves by a vertical partition called the *septum nasi*. The cavity is protected above by the nasal bone and on the sides of the cavity it is enclosed by the maxilla bone and the ethmoid bone (see Figure 2.1). The ethmoid bone separates the nasal cavity from the brain, while it is separated from the mouth by the palate. The paranasal sinuses are connected to the the nasal cavity via small tubes called *ostia*. The paranasal sinuses are further discussed in Section 2.1.3.

The front of the nasal cavity protrudes inside the nose, while the back is continuing with the pharynx. The function of the pharynx is to close the esophagus by a series of reflex mechanisms during breathing and swallowing.

There are, in both the right and left side of the nasal cavity, three horizontal outgrowths called *conchae* (the inferior, middle, and superior concha), depicted in Figure 2.2. The superior and middle conchae are parts of the ethmoid bone, whereas the inferior conchae are separate bones. The conchae disrupt the airflow

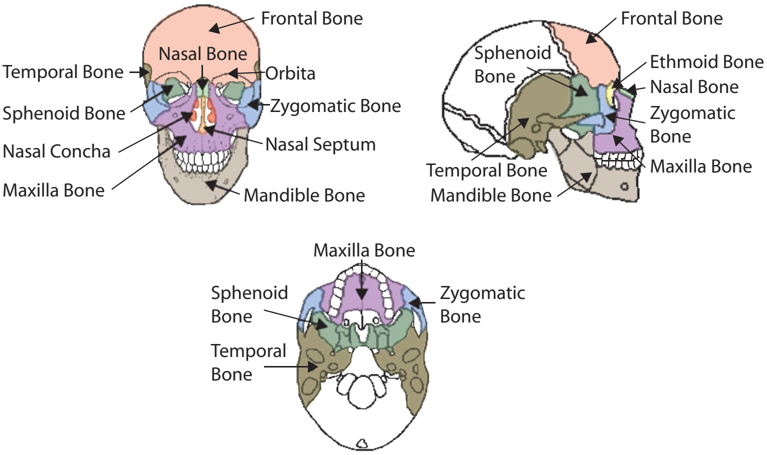

Figure 2.1. *Anterior, lateral, and inferior view of the human skull with some of its bones indicated (Adapted and modified from Ref. 4).*

and direct the air towards the olfactory epithelium (special tissue involved in the process of smelling) in the roof of the nasal cavity. It increases the surface area of the inside of the nose, thus further enhancing the sense of smell.

The tissue which covers the wall of the nasal cavity contains many blood vessels, which is of importance for the function of the nasal cavity to heat and humidify the inhaled air. Heat from the blood in the vessels helps to increase the temperature of the air. Moisture is added to the inhaled air by special cells in the mucous membrane, which is a thin layer of tissue covering the inside walls of the nasal cavity. In the process, the air is thereby heated and moistened before it reaches the lungs.

As mentioned before the inside walls of the nasal cavity consist of the mucous membrane. This membrane produces mucus. The inside of the cavity is also covered by small hairs, called *cilia*. The mucus and the cilia trap and remove dust and germs from the air as it flows through the nasal cavity. The cilia also move the mucus from the nasal cavity down to the pharynx, where it can be swallowed.

2.1.2 The oral cavity

The oral cavity or *buccal* cavity is commonly known as the mouth. Through the oral cavity and the nasal cavity air is inhaled during breathing.

The roof of the mouth is formed by the palate. It separates the oral cavity from the nasal cavity. The palate consists of the

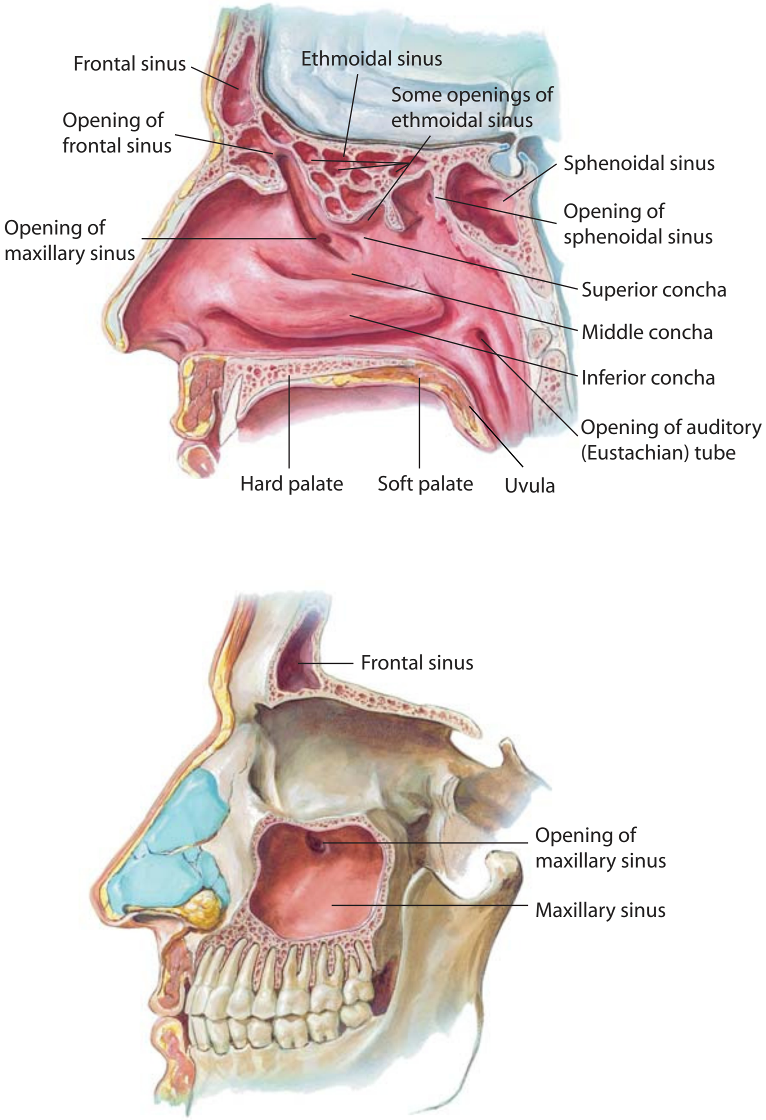

Figure 2.2. *Sagittal planes of the human skull with indications of some parts of the nasal cavity, oral cavity and the paranasal cavities. The openings between the nasal cavity and the paranasal cavities are also indicated (Reproduced with permission of Netterimages.com).*

hard palate (the frontal 2/3 of the palate) and the soft palate. The hard palate is supported by bone, while the soft palate is formed by skeletal muscle and connective tissue. The dorsal continuation of the soft palate is called the *uvula*. The palate and the uvula are depicted in Figure 2.2. During swallowing, the soft palate and uvula move upward to direct food away from the nasal cavity down towards the throat.

2.1.3 The paranasal sinuses

A number of air-filled cavities, called the paranasal sinuses, are located within the bones of the human skull [1, 5]. These sinuses are divided into four subgroups (indicated in Figure 2.2) that are named according to the bones (depicted in Figure 2.1) in which they are enclosed;

Maxillary sinus:	Located caudally of the eye in the maxillar bones
Frontal sinus:	Located cranially of the eyes in the frontal bones
Ethmoidal sinus:	Located laterally and cranially of the nasal septum, backwards into the skull
Sphenoidal sinus:	Located at the centre of the skull base in the sphenoid bone

The maxillary sinuses, located in the maxillar bones, are the largest of the paranasal sinuses and are pyramidal in shape. The location of these sinuses is close to the floor of the orbital cavities (eye cavities) and to the upper teeth. Therefore, problems with or pain in the teeth are often confused with unhealthy states of these sinuses.

The frontal sinuses, located in the frontal bone, are rarely symmetrical, and the septum between them frequently deviates towards one or the other side of the centre line. The frontal sinuses are not present at birth, but begin to form at about the age of two years and are generally fairly well developed between the seventh and eighth year, but reach their full size first after puberty.

The ethmoid sinus is located behind the bridge of the nose between the eyes in the ethmoid bone. It comprises of a cell system with about 7 to 12 small chambers, that collectively make up the sinus.

Deep within the skull behind the ethmoid sinus are the sphenoid sinuses, located in the sphenoid bone. The sphenoid sinuses have approximately the size of a large grape. The right and left sphenoid sinuses are separated by a thin bone septum.

All the paranasal sinuses are connected to the nasal cavity through small orifices called *ostia*, which allow drainage and exchange of air, liquid and mucus (previously discussed in Section 2.1.1). The openings (*meatii*) are indicated in Figure 2.2.

The paths of airflow between the different sinuses and the nasal cavity are listed below:

Maxillary sinus → Middle concha
Frontal sinus → Middle concha
Ethmoidal sinus → Middle and superior concha
Sphenoidal sinus → Behind the middle and superior concha

So far no one has convincingly been able to demonstrate any important physiological function of the human sinuses. Different hypotheses on the possible functions have been proposed, such as decreasing the weight of the skull, heat insulation, and augmenting the resonance of the voice. However, it appears that the only important issue concerning the sinuses that everyone can agree upon is that they should be kept free from diseases such as inflammation and infections [5, 6].

Sinusitis is either an infection or an inflammation of one or more of the paranasal sinuses of either bacterial, fungal, viral, allergic or autoimmune origin. When a cold is contracted, the mucous membranes in the sinuses, the nasal cavity and the meatal openings connecting them become swollen. This can lead to the blockage of the meatii, which can result in mucus and bacteria filling up the cavities with sinusitis as the outcome. The most common symptoms of sinusitis are facial pain, headache, tenderness of the sinus areas, nasal drainage that is thick and coloured, cough and fluid from the nasal cavity. Often sinusitis includes a combination of the above-mentioned symptoms. Unfortunately, it is very difficult to distinguish between a normal cold, which most often clears up without any treatment, and sinusitis.

Sinusitis can be acute (going on for less than four weeks), subacute (4 – 8 weeks) or chronic (lasting 8 weeks or more). All three types of sinusitis have similar symptoms, and are thus often difficult to distinguish within a limited time span. Acute sinusitis is often induced by bacteria, such as Haemophilus influenzae, streptococci, or staphylococci while the cause of chronic sinusitis is more obscure. It has been suggested that chronic sinusitis is caused by a long-standing viral infection or a response to fungal allergies, but strong evidence is still lacking.

Every year, more than 37 million people in the US are diagnosed with sinusitis [7]. In a Swedish study it was shown that 2.2 % of all consultations in a Primary Care Unit were due to sinusitis [5]. Today, the diagnosis of sinusitis is mostly based on the anamnesis given by the patient, and in some cases on paraclinical investigations such as X-ray, ultrasound, and low-dose computerised tomography [8]. Sinusitis is treated with antibiotics and often followed by one week of sick-leave. Unfortunately, unnecessary antibiotic treatment is very common due to the non-specific diagnostics, as investigations based on ultrasound and X-rays are performed only in cases with persisting symptoms.

If sinusitis is untreated, it can lead to bronchitis and pneumonia. Bronchitis is a pulmonary disease characterised by inflammation of the bronchi of the lungs. Pneumonia is an infection illness of the lungs and the respiratory system in which the alveoli (microscopic air-filled sacs of the lung responsible for absorbing oxygen from the atmosphere, further discussed in Section 2.2.2) become inflamed and flooded with fluid quenching the respiration to work correctly.

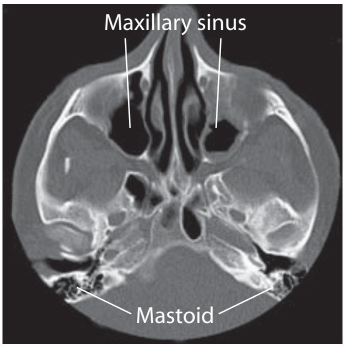

Figure 2.3. *CT image with mastoid and maxillary sinuses indicated (transversal section).*

2.1.4 The mastoid bone

The mastoid bone is an air-filled, honeycomb-like structure located behind the middle ear as a portion of the temporal bone (depicted in Figure 2.1). Its function is largely unknown. The air containing cells are connected to the middle ear through an air-filled cavity called the mastoid antrum. This means that the ventilation of the mastoid depends on the ventilation of the middle ear itself through the Eustachian tube, as indicated in Figure 2.2.

Although the mastoid bone serves as a reservoir of air to allow normal movement of the eardrum, its connection to the middle ear may also result in the spread of middle ear infections to the mastoid bone (mastoiditis). The mastoid bone then becomes filled with infected material and its honeycomb-like structure may be destroyed. The diagnosis of mastoiditis is often based on the medical history of the patient, a physical examination and paracentesis of the eardrum. Sometimes a CT scan is done providing additional information. Mastoiditis is treated with antibiotics. In some cases, surgery is needed for drainage. If left untreated, the inflammation can spread to the surrounding tissue, including the brain, causing serious complications.

Figure 2.3 shows a CT image on which the mastoids and the maxillary sinuses are indicated. The mastoids appear as irregular dark shapes.

2.2 Respiration

2.2.1 Cellular respiration

Cellular respiration is a key feature of life and occurs in all living cells. During respiration carbohydrates, particularly glucose, are broken down to release energy needed for the cell. The cells in the body need energy, for example, to maintain temperature, and cells in horticultural products need it for the ripening process.

There are two kinds of respiration in organisms; aerobic and anaerobic. Aerobic respiration is a complex process of chemical reactions in which oxygen is used to break down glucose into carbon dioxide and water. This releases energy in the form of energy-

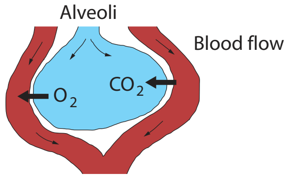

Figure 2.4. *The gas exchange in the alveoli of the lungs.*

carrying molecules. A simplified reaction for aerobic respiration can be written as;

$$C_6H_{12}O_6 + 6O_2 \rightarrow 6CO_2 + 6H_2O + energy$$

Respiration sometimes occurs without oxygen, and this is called anaerobic respiration. In this case, glucose is only partially broken down, and the end products are energy and either lactic acid or ethanol (alcohol) and carbon dioxide; this process is termed fermentation.

2.2.2 Gas exchange in the lungs

The essential organs for gas exchange in the human body are the lungs. The principal function of the lungs is to transport oxygen from the atmosphere into the bloodstream and to excrete carbon dioxide from the bloodstream into the atmosphere. The gas exchange occurs in the *alveoli* in the lungs. These are small cavities with a radius of about 0.1 mm and a wall about 0.2 μm thick. The gas exchange does not require energy since it is driven by passive diffusion. Oxygen and carbon dioxide diffuse across the walls between the alveoli and the blood; see Figure 2.4. Factors that influence diffusion include the surface area, the diffusion distance, and the concentration gradient.

In the human lung, the alveoli provide a large surface area (about the size of a tennis court) and their thin walls provide a short diffusion distance. A high concentration gradient is ensured by

- directing blood with low oxygen and high carbon dioxide levels to the lungs,
- pulmonary ventilation (breathing), which maintains a high level of oxygen and a low level of carbon dioxide in the alveolar air.

Thus, the alveoli and associated blood supply are well suited for the diffusion of oxygen into the blood and carbon dioxide into the air in the alveoli.

An average person will normally exchange about ten litres of air per minute. The inhaled air contains approximately 21% oxygen and the air exhaled contains about 17% oxygen and 4% carbon dioxide [1, 9].

2.2.3 Respiration in horticulture

Oxygen and carbon dioxide are biologically active molecules of importance in metabolic processes in horticultural products through their influence on the respiration process. The concentration of oxygen is recognised to be one of the main factors in the respiration of fruit and vegetables. However, it has been shown that the consumption of oxygen, and thus the respiration rate, also depends on the concentration of carbon dioxide [10, 11]. A reduction of respiration rate is often regarded as the main cause for a slower rate of maturation and change of quality. To slow down the respiration rate, the optimal conditions are a low concentration of oxygen and a high concentration of carbon dioxide. However, too low concentration of oxygen will result in fermentation. Thus, a critical concentration of oxygen exists [12]. It should be noted that the metabolic processes and thus the respiration process of horticultural products is highly dependent on the species [13].

The respiration rate does not only depend on the concentrations of the gases involved in the respiration process, but also on the temperature. As the temperature increases, the oxygen uptake also increases [14]. Different techniques have been developed to reduce the respiration rate of various kinds of fresh horticultural produce for the purpose of extending storage duration and shelf-life [11, 15]. The two most common methods are controlled-atmosphere storage (CA) and modified-atmosphere packaging (MAP). In CA, the gaseous composition of atmosphere around the product is artificially modified to regulate the respiration rate. The temperature is also often controlled. Different films, which are highly permeable to oxygen, are used in MAP. These are used to optimise the conditions for the product. It is of importance to design MAP according to the highest expected temperature during the storage period, since, as mentioned, the oxygen consumption increases with the temperature while the permeability of the film might not change to the same extent.

2.3 Pharmaceutical tablets

Medication is commonly administered as pharmaceutical tablets to cure or to reduce the symptoms of a disease. They consist of an active substance together with an inactive substance serving as a carrier. The chemical form of the active substance used and its mixture with the inactive substance depend on the disease the tablet is being administered for, and the rate of drug release required to achieve the therapeutical performance.

It is important that each tablet of the same kind delivers the same dose of the active substance to be absorbed by the body after administration. For optimisation, the ingredients, which may be powdered or granular, should be fairly dry and have a uniform particle size. The porosity of the tablet is also directly linked to this issue.

Tablets are often coated. This is done, for example, to prevent the tablets from sticking together, to decrease an unpleasant taste, and/or to make them easier to swallow. In some cases, coating is important to protect substances which are sensitive to oxidation and moisture. The type of coating used can effect the dissolution rate of the tablet and thus the release of the drug into the body, which can be both an advantage and a drawback.

Tablets as medication are often ordinated by the physician to be taken more than once during a treatment period. This is done in order to maintain a high concentration of the active substance over a longer time to achieve an efficient dose to fight the disease. In Figure 2.5 a typical concentration curve for the drug in the blood as a function of time after a tablet is administrated is depicted. The tablet starts to dissolve in the stomach as soon as it is swallowed, which results in an increase of the dose delivered to the blood. After the maximum is reached, which depends, for example, on the factors discussed above, the release of the drug to the blood takes place through diffusion [16].

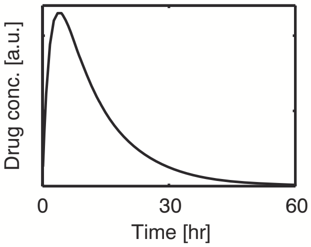

Figure 2.5. *Schematic illustration of drug concentration in the blood as a function of time after a pharmaceutical tablet is administrated.*

2.4 Moisture in wood

Wood is a very important material in the world today. The worldwide production of timber was approximately $3.4 \cdot 10^9$ m^3 in 1993. About 55% of the this volume was used as fuelwood and almost all of the rest for industrial and construction purposes [17].

In many applications, the moisture content of the wood is of importance. It is usually defined as the weight of water in the wood expressed as a fraction (often percentages) of the weight of oven-dry wood. The moisture can exist in three different ways:

(i) As liquid water (free water)
(ii) As water vapour in cell lumina and cavities
(iii) As water held chemically (bound water) within cell walls

In trees, the moisture content can range from about 30% to 200%. It might seem strange that the moisture content can exceed 100% but this just means that the weight of the water is higher than the wood matrix when it is dry. The fibre saturation point (FSP) of wood is defined as the point when the cell walls are completely saturated and no water exists in the cell lumina. This state gives a moisture content of about 30% on the average for all wood species, but can vary by several percent between individual species and individual samples [18, 19].

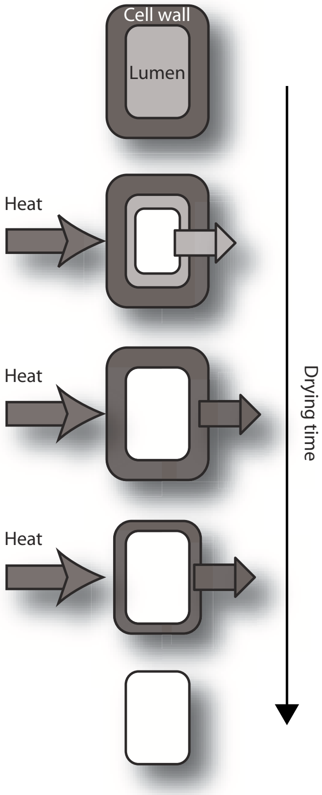

Figure 2.6. *Illustration of the drying process of wood.*

The drying process of wood starts directly after the tree is felled; see Figure 2.6. The capillary forces will transport the liquid water towards the surface where it will evaporate due to the heat being transported to it from the surrounding atmosphere. The bound water in the cell walls will then also evaporate until an equilibrium is reached with the surrounding atmosphere. As the liquid water evaporates, the cells have a partial pressure of fully saturated water vapour (100% relative humidity) until there is no more liquid water in the cells walls. The water vapour partial pressure then decreases through diffusion to the surrounding environment. The moisture content of the wood will, in the end, depend on the relative humidity and the temperature of the surrounding environment [19, 20].

CHAPTER 3

LIGHT INTERACTION WITH MATTER

By studying light that has interacted with matter, important information for diagnostic as well as therapeutic purposes can be gained in many applications. This information originates in the fact that every atom and molecule has its specific way of interacting with light.

In this chapter different processes that may occur when electromagnetic radiation is propagating in matter will be discussed. Some basic principles concerning light are presented as a start. This is followed by a short description of the configurations of atoms and molecules, giving rise to the so-called spectral fingerprint, which can be used to distinguish different species.

3.1 Electromagnetic radiation

In everyday life people refer to light as the narrow portion of electromagnetic radiation which is visible to the human eye. A basic characteristic of electromagnetic radiation is the frequency or the wavelength. The human eye is sensitive to wavelengths from about 400 nm to 700 nm. Depending on the wavelength, the eye will perceive different colours of the electromagnetic radiation. The light from the sun contains all wavelengths, and is an example of polychromatic light. If the light contains only one wavelength the light is called monochromatic, which is the case for laser light.

The electromagnetic spectrum is divided into different regions with different ways of production and detection. The most common regions of interest are shown in Figure 3.1, where also the visible region is enlarged.

The elementary particle that defines light is the photon. According to Planck, each photon has a well-defined energy, depending on the wavelength, λ [m], or frequency, ν [Hz], as;

$$E = \frac{hc}{\lambda} = h\nu, \tag{3.1}$$

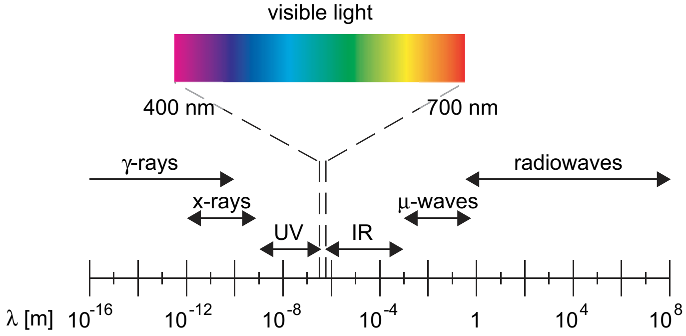

Figure 3.1. *Electromagnetic spectrum arranged by wavelength. The visible spectrum is highlighted.*

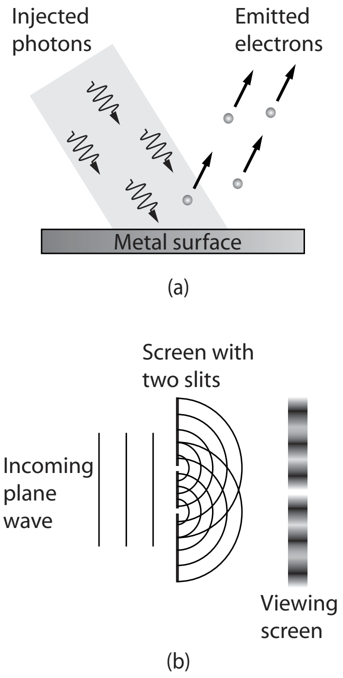

Figure 3.2. ***a*** *Illustration of the photoelectric effect supporting the theory that light can be considered as particles.* ***b*** *Young's double slit experiment supporting the theory that light can be considered as waves.*

where h is Planck's constant ($6.63 \cdot 10^{-34}$ Js) and c the speed of light ($3.00 \cdot 10^{8}$ m/s). The concept that light can be considered as particles was expressed by A. Einstein [21] and is in the citation for his Nobel prize 1921. The theory was experimentally supported by the photoelectric effect, schematically depicted in Figure 3.2**a**. When electromagnetic radiation interacts with a metal surface, the energy of the radiation is absorbed and photoelectrons are emitted. Even though the intensity of the radiation is increased, nothing will happen if the frequency of the light is not sufficiently high. However, above the threshold the number of photoelectrons emitted will increase with the intensity of the beam. This observation can be explained by considering the impinging beam as consisting of individual particles, each with a specific energy. For an electron to be emitted a particle with an energy above the threshold is required. One interacting particle results in one emitted electron. When the intensity of the beam is increased, i.e., thus increasing the number of particles in the beam, more particles will interact with the matter and more electrons will be emitted [22].

Before Einstein's discoveries, light was considered as having wave properties. One of the most important experiments of wave theory is Young's double slit, depicted in Figure 3.2**b**. Consider a plane wave propagating towards a screen with two small slits. If the light pattern is studied behind the screen, a pattern consisting of intense light alternating with darkness can be observed. This pattern can be explained by assuming the light to have wave properties. After propagating through the small slits, the light is diffracted and bulges outwards causing two wavefronts propagating towards the viewing screen. The two wavefronts will then interfere constructively and destructively resulting in maximum light intensities alternating with minimum light intensities [23].

As previously discussed, it has been shown experimentally that light exhibits both particle and wave properties. Which assumption is chosen often depends on which phenomenon or experiment is being considered.

3.2 Atoms and molecules

Atoms consist of positively charged protons and neutral neutrons forming the nucleus, and negatively charged electrons circling it. The electrons can be considered as being arranged in well-defined configurations described by quantum mechanics [24], where each configuration has an energy associated with it. This is often depicted by an energy level diagram as shown in Figure 3.3.

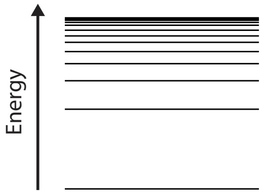

Figure 3.3. *A schematic energy level diagram of an atom.*

A molecule is formed by two or more atoms that are bound together and settle at a mean internuclear distance (typically of the order of a few Å) such that the total energy of the whole system is minimised. Apart from the discrete energy states that atoms have, molecules also have vibrational and rotational energy levels. These energy levels exist due to the motions of the atoms with respect to each other (see Figure 3.4).

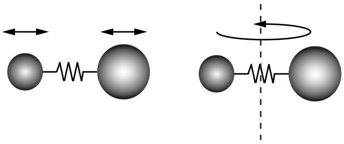

Figure 3.4. *The origin of vibrational and rotational energy levels in a molecule.*

The bond between the atoms in a molecule is elastic and will stretch and compress with a certain frequency related to the mass of the nuclei and the elasticity of the bond. The compression and extension of the bond can be likened to the behaviour of a spring giving rise to the simple harmonic oscillator model. This model is often used in the literature as a good starting model when discussing vibrational levels of a molecule. A more expanded potential model is the Morse function, which is an empirical expression, derived by P. Morse, depicted in Figure 3.5. The shape of the potential curve from this expression also takes into account the fact that a molecule can break and dissociate into atoms when the bond is stretched to a certain extent. The separation between the energy states due to vibration is of the order of 0.1 eV where spectroscopy in the IR region is applicable, in contrast to the energy difference of electronic states which is a few eV, suitable for spectroscopy in the visible and UV region.

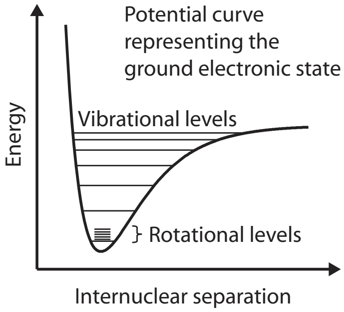

Figure 3.5. *Illustration of an electric state of a molecule according to the Morse function with vibrational and rotational energy levels indicated.*

The rotational energy levels of a molecule occur due to rotation around the centre of mass of the molecule. The energy levels due to rotation are separated by about 0.001 eV, suitable for spectroscopy in the microwave region [25].

3.3 Physical processes

This section will describe the fundamental processes absorption, stimulated emission, spontaneous emission and fluorescence that can occur when electromagnetic radiation interacts with an atom or a molecule. Scattering phenomena will also be discussed. The description of these processes follows the one presented in Ref. 26.

3.3.1 Absorption

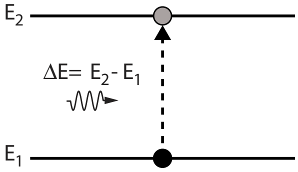

Figure 3.6. *Absorption of a photon corresponding to the energy difference between two states involved in the transition.*

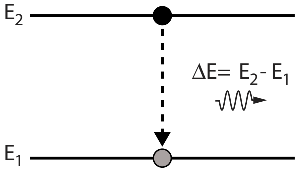

Figure 3.7. *Spontaneous emission of a photon with the energy corresponding to the difference between the two states involved in the transition.*

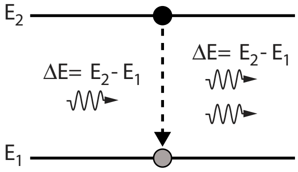

Figure 3.8. *Stimulated emission. An incoming photon, with an energy corresponding to the energy difference between the two states involved in the transition, stimulates the atom to decay. A photon with the same properties as the incoming one is emitted.*

Consider two energy states, 1 and 2, of an atom, with energies, E_1 and E_2, respectively. The atom is initially found in state 1. If the energy of the incoming photon corresponds to the energy difference between the two energy states it can be absorbed. The energy of the photon is then transferred to the atom by exciting it to level 2; see Figure 3.6. The rate of change of the population in level 1, $\left(\frac{dN_1}{dt}\right)_{abs}$, must be proportional to the population of the level, N_1, and to the absorption rate, W_{12}, as expressed by

$$\left(\frac{dN_1}{dt}\right)_{abs} = -W_{12} \cdot N_1, \tag{3.2}$$

where W_{12} is proportional to the absorption cross-section, σ_{12}, and the intensity of the incoming radiation, F, as

$$W_{12} = \sigma_{12} \cdot F, \tag{3.3}$$

where σ_{12} depends on the particular transition considered in the absorption process.

3.3.2 Spontaneous emission

If an atom has been excited to energy level 2, it tends to decay back to energy level 1, which is at a lower energy. The redundant energy must then be released in some way. One possibility to do this is by spontaneous emission of a photon with an energy corresponding to the energy difference between the two states involved; see Figure 3.7.

The rate of change of population in level 2 due to spontaneous emission, $(\frac{dN_2}{dt})_{sp}$, depends on the rate of spontaneous emission, A, and the population of the level, N_2, according to

$$\left(\frac{dN_2}{dt}\right)_{sp} = -A \cdot N_2. \tag{3.4}$$

The positive constant A is inversely proportional to the lifetime of the state, τ_{sp};

$$A = \frac{1}{\tau_{sp}}. \tag{3.5}$$

3.3.3 Stimulated emission

Another way for an excited atom to release its energy when decaying to the lower state is by stimulated emission. An incoming photon with energy corresponding to the energy difference between the states considered in the transition can stimulate the atom to decay. During stimulated emission, an additional photon to the incoming one is emitted with exactly the same phase, direction and energy as the incoming one; see Figure 3.8.

The rate of change of population in level 2 due to stimulated emission, $(\frac{dN_2}{dt})_{st}$, can be written as

$$\left(\frac{dN_2}{dt}\right)_{st} = -W_{21} \cdot N_2, \tag{3.6}$$

where W_{21} is the rate of stimulated emission, which is equal to;

$$W_{21} = \sigma_{21} \cdot F. \tag{3.7}$$

σ_{21} is the stimulated emission cross-section and depends on the particular transition being considered. The similarities between Eq. 3.2 and Eq. 3.6 should be noted. If the two states considered are non-degenerate, then $W_{12} = W_{21}$ (which also means that $\sigma_{12} = \sigma_{21}$). In the case of degenerate states (when the state consists of a number of sublevels with the same energy) the two constants g_1 and g_2 can be introduced representing the number of sublevels in the states. This results in

$$g_1 W_{12} = g_2 W_{21} \Rightarrow g_1 \sigma_{12} = g_2 \sigma_{21}. \tag{3.8}$$

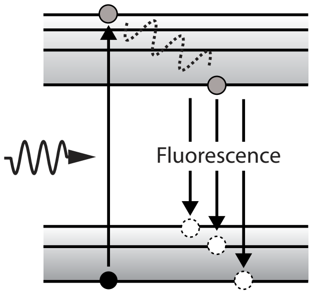

Figure 3.9. *Illustration of fluorescence.*

3.3.4 Fluorescence

Basic principle

Fluorescence can be considered as emitted light during the relaxation of an excited atom or molecule, as depicted in Figure 3.9. An atom or molecule can also decay from a state with higher energy to a state with lower energy without the emission of light. This process, known as quenching, is a non-radiative decay. The energy is then released by collision processes with surrounding atoms or molecules and results in heat generation. The longer the lifetime of the state the higher is the possibility for non-radiative decay. In the gaseous phase, higher pressure also results in a higher probability of quenching. At lower pressure, quenching can be neglected and strong fluorescence is obtained, while at atmospheric pressure the fluorescence can be reduced by a factor of 10^3 to 10^5 [27].

An excited molecule will, through internal conversion, very rapidly end up in the lowest excited state (on a picosecond time-scale), depicted as a dotted wave in Figure 3.9. From here the molecule can decay back to the levels within the ground state through a non-radiative process or under emission of fluorescent light (on a nanosecond time-scale). In the liquid and solid phase, the energy levels are not discrete as in the case of free atoms or molecules in the gaseous phase. Rather, the energy levels consist of a continuum of levels due to the interaction between the different molecules. The fluorescence spectrum will then arise from an assembly of molecules and consists of many superimposed lines to give a smooth appearance.

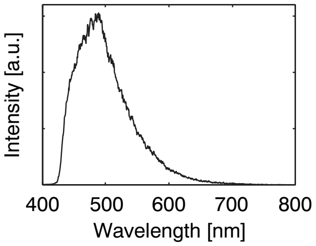

Figure 3.10. *A typical fluorescence spectrum of normal tissue illuminated by light at 405 nm.*

Figure 3.10 shows a typical fluorescence spectrum of tissue illuminated by light at 405 nm. The spectrum is built up of contributions from various fluorophores, for example collagen, elastin, and NADH. The excitation wavelength and corresponding emission maxima for the different fluorophores are discussed in Ref. 28.

Photodynamic therapy

The fluorescence spectrum can be used in medicine to characterise tissue. A therapeutic treatment, which has been developed, based on knowledge of molecular interaction, is photodynamic therapy (PDT). This is a treatment for some types of cancers. It may also be used to treat some non-cancerous conditions of the skin and eye [29–31]. For a photodynamic effect to occur, three basic elements are needed; photosensitizer, light and oxygen. The photosensitizer can frequently be seen as a tumour-seeking agent, which is administered in a stable form systematically or topically to the body and will accumulate to a higher degree in the diseased cells. The lesion under treatment is then exposed to light of a specific wavelength which excites the sensitizer; see Figure 3.11. The sensitizer molecule returns to the ground state after a certain time and can release its energy in three different ways, namely, emission of heat, emission of light, or conversion to an intermediate energy state (triplet state) which is the case illustrated in Figure 3.11. In the triplet state the sensitizer can convert molecular tissue oxygen to form singlet oxygen. The singlet oxygen can then react with the cells and cause functional and structural damage which leads to cell death and bleaching of the sensitizer.

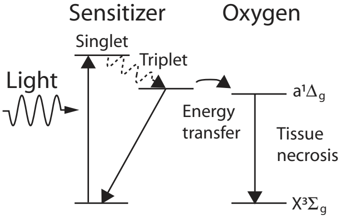

Figure 3.11. *A schematic drawing of the physical mechanism behind photodynamic therapy, PDT, with its three basic elements, light, photosensitizer and oxygen causing cell death.*

The effect of the treatment can be studied by recording the fluorescence of the tissue before and after PDT, which was done in Paper **IX**. In this particular paper the PDT effect is investigated by using a photosensitizer called Temoporfin with a fluorescence peak at 652 nm. The substance is topically applied on skin tumours. The amount of photosensitizer fluorescence remaining after the treatment compared to before treatment was used to determine the effect of the treatment. In Figure 3.12 typical spectra recorded before and after treatment at the centre of a tumour during this study are shown. By comparing the intensity of the peak at 652 nm, a bleaching of about 70% was obtained in this particular case.

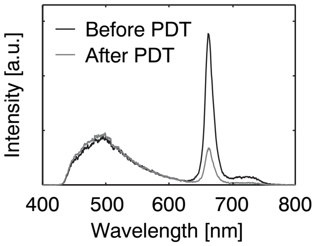

Figure 3.12. *Typical recorded spectra before and after PDT treatment.*

Many different tumour-seeking agents exist, such as phtalocyanine and TOOKAD, developed and used for different types of cancers. In this thesis we will not discuss different photosensitizers, but refer to Refs 32, 33. In contrast to many other treatments for cancer, PDT is not known to have any form of cumulative toxicity. Therefore it can be repeated if required without any danger.

3.3.5 Light scattering

When light interacts with matter it may be scattered. There are two different types of scattering processes; elastic scattering and inelastic scattering which will be discussed in the current section. Elastic scattering basically means that a photon encounters a particle and changes its direction but retains its energy; see Figure 3.13**a**. In the case of inelastic scattering both the direction of the photon and its energy will be changed; see Figure 3.13**b**. The inelastically scattered photon can either gain energy or lose energy in the interaction event.

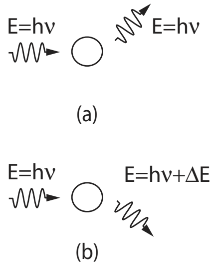

Figure 3.13. ***a*** *Elastic scattering; the scattered photons change the direction but remain the same energy.* ***b*** *Inelastic scattering; the scattered photons change both direction and energy.*

Rayleigh and Raman scattering

When light interacts with particles which are much smaller in size than the wavelength of the light, Rayleigh scattering can occur. This is an elastic process. This process can be seen as excitation by the injected light to a virtual energy level and very rapid decay back to the original state with light emission at the same energy but in a new direction; see Figure 3.14. Rayleigh scattering has a strong wavelength dependence (λ^{-4}) which means that blue light is scattered much more than red light. In the atmosphere, this process is often used to explain why the sky is blue; since the blue wavelength is scattered to a greater extent than longer wavelengths, one then experiences blue light coming from all regions of the sky.

Raman scattering is similar to Rayleigh scattering with the difference that it goes through an energy change, making it an inelastic scattering process. The molecule is excited to a virtual energy level but de-excited into a different energy level, see Figure 3.14. The emitted photon can both gain and lose energy, resulting in Anti-Stokes and Stokes Raman lines, respectively. In the case of Stokes scattering the molecule absorbs energy while in the case of Anti-Stokes scattering the molecule loses energy [27].

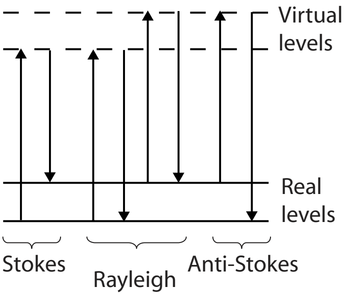

Figure 3.14. *Illustration of Rayleigh and Raman scattering.*

Mie Scattering

Mie scattering may occur when the size of the particle is of the same order or larger than the wavelength of the light. The behaviour of the scattered light is more complex than Rayleigh scattering. It does not depend only on the size of the particle but also on the shape and the index of refraction. Mie theory considering spherical particles is frequently a starting point in the investigation of light interaction with biological tissue, since the cellular structures in the tissue are of the order of hundreds of nanometers to a few micrometers, which is comparable in dimension to the wavelengths generally used in biomedical applications [34, 35].

Chapter 4

Tunable laser spectroscopy

Spectroscopy is considered as the study of the interaction between radiation and matter, as discussed in the Introduction. It has been used for decades for numerous applications. Lasers are nowadays commonly used to pursue spectroscopy of gases. In this chapter the basic principles of the light source mostly used in this thesis will be presented, namely, tunable semiconductor lasers. Before these lasers are introduced a brief overview will be given of the basic principles of laser light and its characteristics. In the final section gas absorption spectroscopy based on the Beer-Lambertian law will be presented together with some basic ideas that are needed to understand the spectral signals generated. To achieve high sensitivity when performing gas absorption spectroscopy a technique referred to as wavelength modulation spectroscopy (WMS) is commonly used. The basic idea is to shift the detection to higher frequencies to minimise the 1/f noise. This method is also described in the last section together with a brief overview of interference fringes, originating from interference between surfaces in the light path between the light source and the detector. In many cases these fringes set the detection limit for gas absorption measurements when WMS is applied.

4.1 General principles of laser light

Laser is an acronym of Light Amplification by Stimulated Emission of Radiation and is, as the name implies, amplified light which is based on stimulated emission (discussed in Section 3.3.3). The action of lasing was first seen experimentally in 1960 [36] and was based on work published a few years earlier. This work led to the Nobel prize for 1964 being awarded to N. Basov, A. Prokhorov and C. Townes [37, 38]. Since then lasers have become one of the most rapidly growing technologies in the world.

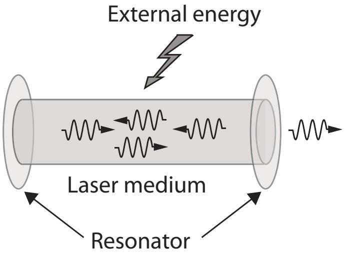

Figure 4.1. *Operational principle of a laser with its three basic elements; external energy source, laser medium, and resonator.*

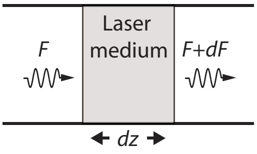

Figure 4.2. *Illustration of photon flux change when propagating through a medium where absorption and stimulated emission can occur.*

A laser device consists of three basic elements, namely, an external energy source or pump, an amplifying medium or laser medium, and an optical cavity or resonator (see Figure 4.1). To achieve laser operation a prerequisite is population inversion in the laser medium. Assume a system with two energy states. If more atoms or molecules exist in the higher state than in the lower state the system is said to have population inversion. This is created and maintained by the pump, which is an external energy source. It can be optical, electrical, chemical, or thermal in nature. The pump energy is absorbed by the laser medium. The most important requirement of the laser medium is its ability to support population inversion between the two energy levels involved in the laser action (in practise this requires a third energy level). The laser medium is the part of the laser which determines the wavelength of the laser radiation depending on the transition used for lasing. The medium may be a gas, liquid or solid (the case of a semiconductor medium will be further discussed in Section 4.2). Due to the wide selection of media, laser light is available from the deep ultraviolet region well into the infrared region. The laser medium is placed into an optical resonator, which usually consists of two mirrors directing the photons back and forth through the laser medium, creating a standing wave by constructive interference in the cavity, to achieve amplification. One of the mirrors has 100% reflectivity while the other has somewhat less to allow the laser beam to propagate out through the cavity [23, 39].

In the laser medium, amplification is obtained through stimulated emission. Assume that a beam of photons, with the flux F, is injected into the medium in the z-direction, see Figure 4.2. The difference of flux in this direction before and after the medium will then be dF due to absorption and stimulated emission (assuming that spontaneous emission can be neglected). Absorption will remove photons and stimulated emission will add photons. If S is the cross-sectional area of the beam, SdF must be equal to the difference between stimulated emission and absorption events occurring in the shaded area in the figure per unit time. The difference in flux can then be written as

$$dF = \sigma_{21} F \left[N_2 - \left(\frac{g_2 N_1}{g_1} \right) \right] dz, \tag{4.1}$$

where σ_{21} is the stimulated emission cross-section, N_1 and N_2 the population in two states involved in the process, and g_1 and g_2 their degeneration. The relationship between absorption cross-section and emission cross-section has been used (Eq. 3.8) which states that

$$g_2 \sigma_{21} = g_1 \sigma_{12}. \tag{4.2}$$

To obtain a positive dF, or, in other words, for the medium to behave as an amplifier (i.e., $dF/dz > 0$), N_2 must be larger than

g_2N_1/g_1. This means that a population inversion has to exist in the medium [26].

The first laser, operating with ruby (aluminium oxide with chromium), was based on a three-level system [36] (see Figure 4.3**a**). The Cr^{3+} ions are raised by the external source from level 1 to level 3 and decays to level 2, which is a state with a much longer lifetime (i.e., $\tau_3 << \tau_2$). The laser action then occurs between level 2 and 1 where a population inversion has been achieved. This scheme involves the ground state (level 1) of an atom, which is a well-populated state and therefore the pumping process needs to be very efficient. This difficulty can be avoided by using one more state, in an arrangement called a four-level laser (see Figure 4.3**b**). In this scheme, the atoms are raised from level 1 to level 4 by an external pumping process from where they rapidly decay to level 3. Inversion population is then created between level 3 and 2 where level 2 is chosen with a very short lifetime [27].

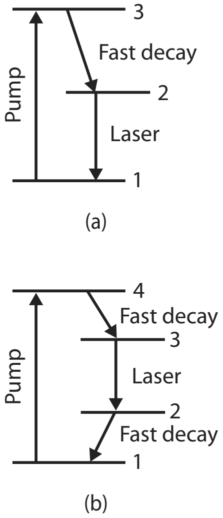

Figure 4.3. ***a*** *Three-level laser scheme.* ***b*** *Four-level laser scheme.*

Characteristics of laser light are that it is coherent, directed and monochromatic. This is due to the fact that all photons have been created through stimulated emission and therefore have the same phase and direction. Strongly monochromatic light is achieved since oscillation can only occur corresponding to the resonant frequency of the cavity, creating constructive interference (standing-waves) of the light given as

$$L = q \cdot \frac{\lambda}{2n}, \tag{4.3}$$

where L is the length of the cavity, n the refractive index in the cavity and q an integer number. Two examples of different numbers of q, creating standing waves through constructive interference inside the cavity, are depicted in Figure 4.4. Normally the q numbers are much larger. Generally, a number of modes will oscillate under the gain profile of the medium, where population inversion exists, and it is said that the laser operates in multi-mode.

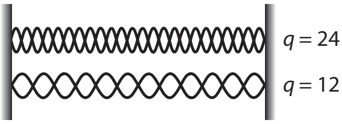

Figure 4.4. *Example of standing waves created inside the cavity by constructive interference with $q = 24$ and $q = 12$, respectively.*

4.2 Tunable semiconductor lasers

Since the introduction of semiconductor lasers in the 1960's [40–43], only two years after the first laser was demonstrated, they have today become a common device in our daily life. Their small size, low cost and tunability are some of the reasons behind their popularity in many opto-electronic devices. Today semiconductor lasers can be found in applications ranging from everyday items such as laser pointers and CD players, to devices used in research projects such as the cooling and trapping of atoms. This section presents the basic principle of semiconductor lasers, or laser diodes, and gives an overview of the different designs used and their characteristics.

4.2.1 Basic principles

The semiconductor laser is based on the interaction between electromagnetic radiation and a semiconductor. Electrons in semiconductors can interact with radiation in the same ways as they do in atoms; by spontaneous emission, by stimulated emission and by absorption (processes discussed in Section 3.3). The electron transitions in the semiconductor lasers occur between bands of states.

The basic operating principle for semiconductor lasers is shown in Figure 4.5. Assume a semiconductor at zero temperature with a valence band completely filled with electrons while the conduction band is completely empty (see Figure 4.5**a**). Some electrons are excited from the valence band to the conduction band by a suitable pumping process. After a very short time, typically a few picoseconds, electrons in the conduction band will drop down to the lowest unoccupied state in the conduction band at the same time as electrons in the top of the valence band fall down to lower, unoccupied levels in the valance band, leaving "holes" in the top of the valence band. Two Fermi levels can now be introduced, E'_{F_V} and E'_{F_C} for the valence and conduction band, respectively. The Fermi level defines the energy at which the states below are completely occupied by electrons and with empty states above. Light emission can now occur when electrons in the conduction band recombine with holes in the valence band (see Figure 4.5**b**) [26].

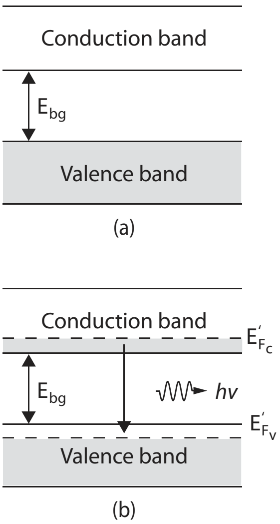

Figure 4.5. *Operation principle of a semiconductor laser.*

The first semiconductor laser demonstrated was called a homostructure laser. It was made from chips of heavily doped gallium arsenide [40–43]. In the homojunction structure, two semiconductors are grown together; one n-doped (containing extra electrons not bound to the neighbouring atoms) and one p-doped (not electrons enough to completely bond with the neighbouring atoms thus resulting in holes in the valence band). An energy level diagram of a p-n junction is shown in Figure 4.6**a**.

In thermal equilibrium, the Fermi level must be the same throughout the system. The doping levels, the donor and acceptor concentration, are chosen to assure that the Fermi level, indicated in the figure by a dotted line, lies within the conduction band on the n-doped side and within the valence band on the p-doped side. The holes and the electrons cannot recombine due to the potential barrier. However, if a positive voltage V_{fb} (pumping process), called a forward bias voltage, is applied to the p-type region the potential barrier is lowered, see Figure 4.6**b**. This will allow electrons to be injected into the conduction band from the n-type region, while holes will be injected into the valence band from the p-type region. If the voltage is chosen such that the product $e \cdot V_{fb}$ approaches the band gap energy E_{bg}, population inversion will be created in the active region. Stimulated emission of light will occur in the active region with photon energy corresponding to the band gap. To provide feedback for laser action, two parallel sides

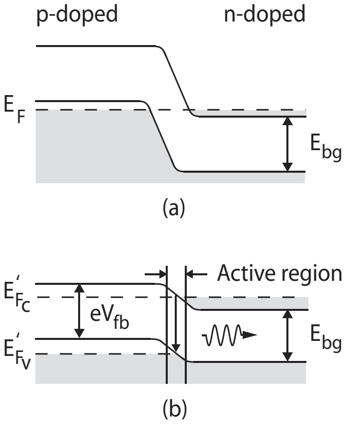

Figure 4.6. **a** *Energy level diagram of a p-n junction.* **b** *Junction with a forward bias voltage applied comparable to the band gap.*

are polished for semitransparent mirror action. A resonator is thus formed.

4.2.2 Tunability

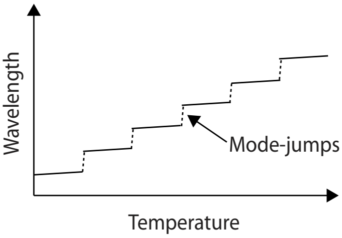

Figure 4.7. *A schematic drawing of wavelength tunability of a semiconductor laser by changing the operating temperature. Mode-jumps are indicated.*

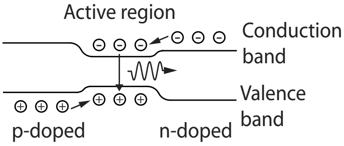

Figure 4.8. *A schematic drawing of a semiconductor laser based on double-heterostructure.*

The wavelength of the emitted radiation is, as mentioned, determined by the band gap of the semiconductor material used. Today diode lasers are available from the UV region to the infrared region. The band gap of the semiconductor depends slightly on the temperature, which can be used to tune the wavelength of the light. A typical tuning rate is about 0.3 nm/°C. Normally, diode lasers allow temperatures between 10°C to about 50°C, which means that the wavelength can be tuned through about 10 nm. An alternative method and more convenient to change the wavelength is to change the driving current. This results in a temperature change of the junction [44].

It is not only the band gap that changes with temperature but also the cavity length and the refractive index. As discussed in Section 4.1, the cavity length will determine which wavelength will be amplified by constructive interference; see Figure 4.4. The cavity change leads to mode-jumps, meaning that not all wavelengths in the tuning region offered by temperature changes are available. This is depicted in Figure 4.7 [44]. Clearly, mode-jumping behaviour is normally highly unwanted. Different designs have been developed to overcome this problem, which is discussed in the next section. However, the phenomenon can also be turned into an advantage when performing diode laser gas spectroscopy. If a rapidly mode-jumping laser, switching between many individual modes, is used, these modes will sometimes hit an absorbing wavelength in a complex molecular spectrum, and sometimes hit in between. The transmitted intensity will depend both on the presence of absorption as well as the output power of the specific mode. By comparing the intensity pattern obtained for a laser beam coming from a region of unknown gas composition with the clear pattern obtained for a gas-filled reference cell, the amount of the particular gas can be estimated (Paper **XIII**).

4.2.3 Designs

Since the introduction of the semiconductor laser, several alternative designs to the homostructure have been developed. The main problem with the homostructure laser is the high threshold current required to obtain population inversion in the active region and therefore making room temperature operation difficult due to strong absorption of the semiconductor material leading to excessive temperature rise. A few years after the homostructure laser was introduced, a more efficient, double-heterostructure scheme was introduced [45, 46]. This structure is based on a low band gap material sandwiched between two high band gap layers, as depicted in Figure 4.8. This allows more of the electron-hole pairs to contribute to amplification and less light to be absorbed by the surrounding layers, resulting in a higher concentration of the beam within the active region [47].

The most common type of diode lasers, and the most economical ones are those called Fabry-Pérot diodes. These lasers are based on the description above where two artificial mirrors (different refractive index on opposite sides of the active medium) are used to create a cavity. The drawback of these lasers is that they are noisy and often operate in longitudinal multi-mode (not only one single wavelength is emitted). To achieve single-mode operation of these lasers an external cavity can be used. Two different designs are commonly used, namely, the Littrow and the Littman configuration, depicted in Figure 4.9 [48, 49]. These are based on using a grating to back-couple the light emitted from the diode laser into the cavity. The first diffraction order is coupled back to the laser while the zeroth order is used as the output. In the Littrow configuration only one component is used, namely, a diffraction grating, and the wavelength is tuned by rotating this grating. In the Littman configuration the diffraction grating is fixed while a rotatable mirror is used for the tunability. The advantage of the Littman configuration is that as the grating is fixed the direction of the output beam is not affected during tuning, in contrast to the Littrow configuration. On the other hand, the Littrow configuration is more compact.

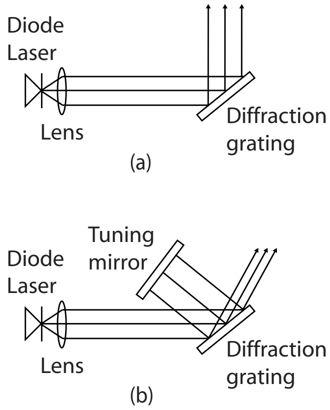

Figure 4.9. *A schematic drawing of external cavity diode laser designs using* ***a*** *the Littrow configuration.* ***b*** *the Littman configuration.*

More expensive diode lasers are the distributed feedback (DFB) laser and the distributed Bragg reflector (DBR) laser. These lasers can be said to be Fabry-Pérot single-mode lasers containing an integrated grating structure. In the DFB laser the grating is placed within the active region where one of the reflecting mirrors is replaced by a grating along the cavity. In the DBR laser the grating is located outside the active region.

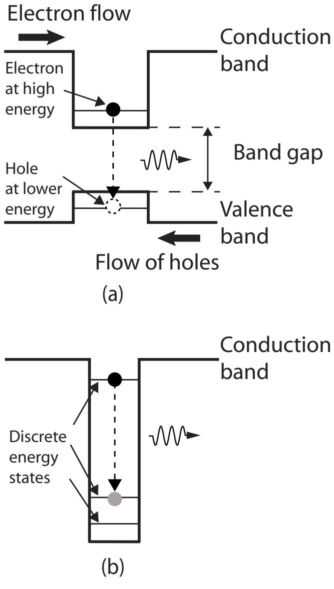

Figure 4.10. *Schematic drawing of the difference of laser action between a common semiconductor laser (****a****) and a quantum cascade laser (****b****).*

In contrast to the semiconductor lasers discussed, where the laser action occurs between the conduction band and the valence band, the laser action in quantum cascade lasers, QCLs, involves only the conduction band; see Figure 4.10. These lasers were introduced in 1994 [50–52] and are often compared to an electronic waterfall as "when an electric current flows through a quantum-cascade laser, electrons cascade down an energy staircase emitting a photon at each step". The QCLs operate in the mid-infrared region. They consist of sandwiched thin layers of semiconductor materials. These layers produce coupled quantum wells working together as active regions in which the laser action will occur through the relaxation of electrons. The electron in one of the wells (active region) tunnels into the next well (through the injection/relaxation region) and stimulates the next photon to be emitted and so on, as depicted in Figure 4.11. This process of a single electron causing the emission of multiple photons as it traverses through the QCL structure gives rise to the name cascade. The wavelength of the emitted light is determined by the thickness of the layers of the semiconductor materials, in contrast to the other diode lasers discussed, where the band gap sets the wavelength. The stack of active regions and injection regions is clad with two thick semiconductor layers with low refraction index, that serve as a waveguide to direct the light produced along the active regions.

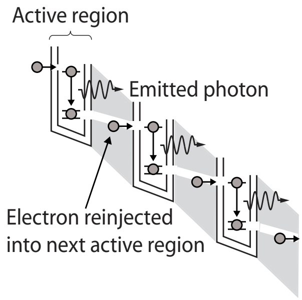

Figure 4.11. *Operating principle of quantum cascade lasers.*

4.3 Gas absorption spectroscopy

Laser-based gas absorption spectroscopy utilises spectral absorption lines to examine the quantity of a certain molecule present in a gaseous mixture. The absorption lines represent transitions between different energy states of the molecule, which can originate from a change in the electronic, vibrational or rotational configuration of the molecule (discussed in Section 3.2).

When light is propagating through an absorbing sample such as a gas, it will be attenuated according to the Beer-Lambertian law if the frequency of the light corresponds to an allowed transition. This law will be discussed in this section, but first the processes influencing the strength and the shape of the absorption lines will be briefly discussed. In gas absorption spectroscopy it is important to choose the absorption line carefully. Different factors affecting the decision will be discussed. To achieve high sensitivity a technique called wavelength modulation spectroscopy can be used. This technique decreases the influence of 1/f noise by shifting the detection to a higher sampling frequency, and this is further discussed in this section. Finally, optical interference fringes will be discussed. In many of the experiments carried out for this thesis, the minimisation of the influence of the optical fringes, in order to achieve high sensitivity in gas absorption spectroscopy, have been the most prominent issue.

4.3.1 The intensity of spectral lines

Depending on which transition of an atom or molecule is to be investigated, different intensities of the absorption line occur. The intensity depends on four different factors; the transition probability, the population of the initial states, the concentration of the gas and the optical path length of the light within the sample. In this section an overview concerning these factors will be given.

Transition probability

The probability for a transition to occur is given by quantum mechanics. This requires a knowledge of the precise quantum mechanical wave functions of the two states considered for the transition, which is beyond the scope of this thesis, but is thoroughly described in Ref. 24. However, to determine whether a transition is forbidden or allowed (whether the transition probability is zero or non-zero) the selection rules, which state that the quantum numbers characterising the states cannot change randomly, can be used.

Population of states

Assume the case that a transition has the same probability to occur from two different states to a third state. It is then obvious that the state with the highest population will give rise to the most intense spectral line. In other words, the population of a state is significant for the intensity of the spectral line.

At thermal equilibrium the population of an energy state is given by the Boltzmann distribution. Assume N molecules distributed between two different energy states with energies E_1 and E_2. The ratio between the population at each level is given as

$$\frac{N_2}{N_1} = e^{\frac{-\Delta E}{kT}}, \tag{4.4}$$

where ΔE is the energy difference between the two states ($E_2 - E_1$), T is the temperature [K], and k is a universal constant known as Boltzmann's constant and is equal to $1.38 \cdot 10^{-23}$ JK^{-1} [25]. This shows that, to some extent, it is possible to influence the intensity of the spectral lines by changing the temperature of the sample.

In some applications, such as combustion, it is of great interest to be able rapidly to determine the temperature of a sample. Knowledge about the change of population in the energy levels in relation to temperature can then be used. By detecting more than one absorption line and comparing their relative intensity, the temperature of the sample can be determined [53–56].

Optical path length and concentration

That the path length through a sample and the concentration of the absorber in the sample influence the intensity of the spectral line is obvious. The longer the light travels in a sample and/or the higher the concentration of the absorber in the sample is the higher is the probability for the light to be absorbed. It might seem logical to expect that a path length twice as long would give twice the absorption and *vice versa* for the concentration. However, this is not the case for large absorptions. The relationship between the incident and transmitted intensities of radiation, the concentration of the absorber and the optical path length is further discussed in Section 4.3.3. It should be noted that nothing can become darker than black, which is a basic non-linearity. If all light is absorbed no transmitted light is obtained. The detected signal will not change if the path length is enhanced or the concentration increased.

For air pollution measurements a retro-reflecting mirror is commonly used to increase the path length by a factor of two. The light is then sent from one side of the sample and a mirror is placed on the other side to reflect the light back again, where it is detected; see Figure 4.12**a**.

In gas absorption spectroscopy measurements it is common to use a multi-pass cell to increase the path length and thereby enhance the absorption; see Figure 4.12**b** [57, 58]. The cells are designed, with two high-reflectivity mirrors, so that the incident light will be reflected, in some cases up to a hundred times, within the cell containing the absorbing gas. By using multi-pass cell with a typical length of 0.3 – 1 m the optical path length can be increased to about 100 m.

As will be seen later in Chapter 6, an increased path length can also be achieved by taking advantage of scattering media. In this particular chapter the technique denoted GASMAS (GAs in Scattering Media Absorption Spectroscopy) will be discussed. The parallels between the GASMAS method and long path absorption are discussed in Paper **XIV**.

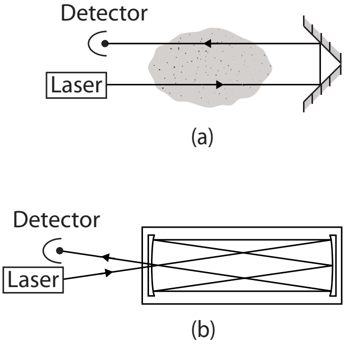

Figure 4.12. *Methods to increase the optical path length.* **a** *Remote sensing using a retro-reflector.* **b** *Multi-path absorption cell.*

4.3.2 The width of spectral transitions

So far we have described transition lines without discussing their actual sharpness. We have stated that the energy of the incident light has to be precisely the right frequency, corresponding to the energy difference between two energy states, in order for it to be absorbed. However, this would result in an infinitely sharp line width which is not the case. The experimentally recorded line width arises from the facts, *(i)* that the transitions in atoms and molecules are not infinitely sharp but have a certain fuzziness *(ii)* that the line width of the light source used in the measurements is not infinitely sharp. In this section different broadening processes giving rise to the line width of spectral transitions will be discussed.

The natural line width

The lower boundary of a sharp line is determined by the Heisenberg uncertainty principle. This states that if a system exists in an energy state for a limited time, Δt, the energy of that state will be uncertain to an extent $\Delta E = h\Delta\nu$ where

$$\Delta t \times h\Delta\nu \approx \frac{h}{2\pi} \approx 10^{-34}\text{Js}. \quad (4.5)$$

The uncertainty of the frequency, $\Delta\nu$, is related to the lifetime of the state, τ, as

$$\Delta\nu = \frac{1}{2\pi\tau}. \quad (4.6)$$

This line broadening, having a Lorentizian profile, is often referred to as the natural line width of the spectral transition and is typically 0.1 – 100 MHz [25].

Doppler broadening

Atoms or molecules in the liquid or gaseous phase are in continuous motion at various velocities and directions in relation to the incident light. Thereby atoms and molecules can emit and absorb light within a certain frequency interval. Shifts to both higher and lower frequencies occur due to this random movement. This will cause a broadening of the absorption line, called Doppler broadening, by which different atoms or molecules contribute to different parts of the line shape. Doppler broadening results in a Gaussian line profile, g_D, defined as

$$g_D(\nu - \nu_0) = \frac{1}{\Delta\nu_D}\sqrt{\frac{ln(2)}{\pi}}exp\left(-\frac{ln(2)(\nu-\nu_0)^2}{\Delta\nu_D^2}\right). \qquad (4.7)$$

The Half Width at Half Maximum (HWHM) of the line profile, $\Delta\nu_D$, is given by

$$\Delta\nu_D = \nu_0\sqrt{\frac{2kT}{Mc^2}ln(2)} = 1.074 \cdot 10^{11}\frac{1}{\lambda_0}\sqrt{\frac{T}{M}}, \qquad (4.8)$$

where λ_0 is the wavelength [nm] at the line centre, M is the molecular mass, and T is the temperature [K] [27]. For example for molecular oxygen at $\lambda_0 = 760$ nm, which is the transition most frequently studied in this work, $\Delta\nu_D \approx 600$ MHz at room temperature.

Pressure broadening

Another process giving rise to broadening of the spectral lines is the pressure broadening process. This arises from the fact that the atoms or molecules investigated undergo frequent collisions with each other. This interaction results in a broadening of the line width with a Lorentzian line shape, g_L. With increasing pressure this broadening mechanism will become more and more prominent. The line profile can be calculated for any temperature and pressure as

$$g_L(\nu - \nu_0) = \frac{1}{\pi\Delta\nu_L\left(1 + \left(\frac{\nu-\nu_0}{\Delta\nu_L}\right)^2\right)}, \qquad (4.9)$$

where ν_0 is the frequency at the line centre, and the HWHM, $\Delta\nu_L$, is defined as

$$\Delta\nu_L(P,T) = \Delta\nu_L(P_0,T_0)\frac{P}{P_0}\left(\frac{T_0}{T}\right)^n, \qquad (4.10)$$

where n is a coefficient that has different values for different gas transitions and $\Delta\nu_L(P_0, T_0)$ is the species-dependent collision width at room temperature and atmospheric pressure and is about 0.5 – 5 GHz [27].

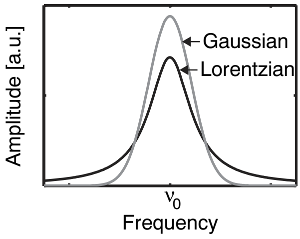

Figure 4.13. *A Gaussian and Lorentizian line profile with the same HWHM and equally strong total absorption.*

Combined broadening

In general it can be said that pressure broadening dominates at high pressure, resulting in a Lorentizian profile, while Doppler broadening dominates at low pressure, giving rise to a Gaussian profile. In the intermediate regime the line profile is determined by a convolution of the two and the line shape has a Voigt profile (which for high pressures turns into a Lorentizian and at low pressure results in a Gaussian profile). No analytical expression exists for a Voigt line profile [59] but an empirical relation has been given for the HWHM as [60]

$$\Delta\nu_V = 0.5346\Delta\nu_L + \sqrt{0.2166\Delta\nu_L^2 + \Delta\nu_D^2}. \tag{4.11}$$

In Figure 4.13 a Gaussian and a Lorentizian line profile with the same HWHM are shown. The areas under the lines are normalised to assume the same total absorption. It can be clearly seen that the peak is higher in the case of a Gaussian line profile and that the Lorentizian profile has wider wings. In the case of atmospheric pressure and room temperature at which most of the experiments in this thesis have been performed, the pressure broadening contribution dominates and it is, as mentioned, of the order of a few GHz.

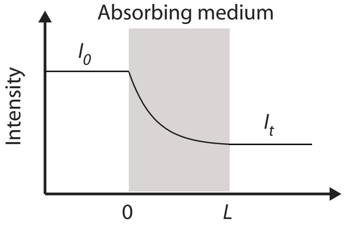

Figure 4.14. *Attenuation of light when propagating through an absorbing gas according to the Beer-Lambertian law (see Eq. 4.14).*

4.3.3 The Beer-Lambertian law

The most fundamental method of spectroscopic gas detection is direct absorption spectroscopy (DAS). This method is based on measuring the intensity of the transmitted light after it has propagated through an absorbing gas and relating it to the initial intensity. The attenuation of the light is described by the Beer-Lambertian law (see Figure 4.14 and Eq. 4.14).

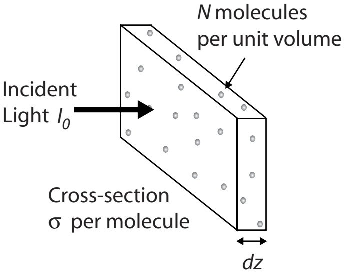

Figure 4.15. *Schematic drawing of a slab of thickness dz with N molecules per unit volume and an absorption cross-section σ (Modified from Ref. 25).*

Consider a beam of light with a specific frequency, ν, and intensity, I_0, which is propagating through a medium with N [m^{-3}] molecules per unit volume, as depicted in Figure 4.15. If the thickness of a slice of the medium is dz, the number of molecules will be $N \cdot dz$ per unit area. Let σ [m^2] describe the absorption cross-section at the specific frequency (the probability of absorption at the specific frequency). After the light has traveled a distance dz the fraction of particles that have absorbed light is equal to $\sigma N dz$, i.e.:

$$\frac{dI}{I_0} = -\sigma N dz. \tag{4.12}$$

When passing through a sample of thickness L [m], the intensity will change from I_0 to I_t, and z will change from 0 to L, which leads to the following equation containing two integrals

$$\int_{I_0}^{I_t} \frac{dI}{I_0} = -\int_0^L \sigma N dz. \tag{4.13}$$

By performing the integration the well-known Beer-Lambertian law is obtained as

$$I_t = I_0 \cdot e^{-\sigma N L}. \tag{4.14}$$

For weak absorption, i.e. low optical density, the Beer-Lambertian law can be rewritten in a linear regime as

$$\ln\left(\frac{I_t}{I_0}\right) = -\sigma N L \approx 1 - \frac{I_t}{I_0} = -\sigma N L \Rightarrow I_t = I_0(1 - \sigma N L) \tag{4.15}$$

where only the first term in the Taylor expansion $\ln\left(\frac{I_t}{I_0}\right) \approx 1 - \frac{I_t}{I_0}$ has been used [24].

4.3.4 Choice of absorption line

To achieve high sensitivity in gas absorption spectroscopy it is important to choose the absorption line wisely. A review of this issue is provided in Ref. 61. Several factors influence which line is best to study. Of course if highest sensitivity is desirable, a line as strong as possible should be used. However, there are many reasons why it is not always possible or most suitable to choose the strongest line available in the wavelength range considered as we will see. When using diode lasers as light sources it may not be possible since the tunability of the diode laser is not always continuous due to mode-jumps; see Figure 4.7. So even if a diode laser is specified to operate with a wavelength close to the strongest line, the line may not be accessible. The characteristics of the laser can also change over time and it may therefore be better to choose a wavelength of the light source with a tunability in a region with many strong lines. This will increase the probability that at least one line will always be accessible.

It is also important, if possible, to choose an absorption line which is isolated from interfering lines from the same or other species present. Absorption of other species can influence the transmission of the light, thereby making it impossible to choose the strongest line available.

In the infrared region (IR), liquid water and water vapour absorb over a wide frequency range. When performing measurements within the human body, an optical tissue window is often discussed. In this wavelength region tissue can be considered as comparatively transparent due to the relatively weak absorption of its major species and thereby offering the possibility to reach deep targets. This window ranges from about 600 nm to 1.3 µm [62]. The lower limit is due to heavy absorption by haemoglobin and the upper limit is due to absorption of water (further discussed in Section 5.1.4, where also the absorption of tissue is depicted in Figure 5.5). In the mid-infrared region (MIR), gas absorption spectroscopy is often performed in one of the two atmospheric windows (3.4 – 5 µm and 8 – 13 µm) where the absorption of water vapour and CO_2 is relatively low. These windows are very rich spectral regions where many gases absorb in their fundamental rotational/vibrational bands.

The choice of absorption lines is made easier with the access to spectral line databases such as HITRAN [63, 64]. This database contains information about more than one million transitions. Information such as the wavelength and intensity of the lines for different temperatures and pressures is available.

4.3.5 Wavelength modulation spectroscopy

The most straightforward method for spectroscopic gas detection is DAS by which the absorption at the line centre is compared with the absorption slightly to the side of the line. However, in the case of weak absorption, this technique is often not used since measuring a small difference in two large signals gives a low detection sensitivity. To improve this, modulation techniques are often applied to reject the large DC-offset related to the transmission and thereby using the dynamics of the electronic system better.

Wavelength modulation spectroscopy, WMS, with second-harmonic detection is a well-known technique for spectroscopic gas detection to increase signal-to-noise ratios (SNR). The technique attempts to increase the sensitivity by shifting the detection to higher sampling frequencies in order to minimise 1/f noise. The method is often referred to as derivative spectroscopy when investigating weak absorption since the appearance of the detected signal at different harmonics is very similar to the corresponding derivative of the absorption profile [53–56, 61, 65–68]. This technique has been used in most of the work presented in this thesis.

In WMS, a fast wavelength modulation is applied to the laser light as the wavelength is slowly scanned across the absorption line under study. The modulation frequency used is typically in the kHz range which is much smaller than the HWHM of the absorption line. The modulation is superimposed on the laser driver current to achieve a frequency variation of the laser light according to:

$$\nu(t) = \bar{\nu} + a_m \cdot cos(\omega t), \tag{4.16}$$

where $\bar{\nu}$ is the constant laser frequency (or slowly varying compared to the sinusoidal modulation due to ramping over the absorption line), a_m is the modulation amplitude and ω is the modulation frequency. The frequency variation leads to the intensity of the laser varying in a similarly way:

$$I_L(t) = I_0 + i_0 \cdot cos(\omega t + \psi), \tag{4.17}$$

where I_0 is the constant laser intensity and i_0 is related to the modulation amplitude. A phase shift, ψ, will also appear between intensity and wavelength modulations.

According to the Beer-Lambertian law (discussed in Section 4.3.3) the intensity of the light detected after propagating through an absorbing medium is

$$I_D(t) = I_0 \cdot \tau(\nu(t)), \tag{4.18}$$

where $\tau(\nu(t))$ is the transmission coefficient, which depends on the absorption coefficient and the optical path length.

By using Eq. 4.16 for the frequency, the transmission coefficient can be written as

$$\tau(\nu(t)) = \tau(\bar{\nu} + a_m \cdot cos(\omega t)). \tag{4.19}$$

This is an even periodic function in ωt and can be expanded in a Fourier cosine series as

$$\tau(\bar{\nu} + a_m \cdot cos(\omega t)) = \sum_{k=0}^{\infty} H_k(\bar{\nu}, a_m) cos(k\omega t), \tag{4.20}$$

where the functions $H_k(\bar{\nu}, a_m)$ are given by

$$H_0(\bar{\nu}, a_m) = \frac{1}{2\pi} \int_{-\pi}^{+\pi} \tau(\bar{\nu} + a_m \cdot cosu) du, \tag{4.21}$$

$$H_k(\bar{\nu}, a_m) = \frac{1}{2\pi} \int_{-\pi}^{+\pi} \tau(\bar{\nu} + a_m \cdot cosu) cos(ku) du, k > 0. \tag{4.22}$$

For weak absorptions and small modulation depths, the kth order Fourier component H_k is proportional to the kth derivative of the absorption signal, which explains why WMS is often referred to as derivative spectroscopy.

In Figure 4.16**a**, a schematic drawing of an absorption profile of a molecule is depicted. The modulation of the laser wavelength transformed to an intensity modulation of the detected signal at different locations of the absorption feature is illustrated. It can clearly be seen that the detected signal will result in a large amplitude fluctuation over the absorption line while the signal is fairly independent of wavelength modulation outside and at the centre of the absorption feature.

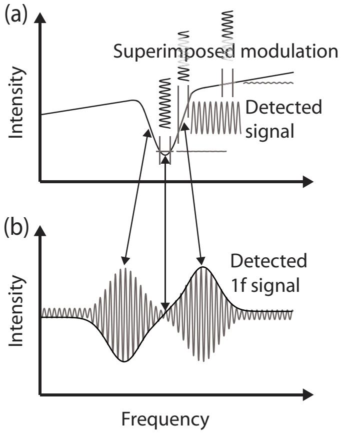

Figure 4.16. ***a*** *Schematic drawing of how the modulation of the laser wavelength is transformed to an intensity modulation of the detected signal at different locations of the absorption feature.* ***b*** *Illustration of detected 1f signal corresponding to the envelope of the harmonic-component of the signal.*

WMS is performed together with phase sensitive detection, using a lock-in amplifier, to isolate a particular harmonic. This detection singles out the component of the detected signal at a specific reference frequency and phase, and detects the envelope of the signal harmonic component. Noise signals at frequencies other than the reference frequency are then rejected and do not affect the measurement. In Figure 4.16**b** the illustration of a detected 1f signal corresponding to the schematic absorption profile depicted in Figure 4.16**a** is shown. Generally, the amplitude of the harmonic components decreases for increasing harmonics, suggesting that 1f detection might be the best choice. However, since the laser output power is increased with frequency due to ramping of the laser current there will be a residual amplitude modulation (RAM) signal also when there is no absorption line. This results in a large offset in the 1f signal requiring a large dynamic range of the detection equipment, which is the main reason why 2f detection is often preferred over 1f detection in WMS.

Figure 4.17 shows an experimentally obtained first-harmonic (1f) signal and a second-harmonic (2f) signal, with the background subtracted, as well as their corresponding direct signal of the R11Q12 absorption line of oxygen. Here the remaining offset of the 1f signal can clearly be seen.

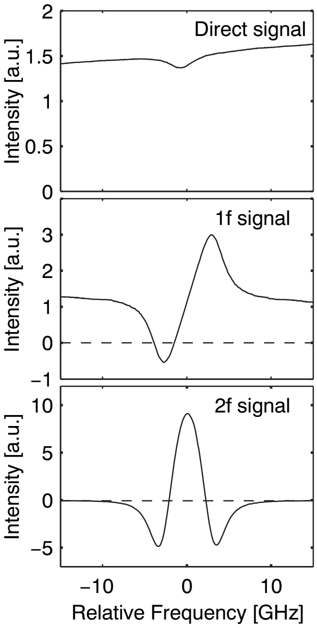

Figure 4.17. *Experimentally obtained signals over an air path of 4.7 m corresponding to an absorption fraction of 0.12. The laser is tuned across the R11Q12 oxygen absorption line at 760.445 nm. The modulation amplitude is chosen to optimise the 2f signal. When recording the direct signal the modulation is switched off.*

The line shape of the 2f signal depends strongly on the modulation amplitude. A too small amplitude will result in a weak and noisy signal, while a too large amplitude will just make the signal broader. The optimal modulation amplitude is somewhere in between. Reid *et al.* describe a procedure to optimise the modulation amplitude in a WMS setup for the 2f signal [65]. Obviously, the optimal modulation amplitude is the one at which the signal is strongest. In Figure 4.18**a** the modulation amplitude has been changed from 1.6 GHz to 8.2 GHz over the R11Q12 signal of molecular oxygen. It can here clearly be observed how the modulation amplitude influences the line-shape of the signal. Reid *et al.* showed that by forming the ratio, R, between the maximum positive value, P, from the baseline of the 2f signal and the maximum negative value, N, from the baseline (indicated in Figure 4.18**b**), the optimal modulation amplitude occurred at a ratio of 1.7. In Figure 4.18**c** and **d**, P and N, and the ratio R are shown for the signals shown in Figure 4.18**a**. It can be seen that for a_m equal to about 6 GHz, P has its maximum and R is approximately 1.7. A ratio of 1.7 corresponds to a modulation index, m, which is the modulation amplitude divided by the HWHM of the absorption line $\left(m = \frac{a_m}{\Delta\nu_{\mathrm{HWHM}}}\right)$, of 2.2. The signals shown were obtained when optimising the setup used for the measurements undertaken in Papers **II**, **III**, **VII** and **XI**.

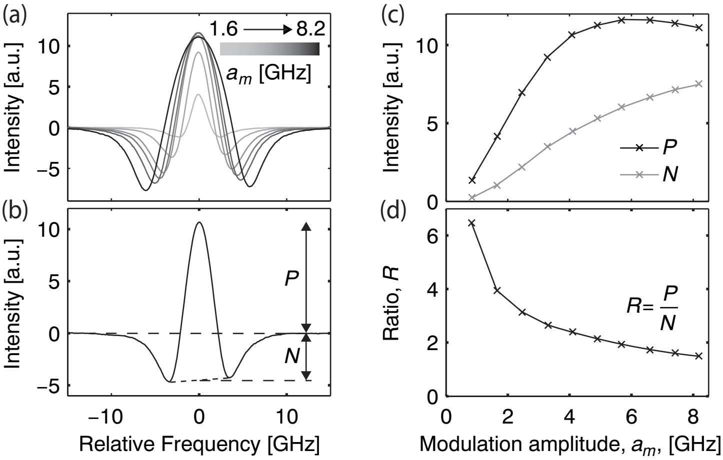

Figure 4.18. *Optimisation of modulation amplitude, a_m, when the laser is tuned across the R11Q12 oxygen absorption line at 760.445 nm according to Ref. 65.* ***a*** *Experimentally obtained signals when changing a_m between 1.6 GHz and 8.2 GHz.* ***b*** *Indications of P and N corresponding to the maximum positive value and maximum negative value from the baseline of the 2f signal, respectively.* ***c*** *P and N as a function of a_m.* ***d*** *The ratio R between P and N.*

4.3.6 Noise - Interference fringes

Many research groups, in different fields, working with optics are daily fighting noise such as 1/f noise (also called flicker-noise) and thermal noise in the electronics. In tunable diode laser spectroscopy, WMS is commonly used, as discussed in Section 4.3.5. This method means that the detection is moved to higher frequencies so that the 1/f noise can be considered as negligible in contrast to interference fringes mimicking the weak absorption line. In practice, these fringes often set the detection limit.

Fabry-Pérot fringes occur through interference of transmitted light between surfaces in the light path [23]. In Figure 4.19**a** a schematic drawing of light being reflected between two surfaces is shown. If the difference in optical path length, Λ, between two transmitted beams corresponds to a multiple, m, of the wavelength according to

$$\Lambda = m\lambda = 2ndcos(\theta), \tag{4.23}$$

where n is the reflective index and d the distance between the two surfaces, the two beams will interfere constructively.

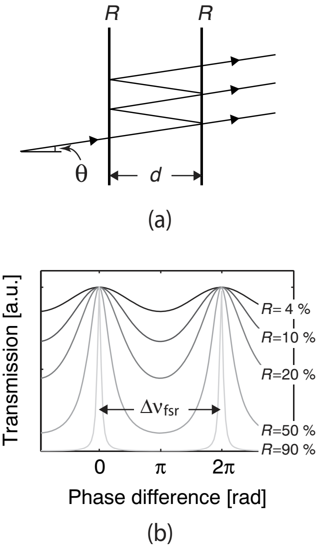

(a)

(b)

Figure 4.19. ***a*** *Schematic drawing of light being reflected between two surfaces.* ***b*** *The transmission or Airy function for different reflection coefficients, R.*

The reflection coefficient, R (further discussed in Section 5.1.1), of the surfaces plays an important role for the variation of the intensity in the fringe pattern. In Figure 4.19**b** the transmittance, T, also called the Airy function in the literature, as a function of the phase difference ($\delta = k\Lambda$ where $k = \frac{2\pi}{\lambda}$) is plotted for different reflection coefficients. The transmission is given by

$$T = \frac{I_T}{I_i} = \frac{1}{1 + [4R/(1-R)^2] sin^2(\delta/2)}, \tag{4.24}$$

where I_T is the intensity of the light after propagation through the sample and I_i the intensity of the incident light. The $4R/(1-R)^2$ term is often called the coefficient of finesse, $\mathfrak{F}$.

In diode laser gas absorption spectroscopy measurements, fringes can mimic absorption lines and thereby become a problem in weak absorption measurements. If the free spectral range, $\Delta\nu_{fsr}$, which is the separation between maxima (indicated in Figure 4.19**b**), is of the same order as the line width of the absorption line, fringes can become a problem. $\Delta\nu_{fsr}$ is defined as

$$\Delta\nu_{fsr} = \frac{c}{2nd}, \tag{4.25}$$

where c is the speed of light. For example, the HWHM of the absorption lines used in this thesis are in the GHz regime. Fringes mimicking these lines occur by the interference between two surfaces separated by a few cm. However, to suppress fringes mimicking the absorption line when performing gas absorption spectroscopy measurements, it is unfortunately not sufficient to avoid distances in this range, as the detected interference fringes are a superposition of many fringes arising from different distances.

By forming the ratio between I_{max} and I_{min} a measure of the contrast can be achieved. Weak absorption can be confused with low contrast fringes. For example for R= 4%, $\frac{I_{max}}{I_{min}}$ ≈1.2.

Different approaches to minimise the influence of optical interference fringes can be used. First of all, it is important to design the optical setup carefully. This can be done by using anti-reflex-coated optics and by wedging and angling all windows and surfaces a few degrees away from the beam normal to hinder constructive interference. Vibrators placed at locations where the fringes occur are often used to mechanically modulate the etalon spacing. The fringes can then be averaged to zero, since they will shift relative to the absorption spectrum [66, 69]. This method was the main approach used in Papers **V**, **VI** and **VIII** to minimise the influence of optical fringes.

Another approach is to use balanced detection. The basic principle is to divide the original beam into two beams. One of these beams is sent through the sample while the other is sent directly to the detector and will thereby contain information only about noise. This signal can then be used as a reference signal and be subtracted from the signal obtained from the beam that has traveled through the sample. This approach has been used in the measurements presented in Papers **II**, **III**, **IV**, **VII**, **XII** and is further explained in Paper **XI**.

Chapter 5

Modeling of light in scattering media

When electromagnetic radiation interacts with matter the light can be reflected at the surface of the medium, transmitted through the medium, absorbed by the medium and/or scattered inside the medium; see Figure 5.1. When multiple scattering events occur light may be scattered back into the original direction of propagation.

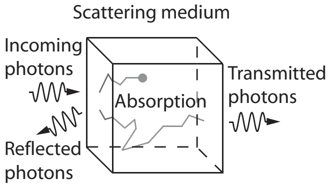

Figure 5.1. *Different processes that can occur when light interacts with a medium.*

To model light propagation in scattering media the radiative transport equation (RTE) is commonly used. The RTE will be briefly discussed in this chapter. To use the equation, certain optical properties, which characterise the propagation in the medium, have to be known. A short description of these will be given. To solve the RTE, different approximations are often necessary. In this chapter one of them, the diffusion approximation, will be discussed. The Monte Carlo method, which is based on statistics and is commonly used when simulating light propagation in scattering media, such as biological tissue, is then discussed. This method was used in Papers **III** and **X**. For further reading, see, for instance, textbooks such as Refs 34, 35.

5.1 Optical properties

The optical properties are macroscopic average properties of importance when studying light propagation in scattering media. The properties are listed below, and each of them will be discussed in this section.

Optical property	Denotation	Unit
Refractive index	n	1
Scattering coefficient	μ_s	m^{-1}
Anisotropy factor	g	1
Absorption coefficient	μ_a	m^{-1}

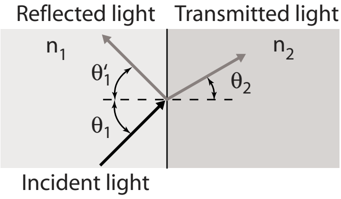

Figure 5.2. *Illustration of Snell's law in the case of* $n_1 < n_2$.

5.1.1 Refractive index

When light propagates in a medium, with a given index of refraction, n_1, towards a medium with a different index of refraction, n_2, a fraction of the light will be reflected back at the surface while some will be transmitted into the other medium in a different direction; see Figure 5.2. The indices of refraction, n_1 and n_2, together with the angle of incidence, θ_1, will determine the direction, θ_2, in which the transmitted light will propagate, according to Snell's law [23]:

$$\sin\theta_2 = \frac{n_1}{n_2}\sin\theta_1. \tag{5.1}$$

The wavelength of the light within the second medium, λ_2, will also change with respect to the wavelength of the incident light, λ_1, as

$$\lambda_2 = \frac{n_1}{n_2}\lambda_1. \tag{5.2}$$

The angle of the reflected light, θ_1', is equal to the angle of the incident light.

There are two physically different situations to deal with in the interpretation of Snell's law:

External reflection:	Light propagating towards an optically denser medium $n_1 < n_2$
Internal reflection:	Light propagating towards an optically thinner medium $n_1 > n_2$

When light propagates towards an optically thinner medium (internal reflection) Snell's law states that at a specific angle of incidence, referred to as the critical angle, and angles above no light will be transmitted. For example, if light is propagating in biological tissue with a refractive index of $n_1 = 1.4$ (for biological tissue the refractive index normally ranges from 1.38 to 1.42 [70, 71]) towards air ($n_2 = 1$), the critical angle for internal reflection will be 46°. If we instead consider the case discussed in Paper **X** where light propagation is investigated in Delrin plates ($n_1 = 1.48$) separated by an air gap, the critical angle for internal reflection will be 42°.

The fraction of the light intensity that is reflected, referred to as the reflectance R, and that which is transmitted, referred to as transmittance T, is determined by Fresnel's formulae [23];

$$R = \frac{1}{2}\left(\frac{\tan^2(\theta_1-\theta_2)}{\tan^2(\theta_1+\theta_2)} + \frac{\sin^2(\theta_1-\theta_2)}{\sin^2(\theta_1+\theta_2)}\right), \tag{5.3}$$

$$T = 1 - R. \tag{5.4}$$

In the case of normal incidence ($\theta_1 = 0$) these formulae can be simplified to

$$R = \frac{(n_1 - n_2)^2}{(n_1 + n_2)^2}, \tag{5.5}$$

$$T = 1 - R = \frac{4 n_1 n_2}{(n_1 + n_2)^2}. \tag{5.6}$$

For the Delrin case discussed above and presented in Paper **X**, the fraction of reflected light for normal incidence from the Delrin plates ($n_1 = 1.48$) towards air ($n_2 = 1$) is about 4%, which means that 96% is transmitted across the interface. The same process occurs when light propagates from air towards the Delrin plates at normal incidence.

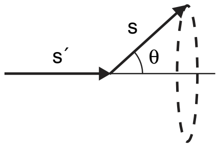

Figure 5.3. *The angular probability of scattering events from direction* $\mathbf{s}'$ *to* $\mathbf{s}$. *It is usually assumed that the scattering probability is symmetric for the azimuthal angle.*

5.1.2 Scattering coefficient

When light interacts with media it may be scattered, as previously discussed in Section 3.3.5. In the case of biological tissue, Mie scattering is the dominating scattering process. The scattering probability for a medium containing a uniform distribution of identical scatterers is characterised by the scattering coefficient, μ_s [m^{-1}]. The reciprocal is called the scattering mean free path, l_s [m], and represents the average distance a photon travels between consecutive scattering events. The scattering coefficient depends on the wavelength of the light; it decreases with increasing wavelength [34, 35].

5.1.3 Anisotropy factor

When light scatters, the direction of propagation changes. This can be characterised by a scattering phase function, $p(\mathbf{s}, \mathbf{s}')$, which describes the angular probability of scattering events from direction $\mathbf{s}'$ to $\mathbf{s}$. The new direction is characterised by two angles; the deflection angle, θ, and the azimuthal angle, ψ. It is usually assumed that the scattering probability is symmetric for the azimuthal angle as depicted in Figure 5.3.

In biological tissue, the Henyey-Greenstein function is often utilised to describe the scattered light. The function describes the probability distribution for the cosine of the deflection angle, $\cos\theta$, as follows

$$p(\cos\theta) = \frac{1 - g^2}{2(1 + g^2 - 2g\cos\theta)^{3/2}}, \tag{5.7}$$

where g is the anisotropy factor and is equal to $\langle\cos\theta\rangle$. This factor can have values between -1 and 1. A positive g-factor indicates forward-directed scattering, isotropic scattering is characterised by a g-factor of 0, and a negative g-factor describes backward-directed scattering. The g-factor normally varies between 0.6 and

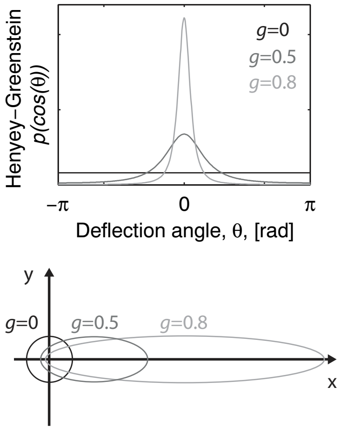

Figure 5.4. *The Henyey-Greenstein phase function for three different values of the anisotropy factor, g.*

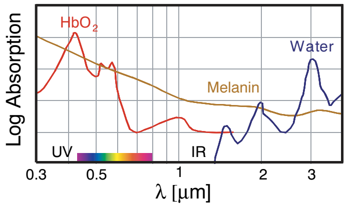

Figure 5.5. *The absorption spectrum for human tissue in the optical region (Adapted from Ref. 75).*

1.0 for different tissue types [72]. The Henyey-Greenstein function is shown for $g = 0$, 0.5 and 0.8 in Figure 5.4. The function was originally proposed for galactic scattering [73], but it has been shown to represent scattering in tissue very well [74].

5.1.4 Absorption coefficient

If the medium being studied contains absorbers, the light is subject to absorption as it propagates. As in the case for scattering events to take place, an absorption coefficient, μ_a [m^{-1}], can be used to characterise the probability for an absorption event to take place in a medium containing a uniform distribution of identical absorbers. The reciprocal is the absorption mean free path, l_a [m], and represents the average distance a photon travels before being absorbed. The total absorption coefficient is the sum for the different absorbers in the medium considered and it is strongly dependent on the wavelength, since the different absorbers interact with light of different wavelengths [34, 35]. Tissue, for example, contains many different absorbers. The dominating ones are deoxy- and oxyhaemoglobin, water and melanin, as depicted in Figure 5.5 [75].

5.2 Transport equation

One approach, which can be used to model light propagation in scattering media, is described by the radiative transport equation (RTE), also known as the Boltzmann equation [34, 35, 72]. The equation is based on energy conservation within a small volume, dV. A small package of energy, which is defined by its position, $\mathbf{r}(t)$, and its direction, $\mathbf{s}$, can lose energy by absorption or scattering events and gain energy by light scattered into the $\mathbf{s}$-direction or from a local light source positioned at $\mathbf{r}(t)$. The RTE describes the change of radiance, $\frac{\partial L}{\partial t}$, at the position $\mathbf{r}(t)$ in the $\mathbf{s}$-direction inside dV. The radiance, L, has the unit [W/m^{2}sr]. The RTE consists of various terms, which take the events described into account, as:

$$\frac{1}{c_m}\frac{\partial L(\mathbf{r},\mathbf{s},t)}{\partial t} = -\mathbf{s}\cdot\nabla L(\mathbf{r},\mathbf{s},t) - (\mu_a+\mu_s)L(\mathbf{r},\mathbf{s},t) + \mu_s\int_{4\pi} L(\mathbf{r},\mathbf{s}',t)p(\mathbf{s},\mathbf{s}')d\omega' + q(\mathbf{r},\mathbf{s},t), \quad (5.8)$$

where c_m is the speed of light within the medium. The different terms on the right-hand side of the equation are listed and described below:

$-\mathbf{s}\cdot\nabla L(\mathbf{r},\mathbf{s},t)$:	Losses of energy over the boundary of dV
$-(\mu_a+\mu_s)L(\mathbf{r},\mathbf{s},t)$:	Losses of energy due to absorption and scattering within dV

$\mu_s \int_{4\pi} L(\mathbf{r}, \mathbf{s}', t)p(\mathbf{s}, \mathbf{s}')d\omega'$: Gain of energy due to light scattered into the $\mathbf{s}$-direction from the $\mathbf{s}'$-direction
$q(\mathbf{r}, \mathbf{s}, t)$: Gain of energy due to local light sources within dV

The RTE is in many cases difficult to solve analytically. Most of the complications arise from dealing with boundaries and geometric aspects of tissue, and light sources.

5.3 Diffusion approximation

When $\mu_s \gg \mu_a$, the transport equation can be approximated by the diffusion equation [34, 35]. This approximation requires that the light can be considered to be diffuse, which can be fulfilled when the light source and the detector are separated by a certain distance. A rule of thumb, often applied in tissue optics, is that diffusive conditions can be assumed to pertain after ten scattering events when g is assumed to be 0.9 for tissue [72]. This is explained by the reduced scattering coefficient, which will be further discussed below.

In the description of the diffusion approximation, the radiance is expanded in spherical harmonics according to

$$L(\mathbf{r}, \mathbf{s}, t) = \sum_{l=0}^{\infty} \sum_{m=-1}^{l} \sqrt{\frac{2l+1}{4\pi}} L_{lm}(\mathbf{r}, t) Y_{lm}(\mathbf{s}). \tag{5.9}$$

For practical use the expansion is truncated after N terms giving rise to the P_N-approximation. In the diffusion approximation the P_1-approximation is usually employed, implying that only terms corresponding to $l = 0, 1$ are taken into account. The radiance can then be written as

$$L(\mathbf{r}, \mathbf{s}, t) \approx \frac{1}{4\pi}\phi(\mathbf{r}, t) + \frac{3}{4\pi}\mathbf{F}(\mathbf{r}, t) \cdot \mathbf{s}. \tag{5.10}$$

The integrated radiance over all directions at position $\mathbf{r}$ is described by $\phi(\mathbf{r}, t)$ [W/m^2], which is an isotropic term. This term is also called the radiant energy fluence rate. The net radiance vector (radiant flux vector) is equal to $\mathbf{F}(\mathbf{r}, t)$ [W/m^2].

The time-resolved diffusion equation for the photon fluence rate can now be created from the RTE by assuming an isotropic light source and a flux vector constant over time, as

$$\frac{1}{c_m}\frac{\partial \phi(\mathbf{r}, t)}{\partial t} = D\nabla^2\phi(\mathbf{r}, t) - \mu_a\phi(\mathbf{r}, t) + q(\mathbf{r}, t), \tag{5.11}$$

where c_m is the velocity of the light in the medium and D is the diffusion coefficient usually expressed as

$$D = \frac{1}{3(\mu_a + \mu_s')}. \tag{5.12}$$

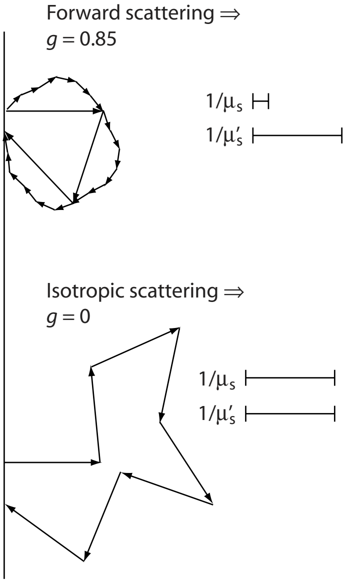

Figure 5.6. *Illustration of how light can be considered as isotropic on a length scale defined by the reduced scattering coefficient, μ'_s. Two photon paths are depicted, one with an anisotropy factor representing forward scattering and one with an anisotropy factor representing isotropic scattering. The two paths result in the same reduced scattering coefficient.*

The property μ'_s is called the reduced scattering coefficient and describes the isotropic scattering as:

$$\mu'_s = \mu_s(1 - g). \tag{5.13}$$

This property shows that it is not possible to separate μ_s and g when the light can be considered to be diffuse, and is depicted in Figure 5.6. This figure shows that light interacting with matter with a g-factor corresponding to forward-scattering can be considered as isotropic on a length scale defined by μ'_s.

This equation is complicated to solve analytically in practical situations. However, solutions do exist for simple geometries. For a homogeneous medium and an isotropic point source, the equation can be solved by its corresponding Green functions. For inhomogeneous samples, the finite-element method can be used. The medium is then divided into a mesh and the diffusion equation is solved numerically for each mesh element.

5.4 The Monte Carlo method

As stated above, analytical solutions of the RTE for realistic scenarios are more or less impossible. Numerical techniques are frequently used. One of the most common approaches is the Monte Carlo (MC) method. The method is today widely used to simulate light transport in scattering media. It is based on launching a large number of photons into a model representing the sample and then following their propagation and recording the photon histories as the particles are scattered and absorbed [76, 77].

In the simulations, the photons enter the model in packages of a given weight, W. The packages then propagate in the model in step of variable size before photon-sample interaction occurs. Each individual step is simulated by statistical methods. Both step size and direction are governed by probability functions and a random number generated. After each step, a fraction of the weight is absorbed while the remaining weight is scattered. The probability function for the scattering direction is the scattering phase function. This process is repeated until the photon escapes the model by reflection or transmission, described by Fresnel's formulae discussed in Section 5.1.1, or the weight is below a certain threshold. In the latter case, the photon package is either terminated or gains some weight, decided by a technique called Russian roulette. The technique gives the photon one chance out of m to survive and in that case it receives a new weight equal to mW. Otherwise the weight is reduced to zero. This means that the energy is conserved.

Since the method is statistical in nature, it requires a large number of injected photons to obtain a reliable result. This can in many cases be very time-consuming and demands large computer resources.

Monte Carlo simulations have been used in Papers **III** and **X**, where light propagation in models representing human sinuses are investigated. The simulations were performed by using a software called ASAP™ (Advanced Systems Analysis Program) [78]. This software, however, handles rays with a certain flux instead of photons with a certain weight. The software is supported by many drawing programs, such as Rhinoceros, making three-dimensional models easy to create and investigate. Every ray is followed throughout the model and every change of direction together with the remaining flux is recorded. This makes it easy to analyse the result and to understand the propagation through the model.

CHAPTER 6

GAS IN SCATTERING MEDIA ABSORPTION SPECTROSCOPY

Tunable diode laser spectroscopy is frequently used for gas measurements in biological and medical applications. The common approach is to apply the Beer-Lambertian law, discussed in Section 4.3.3, directly to measurements on samples with a well-defined optical path length where the scattering properties are negligible compared to the absorption properties, as depicted in Figure 6.1**a**. In 2001 a technique referred to as GAs in Scattering Media Absorption Spectroscopy (GASMAS) was introduced, which non-intrusively investigates free gas dispersed in highly scattering, porous media [79]. This technique combines knowledge of light propagation in scattering media together with common tunable diode laser spectroscopy. Light injected into these samples will not propagate straight through the sample but will instead be scattered and its path length within the sample will increase; see Figure 6.1**b**. This prevents the straightforward utilisation of the Beer-Lambertian law since no direct information about the optical path length can be obtained. This section will first discuss the basic principles of the technique and then go through some of the applications so far investigated.

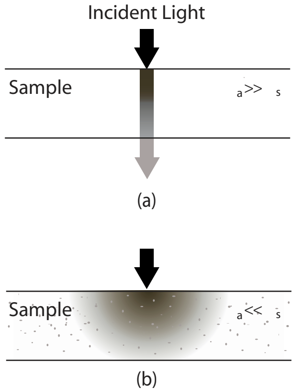

Figure 6.1. *Schematic drawing of light propagation in a sample.* ***a*** *shows a situation where the absorption properties dominate over the scattering properties and* ***b*** *shows when the scattering properties dominate over the absorption properties.*

6.1 Basic principle

The GASMAS technique relies on the fact that the absorption features of free gases are about a factor of 10.000 narrower than those of solid materials. Figure 6.2 shows the absorption spectrum of human tissue from the UV region to the IR region where broadband absorption features can be observed. In the lower part of the figure the absorption lines of the A-band of molecular oxygen have been inserted, corresponding to the wavelength interval of about 10 nm.

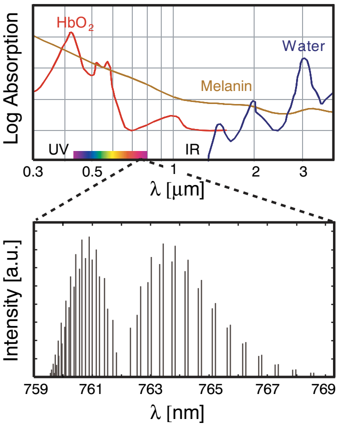

Figure 6.2. *The GASMAS technique investigates the 10.000 times narrower absorption features of free gas compared to tissue. Top: The absorption spectrum of human tissue (Adapted from Ref. 75). Bottom: The absorption lines of the A-band of molecular oxygen obtained from the HITRAN data base [63, 64].*

In Papers **VIII** and **IX** broad structures arising from the absorption of water in the liquid phase and fluorescent light of a sensitizer used in PDT treatment (discussed in Section 3.3.4) have been investigated. However, during GASMAS measurements the gas content in a sample is studied by tuning the wavelength of a diode laser across an absorption line. These absorption lines have a HWHM in the GHz range corresponding to a wavelength increment of about 0.001 nm. Over this frequency range the absorption of the bulk material can be considered constant.

To achieve higher sensitivity, the WMS technique, together with lock-in detection, is employed (discussed in Section 4.3.5). An equivalent mean path length, L_{eq}, is estimated from the second-harmonic signal. L_{eq} corresponds to the distance the light has to travel in ambient air to achieve the same signal strength. It should be noted that this quantity depends both on the scattering coefficient of the sample and the gas concentration within the sample. By applying time-resolved spectroscopy, which was done in Ref. 80, the scattering properties of the sample can be estimated and the gas concentration can be evaluated from L_{eq}. In the measurements presented in Paper **III** information about the gas concentration was extracted from L_{eq} by detecting two gases at wavelengths with similar scattering coefficient and forming the ratio. In this particular work molecular oxygen at 760 nm and water vapour at 935 nm were detected inside the human sinuses. However, any two gases with reachable absorption lines located close enough to each other to make it possible to assume similar scattering properties could be used.

In the case of studies of tissue, the absorption lines have to be located within the optical window (600 nm – 1.3 μm) allowing penetration of the light into the tissue. The optical window boundaries are in the lower wavelength region, limited by haemoglobin absorption and in the upper part by liquid water absorption which can be seen in the upper part of Figure 6.2 (previously discussed in Section 5.1.4).

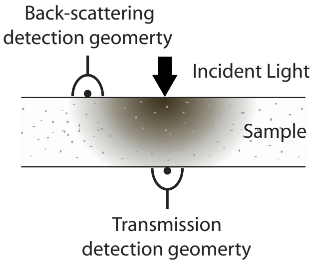

Figure 6.3. *Schematic drawing of different detection geometries applicable during GASMAS experiments.*

Due to the fact that light is highly scattered, two detection geometries can be applied when performing GASMAS measurements; a transmission detection geometry and a back-scattering detection geometry. These are depicted in Figure 6.3. In the transmission geometry, the light is injected into one side of the sample and detected on the other side. This geometry has been used in the work presented in Papers **V** and **VII**. For some applications, it is difficult to access both sides of the sample, in which case a back-scattering detection geometry is more suitable. The light is then injected and detected on the same side of the sample. This is for example the case in the measurements presented in Papers **I** and **VI**.

6.2 Applications

Many different studies have been performed by using the GASMAS technique. So far only molecular oxygen at about 760 nm and water vapour at either 935 nm or 980 nm have been detected, but, in principle, any gas can be studied.

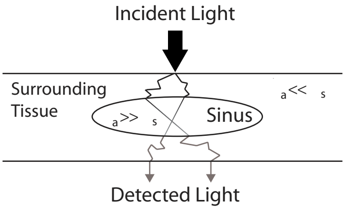

Figure 6.4. *Illustration of light propagation when performing measurements on human sinuses. The light is scattered in the surrounding tissue and gets attenuated when crossing the sinuses containing absorbing gas. Photon paths are shown containing gas imprint in transmission detection geometry.*

6.2.1 Cavities in the human skull

As discussed in Section 2.1.3, the human skull contains air-filled cavities, called sinuses. These have been investigated by detecting molecular oxygen and water vapour with the GASMAS technique. This is not a typical GASMAS sample, since it contains one large gas cell within scattering tissue; see Figure 6.4. However, the principle is still the same.

The first measurements on a human were performed in a backscattering geometry, detecting oxygen in the frontal sinuses (Paper **I** and Ref. 81). Even with a poor signal-to-noise ratio (SNR), a significant difference in the level of the oxygen signal was obtained when comparing measurements on the frontal sinuses with measurements outside the sinuses. The noise arose mainly from optical interference fringes (discussed in Section 4.3.6) created by the in-coupling of the laser light to the fibre. Also the statistics obtained for the photons were poor. The setup was improved by pigtailed lasers, allowing balanced detection, resulting in improved SNR (Paper **XI**). This setup made it possible to detect oxygen and water vapour in the maxillary and the frontal sinuses of several volunteers (Paper **III**). The ostial function (ventilation between the nasal cavity and the sinuses) was also studied by flushing pure nitrogen into the nasal cavity while measuring the oxygen and water vapour contents in the human sinuses. The invasion of nitrogen could be recorded as it replaced oxygen in the cavities as well as the reinvasion of oxygen after terminating the flushing for healthy volunteers.

Different detection geometries were applied to achieve interaction between the light and the different cavities (Paper **III**). From these promising results, an application was submitted to and approved by the Local Ethics Committee of Lund University Hospital allowing a clinical trial in cooperation with the Ear, Nose and Throat Clinic, the Radiology Clinic and the Oncology Clinic at Lund University Hospital. Oxygen and water vapour measurements as well as ostial function studies of the maxillary and the frontal sinuses will be performed and compared to the CT images of the skull provided for all patients. These CT images also include information about the mastoid bone (discussed in Section 2.1.4). Thus, a preliminary study of the mastoid bone was included in the ethical application and approved. In this mastoid bone case, the fibre will be positioned behind the ear at the tip of the mas-

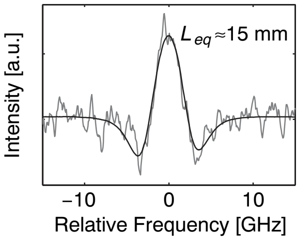

Figure 6.5. *One of the first oxygen balanced detected 2f signals obtained from the mastoid bone on a healthy volunteer [82].*

toid bone and the lower part of the detector at the level of the upper part of the ear. One of the first oxygen signals detected from the mastoid bone in a healthy volunteer in the laboratory is shown in Figure 6.5. This signal corresponds to an L_{eq} of about 15 mm [82].

To perform measurements outside the laboratory the system had to be mobile. The setup that is used during the clinical trial is explained in Paper **IV**, the planning of which is based on the experience gained from the one presented in Paper **XII**. Preliminary results from the ongoing clinical trial are also presented in Paper **IV**. A full analysis of the clinical data for all patient included in the study will be presented for the frontal and maxillary sinuses as well as for the mastoid bones in forthcoming publications.

6.2.2 Respiration

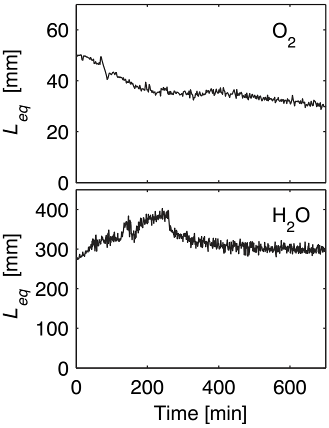

Figure 6.6. *L_{eq} of oxygen and water vapour as a function of time from measurements on minced meat at room temperature [83].*

Molecular oxygen, which has a significant role in the respiration process of biological tissue (previously discussed in Section 2.2) was studied in fruit, particularly apples, in Papers **V** and **VI**. In this application, the gas exchange between the product and the atmosphere is very important, for example, in the modified atmosphere packaging (MAP) industry, different packaging techniques are used to prevent the product from being exposed to a high oxygen concentration and thus to prevent quick maturation. Gas exchange studies were performed by placing the sample, with and without plastic films wrapped around it, in an atmosphere of low oxygen gas concentration. The response of the oxygen signal was then measured when the sample was placed in ambient air. The advantage of measuring gas exchange by the GASMAS technique is that it can be assumed that the scattering properties remain constant during the gas exchange and therefore the changes of measured L_{eq} can directly be related to the gas concentration.

Preliminary results have been obtained from measurements of oxygen and water vapour in minced meat. After processing, the meat is placed in a plastic package to prevent fouling. Measurements were performed with the packages at room temperature. As mentioned in Section 2.2, the respiration process is, apart from being dependent on the oxygen concentration, also dependent on temperature. In Figure 6.6 L_{eq} for oxygen and water vapour can be seen [83]. The data were recorded with two different setups on two different packages of meat. It is difficult to draw any other conclusion from the recorded data than that it is possible to detect some signals, since L_{eq} depends on both the gas concentration and the scattering properties of the sample. Another issue is that two different setups and samples were used. In the future, it would be interesting to use the setup explained in Paper **IV** to simultaneously detect the two gases at the same location on the sample and to find the ratio to extract information about the gas concentration.

6.2.3 Pharmaceutical tablets

In the pharmaceutical industry, knowledge of the porosity or density of tablets is of great interest in order to maintain the same dissolution rate in tablets of the same kind (discussed in Section 2.3). This is related to the process of pressing the tablets. The density of the tablets will influence the L_{eq} measured by the GASMAS technique. A higher density can intuitively be expected to give rise to a larger L_{eq} since the scattering properties will increase. At the same point, a higher density can also result in a decrease of the L_{eq} since it will contain less space with gas inside the sample. In the measurements presented in Paper **VII** it was observed that the recorded L_{eq} for oxygen increased with decreasing density. In this study, a constant volume of the substance was pressed to different thicknesses. Thus, a thicker sample means a lower density. It was also observed that smaller particles of the substance resulted in an increase in L_{eq}. It is difficult to extract any conclusion from the measured L_{eq} in this paper due to the fact that it depends on both gas concentration and scattering properties. Again, this calls for measuring two gases simultaneously or for measuring the scattering properties by time-resolved spectroscopy [80], to extract information about gas concentration in the sample. However, frequently it might be sufficient to perform a calibration relating the product of the path length and concentration, i.e. L_{eq}, to the property of the tablet required.

6.2.4 Moisture in wood

The moisture content in wood is of great interest in many applications, since in most cases it is required to be low (discussed in Section 2.4). After the tree is felled, the wood is dried until it reaches a certain moisture content, appropriate for the particular application for which it is to be used. When studying the drying process of wood, the amount of water in the liquid phase is often investigated.

In Refs 79, 84 oxygen was measured in samples of wood by the GASMAS technique. Gas exchange studies were performed by exposing the samples to pure nitrogen and then studying the reinvasion of oxygen by measuring the L_{eq} while they were exposed to ambient air. Again, as described in Section 6.2.2, the change of recorded L_{eq} is due only to changes of the gas contents since the scattering properties of the sample are assumed to be constant. In the work presented in Paper **VIII** and Ref. 85, oxygen and water vapour in samples of wood were measured by the GASMAS technique as the samples were drying after having been soaked in liquid water. It could be shown that the gas contents could be related to the moisture content. An advantage of the GASMAS technique is that it is non-intrusive in contrast to most techniques used in the industry today to estimate moisture in wood.

COMMENTS ON THE PAPERS

I **On the potential of human sinus cavity diagnostics using diode laser gas spectroscopy**
The first *in vivo* experiments on gas monitoring in the human sinuses are presented. Molecular oxygen at 760 nm was detected by using tunable diode laser absorption spectroscopy. The main part of the experiments were performed on phantoms consisting of two scattering plates separated by a variable air gap representing measurements of the human maxillary and frontal sinuses. Some preliminary results of frontal sinus measurements performed in a back-scattering detection geometry on a human volunteer are presented.

Contribution: I took a substantial part in system integration, measurements, data evaluation and manuscript preparation.

II **Non-intrusive optical study of gas and its exchange in human maxillary sinuses**
Molecular oxygen at 760 nm was detected in the maxillary sinuses by using tunable diode laser absorption spectroscopy. The setup used was based on a pigtailed laser and balanced detection. Measurements were performed on two volunteers; one with constantly recurring sinus problems and the other with no history of such problems. Significant differences in signal level were obtained. The communication between the sinuses and the nasal cavity was investigated by flushing pure nitrogen through the nostril while continually recording the oxygen signal. A decrease of the signal was observed on the healthy volunteer.

Contribution: I took a substantial part in system integration, measurements, data evaluation and manuscript preparation.

III **Gas monitoring in human sinuses using tunable diode laser spectroscopy**

Molecular oxygen at 760 nm was detected in the maxillary sinuses on 11 volunteers by using tunable diode laser spectroscopy. The signal levels were compared to Monte Carlo simulations. In the experimental data a significant difference in signals arising from oxygen imprint were observed when volunteers with widely different anamneses regarding maxillary sinus status were compared. Detection of water vapour at 935 nm was also performed. Three different detection geometries were investigated to access information of both the maxillary sinuses and the frontal sinuses. Gas exchange studies between the sinuses and the nasal cavity were performed and interesting information of the gas contents in the sinuses was obtained.

Contribution: I took a substantial part in system integration, measurements, data evaluation and manuscript preparation.

IV **Simultaneous detection of molecular oxygen and water vapour in the tissue optical window using tunable diode laser spectroscopy**

A transportable system for gas detection is presented based on two pigtailed diode lasers to simultaneously detect molecular oxygen at 760 nm and water vapour at 935 nm. The wavelength of the lasers is scanned across the absorption lines by using a computer board. The same board is used to record the signals. Software-based lock-in detection is employed. Preliminary results on gas measurements of human sinuses from an ongoing clinical trial obtained at the local hospital are presented.

Contribution: I took a substantial part in system integration, measurements, data evaluation and manuscript preparation. I participated only to a minor extent to the programming of the computer board.

V **Diode laser absorption spectroscopy for studies of gas exchange in fruits**
Molecular oxygen at 760 nm is measured non-intrusively in horticulture produce, particularly apples, by using tunable diode laser spectroscopy. Gas exchange studies are presented with differently treated apples by exposing the apples to pure nitrogen and recording the reinvasion of oxygen while exposure to ambient air. The influence of different packaging techniques is discussed.

Contribution: I took a substantial part in system integration, measurements, data evaluation and manuscript preparation.

VI **Studies of gas exchange in fruits using laser spectroscopic techniques**
Molecular oxygen at 760 nm is measured non-intrusively in horticulture produce, in particular apples, by employing wavelength modulation diode laser absorption spectroscopy. A practical detection geometry, namely, back-scattering geometry, for applications in industry is presented. Application in food packaging, e.g., studies of modified atmosphere packaging process are discussed.

Contribution: I took a substantial part in system integration, measurements, data evaluation and manuscript preparation.

VII **Noninvasive characterization of pharmaceutical solids by diode laser oxygen spectroscopy**
Molecular oxygen is measured at 760 nm non-intrusively in pharmaceutical solids by employing tunable diode laser absorption spectroscopy in combination with wavelength modulation spectroscopy. The possibility of relating the signals obtained to the porosity of the tablets is investigated. Promising results are presented.

Contribution: I was involved in the experimental build-up and took part in the experimental work. I contributed to a minor part of preparing the manuscript.

VIII **Spectroscopic studies of wood-drying processes**

The drying process of wood is studied by simultaneously measuring the contents of molecular oxygen at 760 nm and water vapour at 980 nm using tunable diode laser absorption spectroscopy. The results are compared with commercially available techniques to measure moisture contents which are based on measurements related to liquid water. The results of the technique demonstrated show that it is possible to extract additional information of the drying process not provided by the standard techniques.

Contribution: I contributed to the preparation and the experimental work which is based on tunable diode laser spectroscopy. I wrote a minor part of the manuscript.

IX **Fluorescence monitoring of a topically applied liposomal Temoporfin formulation and photodynamic therapy of non-pigmented skin malignancies**

A new sensitizer is studied in connection with photodynamic therapy of non-pigmented skin malignancies in humans in a clinical trial. The distribution of the sensitizer within the tumour and the surrounding tissue was investigated prior to, during and after the treatment by recording the fluorescent light using a point-monitoring system and an fluorescence imaging system. A bleaching of about 30% was obtained at the centre of the tumour providing promising possibilities for the sensitizer.

Contribution: I took part in most of the clinical work. I was responsible of the data evaluation from the point monitoring measurements. I wrote a minor part of the manuscript.

X **Monte Carlo simulations related to gas-based optical diagnosis of human sinusitis**

Monte Carlo simulations are performed by using a software called ASAP™ (Advanced Systems Analysis Program) related to phantom measurements provided in Paper **I** based on tunable diode laser spectroscopy. Good agreement was obtained between the simulations and the experimental data. Simulations were performed to optimise the detection geometry. The possibility of using the experimental technique to perform imaging of the human frontal sinuses was investigated. Promising results are presented.

Contribution: I took a substantial part in the preparations and in the analysis of the simulations. I wrote the major part of the manuscript.

XI **Approach to optical interference fringes reduction in diode laser absorption spectroscopy**

A new approach based on software to reduce the influence of interference fringes in tunable diode laser spectroscopy when studying weak absorption lines is put forward. The idea behind the method is to perform balanced detection by dividing the light from the laser into two beams, one which is directly guided to a detector while the other first goes through the sample. A set of parameters is estimated by comparing the reference signal and the sample signal at frequency regions outside the expected gas imprint. A matched version of the reference signal is then subtracted from the sample signal over the whole frequency scan. Signals better by a factor of about two are obtained when comparing this approach to standard, balanced detection systems.

Contribution: I took a substantial part in the setting up of the experiment and in the experimental work based on the software approach. I contributed to a major part of the implementation of the algorithm presented. I wrote the major part of the manuscript.

XII Flexible lock-in detection system based on synchronized computer plug-in boards applied in sensitive gas spectroscopy

A compact and flexible diode laser absorption spectroscopy system based on computer boards is presented. Software-based lock-in detection was performed. The system is demonstrated by measuring molecular oxygen at 760 nm in scattering media such as a bamboo stalk and the human frontal sinuses. Promising results have been obtained in the work aimed at developing a compact, transportable system.

Contribution: I participated in the planning of the setup and in some of the spectroscopic measurements. I contributed to a minor degree to the preparation of the manuscript.

XIII Temporal correlation scheme for spectroscopic gas analysis using multimode diode lasers

A method to perform gas measurements using multimode diode lasers is presented. The method is based on simultaneously detecting two signals; one which has passed through a reference cell containing the gas under investigation and the other after passing an external gas cell with an unknown gas composition. This is done while the wavelength of the laser is scanned across several absorption lines of the gas of interest. The two spectra obtained are compared and the elimination of light intensity fluctuations due to mode competitions is achieved.

Contribution: I participated in a minor part of the experiments and in the writing process of the paper.

XIV **Laser spectroscopy of gas in scattering media at scales ranging from kilometers to millimeters**

This paper presents a review of the work performed in the molecular spectroscopy group at our department. Parallels between free gas monitoring using diode laser absorption spectroscopy in scattering media and monitoring of gases in the atmosphere using differential absorption Lidar (LIght Detection And Ranging) are discussed. We show that the basic ideas are very similar, while the spatial and temporal scales vary greatly.

Contribution: I participated in most of the experimental work based on tunable diode laser spectroscopy. I took a minor part in the preparation of the manuscript.

ACKNOWLEDGEMENTS

First of all I would like to thank my amazing supervisor Sune Svanberg. You have thoroughly inspired me throughout my time at the Atomic Physic Division. I do not know how you always manage to be so enthusiastic about everything. It is a very rare quality among people. I have deeply appreciated your trust in me over all these years, and for all the exciting trips you have made possible which have involved traveling in Europe, to Asia, to America, to Africa etc. I do not know how I will be able to thank you enough for all the support and guidance you gave me whenever I have needed it. I am sure that your own defined sayings will be with me for the rest of my life:

- *"Never stop an experiment that is working..."*
- *"The things that have to be done during this day will by definition be done. So do all the other things first, and you will manage to do so much more during the day..."*

I have also had two wonderful co-supervisors; Katarina Svanberg and Stefan Andersson-Engels. Katarina, I have really enjoyed working with you. It is definitely thanks to you that we have been able to push our experiments all the way from an idea late an evening in the laboratory (Sune with a strong cup of coffee as he always says is needed) to the hospital performing measurements on real patients. We also had the opportunity to travel together and we certainly took bargaining up to a new level. I hope I will have the same skills when I am standing there on my own. Stefan, I am very grateful for having you as my co-supervisor. Specially I want to thank you for all your help in connection with the part of my thesis involving light propagation in scattering media. We also had the opportunity to travel together. Your rhythmic movements to African music will certainly remain with me.

Further, I want to thank the whole Molecular Spectroscopy Group. I want to thank Rasmus Grönlund for being an amazing room mate throughout my whole time at the department. You have had to put up with a lot. Whenever I have needed to talk about physics or more private things you have always been there for me. Thank you so much for everything. To my fellow PhD students in the group; Mikael Sjöholm and Gabriel Somesfalean, thank you for making it easier in the beginning to get started. Then to later group members; Mats Andersson and Märta Cassel-Engquist, it has been a pleasure to get you into the group. Thank you Mats for letting me know that the problems that I have are exactly the same as you had 10 years ago. That makes me believe in the future. Thank you Märta for excellent teamwork when it comes to the ongoing clinical trial. Then to Tomas Svensson, the half time member of our group. Thank you for taking me with you on one of your calls. You really made me understand what ”bird” watching is all about.

I also would like to give special thanks to Laila Lewin, who unfortunately passed away, far too young, after a short time of illness. All those chats we had in your room will always be remembered. You were an amazing person with so much love and care. I am so happy that our roads crossed. And as I said to you: Your words have meant more to me than you will ever know.

This thesis would never been possible without all administrative, technical and electronic help I have received. Thank you Marie Holmdahl-Svensson, Minna Ramkull, Henrik Steen, Bertil Hermansson, Åke Bergquist, and everybody at the workshop.

During my PhD time I have also been involved in some teaching. Thank you, all of you who let me teach parts of your courses. A special thanks to Nina Reistad who gave me the trust to hold seminars. I was definitely nervous the first time I had more than 100 quiet students in front of me holding a pencil in their hands ready to make notes of everything I wrote on the white board. Thank you Nina for letting me do it. I learned so much.

I am also grateful for all help and support I received concerning the medical part of my thesis. I would specially like to thank Morgan Andersson, Niels Bendsøe, Karolina Falkenius-Schmidt, Kjell Jonsson, Sven Lindberg, Mette Forseth, Karin Prellner, Bo Paulsson, Roger Siemund, and all the staff at the Radiology Clinic and the Ear, Nose and Throat Clinic at Lund University Hospital.

There are so many I would like to thank at the department. However, if I do, this acknowledgment will take the major part of this thesis. Instead I say; Thanks to all the colleagues, staff and master students at the Atomic Physics Division for making it such a lovely place. I will certainly miss it!

I also would like to take this opportunity to thank Arunima Ganguli and Iona Evans, my former colleagues and close friends at the Cell Biology Department at Hallamshire Hospital, Sheffield. Thank you so much for everything you have done for me. You were the ones who brought me into research. Not only that, you have also opened up your homes to me after my moving back to Sweden. I have always had a bed waiting for me in England whenever I have needed a break. And as we always say after some wine at

the pub or on the terrace at Runi's place or in the darkness in the confocal room together with the green cells (most of the time the transfection actually worked); everything that has happened has only made us stronger.

To all my friends - thank you for being there!!! I would like to give special thanks to Maria and Cecilia for being such amazing and understanding friends.

Moreover, I want to thank my cousin; Åsa. You are simply the best. Sometimes it is a bit scary to have somebody who can see straight through you. You just know, without me having to say anything. It must be the genes. I hope that everyone have someone like you in their life.

Till min familj: Mamma, Pappa, Andreas, Lisa, Tobias och Hanna. Tack för att Ni finns och för allt stöd genom åren. Till sist vill jag nämna mina fantastiska brorsbarn som under de senaste åren gett mig och vår familj så mycket glädje och energi; Ida och Elin. Ni är sötast och underbarast i världen!

REFERENCES

1. R. Craft. *A textbook of human anatomy.* The Ronald Press Company, New York (1966).

2. T. Petrén. *Lärobok i anatomi, Del 1, Rörelseapparaten.* Aktiebolaget Nordiska Bokhandlens Förlag, Stockholm, in Swedish (1976).

3. B. Sonesson. *Människans anatomi.* Almqvist & Wiksell Förlag AB, Stockholm, in Swedish (1974).

4. Teaching material from California State University, Anthropology Department (2007). URL `http://www.csuchico.edu/anth/Module/`.

5. P. Stierna, G. Karlsson, I. Melén and M. Jannert. *Aspect on sinusitis - Diagnosis and threatment in adults.* Proceedings from Meeting of the Swedish Association of Otorhinolaryngologists, HNS, Stockholm (1995).

6. B. Drettner. *In: The nose: Upper airway physiology and the atmospheric enviroment,* pages 145 – 162. Elsevier Biomedical Press, Amsterdam (1982).

7. Health Matters, Sinusitis. Technical report Nat. Inst. of Allergy and Infectious Diseases, US Dept. of Health and Human Services, Bethesda (2005).

8. T. Jansson, H. Persson, N. Holmer, P. Sahlstrand-Johnson and Magnus Jannert. *Ultrasound Doppler for improved diagnosis of disease in the paranasal sinuses.* In *Proceeding IEEE Ultrasonics Symposium* pages 839 – 841. Proceeding IEEE Ultrasonics Symposium (2005).

9. L. Öhman and A. Boierth. *Människokroppen och dess funktioner.* Geber Förlag AB, Uppsala, in Swedish (1966).

10. J. Fidler and J. Northe. *The effect of conditions of storage on the respiration of apples.* Journal of Horticultural Science **42**, 189–206 (1967).

11. Y. Hening and S. Gilbert. *Computer analysis of the varibles affecting respiration and quality of produce packaged in polymeric films.* Journal of Food Science **40**, 1033–1035 (1975).

12. H. Peppelenbos, L. Tijskens, J. van't Leven and E. Wilkinson. *Modelling oxidative and fermentative carbon dioxide production of fruits and vegetables.* Postharvest Biology and Technology **9**, 283–295 (1996).

13. R. Beaudry. *Effect of O_2 and CO_2 partial pressure on selected phenomena affecting fruit and vegetable quality.* Postharvest Biology and Technology **15**, 293–303 (1999).

14. C. Yearsley, N. Banks and S. Ganesh. *Temperature effects on the internal lower oxygen limits of apple fruit.* Postharvest Biology and Technology **11**, 73–83 (1997).

15. P. Renault, M. South and Y. Chambroy. *Gas exchange in modified atmosphere packaging. 1: A new theoretical approach for micro-perforated packs.* Journal of Food Science and Technology **29**, 365–378 (1994).

16. M. Aulton. *Pharmaceutics - The science of dosage from design.* 2nd edn., Churchill Livingstone, London (2002).

17. J. Dinwoodie. *Timber: Its nature and behavior.* 2nd edn., E & FN Spon, New York (2000).

18. W. Simpson and A. Tenwolde. Wood Handbook, Chap. 3 - Physical properties and moisture relations of wood. Technical report Department of Agriculture, Forest Service, Forest Products Laboratory, Madison, U.S. (1999).

19. S. Berry and M. Roderick. *Plant-water relations and the fibre saturation point.* New Phytologist **168**, 25–37 (2005).

20. M. Goyeneche, D. Lasseux and D. Bruneau. *A film-flow model to describe free water transport during drying of a hydroscopic capillary porous medium.* Transport in Porous Media **48**, 125–158 (2002).

21. A. Einstein. *Über einen die Erzeugung und Verwandlung des Lichtes betreffenden heuristischen Gesichtspunkt.* Annalen der Physik **17**, 132–148 (1905).

22. H. Young and R. Freedman. *University physics.* 9:th edn., Addison-Wesley Publishing Company, Inc., New York (1996).

23. F. Pedrotti and L. Pedrotti. *Introduction to optics.* Prentice-Hall, Inc., New Jersey (1993).

24. C. Foot. *Atomic physics.* Oxford University Press (2005).

25. C. Banwell and E. McCash. *Fundamentals of molecular spectroscopy.* 4th edn. McGraw-Hill Publishing Company, London (1994).

26. O. Svelto. *Principles of lasers.* 4th edn., Plenum Press, New York (1998).

27. S. Svanberg. *Atomic and molecular spectroscopy.* 4th edn. Springer, Berlin (2004).

28. S. Andersson-Engels, A. Gustafson, J. Johansson, U. Stenram, K. Svanberg, and S. Svanberg. *Investigation of possible fluorophores in human atherosclerotic plaque.* Lasers in the Life Sciences **5**, 1–11 (1992).

29. T. Dougherty, C. Gomer, B. Henderson, G. Jori, D. Kessel, M. Korbelik, J. Moan and Q. Peng. *Photodynamic Therapy.* Journal of the National Cancer Institute **90**, 889–905 (1998).

30. U. Schmidt-Erfurth, J. Miller, M. Sickenberg, A. Bunse, H. Laqua, E. Gragoudas, L. Zografos, R. Birngruber, H. van den Bergh, A. Strong, U. Manjuris, M. Fsadni, A. Lane, B. Piguet and N. Bressler. *Photodynamic therapy of subfoveal choroidal neovascularization: clinical and angiographic examples.* Graefes Archive for Clinical and Experimental Ophthalmology **236**, 365–374 (1998).

31. C. Moore, I. Hoh, S. Bown and M. Emberton. *Does photodynamic therapy have the necessary attributes to become a future treatment for organ-confined prostate cancer?* BJU Intetnational **96**, 754–758 (2005).

32. M. Kreimer-Birnbaum. *Modified porphyrins, chlorins, phthalocyanines, and purpurins: Second-generation photosensitizers for photodynamic therapy.* Seminars in Hematology **26**, 157–173 (1989).

33. Q. Peng, T Warloe, K. Berg, J Moan, M. Kongshaug, K-E Giercksky and J Nesland. *5-Aminolevulinic acid-based photodynamic therapy: Clinical research and future challenges.* Cancer **79**, 2282–2308 (1997).

34. T. Vo-Dinh. *Biomedical photonic handbook.* CRC Press LLC, Washington, D.C. (2003).

35. A. Welch and M. van Gemert. *Optical-thermal response of laser-irradiated tissue.* Plenum Press, New York (1995).

36. T. Maiman. *Stimulated optical radiation in ruby.* Nature **187**, 493–494 (1960).

37. A. Schawlow and C. Townes. *Infrared and optical masers.* Physical Review **112**, 1940–1949 (1958).

38. Nobel Laureates in Physics (1964). URL `http://nobelprize.org/nobel_prizes/physics/laureates/1964/index.html`.

39. C. Townes. *How the laser happened.* Oxford University Press, Oxford (1999).

40. R. Hall, G. Fenner, J. Kingsley, T. Soltys and R. Carlsson. *Coherent light emission from GaAs junctions.* Physics Review Letters **9**, 366–368 (1962).

41. M. Nathan, W. Dumke, G. Burns, F. Dill and G. Lasher. *Stimulated emssion of radiation from GaAs p-n junctions.* Applied Physics Letters **1**, 62–64 (1962).

42. N. Holonyak and S. Bevacqua. *Coherent (visible) light emission from* $Ga(As_{1-x}P_x)$ *junctions.* Applied Physics Letters **1**, 82–83 (1962).

43. T. Quist, R. Rediker, R. Keyes, W. Krag, B. Lax, A. McWhorter and H. Zeigler. *Semiconductor maser of GaAs.* Applied Physics Letters **1**, 91–92 (1962).

44. C. Wieman and L. Hollberg. *Using diode lasers for atomic physics.* Review of Scientific Instruments **62**, 1–20 (1990).

45. H. Kroemer. *A proposed class of heterojunction injection lasers.* Proceedings of IEEE **51**, 1782–1784 (1963).

46. Z. Alferov and R. Kazarinov. *Semiconductor laser with electric pumping.* Inventor's cerificate No. 181737 (U.S.S.R.) Application No. 950840, priority as of March 30 (1963).

47. P. Ripley. *The physics of diode lasers.* Lasers in Medical Science **11**, 71–78 (1996).

48. K. Liu and M. Littman. *Novel geometry for single-mode scanning of tunable lasers.* Optics Letters **6**, 117–118 (1981).

49. L. Ricci, M. Weidemüller, T. Esslinger, A. Hemmerich, C. Zimmermann, V. Vuletic, W. König and T. Hänsch. *A compact grating-stabilized diode laser system for atomic physics.* Optics Communications **117**, 541–549 (1995).

50. J. Faist, F. Capasso, D. Sivco, C. Sirtori, A. Hutchinson and A. Cho. *Quantum cascade laser.* Science **264**, 553–556 (1994).

51. J. Faist, F. Capasso, D. Sivco, C. Sirtori, A. Hutchinson and A. Cho. *Quantum cascade laser: An intersub-band semiconductor laser operating above liquid nitrogen temeprature.* Electronics Letters **30**, 865–866 (1994).
52. F. Capasso, J. Faist, C. Sirtori, J. Baillargeon, A. Hutchinson and A. Cho. *Quantum cascade lasers: New resonant tunnelling light source for the mid-infrared.* Philosophical Transactions: Mathematical, Physical and Engineering Sciences **354**, 2463–2467 (1996).
53. L. Philippe and R. Hanson. *Laser diode wavelength-modulation spectroscopy for simultaneous measurement of temperature, pressure, and velocity in shock-heated oxygen flows.* Applied Optics **32**, 6090–6103 (1993).
54. J. Silver and D. Kane. *Diode laser measurements of concentration and temperature in microgravity combustion.* Measurement Science & Technology **10**, 845–852 (1999).
55. T. Aizawa. *Diode-laser wavelength-modulation absorption spectroscopy for quantitative in situ measurments of temperature and OH radical concentration in combustion gases.* Applied Optics **40**, 4894–4903 (2001).
56. J. Liu, J. Jeffries and R. Hanson. *Wavelength modulation absorption spectroscopy with 2f detection using multiplexed diode lasers for rapid temperature measurements in gaseous flows.* Applied Physics B **78**, 503–511 (2004).
57. D. Herriott and H. Schulte. *Folded optical delay lines.* Applied Optics **4**, 883–889 (1964).
58. J. White. *Very long optical paths in air.* Journal of the Optical Society of America **66**, 411–416 (1976).
59. J. Humlicek. *Optimized computation of the Voigt and the complex probability function.* Journal of Quantitative Spectroscopy & Radiative Transfer **27**, 437–444 (1982).
60. J. Olivieri and R. Longbothum. *Empirical fits to Voigt line width: A brief review.* Journal of Quantitative Spectroscopy & Radiative Transfer **17**, 233–236 (1977).
61. P. Werle. *A review of recent advances in semiconductor laser based gas monitors.* Spectrochimica Acta A **54**, 197–236 (1998).
62. J. Parrish. *New concepts in therapeutic photomedicine: Photochemistry, optical targeting and the therapeutic window.* Journal of Investigative Dermatology **77**, 45–50 (1981).
63. L. Rothman, A. Barbe, D. Benner, L. Brown, C. Camy-Peyret, M. Carleer, K. Chance, C. Clerbaux, V. Dana, V. Devi, A. Fayt, J. Flaud, R. Gamache, A. Goldman, D. Jacquemart, K. Jucks, W. Lafferty, J. Mandin, S. Massie, V. Nemtchinov, D. Newnham, A. Perrin, C. Rinsland, J. Schroeder, K. Smith, M. Smith, K. Tang, R. Toth, J. Vander Auweraf, P. Varanasi and K. Yoshino. *The HITRAN molecular spectroscopic database: Edition of 2000 including updates through 2001.* Journal of Quantitative Spectroscopy & Radiative Transfer **82**, 5–44 (2003).
64. Database from Harvard University (2007). URL `http://www.cfa.harvard.edu/hitran`.
65. J. Reid and D. Labrie. *Second-harmonic detection with tunable diode lasers - Comparison of experiment and theory.* Applied Physics B **26**, 203–210 (1981).

66. D. Bomse, A. Stanton and J. Silver. *Frequency modulation and wavelength modulation spectroscopies: Comparison of experimental methods using a lead-salt diode laser.* Applied Optics **31**, 718–731 (1992).

67. J. Silver. *Frequency-modulation spectroscopy for trace species detection: Theory and comparison among experimental methods.* Applied Optics **31**, 707–717 (1992).

68. I. Linnerud, P. Kaspersen and T. Jæger. *Gas monitoring in the process industry using diode laser spectroscopy.* Applied Physics B **67**, 297–305 (1998).

69. P. Werle, R. Mücke and F. Slemr. *The limits of signal averaging in atmospheric trace-gas monitoring by tunable diode-laser absorption spectroscopy (TDLAS).* Applied Physics B **57**, 131–139 (1993).

70. F. Bolin, L. Preuss, R. Taylor and R. Ference. *Reflective index of some mammalian tissues using a fiber optic cladding method.* Applied Optics **28**, 2297–2303 (1989).

71. G. Tearney, M. Brezinski, J. Southern, B. Bouma, M. Hee and J. Fujimoto. *Determination of the refractive index of highly scattering human tissue by optical coherence tomography.* Optics Letters **20**, 2258–2260 (1995).

72. W. Cheong, S. Prahl and A. Welch. *A review of the optical properties of biological tissues.* IEEE Journal of Quantum Electronics **26**, 2166–2185 (1990).

73. L. Henyey and J. Greenstein. *Diffuse radiation in the galaxy.* Journal of Astrophysics **93**, 70–83 (1941).

74. S. Jacques, C. Alter and S. Prahl. *Angular dependence of HeNe laser light scattering by human dermis.* Laser Life Science **1**, 309–333 (1987).

75. J. Boulnois. *Photophysical processes in recent medical laser developments: A review.* Lasers in Medical Science **1**, 47–66 (1986).

76. S. Prahl, M. Keijzer, S. Jacques and A. Welch. *A Monte Carlo method of light propagation in tissue.* SPIE Institute Series **IS 5**, 102–111 (1989).

77. L. Wang, S. Jacques and L. Zheng. *MCML - Monte Carlo modeling of light transport in multi-layered tissues.* Computer Methods and Programs in Biomedicine **47**, 131–146 (1995).

78. B. Michel and T. Beck. *Raytracing in medical applications.* Laser & Photonics **5**, 38–41 (2005).

79. M. Sjöholm, G. Somesfalean, J. Alnis, S. Andersson-Engels and S. Svanberg. *Analysis of gas dispersed in scattering media.* Optics Letters **26**, 16–18 (2001).

80. G. Somesfalean, M. Sjöholm, J. Alnis, C. af Klinteberg, S. Andersson-Engels and S. Svanberg. *Concentration measurement of gas embedded in scattering media by employing absorption and time-resolved spectroscopy.* Applied Optics **41**, 3539–3544 (2002).

81. S. Svanberg, L. Persson and K. Svanberg. *Human cavity gas measurement method and device.* Swedish Patent Application 0500878-4 (2005); PCT and US Provisional applications (2005).

82. K. Falkenius-Schmidt, L. Persson, M. Cassel-Engquist, K. Svanberg, S. Svanberg and S. Lindberg. Unpublished results (2007).

83. M. Cassel-Engquist, L. Persson, S. Svanberg and A. Olsson. Unpublished results (2007).

84. J. Alnis, B. Andersson, M. Sjöholm, G. Somesfalean and S. Svanberg. *Laser spectroscopy of free molecular oxygen dispersed in wood materials.* Applied Physics B **77**, 691–695 (2003).

85. S. Svanberg, M. Andersson, L. Persson and M. Sjöholm. *Apparatus and method for determining the moisture content in porous media using optical spectroscopy.* Swedish Patent Application (February 2006).

PAPERS

PAPER I

On the potential of human sinus cavity diagnostics using diode laser gas spectroscopy

L. Persson, K. Svanberg, and S. Svanberg.

Applied Physics B **82**, 313–318 (2006).

Appl. Phys. B 82, 313–317 (2006)
DOI: 10.1007/s00340-005-1968-1

Applied Physics B
Lasers and Optics

L. PERSSON[1]
K. SVANBERG[2]
S. SVANBERG[1,✉]

On the potential of human sinus cavity diagnostics using diode laser gas spectroscopy

[1] Atomic Physics Division, Lund Institute of Technology, P.O. Box 118, 221 00 Lund, Sweden
[2] Department of Oncology, Lund University Hospital, 221 85 Lund, Sweden

Received: 10 May 2005/Revised version: 28 July 2005
Published online: 1 December 2005 • © Springer-Verlag 2005

ABSTRACT A method for studying human sinus cavities and inflammation status is described. Diode laser spectroscopy of molecular oxygen gas in the cavity is performed at 760 nm through the strongly scattering facial tissue in a backscattering geometry. Model experiments on tissue-like scattering plastics were made to elucidate the possible penetration depths and the expected signal levels. Measurements on the frontal sinuses of a healthy volunteer verify the viability of the technique. The potential for dynamic gas measurements of the possible occlusion of the channels connecting the sinuses with the nasopharyngeal cavity are discussed, and demonstrated in model experiments using a gas with a composition different from that of the ambient air. Extensions to other biomedical diagnostics arenas are discussed. The results obtained suggest that a complementary method for real-time and non-intrusive medical diagnostics using compact instrumentation could be developed.

PACS 39.30.+w; 87.64.-t; 87.80.-y

1 Introduction

Sinus cavity inflammation affects 37 million people annually in the US [1]. In the present paper, we describe a method for diagnostics of sinusitis, based on absorption spectroscopy on free oxygen gas. The human sinus cavities are normally air-filled and the presence of this gas can be observed by wavelength modulation spectroscopy using tunable diode lasers. Viral infection may lead to mucosal swelling followed by liquid and pus filling the cavities thereby altering the gas signal. This is the basis of the present work, where we demonstrate how the molecular oxygen signal around 760 nm can be observed through the external facial tissue as light is backscattered from deeper lying structures through the gas filled cavity. Alternatively, a transmission geometry is also considered for the maxillary sinuses using fibre-optic light injection from the oral cavity and cheek monitoring.

The sinus gas signal can be studied statically, but also dynamically, by observing the presence or absence of gas transport through open or occluded nasal channels, respectively. In such measurements, a gas of non-ambient oxygen composition is used, such as air exhaled from the lungs. Human tissue exhibits a comparatively low absorption in the range 600–1400 nm (tissue optical window), where scattering, however, is strongly dominant. Optical transillumination in this wavelength interval is being investigated for optical mammography [2, 3]. The technique presented in the present paper utilizes experience gained in gas in scattering media absorption spectroscopy (GASMAS) [4, 5], where, however, gas distributed throughout the scattering medium is studied. Such distributed gas gives rise to a very sharp (0.001 nm) absorptive imprint in contrast to the broad structures due to molecules in liquids or solids [6, 7]. In the present work, light passes through a macroscopic gas cavity mediated through diffusely scattering "mirrors", and the cavity status can be assessed from a measurement head pressed towards the facial tissue.

2 Medical background and investigational plan

2.1 *Facial anatomic background*

The facial skeleton in the nasopharyngeal areas features several cavities, also called sinuses (Fig. 1). The frontal sinus most often consists of one single cavity but can sometimes have different compartments. The maxillary and sphenodial sinuses are bilateral. The ethmoidal cellular system is also bilateral and consists of many smaller communication cavities. The frontal sinus is located in the frontal bone of the skull just above the eye bulbs. The maxillary sinuses are located on each side in the maxillary part of the cheek just below the orbital floor. The ethmoidal cells and the spheodal sinus (not shown in Fig. 1) are located in the medial and dorsal part of the nose. All sinuses are connected to the nose cavity for drainage and air exchange.

2.2 *Sinus inflammation and diagnostics*

Inflammation of the nasal accessory sinuses is most often related to viral infections in the area or to allergic reactions. This usually causes a swelling of the mucosal tissue, resulting in an occlusion of the drainage passage. In these closed cavities, bacteria will grow and cause clinical manifestations, called sinusitis. The diagnosis of sinusitis is based on the anamnestic history of the patient along with clinical investigations, such as cheek palpation and visual inspection with a speculum for purulent fluid of the nasal cavity. Paraclinical investigations include sinus X-ray, ultrasound, and low

---

✉ Fax: +46-46-2224250, E-mail: sune.svanberg@fysik.lth.se

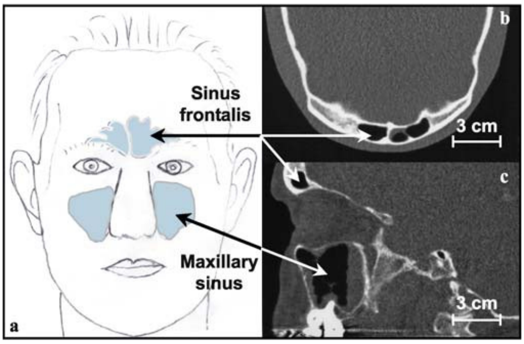

FIGURE 1 (**a**) Illustration showing the location of the frontal and maxillary sinus. (**b**) CT image of human frontal sinus, horizontal section (**c**) CT image of frontal and maxillary sinuses, vertical section

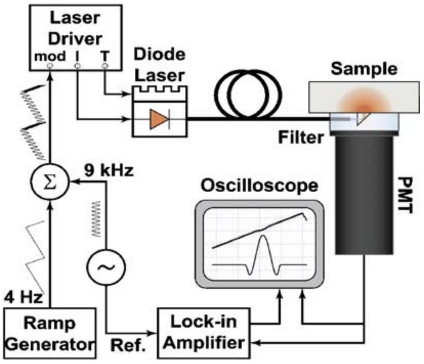

FIGURE 2 Schematic diagram of the experimental arrangement

dose computerized tomography. Among these methods, ultrasound and sinus X-ray investigations are seldom used these days. Assessing the sinus status is sometimes not straightforward, and a simple tool for additional diagnostics would be welcome. A powerful diagnostic modality might lead to a reduction in unnecessary antibiotic treatment.

Here, we discuss the potential for an optical technique based on laser spectroscopy. The location of both the frontal and the maxillary sinuses is well suited for optical investigations from the outer part of the face. The frontal sinus is separated by a bone and tissue structure of approximately 10 mm and the cavity has a thickness of typically 10 mm. The maxillary sinuses are located behind approximately the same thickness of bone and muscle tissue. The cavities exhibit a larger transverse air distance of up to 3 cm. As discussed below, this might sometimes call for measurements in transmission. The ethmoidal cells as well as the sphenoidal sinuses, may be reached from the nasal cavity for light injection as well as detection. The former aggregation of cells can be infected (ethmoiditis), especially in children, which is considered as a particularly serious condition, given the close proximity to the orbital cavities.

2.3 *Study design*

The present exploratory investigation of sinusitis diagnostics based on gas spectroscopy was performed in two stages. First, a model system consisting of two air-spaced plastic scatterers was investigated in backscattering and in transmission with a number of parameters being varied. Second, measurements on the sinus cavities on a volunteer were performed.

3 Experimental set-up

The gas detection setup performs absorptive laser spectroscopy in diffusely scattered light. A schematic diagram of the setup is shown in Fig. 2. A near-IR single mode diode laser, Sharp LT031MDO, with a nominal output power of 7 mW, was used as the spectroscopic light source. By applying a ramp at a repetition rate of 4 Hz to the driving current, the diode laser was temperature tuned across the R7R7 molecular oxygen line, situated at 761.003 nm (vacuum wavelength). A 9 kHz sine-wave was superimposed onto the current ramp to produce a wavelength modulation of the light, thereby allowing sensitive wavelength modulation spectroscopy (WMS).

An optical fibre with a 600 μm core diameter was used to guide the light to the sample. For backscattering measurements, a small right-angle prism positioned in front of the fibre and centrally located to the detector, was used to provide total internal reflection in order to launch the light into the sample, which effectively was exposed to about 2 mW. An annular aperture with an inner and an outer aperture diameter of 10 and 21 mm, respectively, was used to collect the backscattered photons from the sample. For the transmission geometry, the fibre was positioned above the sample and a circular aperture with a diameter of 5 mm was used in front of the detector. In order to achieve efficient photon collection with a high dynamic range, the light was detected with a photomultiplier tube, Hamamatsu 5070A, protected from visible light by a blocking colored glass filter, Schott RG715.

The absorption signal was detected by splitting up the signal from the photomultiplier tube into two parts. One part, referred to as the direct signal, was directly sent to a computer controlled digital oscilloscope. The other part, referred to as the WMS signal, was sent to a lock-in amplifier, EG&G Princeton Applied Research 5209, providing phase-sensitive detection at twice the modulation frequency, before sent to another channel on the oscilloscope. Wavelength modulation spectroscopy with lock-in detection is often referred to as derivative spectroscopy, since the signal looks like the derivative of the absorption profile. In this case, when detection is performed at twice the modulation frequency, the lock-in signal looks like the second derivative of the absorption profile.

The amplitude of the WMS signal is determined by the absolute size of the narrow gas absorption feature, i.e., the fractional absorption due to the gas and the amount of light reaching the detector. By measuring the peak-to-peak value of the absorption signature in the WMS signal and normalising it with respect to the amount of light reaching the detector (the direct signal), we can estimate the absorption due to the gas of interest. For small absorptions, the WMS signal is proportional to the absorbance and thus to the product of the gas concentration and the path length travelled by the light.

A method called standard addition was adopted in order to calibrate a normalized measured WMS signal and transform it into a more meaningful quantity. By adding known path lengths of ambient air to be traversed by the laser light in addition to the scattering object and by plotting the acquired normalized WMS values as a function of added air, we can estimate an equivalent air distance. The data points in this plot are expected to fall on a straight line. The zero crossing yields the equivalent distance in ambient air, L_{eq}, giving rise to a signal with the same magnitude as a signal from the sample [8].

4 Measurements

4.1 *Model system measurements*

Our human phantom measurements were performed on the system shown in Fig. 3. Laser light is injected into a primary scatterer S_1 of thickness l_1, separated by a distance d from a secondary scatterer S_2 of thickness l_2. The scatterers are made from white Delrin-type plastic, which has an estimated reduced scattering coefficient of about $2\,\mathrm{mm}^{-1}$ in the NIR region, similar to that of human tissue [9]. As in the case of human tissue, its absorption coefficient at the wavelength used, 760 nm, is negligible compared to its scattering coefficient.

In Fig. 3a (backscattering geometry) photons injected into S_1 are multiply scattered internally. Some photons escape into the air gap separating the scatterers and cross it along straight lines before penetrating into S_2. Here, multiple scattering occurs and some photons cross the air gap again to be scattered again in S_1. A small fraction of the photons primarily injected into S_1 will ultimately pass this scatterer again after passing the air gap twice before being detected by the photomultiplier. Such photons have travelled an air distance longer than $2d$. For a pathlength of $2d = 20$ mm, a fractional absorption of 4×10^{-4} due to the R7R7 oxygen line, is expected for air of normal ambient composition. Most of the light reaching the photomultiplier is backscattered only from S_1 and thus will not have a gas absorptive imprint. Therefore, the fractional absorptive signal will be diluted. Gas signal contributions from multiple passes through the air gap will be negligible. Clearly, the unwanted contribution from photons scattered in S_1 can only be strongly reduced by choosing a sufficiently large central beam stop before the photomultiplier cathode. This is in accordance with the normal observation that by increasing the distance between the source and the detector, deeper volumes of the scattering medium are probed [10].

Measurements in transmission geometry are illustrated in Fig. 3b. The main difference with the backscattering case is that all photons reaching the detector must now have crossed the air gap. However, the dominant signal contribution now comes from a single air-gap pass.

In order to study the influence of the primary and secondary scatterers in the backscattering geometry, thus emulating measurements on the frontal sinuses, a first series of measurements was performed where the oxygen signal was measured for a fixed value of l_1, while d and l_2 were varied, see Fig. 4a. In a second series of measurements, the same procedures were carried out, this time, with a fixed value of l_2, while l_1 was varied; see Fig. 4b. From Fig. 4a, we note that the total oxygen signal increases with increasing secondary scatterer thickness. This increase, however, rapidly decays and eventually stops after a certain thickness, around 30 mm, beyond which the secondary scatterer can be considered as an infinitely thick scatterer. This case pertains to clinical measurements where bone and brain constitute the massive secondary scatterer and large variations due to the properties of this scatterer are not expected. However, as can be seen in Fig. 4b, the primary scatterer will effect the measurements

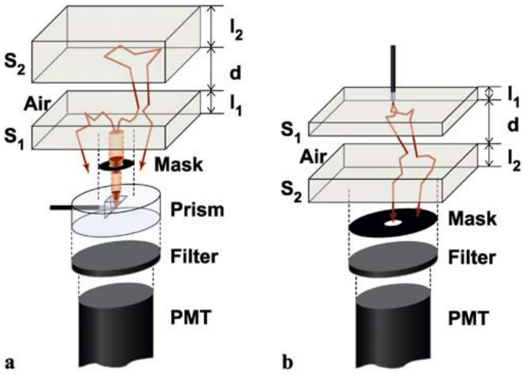

FIGURE 3 Arrangement of a phantom imitating the case of measurements on the (**a**) frontal sinuses (backscattering geometry) (**b**) maxillary sinuses (transmission geometry)

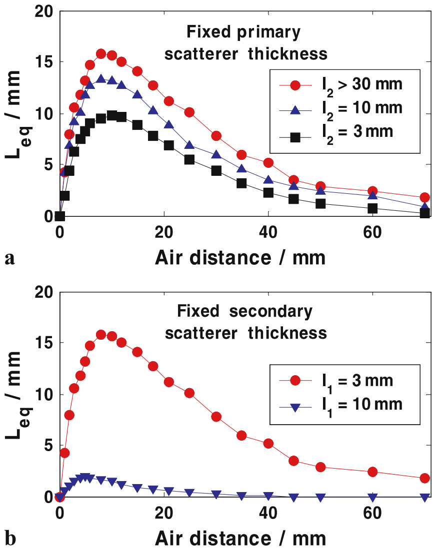

FIGURE 4 (**a**) Oxygen signal as a function of cavity thickness for different secondary scatterer dimensions with a fixed primary scatterer of thickness 3 mm, measured in backscattering geometry. (**b**) Oxygen signal as a function of cavity thickness for different primary scatterer thicknesses with a fixed secondary scatterer thickness above 30 mm, measured in backscattering geometry

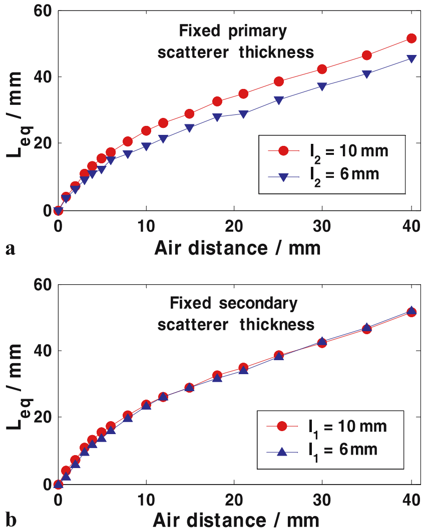

FIGURE 5 (**a**) Oxygen signal as a function of cavity thickness for different secondary scatterer dimensions with a fixed primary scatterer of thickness 10 mm, measured in transmission geometry. (**b**) Oxygen signal as a function of cavity thickness for different primary scatterer dimensions with a fixed secondary scatterer of thickness 10 mm, measured in transmission geometry

to a much larger extent since different humans have different depths into the sinuses. The signal starts to fall off for air distances above a certain threshold since photons from S_2 are more likely to be scattered outside of the finite size detector. By the same rationale, the signal levels are lower for a thicker primary scatterer. Since the maximum oxygen signal occurs for air distances of the order of 5–10 mm, this effect will most likely not be a limitation in human measurements on the frontal sinuses. However, for the thicker maxillary sinuses, the occurrence of the same signal for two different path lengths might cause problems. The transmission alternative pertaining to that case yielded data shown in Fig. 5.

In this geometry, the detection area and the thickness of the primary and the secondary scatterers do not have the same impact on the oxygen signal. The oxygen signal will always increase with air distance, since all collected photons must have travelled through the air distance. In Fig. 5a, where the primary scatterer thickness has been kept fixed, it can be seen that the oxygen signal increases with thicker secondary scatterer. Increasing the secondary scatterer thickness is equivalent to increasing the effective collection angle of the detector, giving added weight to oblique light rays through the air gap. In Fig. 5b the influence of the thickness of the primary scatterer has been studied. Little influence is observed, except from a minor effect at small air gaps. This effect comes from the fact that for a thicker primary scatterer a larger emission area results, presenting a larger solid angle to the detector arrangement. This introduces an additional path length for certain photons that reach the detector through the secondary scatterer. However, this effect decays rapidly with larger air gap since the additional path length becomes an increasingly smaller fraction of the air gap at hand.

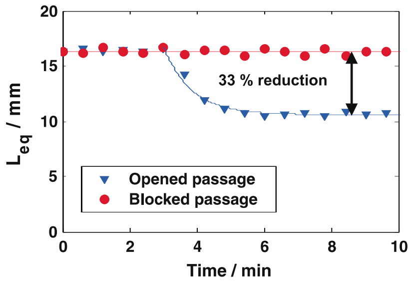

FIGURE 6 Change in oxygen signal as the gas in the phantom airspace is gradually replaced by a different gas mixture supplied by diffusion ($l_1 = 3$ mm, $l_2 > 30$ mm, $d = 8$ mm). The measurements were performed in backscattering geometry

In order to simulate gas transport between a sinus cavity and the nasal cavity, the air gap was replaced with a small air filled plastic bag filling the gap. This experiment can be done in both backscattering and transmission geometries on the maxillary sinuses and in backscattering geometry on the frontal sinuses. In all cases the oxygen signal is expected to change for the fixed geometry at hand. The bag was connected with a larger nitrogen filled bag via a valve and a plastic tube, in which cotton wool was inserted to reduce the passage. Figure 6 shows the change in oxygen signal when the gap oxygen content is reduced through diffusion, measured in backscattering geometry with $l_1 = 3$ mm and $l_2 > 30$ mm. Specifically, no change in signal is expected when the passage is blocked, as is also shown in the figure.

4.2 *Human tests*

In order to investigate the viability of the method for real human diagnostics, signals were recorded with the measurement head against the forehead of a volunteer. Data from measurements on the left and right frontal sinuses, and at closely-lying reference (solid tissue) locations are given in Fig. 7. The average L_{eq} on a frontal sinus varies substan-

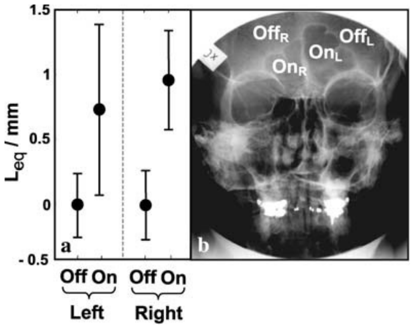

FIGURE 7 (**a**) The average L_{eq} from measurements on and off the frontal sinus on a healthy volunteer (as shown in Fig. 7b) together with error bars corresponding to one standard deviation. (**b**) X-ray image on the volunteer, showing the extent of the frontal sinuses

tially, which is expected since the sinus is not a cavity with fixed thickness. The measured L_{eq} is in the same order as the phantom measurement in backscattering geometry with $l_1 = 10$ mm and $l_2 > 30$ mm, see Fig. 4b. On the other hand, reference measurements outside the frontal sinuses results in a very stable zero signal, see Fig. 7a. Consistently, it was also noted that a human underarm yielded a stable zero level. These results indicate the possibility for real-time monitoring of the gas content across the frontal sinuses resulting in a low-resolution oxygen gas image. Clearly, a substantially improved signal-to-noise level would be required, which can be expected from an optimized set-up.

5 Discussion

The measurements presented for the phantom and for the volunteer show that the method proposed is viable for monitoring the presence of gas in normal human sinus cavities, as well as gas exchange through the connecting passages. The results suggest that anomalies due to sinus infections, with air being replaced by liquid, and a clogged passage way will be detectable, and that a new method for nonintrusive and real-time diagnostics can be developed. For the dynamic gas measurements, the difference in oxygen content in inhaled and exhaled air, 21 and 16%, respectively, might be used, employing the proper breathing technique.

A clinical trial including patients affected by inflammation and healthy volunteers must be performed in order to demonstrate the clinical usefulness of the approach. In particular, patient-to-patient variations could then be studied. The prospects for the construction of a compact handheld instrument with substantial diagnostic power seem good. Future developments may include measurements on other physiological gases such as carbon dioxide or methane with overtone absorption bands in the tissue optical window. In particular, measurements of concentration ratios are independent of the scattering properties and may supply valuable diagnostic information for occluded sinus cavities. Dynamic measurements might also take advantage of the higher contrast provided by using carbon dioxide, for which the concentration increases from close to zero in ambient air to about 5 percent in exhaled air. Alternatively, air with a high helium content, or with anomalous oxygen or nitrogen contents, might be used in the dynamic measurements. Helium is being employed in lung spirometry and for magnetic resonance imaging using hyperpolarized nuclei [11].

The techniques demonstrated in the present paper should be applicable to further diagnostics tasks in medicine. The lungs are normally surrounded by an air enclosure in the pleural room, which can be displaced by pleural fluid in connection with various illnesses. This condition is clinically identified by percutation at the chest wall. A much more exact diagnostic might be the application of the present technique in a backscattering geometry, where areas containing air could be distinguish from those filled with pleural liquid. Measurements through the ear drum should also be straight forward, although many conventional techniques for ear diagnostics are available.

With light penetration depth being a limiting factor in measurements of the kind discussed here, neonatal and premature children allow further possibilities, including lung and gastrointestinal gas surveillance.

ACKNOWLEDGEMENTS This work was supported by the Swedish Research Council, and the Knut and Alice Wallenberg Foundation. The authors are grateful for interaction with and support from Mikael Sjöholm, Mats Andersson, Henrik Fält, and Kjell Jonsson.

REFERENCES

1 *Health Matters*, Sinusitis, Nat. Inst. of Allergy and Infectious Diseases, US Dept. of Health and Human Services, Bethesda (2005)

2 S. Andersson-Engels, R. Berg, S. Svanberg, O. Jarlman, Opt. Lett. **15**, 1179 (1990)

3 G. Müller, B. Chance, R. Alfano, S. Arridge, J. Beuthan, E. Gratton, M. Kaschke, B. Masters, S. Svanberg, P. van der Zee (eds.), *Medical Optical Tomography, Functional Imaging and Monitoring SPIE Institute Series*, Vol. 11 (SPIE, Bellingham 1993)

4 M. Sjöholm, G. Somesfalean, J. Alnis, S. Andersson-Engels, S. Svanberg, Opt. Lett. **26**, 16 (2001)

5 G. Somesfalean, M. Sjöholm, J. Alnis, C. af Klinteberg, S. Andersson-Engels, S. Svanberg, Appl. Opt. **41**, 3538 (2002)

6 C. af Klinteberg, A. Pifferi, S. Andersson-Engels, R. Cubeddu, S. Svanberg, Appl. Opt. **44**, 2213 (2005)

7 C. Abrahamsson, T. Svensson, S. Svanberg, S. Andersson-Engels, J. Johansson, S. Folestad, Opt. Express **12** 4103, (2004)

8 L. Persson, H. Gao, M. Sjöholm, S. Svanberg, *Diode laser absorption spectroscopy for studies of gas exchange in fruits*, Lasers Opt. Eng., in press

9 R. Berg, S. Andersson-Engels, O. Jarlman, S. Svanberg, Appl. Opt. **35**, 3432 (1996)

10 T.J. Farrell, M.S. Pattersson, B. Wilson, Med. Phys. **19**, 879 (1992)

11 J.R. MacFall, H.C. Charles, R.D. Black, H. Middleton, J.C. Schwartz, B. Saam, B. Driehuis, C. Erickson, W. Happer, G.D. Cates, G.A. Johnson, C.E. Ravin, Radiology **200**, 553 (1996)

PAPER II

Non-intrusive optical study of gas and its exchange in human maxillary sinuses

L. Persson, M. Andersson, T. Svensson, M. Cassel-Engquist,
K. Svanberg, and S. Svanberg.

Proceeding of SPIE-OSA Biomedical Optics **6628**, Art. ID: 662804 (2007).

Non-intrusive optical study of gas and its exchange in human maxillary sinuses

L. Persson[a], M. Andersson[a], T. Svensson[a], M. Cassel-Engquist[a],
K. Svanberg[b], and S. Svanberg[a]

[a]Division of Atomic Physics, Lund University, P.O. Box 118, SE-221 00 Lund, Sweden
[b]Department of Oncology, Lund University Hospital, SE-221 85 Lund, Sweden

ABSTRACT

We demonstrate a novel non-intrusive technique based on tunable diode laser absorption spectroscopy to investigate human maxillary sinuses *in vivo*. The technique relies on the fact that free gases have much sharper absorption features (typical a few GHz) than the surrounding tissue. Molecular oxygen was detected at 760 nm. Volunteers have been investigated by injecting near-infrared light fibre-optically in contact with the palate inside the mouth. The multiply scattered light was detected externally by a handheld probe on and around the cheek bone. A significant signal difference in oxygen imprint was observed when comparing volunteers with widely different anamnesis regarding maxillary sinus status. Control measurements through the hand and through the cheek below the cheekbone were also performed to investigate any possible oxygen offset in the setup. These provided a consistently non-detectable signal level. The passages between the nasal cavity and the maxillary sinuses were also non-intrusively optically studied, to the best of our knowledge for the first time. These measurements provide information on the channel conductivity which may prove useful in facial sinus diagnostics. The results suggest that a clinical trial together with an ear-nose-throat (ENT) clinic should be carried out to investigate the clinical use of the new technique.

Keywords: Diode lasers, Near infrared spectroscopy, Absorption, Molecular oxygen, Medicine, Human sinuses

1. INTRODUCTION

In addition to the mouth and nasal cavities, the human head comprises further air volumes, all connected to the nose and the epipharyngeal area by venting channels. The middle ear, the frontal and maxillary sinuses are such air-filled volumes that are all quite vulnerable to infection (conditions called otitis and sinusitis, respectively). The cavities may then be filled with swollen mucosa, mucus and pus, and treatment with antibiotics is frequently considered appropriate. Each sinus is connected by a channel with a mucous membrane lining to the nose for free exchange of air and mucus. Anything that causes a swelling in the nose such as an infection, an allergic reaction, or another type of immune reaction, can affect the sinuses. With any of these above mentioned conditions, these passages may be blocked. In view of the many million patients suffering from this type of infection, improved diagnostic tools, complementing or replacing ultra-sound and CT scans are desirable.[1–6]

Recently, we reported on a new technique for assessing the sinuses relying on the monitoring of the oxygen absorption at about 760 nm. The absorption features are more then a factor of 1000 sharper than the spectral signatures of the tissues. In the first study, a faint oxygen signal could be observed in a backscattering geometry for the frontal sinuses of a healthy volunteer.[7] We have now explored the technique in a transmission geometry probing the maxillary (cheek) sinuses by injection of light using fibre optics in contact with the palate, and detecting the diffusely scattered light emerging out through the cheek bone. Strong signal differences in oxygen imprint between two volunteers with widely different anamnesis regarding maxillary sinus status were observed. By improved handling of noise and detrimental interference fringes, we now obtained prominent signals, which also allowed a dynamic study of gas exchange through the venting channels. Sinus ventilation studies have previously been performed by radioactive tracer gases, such as Xe^{133}, in combination with single photon emission computed tomography (SPECT).[8] Another method attempted is to use stable xenon inhalation followed by computer tomography (CT).[9]

E-mail: linda.persson@fysik.lth.se

Diagnostic Optical Spectroscopy in Biomedicine IV, edited by Dietrich Schweitzer, Maryann Fitzmaurice,
Proc. of SPIE-OSA Biomedical Optics, SPIE Vol. 6628, 662804, © 2007 SPIE-OSA · 1605-7422/07/$18

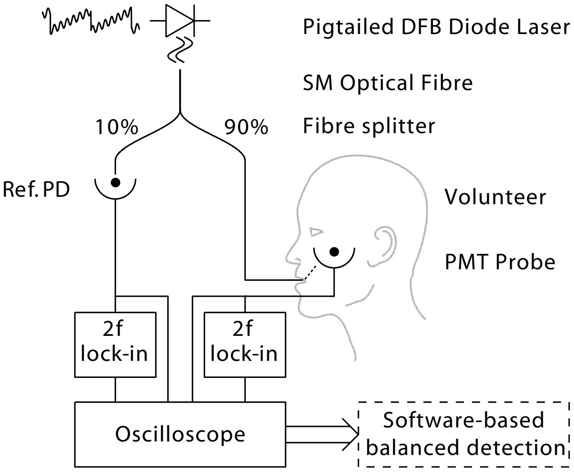

Figure 1. Schematic drawing of experimental arrangement for tunable diode laser gas absorption spectroscopy of oxygen probing the human maxillary sinuses.

In the following section the experimental setup, the data evaluation and the measurement procedure will be discussed. Results from two volunteers with widely different anamnesis regarding maxillary sinus status will then be shown. At the end conclusions of the presented work will be drawn. An outlook of future work will then be discussed.

2. MATERIAL AND METHOD

2.1. Experimental setup

A schematic drawing of the arrangement used in this study is shown in Fig. 1. The setup is based on a distributed feedback (DFB) diode laser that is single-mode (SM) fibre-pigtailed and thermoelectrically cooled (Nanoplus, Germany). The laser operates with an output power of about 4 mW. The light was scanned across the R11Q12 molecular oxygen absorption line at 760.445 nm (vacuum wavelength) by supplying a 4 Hz saw-tooth ramp to the laser driver current. A 9 kHz sinus-shaped wave was superimposed on the laser driver current in a wavelength modulation scheme to achieve sensitive detection.

The light from the fibre was split 90/10(%) with a single-mode fibre-coupled beamsplitter (Laser2000, Sweden) to allow balanced detection. The fibre carrying the lower intensity was directly guided to a photo diode, PD, (10DP/SB, OSI Optoelectronics), producing the reference signal. The other fibre part (90% of the intensity) was positioned on the palate inside the mouth. The light then travels through the tissue with a fraction part of it crossing the maxillary sinuses. The multiply scattered light was detected by a photomultiplier tube, PMT, (5070A, Hamamatsu) at different locations on the cheek bone by a handheld probe. This signal is denoted as the sample signal. The two signals were each split into two parts; one of the parts was directly connected to an oscilloscope remote controlled, called the direct signal, while the other parts was first sent via a lock-in amplifier (5209, EG&G Princeton Applied Research), where the 2f signal was detected.

2.2. Data evaluation

To suppress noise and perturbations, like optical interference fringes, software based balanced detection was used. These procedures have been described in detail elsewhere.[10] Briefly, the two detected 2f signals are first normalised with the direct signals. A set of parameters is then estimated by comparing the normalised reference signal and the normalised sample signal at frequency regions outside the expected oxygen imprint. A matched version of the reference signal is then subtracted from the sample signal over the whole frequency scan.

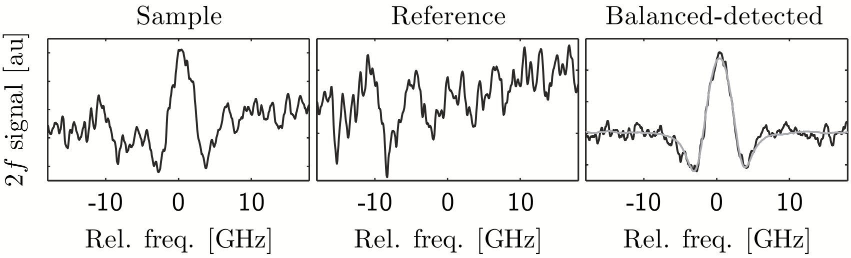

Figure 2. Typical recorded signals in this study from the sample detector (to the left) and the reference detector (center). The balanced-detection signal is also included with a fitted ideal function (to the right). The signal corresponds to an L_{eq} of 25 mm corresponding to an absorption fraction of $3.8 \cdot 10^{-4}$.

Once a balanced-detection signal is computed, an ideal signal is fitted to it. This signal obtained from a measurement where the oxygen imprint is many orders larger than the noise, created by measuring over an air distance of several meters. Fig. 2 shows typical recorded signals. To the left a signal from the sample detector is shown, in the center a corresponding signal from the reference detector is given, and to the right the computed balanced-detection signal is included together with the fitted ideal signal.

A quantity called the equivalent mean path length, L_{eq}, was estimated from the amplitude of the balanced-detection signal. This quantity corresponds to how far light has to travel in ambient air to achieve the observed absorption imprint. The calibration was done by employing the standard-addition method.[7, 10] The signal shown in Fig. 2 corresponds to an L_{eq} of 25 mm. We note that the L_{eq} signals depend on the gas concentration as well as the effective light path way that becomes an undefined quantity in a scattering medium. However, as we shall see, this difficulty can be suppressed under certain conditions.

2.3. Measurement procedure

Measurements were performed on two volunteers; one with constantly recurring sinus problems (Volunteer I) the other one with no history of such problems (Volunteer II). A CT image of Volunteer I is shown in Fig. 3a. It can clearly be seen that the left maxillary sinus is completely filled with inflamed swollen mucosa while the right one is only partly filled.

Four different measurements are presented in this study and are listed below:

Signal levels: The L_{eq} was measured on both volunteers in the left and right maxillary sinuses. The fibre was placed on the palate inside the mouth in close proximity to the particular sinus. The light was detected at two different locations; on the cheek bone and translated towards the nose (about 2 cm). Measurements were performed once a day during about a week.

Control: Two types of reference measurements were performed to investigate any possible L_{eq} offset in the current setup. The signal was measured through the cheek and the hand of the volunteers. In the case of reference measurements through the cheek, the fibre was placed inside the mouth in contact with the cheek and the detector was positioned on the opposite side of the cheek. In the case of reference measurements through the hand, the fibre was placed in contact with the palm and the detector was positioned on the opposite side of the hand.

Reproducibility: The reproducibility of the measured L_{eq} values was also investigated for Volunteer II. 10 measurements were done on the each sinuses by removing the detector and fibre between each recording. Measurements were done for the both the detector positions explained above.

Gas exchange: To study the ostia function (ventilation between nasal cavity and sinus cavity) L_{eq} was measured continuously during inhalation of non-ambient air (pure nitrogen). Data was collected for about 3.5 min;

1 min before flushing with nitrogen, 30 s during nitrogen flush through the nostril and for about about 2 min after terminating the flush, all the time pursuing normal mouth breathing. Each recorded signal was averaged for about 15 s. Measurements were performed on both the left and right maxillary sinuses on Volunteer I and II.

3. RESULT

Signal levels

The average measured L_{eq} values from the two volunteers together with error bars corresponding to two standard deviations are shown in Fig. 3b. It was observed that similar values were measured at the different detector locations. This is consistent with the results from Monte Carlo simulations of the signal strengths.[11, 12] In the figure it can be seen that Volunteer I exhibits a small signal on the right sinus ($L_{eq} \approx 10$ mm) while nothing was detectable on the left side. The setup presented has a detection limit of L_{eq} of about 2 mm, corresponding to an absorption fraction of $3 \cdot 10^{-5}$.[10] In contrast to the measurements performed on Volunteer I, a much larger signal was observed on Volunteer II in both the right ($L_{eq} \approx 26$ mm) and left sinus ($L_{eq} \approx 20$ mm). Clearly, a significant difference on the oxygen imprint could be observed between the volunteer with constantly recurring sinus problems and the volunteer with no history of such problems.

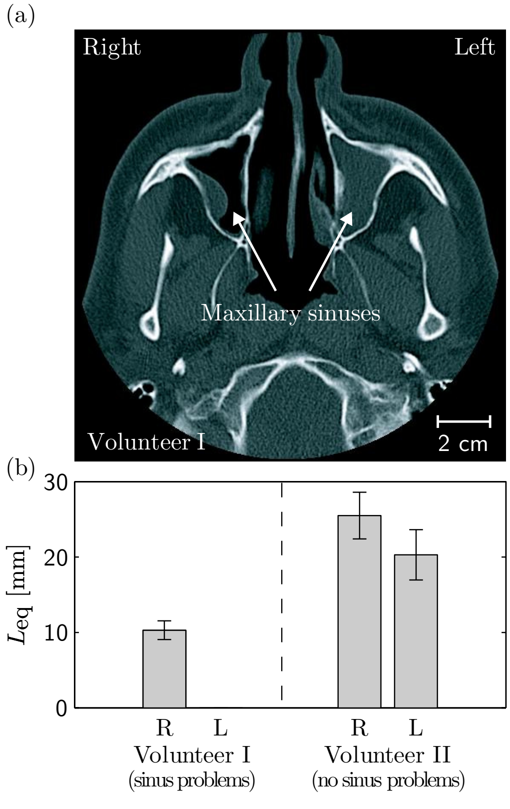

Figure 3. a) A CT image of Volunteer I with constantly recurring sinus problems. b) Signal levels study - Measured L_{eq} for both volunteers on the right and left maxillary sinus (Volunteer I with constantly recurring sinus problems, Volunteer II with no history of such problems).

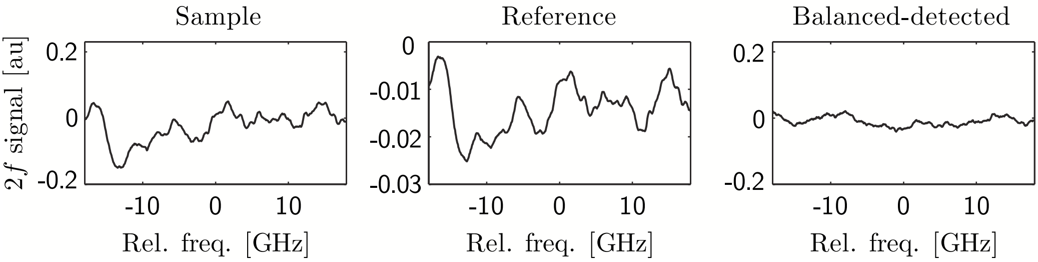

Figure 4. Control study - Typical recorded signals in this study from the sample detector (to the left) and the reference detector (center) when performing reference measurements. The fibre has been placed inside the mouth in contact with the cheek and the detector has been positioned on the opposite side of the cheek. The balanced-detection signal is also included. The remaining noise floor corresponds to about a L_{eq} of 2 mm (absorption fraction of $3 \cdot 10^{-5}$).

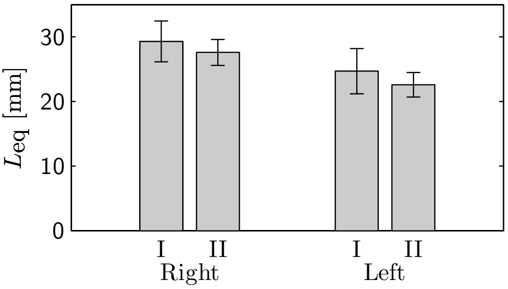

Figure 5. Reproducibility study - Average L_{eq} together with two standard deviations obtained from 10 measurements at each detector position (I : Cheek bone, II : Towards nose) and maxillary sinus for Volunteer II. The fibre and the detector were removed in between each recording.

Control

Before each measurement two reference measurements were performed. These measurements resulted in a consistently non-detectable signal providing the information that no oxygen offset is present in the setup. In our case a non-detectable signal corresponds to a L_{eq} of less than 2 mm as previously mentioned.[10] In Fig. 4 typical signals when performing reference measurements can be seen. From the balanced-detection signal the remaining noise floor can be observed.

Reproducibility

Fig. 5 shows the average L_{eq} together with error bars corresponding to two standard deviations obtained from 10 measurements at each detector position (I : Cheek bone, II : Towards nose) and maxillary sinus for Volunteer II when removing the detector and fibre between each recording. As can be seen, the standard deviation corresponds to about 10% for each position.

Gas exchange

Gas exchange studies were performed on both volunteers. No change could be observed in Volunteer I, while Volunteer II showed a decrease of signal when the nose cavity was flushed with pure nitrogen through a plastic tube positioned at the opening of the nostril. In Fig. 6 the invasion of N_2 in the right maxillary sinus of Volunteer II can be seen. The reinvasion of oxygen into the sinus can as well be observed when terminating the N_2 flush. During the measurements the fibre was placed on the palate, and the detector on the right cheek bone without

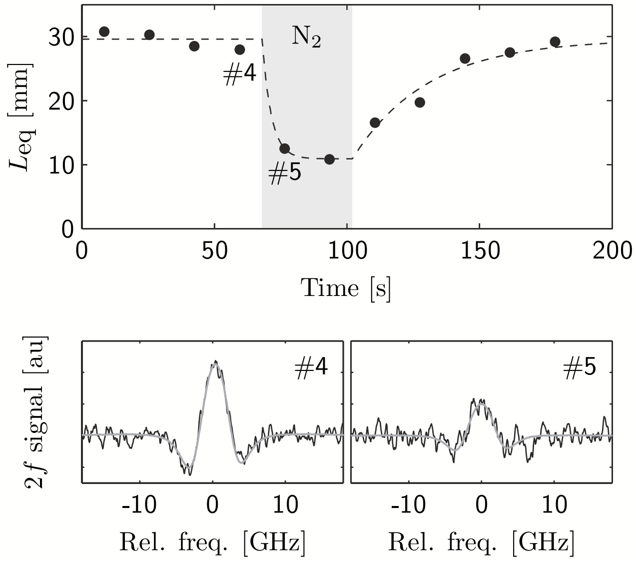

Figure 6. Gas exchange study - The measured L_{eq} (solid dots) together with a trend line (dashed line) in the right maxillary sinus of Volunteer II having no history of sinus problems. The oxygen level is first measured, N_2 is then flushed into the nasal cavity through the nostril and the invasion of the gas in the sinus is measured. The reinvasion of air is then recorded after terminating the N_2 flush. Two balanced-detection signals are also included in the figure; one before and one during N_2 flush.

being moved. Signals were averaged for about 15 s corresponding to the spacing between the measurement points. Two balanced-detection signals are also included in the figure; one signal before the gas is flushed and one during flushing. A reduction of about 2/3 was obtained in the signal for the case presented. More experiments with the same procedure have been performed showing different reductions depending on the N_2 flow.

4. CONCLUSION AND OUTLOOK

The technique described allows the monitoring of free oxygen gas in human sinuses, both in backscattering geometry, as demonstrated in Ref. [7] for the frontal sinuses, and in transmission geometry for the maxillary sinuses, as shown above. Actually, hybrids, where light is injected through the orbital wall close to the upper eye lid and the emerging light is detected against the forehead, or light is injected from the outside below the cheek bone and detected above the cheek bone have proved to be feasible, yielding strong signals, without the need of internal light injection.[13]

A person with sinus problems could readily be distinguished from a non-affected person also when varying scattering conditions were not accounted for. The degree of scattering, however, do not influence the data when the time constants for gas flow through the connecting channels are studied, since only the relative time variation of the signal is recorded. Like-wise, by forming a ratio between signals due to two gases interrogated at similar wavelengths, unknown scattering factors may be taken into account. Referencing around 935 nm to water vapor in the cavity, with its concentration determined only by the temperature (naturally thermostated to approximately 37^{o}C), it should be possible to directly determine the concentration of oxygen in the sinus, which might be related to the type of infection present.[13] Monitoring of free water vapor in scattering media was recently demonstrated in connection with wood drying.[14]

Based on the promising results reported here, a clinical study with well diagnosed patients, for which CT images are available, will be performed. This will be carried out together with an ear-nose-throat (ENT) clinic.

We anticipate, that a new and powerful non-intrusive optical method can be developed for assisting in fast and improved diagnostics of the common sinus problems, which frequently are abated with antibiotics, on sometimes uncertain grounds.

ACKNOWLEDGMENTS

The authors are grateful for fruitful discussions with N.G. Holmer, L. Malm, and M. Jannert. This research was supported by the Swedish Research Council, the Medical Faculty, Lund University, and the Knut and Alice Wallenberg Foundation.

REFERENCES

1. Health Matters, Sinusitis, Nat. Inst. of Allergy and Infectious Diseases, US Dept. of Health and Human Services, Bethesda (2005).
2. P. Stierna, G. Karlsson, I. Melén, and M. Jannert, "Aspect on Sinusitis - Diagnosis and threatment in adults," Proceedings from Meeting of the Swedish Association of Otorhinolaryngologists, HNS, Stockholm (1995).
3. M. Mafee, "Modern imaging of paranasal sinuses and the role of limited sinus computerized tomography; considerations of time, cost and radiation," *Ear Nose Throat J.* **73,** 532–534 (1994).
4. S. Zinreich, "Progress in sinonasal imaging," *Ann. Oto. Rhinol. Laryn.* **196,** 61–65 (2006).
5. D. Leopold, S. Zinreich, B. Simon, M. Cullen, and C. Marcucci, "Xenon-enhanced computed tomography quantifies normal maxillary sinus ventilation," *Otolaryngol. Head Neck Surg.* **122,** 422–424 (2000).
6. R. Rizzi, I. Dimitrov, A. Thompson, G. Jones, T. Gentile, M. Ishii, R. Reddy, M. Schnall, and J. Leigh, "MRI of hyperpolarized ^{3}He in human paranasal sinuses," *Magn. Reson. Med.* **39,** 865–868 (1998).
7. L. Persson, K. Svanberg, and S. Svanberg, "On the potential of human sinus cavity diagnostics using diode laser gas spectroscopy," *Appl. Phys. B* **82,** 313–317 (2006).
8. B. Paulsson, J. Dolanta, P. Ohlin, I. Larsson, and S. Lindberg, "Paranasal sinus ventilation in healthy subjects and in patients with sinus disease evaluated with the 133-Xenon washout technique," *Ann. Oto. Rhinol. Laryn.* **110,** 667–674 (2001).
9. D. Leopold, S Zinreich, B Simon, M Cullen, and C. Marcucci, "Xenon-enhanced computed tomography quantifies normal maxillary sinus ventilation ," *Otolaryn. Head Neck* **122,** 422–424 (2000).
10. L. Persson, F. Andersson, M. Andersson and S. Svanberg, "Approach to optical interference fringes reduction in diode laser absorption spectroscopy," *Appl. Phys. B* **87,** 523–530, (2007).
11. E. Kristensson and L. Simonsson, M.Sc. Thesis, Lund Institute of Technology, Lund Reports on Atomic Physics LRAP-361, LTH, Sweden (2006).
12. L. Persson, E. Kristensson, L. Simonsson, and S. Svanberg, "Monte Carlo simulations of optical human sinusitis diagnostics," *J. Bio. Med. Opt*, in press (2007).
13. L. Persson, M. Andersson, Märta Cassel-Engquist, K. Svanberg, and S. Svanberg, "Gas monitoring in human sinuses using tunable diode laser spectroscopy," *Manuscript in preparation*, (2007).
14. M. Andersson, L. Persson, M. Sjöholm, and S. Svanberg, "Spectroscopic studies of wood-drying processes," *Optics Express* **14,** 3641–3653, (2006).

PAPER III

Gas monitoring in human sinuses using tunable diode laser spectroscopy

L. Persson, M. Andersson, M. Cassel-Engquist, K. Svanberg, and S. Svanberg.

Journal of Biomedical Optics **12**, Art. ID: 053001 (2007).

Journal of Biomedical Optics 12(5), 1 (September/October 2007)

Gas monitoring in human sinuses using tunable diode laser spectroscopy

Linda Persson
Mats Andersson
Marta Cassel-Engquist
Lund University
Division of Atomic Physics
P.O. Box 118
SE-221 00 Lund, Sweden

Katarina Svanberg
Lund University Hospital
Department of Oncology
SE-221 85 Lund, Sweden

Sune Svanberg
Lund University
Division of Atomic Physics
P.O. Box 118
SE-221 Lund, Sweden

Abstract. We demonstrate a novel nonintrusive technique based on tunable diode laser absorption spectroscopy to investigate human sinuses *in vivo*. The technique relies on the fact that free gases have spectral imprints that are about 10.000 times sharper than spectral structures of the surrounding tissue. Two gases are detected; molecular oxygen at 760 nm and water vapor at 935 nm. Light is launched fiber optically into the tissue in close proximity to the particular maxillary sinus under study. When investigating the frontal sinuses, the fiber is positioned onto the caudal part of the frontal bone. Multiply scattered light in both cases is detected externally by a handheld probe. Molecular oxygen is detected in the maxillary sinuses on 11 volunteers, of which one had constantly recurring sinus problems. Significant oxygen absorption imprint differences can be observed between different volunteers and also left-right asymmetries. Water vapor can also be detected, and by normalizing the oxygen signal on the water vapor signal, the sinus oxygen concentration can be assessed. Gas exchange between the sinuses and the nasal cavity is also successfully demonstrated by flushing nitrogen through the nostril. Advantages over current ventilation assessment methods using ionizing radiation are pointed out. *© 2007 Society of Photo-Optical Instrumentation Engineers.*
[DOI: 10.1117/1.2777189]

Keywords: infrared spectroscopy; diode lasers; molecular spectroscopy; medicine; scattering.

Paper 07111R received Mar. 23, 2007; revised manuscript received Jun. 11, 2007; accepted for publication Jun. 11, 2007.

1 Introduction

The human paranasal sinuses are air-filled cavities embedded in the cranial skeleton. The frontal sinuses are located behind the frontal bone, while the maxillary sinuses are located below the orbital floor in the cheek bones. The sphenoidal sinus, split by a partial wall, is located centrally in the cranium. The ethmodial cells are multifocal small cavities located on each side of the upper part of the nose cavity. The sinuses are lined with epithelium-bearing glands and cilia, which transport mucosa toward the channel, or ostium, connecting the sinus to the nasal cavity. The frontal and maxillary sinus ostia connect to the middle nasal meatus. The function of sinuses is still under discussion. They seem to be locations of nitric oxide production important for ventilation functions.[1,2] The anatomy of the head is shown in Fig. 1(a),[3] with the sinuses schematically indicated; the frontal and maxillary sinuses are clearly discerned in the magnetic resonance image (MRI) shown in Fig. 1(b).

Good ventilation seems to be a requisite for healthy sinuses. Infection in the cavities, sinusitis, is affecting a very large number of patients, in the U.S. alone about 37 million people are annually diagnosed.[4] Narrow ostia or partial or full blockage can cause severe problems and chronic sinusitis. Nasal polyps can be one cause. Excessive mucosal and pus production are secondary signs of sinusitis. Infection is frequently treated with antibiotics, and decongestants, such as oxymetazoline and zylometazoline, are prescribed to improve ventilation. Surgical intervention with intended ostial widening is necessary in severe cases for achieving long-term improvement. Clearly, a precise diagnosis of sinusitis is of importance, particularly for deciding whether antibiotics should be administered or not. Common present diagnostics may include the use of ultrasound, capable of seeing from the echo structure if the cavity is air filled or not, and in severe cases the use of x-ray radiography. However, none of these techniques can assess the ventilation of the cavities or the composition of enclosed gas.

Ventilation studies for the paranasal sinuses have been pursued with intrusive and nonintrusive techniques. Among the former, cannulae have been used to measure pressure in the sinuses and in the nasal cavity and their interrelation. Nitrogen gas has also been injected as well as gaseous radioactive isotopes, in particular Xe^{133}, with a half-life of 5.2 days. Scintillation cameras or single photon emission computerized tomography (SPECT) have been used to assess the transport of the gas. Xe^{133} has also been administered noninvasively through breathing, followed by repeatedly performing the Valsalvas maneuver.[5] Stable Xe gas, having a certain radio opac-

---

Address all correspondence to: Linda Persson, Atomic Physics Division, Department of Physics, Lund University - P.O. Box 118, Lund, Skåne 221 00 Sweden; Tel: +46 46 2224138; Fax: +46 46 222 42 50; E-mail: linda.persson@fysik.lth.se

1083-3668/2007/12(5)/1/0/$25.00 © 2007 SPIE

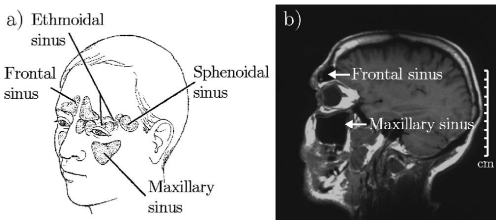

Fig. 1 (a) Illustration showing the location of the human sinuses (adopted from Ref. 3). (b) MRI image indicating the location of human maxillary and frontal sinuses.

ity, has also been used noninvasively, followed by repeated computerized tomographic (CT) recordings.[6] Clearly, these methods expose the patients to a considerable radiological dose. Further, radioactive as well as stable Xe gas is very costly, as is the the use of SPECT and CT installations. Hyperpolarized ^{3}He has been used in MRI studies,[7] also costly investigations. Thus, there is a need for a complementary technique avoiding these hazards and costs while still allowing a detailed assessment of ventilation and gas composition.

We demonstrate the possibility to statically and dynamically nonintrusively study human sinuses by observing the normal physiological gases of oxygen and water vapor. This is done by using tunable diode laser spectroscopy on the gases exhibiting narrow-band absorptive imprints in the near infrared spectral region. The present study extends and establishes the methodology, which was first described in two recent exploratory papers.[8,9]

The new development became possible by taking advantage of optical spectroscopic techniques refined in the environmental monitoring of free gas, and an understanding of tissue optics, developed for purposes such as optical mammography and photodynamic therapy dosimetry (e.g., Ref. 10). We could thus demonstrate the possibility to investigate the frontal sinuses using tunable diode laser spectroscopy employing phase sensitive detection of wavelength-modulated absorption signals.[8] The presence of molecular oxygen was measured close to 760 nm in a backscattering detection geometry. To understand the behavior of the expected signals, a phantom was first investigated. It consisted of two Delrin plates separated by a variable air gap, where the first plate represented the frontal bone, the air space the frontal sinus, and the second plate the underlying tissue. Some preliminary results from a human frontal sinus were obtained. These measurements have been modeled in Monte Carlo simulations, and the possibility of imaging using a scanned probe was discussed.[11] Since then, the experimental techniques have been improved by using pigtailed lasers and balanced detection to suppress noise.[12] This allowed us to study gas exchange between the maxillary sinuses and the nasal cavity by using a transmission detection geometry. The fiber was placed inside the mouth on the palate and the detector externally on the cheek bone. For a short time, the nasal cavity was flushed through the nostril with nitrogen gas and the decay of the oxygen signal was recorded on a healthy volunteer, resulting in the conclusion that the channels between the cavities were open, allowing free gas exchange. No such behavior could be observed on a volunteer with constantly recurring sinus problems.[9]

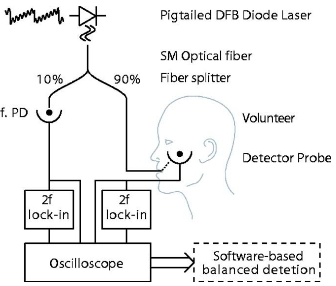

Fig. 2 Schematic drawing of the experimental setup used to study human sinuses.

We demonstrate molecular oxygen measurements on maxillary sinuses for 11 healthy volunteers using the transmission detection geometry discussed. The measured values have been compared with values obtained using Monte Carlo simulations of a model representing the maxillary sinuses. To further investigate the clinical potential of the technique, other different possible detection geometries have been explored, allowing monitoring of both the maxillary and the frontal sinuses. A further gas—water vapor interrogated at 935 nm—has also been studied, providing new information. Water vapor lines around 980 nm were studied in a previous paper on drying processes.[13] Since liquid water, always abundantly present in human tissue, also has an absorption peak at 980 nm, we now choose a shorter wavelength where most of the liquid water absorption is eliminated to allow depth penetration. Investigations of the gas exchange of the sinuses and the nasal cavity in the different geometries have as well been performed using pure nitrogen gas flushed through the nostril.

In the next section, the experimental setup and the data analysis are presented. The gas monitoring procedure, including the different detection geometries used, are described, followed by an explanation of the model used in the Monte Carlo simulations. Results of the measurements of the maxillary and frontal sinuses using the different detection geometries are then presented and discussed. Finally, conclusions are drawn and suggestions for further work are put forward.

2 Materials and Methods

2.1 *Experimental Setup*

A schematic drawing of the experimental setup used in this study is shown in Fig. 2. In the case of molecular oxygen detection, a single-mode pigtailed distributed feedback (DFB) diode laser (Nanoplus, Germany) operating at around 760 nm with an output of about 4 mW is used as a spectroscopic light source. When performing measurements on water vapor, the laser is changed to another unit operating around 935 nm (Nanoplus, Germany) with similar output. The laser is scanned across an absorption line of the gas under study by supplying a saw-tooth ramp (Hz) to the laser driver current. To achieve wavelength modulation spectroscopy (WMS) with lock-in detection, the operating current is also modulated by a sinusoidal wave at 9 kHz, with a modulation index of about 2.2 in both gas cases. In the case of molecular oxygen, the R11Q12 absorption line at 760.445 nm (vacuum wavelength) is used, and in the case of water vapor, the absorption line at 935.686 nm (vacuum wavelength) is used [vibration; (000) $\rightarrow$(121), rotation; $J''=3\rightarrow J'=4$, $K''_a=0\rightarrow K'_a=0$, $K''_c=3\rightarrow K'_c=4$].

The light is fiber optically split 90/10(%) into two parts with a single-mode fiber-coupled beamsplitter (Laser2000, Sweden). The low-intensity part is directly guided to a silicon detector (UDT 10DP/SB). This part is later used in the analysis as the reference beam to obtain balanced detection for efficient noise subtraction.[12] The other part is guided to different positions on the human head, and the multiply scattered light is detected externally on the human head according to different detection geometries further discussed in Sec. 2.3 on the *gas monitoring procedure*. In the case of molecular oxygen detection, a photomultiplier tube (PMT) (Hamamatsu 5070A) with a circular detection area of 20 mm diam is used, and in the case of water vapor detection, a photodiode (Hamamatsu S3584-06) with similar detection area is used. Both detectors are mounted as handheld probes.

The two detected signals are each divided into two parts. They are sent to a computer-controlled digital oscilloscope, one directly, referred to as the direct signal, and one via a lock-in amplifier where the signal at twice the modulation frequency is recorded, referred to as the $2f$ signal. WMS is often referred to as derivative spectroscopy, since the different harmonics are proportional to the corresponding derivative of the signal. Thus, in the case of detection at twice the modulation frequency, the $2f$ signal looks like the second derivative of the direct absorption.

2.2 *Data Analysis*

The $2f$ signals are normalized with the direct signals to make them independent of the amount of light reaching the detector. The normalized $2f$ sample signal is then subtracted with a processed version of the reference signal to achieve a balanced detection signal.[12] An ideal absorption signal is then fitted to the balanced detection signal, and from this the peak-to-peak distance is estimated, referred to as the WMS value. For small absorptions, the WMS value is proportional to the absorbance, and thus to the product of the gas concentration and the path length traveled by the light. To transform the WMS value to a more meaningful quantity, the standard addition method is used.[14] The standard addition procedure is to add known path lengths of ambient air in-between the light source and the detector. At each distance, the WMS value is measured. A so-called equivalent mean path length L_{eq} can then be estimated, corresponding to the air distance that the light has to travel in ambient air to obtain the same oxygen or water vapor absorption imprint. The calibration procedures for both gases were performed at room temperature of 25 °C and a relative humidity of about 20%. It should be noted that one would expect 100% humidity in the sinus cavities due to liquid water in the surrounding tissue, with a temperature close to 37 °C. At such a temperature, the water vapor pressure is about a factor of 2 higher than at 25 °C.[15] Thus, a particular water vapor signal from a sinus corresponds to about 1/10 of the surrounding air path length yielding the same signal. This factor is further discussed in Sec. 4.

2.3 *Gas Monitoring Procedure*

The maxillary and frontal sinuses of human volunteers were investigated using the nonintrusive technique presented. In the case of the maxillary sinus, two different detection geometries were used (*PC* and *CC*), and in the case of frontal sinus studies, a single detection geometry was used (*OF*) as follows.

- (*PC*) *Palate - cheek bone geometry*: fiber placed inside the mouth against the palate close to the sinus under study and the detector positioned on and around the cheek bone.
- (*CC*) *Cheek - cheek bone geometry*: fiber placed outside on the cheek below the cheek bone and the detector positioned on the cheek bone.
- (*OF*) *Orbital edge - frontal bone geometry*: fiber placed on the horizontal part of the frontal bone under the eyebrow pointing up toward the frontal bone and the detector placed at different positions on the frontal bone.

Before any measurements were performed on any human sinuses, two types of reference measurements were carried out to investigate any possible L_{eq} offset in the current setup. The oxygen and water vapor signal were measured through the cheek below the cheekbone and through the hand of the volunteers where no free gas is expected. These measurements resulted in a consistently nondetectable gas imprint signal, showing that no gas offset is present due to gas between the setup components.

Molecular oxygen measurements were performed with geometry *PC* on 11 volunteers, 10 of which have no history of sinus problems (volunteers 1 to 10) and one with constantly recurring sinus problems (volunteer 11). The detector was placed at three different positions; on the cheek bone, slightly toward the nose, and slightly under the cheek bone. At each detector position, three consecutive measurements were performed by removing and repositioning the fiber and the detector between each recording. The reproducibility of the measured L_{eq} values was also investigated by measuring ten consecutive times at each detector position for one volunteer.

Measurements of oxygen and water vapor were performed with detection geometry *PC* on the maxillary sinuses on volunteers 1, 2, and 11, and on volunteer 1 also with geometry *CC*. In addition, frontal sinus measurements with geometry *OF* were performed on volunteer 1. In the case of geometry *PC* and *CC*, the detector was positioned on the cheek bone. In the case of frontal sinus study, detection geometry *OF*, the detector was positioned at three different locations on the fontal bone toward the particular sinus; about 10 mm and about 20 mm straight up above the light source, and about 10 mm straight up over the center of the eyebrow. At each detector position, ten consecutive measurements were performed by removing the fiber and the detector between each recording. Molecular oxygen was measured first, followed by water vapor directly after using the same procedure.

To study the communication and ventilation between the nasal cavity and the human sinuses, we investigated the transient response to pure nitrogen flushing of the nasal cavity for about 1 min through the nostril. These measurements were performed on volunteer 1 with all detection geometries and volunteer 11 with detection geometry *PC*. Measurements were continuously recorded for about 8 min. 1 min before

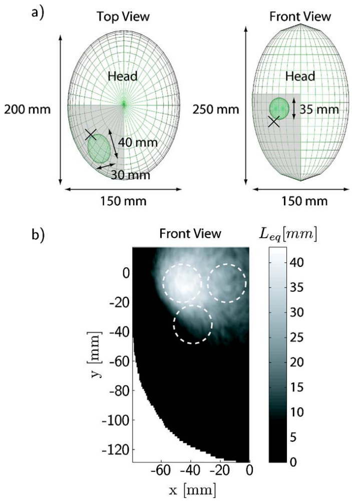

Fig. 3 (a) A model used for Monte Carlo simulations created in ASAP™ representing measurements on the human maxillary sinus according to detector geometry *PC*. The region where the rays were collected is indicated by the gray shaded area. The cross represents the location of the light source. (b) The simulated L_{eq} for the model shown in (a). The different positions of the detector in the case of real measurements are also indicated.

flushing, 1 min during flushing, and 6 min after terminating the flush, all the time pursuing normal mouth breathing. Each recorded signal was averaged for about 15 sec. Measurements of molecular oxygen and water vapor were performed directly after each other. To investigate the stability of the recorded signals for the gas exchange study time period, the same procedure was also carried out without N_2 flush.

2.4 *Simulations*

Monte Carlo simulations were performed by using the Advanced Systems Analysis Program (ASAP) software.[16] In this work, we present a model according to Fig. 3(a) to simulate measurements on the maxillary sinuses employing detection geometry *PC* when detecting the multiply scattered light on and around the cheek bone. The position of the light source is indicated by a cross in the model. The maxillary sinus was represented by an ellipsoid with typical human dimensions. It was placed embedded in a scattering medium with optical properties set to $g=0.87$ (anisotropy factor), $\mu_s=16\ \text{mm}^{-1}$ (scattering coefficient), and $\mu_a=0.0005\ \text{mm}^{-1}$ (absorption coefficient) typical of bone.[17]

The flux and the pattern through the model for rays reaching the detector were recorded. The distance each ray traveled in the ellipsoid was calculated. By summarizing the product of the distance in the cavity and the flux for each ray and normalizing it with the total flux reaching the detector, the L_{eq} value could be estimated. Similar simulations have been presented in Ref. 11 for frontal sinus imaging.

3 Results and Discussion

3.1 *Maxillary Sinus Study*

Figure 3(b) shows L_{eq} obtained through simulation measurements on the maxillary sinuses according to detection geometry *PC*. It can be seen that L_{eq} values between 10 and 40 mm can be expected when performing measurements on volunteers with typical maxillary sinus dimensions when the detector is placed on and around the cheek bone. These values are heavily influenced by the optical properties used in the simulations, but can still be used as an indication of the experimental results to be expected. If, for example, a higher absorption coefficient is used, as was experimentally obtained by Hoshi et al.,[18] a decrease of L_{eq} would be obtained.

The results from the molecular oxygen measurements on the volunteers according to geometry *PC* are presented in Table 1. The L_{eq} value shown is an average from the three different detector positions. It was observed that the lowest L_{eq} is always recorded when the detector is positioned below the cheek bone, in agreement with the simulation results, where the detection areas are also indicated [Fig. 3(b)]. All volunteers with no history of sinus problems presented a detectable oxygen absorption imprint. However, no oxygen imprint could be recorded on the left side of volunteer 11. The reproducibility of the measured L_{eq} values was also investigated at each detector position for one volunteer. A standard deviation of about 10% was obtained when the average measured L_{eq} value was of the order of 30 mm. A clear left-right asymmetry was observed for volunteer 11 as discussed before. Smaller asymmetries were observed also for other volunteers. However, it should be noted that the L_{eq} value depends on concentration as well as path length, and thus detailed analysis regarding anatomy are hard to draw.

The results from the measurements of oxygen and water

Table 1 Measured L_{eq} values for oxygen in the maxillary sinus for volunteers 1 through 11 according to detection geometry *PC*. N represents volunteers with no history of sinus problems and Y the volunteer with constantly recurring sinus problems. The presented values are averaged from three different detector positions; on the cheek bone, slightly toward the nose, and slightly under the cheek bone.

Volunteer history	1	2	3	4	5	6	7	8	9	10	11
	N	N	N	N	N	N	N	N	N	N	Y
Left L_{eq} [mm]	20±4	29±6	8±7	24±3	18±2	12±9	25±0	13±9	28±0	11±2	-
Right L_{eq} [mm]	27±7	31±3	17±2	16±4	21±8	13±6	23±1	12±6	29±9	12±2	10±3

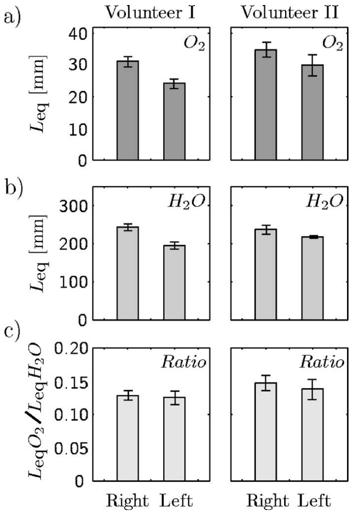

Fig. 4 L_{eq} for (a) molecular oxygen and (b) water vapor measured in left and right maxillary sinuses for volunteers 1 and 2 using detection geometry *PC* with the detector positioned on the cheek bone. The data shown correspond to the average of ten recordings together with two standard deviations. (c) The ratios of the L_{eq} for oxygen and water vapor are shown.

vapor with detection geometry *PC* on the maxillary sinuses on volunteers 1 and 2 are shown in Figs. 4(a) and 4(b). The average L_{eq} values are presented together with two standard deviations. It should be noted that the recorded L_{eq} for water vapor is about 8 larger than the value for oxygen for volunteers 1 and 2. The same types of measurements were attempted on volunteer 11. An oxygen signal of $L_{eq}=13$ mm was detected for the right sinus, whereas no signal could be observed for the left side. No water vapor signal could be detected on the right side due to heavy overall absorption in the tissue and the partially filled sinus cavity.

As discussed previously, the estimated L_{eq} depends on both the concentration of the gas and the scattering properties of the tissue. It can be assumed that the scattering properties are approximately the same for the two different wavelengths used.[19,20] However, the absorption coefficient may be different mostly depending on the degree of oxygenation of the blood and liquid water absorption.[17,19] If the same volume has been sampled for the two wavelengths, the ratio between the L_{eq} values for oxygen and water vapor could provide information on the oxygen concentration inside the sinuses, since the water vapor concentration is always the maximum possible concentration at the given temperature (thermostated to about 37°C and 100% humidity in the cavities). In Fig. 4(c), the ratios for the left and right maxillary sinus are shown. On volunteers 1 and 2, it can be seen that this ratio is about the same for both sides. It can also be seen that the two volunteers maintain similar ratios. The average ratio is 0.13±0.01. Assuming that these volunteers have healthy and well ventilated sinuses with about 20% oxygen concentration, a reduced ratio may indicate a lower oxygen concentration in the cavity.

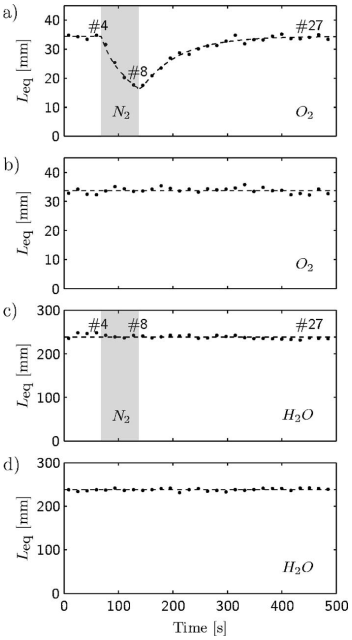

Fig. 5 Gas exchange study for the right maxillary sinuses using detection geometry *PC* on volunteer 1 (see text). (a) L_{eq} for oxygen (solid dots) measured as a function of time with N_2 flushing, together with a line drawn for guidance of the eye (dashed line). (b) Same as (a) without N_2 flushing. (c) L_{eq} for water vapor (solid dots) measured as a function of time with N_2 flushing. (d) same as (c) without N_2 flushing.

Gas exchange studies were performed on volunteers 1 and 11 with the same detection geometry *PC*. A reduction of the oxygen absorption imprint could be observed on volunteer 1 when flushing with N_2, as well as the reperfusion of air when terminating the N_2 flush [Fig. 5(a)]. In Fig. 5(b), the stability of the oxygen signal during the same time scale without N_2 flush can be seen. In the case of water vapor detection, no reduction of the signal could be recorded during N_2 flush [Fig. 5(c)]. A series of water vapor signal measurements is also shown in Fig. 5(d), illustrating the stability of the data. The results indicate that the flushing is not able to change the humidity in the cavities. Figure 6 shows signals recorded at three different time intervals during the gas exchange study (indicated by corresponding numbers in Fig. 5). The fractional absorption was 8.6×10^{-4} and 6.7×10^{-3} for the largest signals observed for oxygen and water vapor, respectively. The signals from reference measurements through the cheek directly after the study are also shown. The same molecular oxygen measurements with nitrogen flushing were performed on the right maxillary sinus of volunteer 11. These measurements did not show any decrease in oxygen signal during the N_2 flush period, indicating lack of communication with the nasal cavity.

Oxygen and water vapor were measured according to ge-

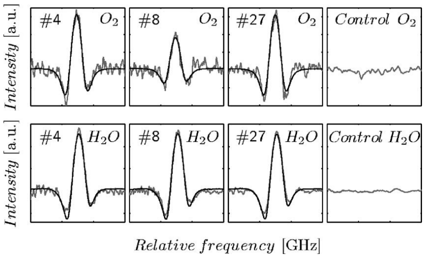

Fig. 6 Balanced detection signals measured for oxygen and water vapor during the gas exchange study using detection geometry *PC*. The numbers correspond to the ones indicated in Fig. 5. The relative frequency range is about 30 GHz. The control signals are also shown for both gases when measuring through the cheek.

ometry *CC* on the maxillary sinuses of volunteer 1 [see Figs. 7(a) and 7(b)]. We note a left-right asymmetry stronger than observed for the same volunteer with data shown in Fig. 4 (left) when using a different detection geometry. This indicates that tomographic information might be extracted regarding anatomy using multiple geometries. The ratio between the signals is shown for both sides in Fig. 7(c). An average ratio of 0.12±0.01 is obtained for this geometry.

The same gas exchange procedure was carried out with detection geometry *CC* on volunteer 1 (see Fig. 8). The same behavior was observed as for detection geometry *PC*.

3.2 *Frontal Sinus Study*

Measurements of the frontal sinuses were performed on volunteer 1 with detection geometry *OF*. In Figs. 9(a) and 9(b), the average L_{eq} together with two standard deviations is shown for the two gases, and the three different detector positions discussed above and seen in the top of Fig. 9. The ratio between the L_{eq} for oxygen and water vapor can be seen in Fig. 9(c). An average of 0.12±0.01 is obtained.

The gas exchange between the nasal cavity and the frontal sinuses was also studied with geometry *OF*. In Fig. 10, the invasion of N_2 and reinvasion of ambient air can be seen for volunteer 1 when detecting oxygen. Again, no such phenomena could be observed when detecting water vapor.

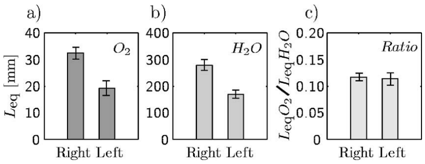

Fig. 7 L_{eq} for (a) molecular oxygen and (b) water vapor measured in left and right maxillary sinuses for volunteer 1 using detection geometry *CC*. The data shown correspond to the average of ten recordings together with two standard deviations. (c) The ratios of the L_{eq} for oxygen and water vapor are shown.

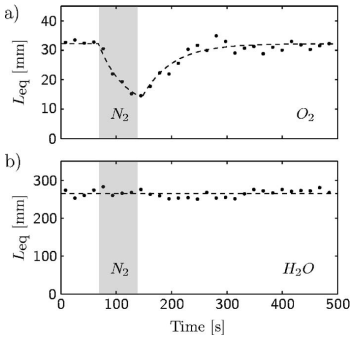

Fig. 8 Gas exchange study for the maxillary sinuses using detection geometry *CC* on volunteer 1 (see text). (a) L_{eq} for oxygen (solid dots) measured as a function of time with N_2 flushing, together with a line drawn for guidance of the eye (dashed line). (b) L_{eq} for water vapor (solid dots) measured as a function of time with N_2 flushing.

4 Conclusion and Outlook

We show that nonintrusive diode laser spectroscopy with monitoring of common physiological gases such as oxygen and water vapor is capable to assess important aspects of hu-

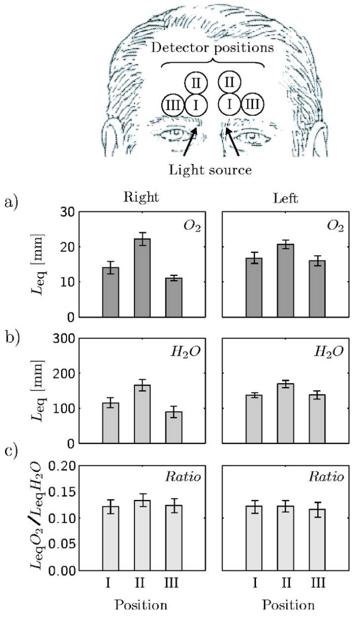

Fig. 9 L_{eq} for (a) molecular oxygen and (b) water vapor measured in left and right frontal sinuses for volunteer 1 using detection geometry *OF* and detection positions according to the top figure. The data shown correspond to the average of ten recordings together with two standard deviations. (c) The ratios of the L_{eq} for oxygen and water vapor are shown.

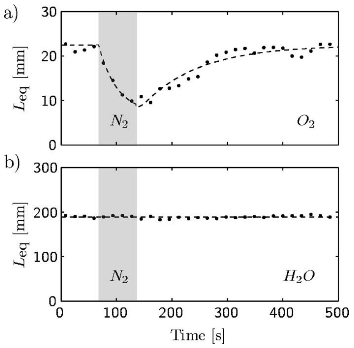

Fig. 10 Gas exchange study for the frontal sinuses using detection geometry *OF* on volunteer 1 (see text). (a) L_{eq} for oxygen (solid dots) measured as a function of time with N_2 flushing, together with a line drawn for guidance of the eye (dashed line). (b) L_{eq} for water vapor (solid dots) measured as a function of time with N_2 flushing.

man sinuses and their potential diseases. It is demonstrated that oxygen as well as water vapor can be detected within the maxillary and frontal sinuses on volunteers by employing different detection geometries discussed in Sec. 2. Individual variations and left-right asymmetries are observed. The oxygen absorption imprint levels detected are in good agreement with the results from Monte Carlo simulations implemented with ASAP™ software. By forming the ratio between the two signals (normalizing the oxygen signal on the water vapor signal), it is shown that basically the same value is obtained for all well ventilated sinuses studied. This is to be expected if a constant concentration of (about 20%) oxygen is assumed in the healthy sinuses, and if 100% water vapor saturation develops in the sinus. Further, a prerequisite would also be that the scattering and absorption coefficients are the same at 760 and 935 nm, resulting in the same effective path length through the gas-filled cavity. Consulting the literature, it can be found that this assumption is not fully warranted.[17,19,20] In particular, the absorption coefficient depends on the degree of blood oxygenation and amount of liquid water, and would tend to increase the absorption at 935 nm, as compared to 760 nm. The scattering coefficient could be expected to be the same within about 10%. The fact that a very similar signal ratio is obtained for different volunteers, sinuses and geometries, suggests that the assumption of a similar effective path length is reasonable. We notice, however, that the experimental ratio was found to be about 0.12. Going from 20% relative humidity to 100% influences the equivalent mean path length by a factor of 5. Likewise, going from 25 to 37 °C introduces a factor of 2 in water potential pressure.[15] Thus an experimental ratio of 0.10 would be expected. The measured value of 0.12 could thus be interpreted in two ways. The air is not attaining 37 °C in dynamic exchange but only about 33 °C, which is not unlikely. A further explanation is that the effective sample pathway for the two wavelengths differ by a factor of 1.2 with a smaller path length at 935 nm due to increased absorption. A combination of the two effects could be present. Given that the experimentally observed effects are rather small, it seems like it should be possible to perform an empirical correction after having gained clinical data. The results of the present work would mean that it would be possible to nonintrusively read off the oxygen concentration in a sealed-off sinus cavity, which might be of clinical value if a correlation to pathology could be established in a clinical trial. It should be noted that a water vapor signal is always expected as soon as there is a gas-filled cavity. A zero reading for oxygen would then by necessity mean that no oxygen is present in the gas, not that the cavity contains no gas at all.

We also demonstrate that the ventilation of the sinuses (the ostial function) could easily be measured observing the oxygen signal, which is reduced when nitrogen gas is given through the nostril as a displacement gas while the patient is breathing normally through the mouth. By instead administering high-concentration oxygen gas, a much stronger signal can favorably be achieved. The time constants for the gas exchange can be determined by fitting the curves. The convenience of a combination of a physiological gas and light for gas exchange studies is in strong contrast to the previous use of stable or radioactive xenon gas in combination with repeated CT scans or SPECT imaging, both leaving the patient with a considerable dose of ionizing radiation. It was found that the concentration of water vapor in the sinuses was not influenced by the flushing with dry nitrogen gas. The conclusion is that 100% water saturated gas is immediately obtained in the sinus. This fact also corroborates the earlier finding that water vapor reliably can be used as a reference gas of known concentration in the well thermostated sinus (at 33 to 37 °C). By recording the relative intensity of two suitable oxygen or water vapor lines, and their half-width with sufficient precision, the temperature and pressure can in principle be measured.

Sequential measurements are made on oxygen and water vapor in the present studies. In a clinically adapted system, the two types of measurements could in principle be made simultaneously using the same detector and different modulation frequencies. When exactly the same geometry pertains for both kinds of measurements an even better stability for the ratio signal can be expected. A clinical trial on sinus patients jointly with an ear-nose-throat (ENT) clinic is planned to assess the clinical practicality and potential benefits of the new technique.

The demonstrated possibility to noninvasively assess the oxygen concentration in a hollow organ by sending light through a substantial layer of human tissue suggests that the new technique might have important applications in assessing the lung function in newborn and small children. With higher power lasers, still without any noticeable thermal effect, corresponding measurements on the lung lobes in adults should be feasible in lung ventilation studies, where, however, the empirical path length difference correction might be larger.

Acknowledgments

The authors are grateful for fruitful discussions with N. G. Holmer, M. Jannert, K. Jonsson, L. Malm, and K. Prellner. We are grateful to L. Simonsson and E. Kristensson for collaboration on ASAP™ simulations. This research was supported by the Swedish Research Council, the Medical Faculty at Lund University, and the Knut and Alice Wallenberg Foundation.

References

1. P. Stierna, G. Karlsson, I. Melén, and M. Jannert, “Aspect on sinusitis—diagnosis and treatment in adults,” *Proc. Mtg. Swedish Assoc. Otorhinolaryngol.*, HNS, Stockholm (1995).
2. T. Runer and S. Lindberg, “Effects on nitric oxide on blood flow and mucociliary activity in the human nose,” *Ann. Otol. Rhinol. Laryngol.* **107**, 40–46 (1998).
3. See http://cfcenter.stanford.edu/CFNews-Sinusitis.html.
4. *Health Matters, Sinusitis*, Nat. Inst. Allergy and Infectious Diseases, U.S. Dept. of Health and Human Services, Bethesda, MD (2005).
5. B. Paulsson, J. Dolata, I. Larsson, P. Ohlin, and S. Lindberg, “Paranasal sinus ventilation in healthy subjects and in patients with sinus disease evaluated with the 133-Xenon washout technique,” *Ann. Otol. Rhinol. Laryngol.* **110**, 667–674 (2001).
6. D. Leopold, S. J. Zinreich, B. A. Simon, M. M. Cullen, and C. Marcucci, “Xenon-enhanced computed tomography quantifies normal maxillary sinus ventilation,” *Otolaryngol.-Head Neck Surg.* **122**, 422–424 (2000).
7. R. R. Rizi, I. E. Dimitrov, A. Thompson, G. Jones, T. R. Gentile, M. Ishii, R. Reddy, M. D. Schnall, and J. S. Leigh, “MRI of hyperpolarized ^{3}He in human paranasal sinuses,” *Magn. Reson. Med.* **39**, 865–868 (1998).
8. L. Persson, K. Svanberg, and S. Svanberg, “On the potential of human sinus cavity diagnostics using diode laser gas spectroscopy,” *Appl. Phys. B* **82**, 313–317 (2006).
9. L. Persson, M. Andersson, T. Svensson, M. Cassel-Engquist, K. Svanberg, and S. Svanberg, “Non-intrusive optical study of gas and its exchange in human maxillary sinuses,” *Proc. SPIE* **6628**, 662804 (2007).
10. S. Svanberg, “Environmental and medical applications of photonic interactions,” *Phys. Scr., T* **T110**, 39–50 (2004).
11. L. Persson, E. Kristensson, L. Simonsson, and S. Svanberg, “Monte Carlo simulations of optical human sinusitis diagnostics,” *J. Biomed. Opt.* (in press).
12. L. Persson, F. Andersson, M. Andersson, and S. Svanberg, “Approach to optical interference fringes reduction in diode laser absorption spectroscopy,” *Appl. Phys. B* **87**, 523–530 (2007).
13. M. Andersson, L. Persson, M. Sjöholm, and S. Svanberg, “Spectroscopic studies of wood-drying processes,” *Opt. Express* **14**, 3641–3653 (2006).
14. S. Svanberg, *Atomic and Molecular Spectroscopy*, 4th ed., Springer-Verlag, Berlin (2004).
15. C. Nordling and J. Österman, *Physics Handbook*, 4th ed., Studentlitteratur (1987).
16. B. Michel and T. Beck, “Raytracing in medical applications,” *Lasers Photon.* **5**, 38–41 (2005).
17. T. Vo-Dinh, *Biomedical Photonics Handbook*, CRC Press LLC, New York (2003).
18. Y. Hoshi, M. Shimada, C. Sato, and Y. Iguchi, “Reevaluation of near-infrared light propagation in the adult human head: implications for functional near-infrared spectroscopy,” *J. Biomed. Opt.* **10**, 064032 (2005).
19. T. Svensson, S. Andersson-Engels, M. Einarsdottir, and K. Svanberg, “In vivo optical characterization of human prostate tissue using near-infrared time-resolved spectroscopy,” *J. Biomed. Opt.* **12**, 014022 (2007).
20. C. Klinteberg, A. Pifferi, S. Andersson-Engels, R. Cubeddu, and S. Svanberg, “In vivo absorption spectroscopy of tumor sensitizers with femtosecond white light,” *Appl. Opt.* **44**, 2213–2220 (2005).

Paper IV

Simultaneous detection of molecular oxygen and water vapour in the tissue optical window using tunable diode laser spectroscopy

L. Persson, M. Andersson, M. Cassel-Engquist, K. Svanberg, and S. Svanberg.

Submitted, (2007).

Simultaneous detection of molecular oxygen and water vapour in the tissue optical window using tunable diode laser spectroscopy

L. Persson,[1] M. Cassel-Engquist,[1] M. Andersson,[1] K. Svanberg,[2] and S. Svanberg[1]

[1] *Atomic Physics Division, Lund University, P.O. Box 118, SE-221 00 Lund, Sweden*
[2] *Department of Oncology, Lund University Hospital, SE-221 85 Lund, Sweden*

We report on a newly developed diode-laser spectroscopic system for simultaneous detection of two gases. The technique is demonstrated by performing gas measurements on absorbing samples, such as an air distance, and on absorbing and scattering samples, such as human tissue. Two pigtailed diode lasers are used, operating in a wavelength modulation scheme, to detect molecular oxygen around 760 nm and water vapour around 935 nm within the tissue optical window (600 nm to 1.3 µm). Different modulation frequencies are used to distinguish between the two wavelengths. No crosstalk can be observed between the gas contents of the two gas channels. The system is made compact by using a computer board and performing software based lock-in detection. The noise floor obtained corresponds to an absorption fraction of about $6 \cdot 10^{-5}$ for both oxygen and water vapour. The power of the technique is illustrated by preliminary results from a clinical trial investigating the human sinuses, performed in collaboration with the Ear, Nose and Throat Clinic, the Radiology Clinic and the Oncology Clinic at Lund University Hospital.

OCIS: 300.6260, 300.1030, 170.3890, 170.7050.

I. INTRODUCTION

Simultaneous detection of more than one gas has during the last years been a hot topic in the tunable semiconductor laser spectroscopy field. The rapid progress is mostly due to the invention of quantum cascade lasers (QCL's) operating in the mid infrared region [1]. In this region, many molecules have strong absorption bands, such as CO, H_2O, NO, and CO_2, which might be overlapping spectrally. Due to the wavelength tunability of the QCL's, it is possible to scan over multiple absorption lines of different species and thus detect more than one gas simultaneously [2, 3]. However, in tissue optics the absorption of fluorophores strongly limits the penetration depth in the mid infrared region. In the tissue optics field, it is common to talk about a tissue optical window, ranging from 600 nm to 1.3 µm, where tissue can be considered as transparent due to relatively weak absorption of major species making light penetration possible. The lower limit is due to absorption of hemoglobin and the upper limit due to absorption of water [4, 5]. In this optical window, the absorption lines of gases are weaker and fewer. This makes it difficult to achieve information about more than one gas by the use of one laser source. A fruitful approach to improve on this is to use sum- and difference-frequency generation. An example of the former type is given in Ref. 6, where water vapour, nitrogen dioxide and sulphur dioxide could be measured using two diode lasers. The latter type is illustrated in Ref. 7, where molecular oxygen, water vapour, and methane could be studied. However, the drawback of these techniques is the low light intensity of the generated frequency (normally a factor of about 1000 lower than the intensity of the light sources).

In the present paper, we report on a newly developed transportable system for diode laser spectroscopy in biological and medical contexts. The system uses two pigtailed diode lasers to simultaneously detect molecular oxygen at 760 nm and water vapour at 935 nm. It employs a computer board and software based lock-in detection. The light beams from the two lasers are fibre-coupled together before entering the sample. Different modulation frequencies of the lasers are used to distinguish between the two wavelengths. The system is not limited to these absorption lines. Any gas could be detected with the presented technique with the assumption that lasers operating at the corresponding wavelengths of the absorption lines of the gases are available. The purpose of this paper is to describe the equipment arrangement and its eventually applicability for clinical use. Examples from detection of the two gases in the human sinuses will be provided. The results of an ongoing clinical trial on human sinus cavities will be presented in forthcoming publications [8, 9].

II. EXPERIMENTAL SETUP

A schematic drawing of the setup is shown in Fig. 1. Two pigtailed DFB lasers (Nanoplus, Germany) are scanned across the molecular oxygen absorption line R11Q12 at 760.445 nm (vacuum wavelength) and the water vapour absorption line at 935.685 nm (vacuum wavelength, vibration: (000)→ (121), rotation: J"=3→ J'=4, K_a"=0→ K_a'=0, K_c"=3→ K_c'=4), respectively. A LabVIEW program creates the input signals, consisting of a ramp with a superimposed sinus wave, to the laser drivers through controlling a computer board (NI-6120, National Instruments). The two ramps have the same frequencies (4 Hz) while the amplitude of the ramps differ due to various responses of the wavelength of the lasers with regard to the driver current. The superimposed sinus waves on the ramps make lock-in detection possible. The laser

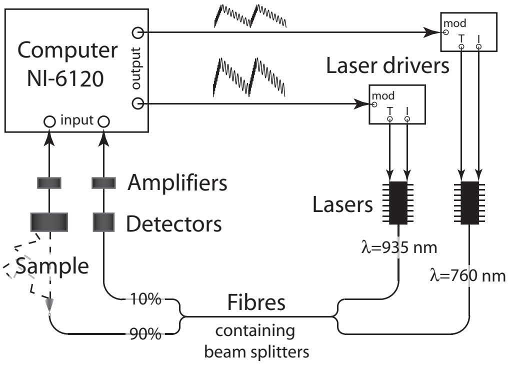

FIG. 1: Schematic drawing of the experimental arrangement for simultaneous detection of molecular oxygen (760 nm) and water vapour (935 nm) using tunable diode laser gas absorption spectroscopy. The sample can either be an absorbing sample, such as an air distance, or an absorbing and scattering sample, such as human tissue.

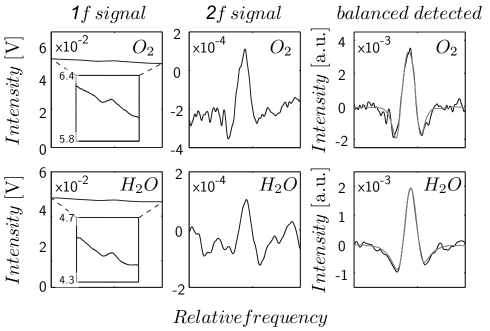

FIG. 2: Typical recorded oxygen and water vapour signals after background subtraction for measurements over an air distance of about 20 mm. Insets can be seen in the 1f signal plots enhancing the intensity region of interest for signals due to gas imprint. The relative frequency range for both gases corresponds to 35 GHz.

used to detect oxygen is modulated by a frequency of 20.216 kHz and the laser used to detect water vapour by a frequency of 9.016 kHz.

The light beams from the lasers are each split into two arms, sample (90%) and reference (10%), by the use of single-mode fibre-coupled beam splitters (Laser2000, Sweden). The light from the two reference arms and the two sample arms are brought together by two fibre-coupled beam splitters (50/50%). The fibre carrying the low-intensity light is directly guided to a photodiode (Hamamatsu S3590-01) providing the reference signal. The light from the sample arm is guided to the sample before being detected by a photodiode (Hamamatsu S3204-08). The sample in this study is either an air path or a scattering medium containing absorbing gas. The intensities reaching the sample are about 1 mW for both laser wavelengths. The signals from the detectors are amplified with two transimpedance amplifiers (Femto DHPCA-100 and DHPCA-200) before being synchronously recorded by two input channels on the computer board.

III. DATA ANALYSIS

The recorded signals are software-based lock-in detected using a LabVIEW program (Lock-in toolkit for LabVIEW). One of the advantage of this approach is no limitation on which harmonic to study. All are available to process from the detected signals. A more detailed discussion of advantage using software-based lock-in detection is provided in Ref. 10. The reference sinus waves needed to perform lock-in detection are internally created in LabVIEW. The 1f and 2f harmonics are computed for both the sample and the reference detector at the two frequencies, corresponding to the two gases. The 2f signals of the two gases are normalised by dividing them with the offset of the corresponding 1f signal. Before analysing the normalised 2f sample signal, balanced detection is performed. This is done to suppress noise and perturbations, like optical interference fringes. This procedure has been described in detail elsewhere [11]. Briefly, a set of parameters is estimated by comparing the 2f reference signal and the 2f sample signal for each gas at frequency regions outside the expected gas imprint. A matched version of the reference signal is then subtracted from the sample signal over the whole frequency scan. An ideal signal is then fitted to the balanced-detection signal which is obtained from measurements over a long air path resulting in a recorded signal with a gas imprint much larger than the noise.

The gas content is obtained for each gas by estimating the peak of the balanced-detection signal with respect to the base line. From this value, a quantity called the equivalent mean path length, L_{eq}, is estimated by the use of the standard addition method [11], which was performed in an atmosphere of about 30% relative humidity and a temperature of about 27°C. The L_{eq} corresponds to how far the light has to travel in ambient air to obtain the same value.

It should be noted that when investigating scattering samples the estimated L_{eq} for each gas does not only depend on the gas concentration but also on the optical properties of the sample. A quantity independent of the latter and thereby directly proportional to the gas concentration can be estimated by forming the ratio between the two recorded L_{eq} for the different gases under the condition that similar optical properties for the two wavelengths can be assumed.

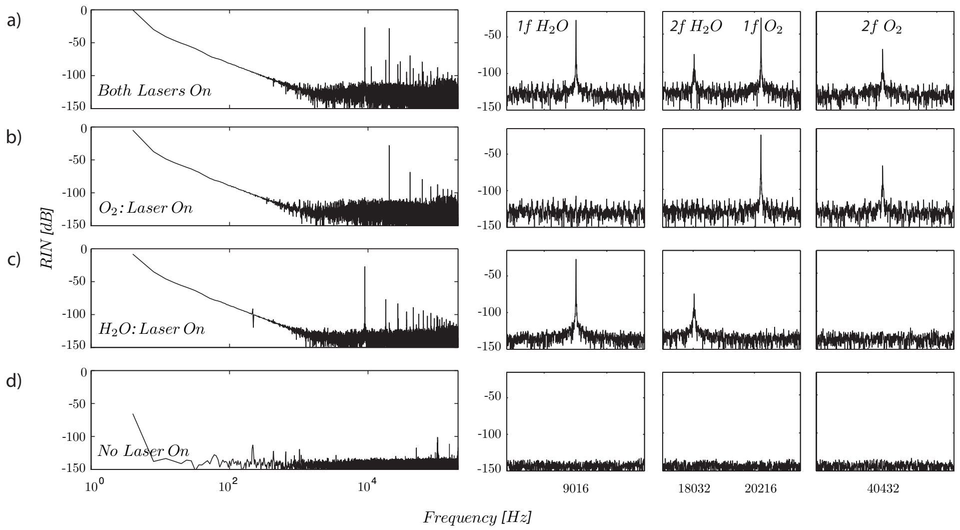

FIG. 3: Recorded laser relative intensity noise (RIN) to investigate possible crosstalk between the two modulation frequencies used to detect two gases simultaneously. The fibre and the sample detector have been separated with an air distance of about 25 mm. a) Both lasers on. b) Only laser for oxygen detection on. c) Only laser for water vapour detection on. d) No laser on.

IV. RESULTS AND DISCUSSION

A. Technique performance investigation

Typical recorded 1f and 2f signals from measurements over an air distance of about 20 mm between the fibre tip and the sample detector are shown in Fig. 2. The signals have been averaged for about 25 s. The balanced-detection signals are also included together with fitted ideal signals. These signals correspond to an absorption fraction of about $5 \cdot 10^{-4}$ and $9 \cdot 10^{-4}$ for oxygen and water vapour, respectively.

To investigate possible crosstalk between the two gas channels, the fibre and the detector were separated by an air distance of about 25 mm. A fast Fourier transform (FFT) was performed on the detected signals; see Fig. 3. Signals were recorded with both lasers on, one laser on at a time, and with no laser on. To the right in the figure, frequency regions of interest for crosstalk investigation are presented. As can be seen, no detectable crosstalk was observed. To further study this issue, ten measurements were recorded for each case. Signals were averaged for about 25 s. In Fig. 4 typical obtained balanced-detection signals can be seen and the averages of the measured L_{eq} for each gas channel together with standard deviations are shown in Table I. This test also verifies that no crosstalk occurs between the two gas channels.

By recording signals with no added air distance between the fibre tip of the sample arm and the detector, the detection limit of the setup could be estimated. The detected noise floor corresponded to an absorption frac-

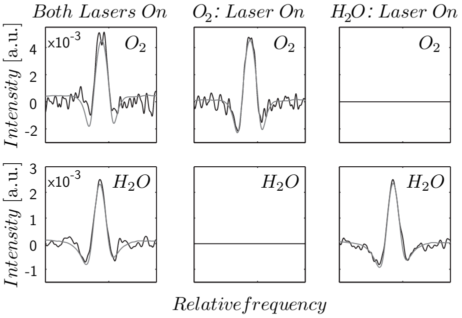

FIG. 4: Investigation of possible crosstalk between the two modulation frequencies used to detect two gases simultaneously. The balanced-detection signals are recorded from measurements over an air distance of about 25 mm. The relative frequency range for both gases corresponds to 35 GHz.

	L_{eq}[mm] O_2	L_{eq}[mm] H_2O
Both Lasers On	23.5±1.5	24±1
O_2: Laser On	24±1.5	-
H_2O: Laser On	-	26±1

TABLE I: The average L_{eq} from ten recordings over an air distance of about 25 mm to investigate possible crosstalk between the two modulation frequencies used to study two gases simultaneously. Examples of detected signals used are provided in Fig. 4.

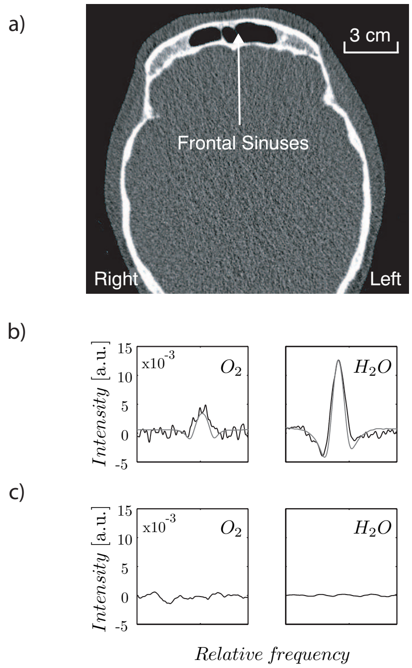

FIG. 5: a) A computed tomography (CT) image of human frontal sinuses of a patient participating in the clinical trial; transversal section. b) Corresponding recorded balanced-detection signals from the left frontal sinus of the patient with CT image shown in Fig. 5a using detection geometry OF (see text). The oxygen signal corresponds to $L_{eq} = 22\ mm$ and the water vapour signal to $L_{eq} = 123\ mm$. c) Recorded balanced-detection control signal through the cheek. The relative frequency range for both gases corresponds to 35 GHz.

tion of about $6 \cdot 10^{-5}$ for both oxygen and water vapour when detected photons were not a limitation. This corresponds to an L_{eq} of about 2.5 mm for oxygen and about 1.5 mm for water vapour with calibration atmosphere. It was observed that the remaining pattern had a periodic structure for both cases. Hence, the conclusion that optical interference fringes set the limitation of detectable signals can be drawn.

B. Initial clinical test

As part of an initiated clinical trial, we present data from test measurements on human frontal and maxillary sinuses performed at the Lund University Hospital in collaboration with the Ear, Nose and Throat Clinic, the Radiology Clinic and the Oncology Clinic. The cavities, located within the human skull, are surrounded by strongly scattering tissue and gas signal recordings for such cavities have previously been demonstrated with laboratory equipment [12, 13]. For a healthy patient the sinuses should be air-filled, while in conditions like sinusitis (inflammation/infection of the sinuses), the mucosa is swollen and they may be filled with pus and liquid. The cause of sinusitis can, in many cases, be due to passage blockage between the nasal cavity and the sinuses preventing proper ventilation. The rationale behind the clinical trial is to investigate the possibility of using noninvasive diode laser based absorption measurements of the sinuses for characterisation regarding gas composition. The gas measurements are performed directly after the patients have undergone a computed tomography (CT) investigation of the skull, which today is one of the most reliable diagnostic method of sinusitis. Unfortunately, this method is expensive and uses ionising radiation. Therefore, complementary and/or alternative techniques are desirable.

1. *Frontal Sinus investigation*

To investigate the human frontal sinuses, a detection geometry referred to as *Orbital edge - Frontal bone geometry* (OF) has been utilised. This means that the sample fibre is placed on the frontal bone below the eyebrow (the roof of the orbita) pointing up toward the frontal bone with the sinus cavity. The diffusely scattered light emerging out through the frontal bone, with a fraction crossing the frontal sinus, is detected by placing the detector on the frontal bone [13].

In Fig. 5a a CT image of the frontal sinuses can be seen of a patient participating in the clinical trial and in Fig. 5b balanced-detection signals for the left frontal sinus are shown. The signals correspond to an L_{eq} of 22 mm for oxygen and an L_{eq} of 123 mm for water vapour, which agree with expected values reported in Ref. 13. It was found that the ratio was about 0.18. The reason for an L_{eq} of water vapour being a factor of about six times larger than that for oxygen is that the calibration for water vapour was performed in an environment with the temperature 27°C and a relative humidity of about 30%. The temperature within the body is approximately 37°C and the humidity in the sinuses is 100% due to water in liquid phase in the surrounding tissue. Both these two factors will result in an increased L_{eq} for water vapour. This is discussed in detail in Ref. 13.

At each occasion of measurements on patients during the clinical trial, a control recording is performed. The purpose of this control is to study any current offset of gas signals in the setup. During these measurements the fibre is placed on the inside of the cheek in the mouth and the light is detected on the outside of the cheek. This should result in non-detectable signals since no free oxygen or water vapour are expected in the tissue. In Fig. 5c recorded balanced-detection signals from the control performed just before the frontal sinus study are shown. As can be seen no offset of either gas could be detected.

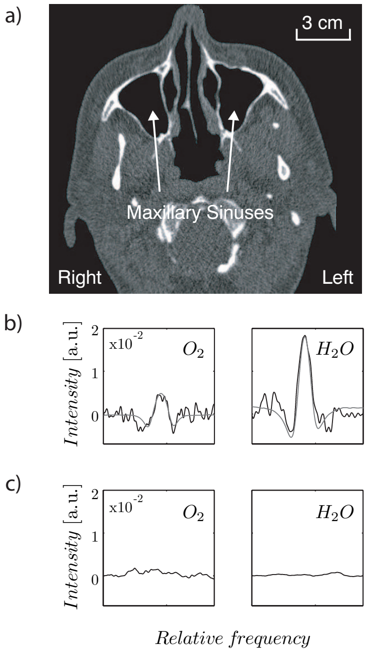

FIG. 6: a) A computed tomography (CT) image of human maxillary sinuses of a patient participating in the clinical trial; transversal section. b) Corresponding recorded balanced-detection signals from the right maxillary sinus of the patient with CT image shown in Fig. 6a using detection geometry *PC* (see text). The oxygen signal corresponds to $L_{eq} = 30\ mm$ and the water vapour signal to $L_{eq} = 185\ mm$. c) Recorded balanced-detection control signal through the cheek. The relative frequency range for both gases corresponds to 35 GHz.

2. Maxillary Sinus investigation

For the maxillary sinus studies a detection geometry referred to as *Palate - Cheek bone geometry* (*PC*) has been used. In this detection geometry the sample fibre is placed inside the mouth in contact with the palate in the area directly under the maxillary sinus investigated. The diffusely scattered light emerging out through the cheek bone, with a fraction crossing the maxillary sinus, is detected by placing the detector on the cheek bone [12, 13].

In Fig. 6a a CT image of the maxillary sinuses can be seen of a patient participating in the clinical trial and in Fig. 6b balanced-detection signals for the right maxillary sinus are shown. The signals correspond to an L_{eq} of 30 mm for oxygen and an L_{eq} of 185 mm for water vapour, which agree with expected values reported in Refs 12, 13. The ratio of the gas signals are similar to the one recorded for the frontal sinus within the margin for error. The obtained balanced-detection control signals can be seen in Fig. 6c. No offset of either gas was obtained.

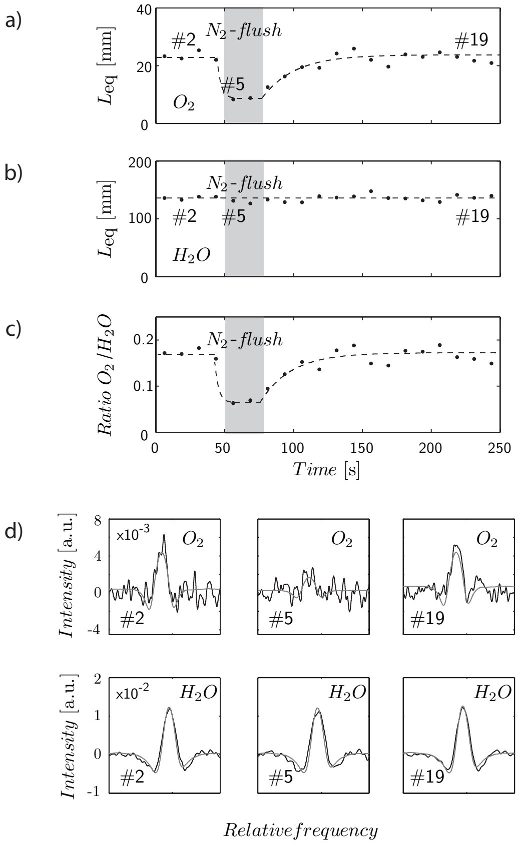

FIG. 7: a) Ventilation study between nasal cavity and maxillary sinus using detection geometry *PC* (see text). a) L_{eq} for oxygen (solid dots) measured as a function of time with N_2 flushing together with a line drawn for guidance of the eye (dashed line). b) L_{eq} for water vapour (solid dots) measured as a function of time with N_2 flushing. c) Ratio between measured oxygen signal and water vapour signal (solid dots) as a function of time with N_2 flushing together with a line drawn for guidance of the eye (dashed line). d) Recorded balanced-detection gas signals. The numbers corresponds to the ones indicated in a and b. The relative frequency range for both gases corresponds to 35 GHz.

Preliminary studies of the ventilation between the nasal cavity and the maxillary sinuses have been performed utilising the *PC* detection geometry. The nasal cavity on a healthy volunteer was flushed with pure nitrogen through the nostril for about 25 s, while continuously measuring the gas composition within the sinuses. Signals were recorded before, during and after termination of the flush. Each recorded signal was averaged for about 12 s. In Fig. 7a and b the measured L_{eq} for oxygen and water vapour, respectively, for one of the maxillary sinuses of the volunteer can be seen. In Fig. 7c the ratio is shown and in Fig. 7d recorded oxygen and water vapour balanced-detection signals corresponding to indicated numbers in Fig. 7a and b are provided. This result agrees with previously presented in Ref. 13. A decrease of oxygen is recorded during the flush and the reinvasion of oxygen is observed after its termination. However, for the water vapour signal, no noticeable change can be observed. This is not either expected since 100% humidity in the sinuses remains during the flush. For the recorded L_{eq} for oxygen during the time period no considerations have to be given with regards to the optical properties of the surrounding tissue since they remain unaffected. However, the water vapour signal is still needed to eliminate possible changes of recorded oxygen signal due to movements of fibre and detector, and thereby different sampling volumes, during the measurements. Thus, the estimated ratio, shown in Fig. 7c, can be considered as a more reliable picture of how the oxygen concentration within the sinus changes than L_{eq} for oxygen itself. The observations shown in Fig. 7 are typical for patients with good ventilation.

V. CONCLUSION

We show the feasibility to detect two gases simultaneously, within the tissue optical window, by applying wavelength modulation spectroscopy. The technique is demonstrated on scattering and non-scattering absorbing samples. Two different modulation frequencies are used for two light sources to distinguish two gases. No detectable crosstalk is obtained between the two gas channels. Lock-in detection is performed by using a lock-in toolkit provided by National Instrument. Pigtailed lasers and fibre optics are used to guide the light from the lasers to the sample providing easy illumination of inaccessible locations. The system is made compact by utilising a computer board to provide modulation signals imposed on the laser driver current and to collect the signals after interaction with the sample. The entire system is placed on a trolley (95 × 45 × 75 cm) making it possible to perform measurements outside the laboratory. Preliminary clinical results from gas measurements within the human frontal and maxillary sinuses recorded at the Lund University Hospital are provided. In the initial clinical measurements substantial signal interference from different types of imaging equipment typical for a Radiological Clinic was occasionally experienced. It should be noted that such an environment would not pertain to locations of intended future clinical use. A full analysis of the clinical data for all patient included in the study will be presented for the frontal and maxillary sinuses as well as for the mastoid bones in forthcoming publications [8, 9].

Acknowledgement

The authors want to acknowledge useful discussions with Morgan Andersson, Karolina Falkenius-Schmidt, Kjell Jonsson, Sven Lindberg, Karin Prellner, Bo Paulsson, and Roger Siemund. We are also grateful for all help during the clinical measurements from the staff at the Radiology Clinic at the Lund University Hospital. This research was supported by the Swedish Research Council, the Medical Faculty Lund University, and the Knut and Alice Wallenberg Foundation.

[1] J. Faist, F. Capasso, D. Sivco, C. Sirtori, A. Hutchinson, and A. Cho, "Quantum cascade laser," *Science* **264**, 553–556 (1994).

[2] G. Wysocki, M. McCurdu, S. So, D. Weidmann, C. Roller, R. Curl, and F. Tittel, "Pulsed quantum-cascade laser-based sensor for trace-gas detection of carbonyl sulfide," *Applied Optics* **43**, 6040–6046 (2004).

[3] M. Silva, D. Sonnenfroh, D. Rosen, M. Allen, and A. O'Keefe, "Integrated cavity output spectroscopy measurements of nitric oxide levels in breath with a pulsed room-temperature quantum cascade laser," *Applied Physics B* **81**, 705–710 (2005).

[4] J. Parrish, "New concepts in therapeutic photomedicine: photochemistry, optical targeting and the therapeutic window," *Journal of Investigative Dermatology* **77**, 45–50 (1981).

[5] J. Boulnois, "Photophysical processes in recent medical laser developments: a review," *Lasers in Medical Science* **1**, 47–66 (1986).

[6] G. Somesfalean, Z. Zhang, M. Sjöholm, and S. Svanberg, "All-diode-laser ultraviolet absorption spectroscopy for sulfur dioxide detection," *Applied Physics B* **80**, 1021–1025 (2005).

[7] U. Gustafsson, J. Sandsten, and S. Svanberg, "Simultaneous detection of methane, oxygen and water vapour utilizing near-infrared diode lasers in conjunction with difference frequency generation," *Applied Physics B* **71**, 853–857 (2000).

[8] L. Persson *et al*, *To appear* (2007).

[9] K. Falkenius-Schmidt *et al*, *To appear* (2007).

[10] M. Andersson, L. Persson, T. Svensson, and S. Svanberg, "Flexible lock-in detection system based on synchronized computer plug-in boards applied in sensitive gas spectroscopy," Submitted (2007).

[11] L. Persson, F. Andersson, M. Andersson, and S. Svanberg, "Approach to optical interference fringes reduction in diode laser absorption spectroscopy," *Applied Physics B* **87**, 523–530 (2007).

[12] L. Persson, M. Andersson, T. Svensson, M. Cassel-Engquist, K. Svanberg, and S. Svanberg, "Non-intrusive

optical study of gas and its exchange in human maxillary sinuses," *Proceeding of SPIE-OSA Biomedical Optics* **6628**, (2007).

[13] L. Persson, M. Andersson, M. Cassel-Engquist, K. Svanberg, and S. Svanberg, "Gas monitoring in human sinuses using tunable diode laser spectroscopy," *Journal of Biomedical Optics* **12**, (2007).

PAPER V

Diode laser absorption spectroscopy for studies of gas exchange in fruits

L. Persson, H. Gao, M. Sjöholm, and S. Svanberg.

Optics and Lasers in Engineering **44**, 687–698 (2006).

Available online at www.sciencedirect.com

SCIENCE DIRECT®

ELSEVIER

Optics and Lasers in Engineering 44 (2006) 687–698

OPTICS and LASERS in ENGINEERING

Diode laser absorption spectroscopy for studies of gas exchange in fruits

L. Persson*, H. Gao[1], M. Sjöholm, S. Svanberg

Department of Physics, Lund Institute of Technology, P.O. Box 118, SE-22100 Lund, Sweden

Available online 22 August 2005

Abstract

Gas exchange in fruits, in particular oxygen transport in apples, was studied non-intrusively using wavelength modulation diode laser absorption spectroscopy at about 761 nm, applied to the strongly scattering intact fruit structure. The applicability of the technique was demonstrated by studies of the influence of the skin to regulate the internal oxygen balance and of cling film in modifying it by observing the response of the signal from the internal oxygen gas to a transient change in the ambient gas concentration.

Applications within controlled atmosphere fruit storage and modified atmosphere packaging are discussed. The results suggest that the technique could be applied to studies of a large number of problems concerning gas exchange in foods and in food packaging.

© 2005 Elsevier Ltd. All rights reserved.

Keywords: Diode laser spectroscopy; TDLS; Food packaging; Gas exchange; Fruit; Oxygen

1. Introduction

Molecular oxygen is a biologically active molecule, and its concentration in fruits is of crucial importance for the ripening process and the quality of the fruits. In particular, the oxygen availability affects the metabolic process of respiration, which releases energy necessary to maintain the life processes by breaking down the organic

---

*Corresponding author.

E-mail address: linda.persson@fysik.lth.se (L. Persson).

[1] Permanent address: School of Science, Harbin Institute of Technology, Harbin, PR China.

0143-8166/$ - see front matter © 2005 Elsevier Ltd. All rights reserved.

doi:10.1016/j.optlaseng.2005.03.014

compounds of the fruit. Thus, a decreased respiration rate causes a prolonged lifetime. The rate of the normal aerobic respiration process in which oxygen is consumed and carbon dioxide is produced, decreases with decreasing oxygen concentration and increasing carbon dioxide concentration. However, an oxygen concentration below a certain critical level initiates an anaerobic metabolic pathway for the respiration. This process, known as fermentation, produces off-flavours and causes a loss of quality and a rapid decay of the fruit. Also, a too high carbon dioxide concentration can cause damage to the fruit tissue [1,2]. Thus, there is great interest in optimising gas concentrations during the postharvest time of fruits.

Methods developed to prolong the postharvest lifetime and inhibit physiological deterioration in fruits include controlled atmosphere (CA) storage and modified atmosphere packaging (MAP). The optimum partial pressures of oxygen and carbon dioxide in CA storage and MAP depend on the metabolic behaviours, especially the physiological tolerance to oxygen and carbon dioxide of the particular fruit [3]. In MAP, films with suitable permeability to oxygen and carbon dioxide are used to optimise the concentrations of the gases which the fruits are exposed to. An ideal type of package would be the one resulting in an oxygen concentration low enough to slow down respiration and maturation but higher than the critical concentration for initiation of anaerobic respiration [2,4]. The respiration rate is also highly dependent on the temperature [5,6]. The oxygen uptake increases with temperature while the permeability of the polymeric film frequently used in MAP does not increase to the same extent. Thus, it is very important to design the MAP according to the highest oxygen uptake that will occur due to temperature changes during shipping and handling [7]. To be able to design an optimal package, there is a need for methods to measure and model the internal gas concentrations and the gas exchange in fruits and package systems.

Techniques for assessing the gas content in the air around horticultural produces are readily available, although the implementation might be complicated. A common technique is to use a flush-through system in which the gas exchange can be estimated from the concentration difference between the inlet and outlet gas flow. In order not to make systematic errors, the flow has to be relatively high [8,9]. However, this requires sensitive detection techniques to be able to monitor the small concentration differences, which is often accomplished by a gas chromatographic system combined with unselective detectors, or more selective spectroscopic devices like laser-based photoacoustic trace gas detectors [10]. When it comes to measurements of the internal gas contents and its dynamics, intrusive electrode-based probes or extraction of gas from the fruit interior by syringes are normally used [10–12]. These methods destroy the tissue, which might affect the ongoing physiological processes.

A non-intrusive, compact and easily implemented technique for measuring gas exchange inside fruits would thus be of interest for assessments of internal gas dynamics relevant to, for instance, the optimisation of CA storage and MAP of fruits. The aim of the present work is to introduce a new non-destructive in-situ technique to study gas inside fruits, based on diode laser absorption spectroscopy on highly scattering media, rather than to reveal new knowledge about fruit physiology in itself. In the present study, we focus on oxygen content and gas exchange measurements in fruits, although other gases such as carbon dioxide and water can be considered. We show the possibility of studying gas exchange in apples through their natural skins. The technique also makes it possible to determine the effect on the gas exchange due to the protective action of cling film, and to study the permeability of different films used in MAP. Although the present study is focused on measurements on fruits, in particular apples, the methodology is general and can be applied to a large number of problems concerning gas exchange in foods and in food packaging.

2. Experimental technique

2.1. Gas absorption measurements

Gas concentrations can in principle be determined by measuring the gas attenuation of narrow-band light, over a certain distance and employing the well-known Beer–Lambertian law. The level of light unaffected by the gas can readily be assessed by also measuring the intensity at wavelengths close to, but outside the absorption profile.

This simple procedure requires a negligible variation of the absorption properties between the different wavelengths, inside and outside the absorption line profile, caused by other constituents than the gas of interest. This is often true in standard gas measurements in the atmosphere [13], but also in porous materials. A methodology based on the fact that absorption features of free gas are about 10 000 times narrower than the spectral features of liquids and solids was recently proposed and demonstrated. The method is referred to as **ga**s in **s**cattering **m**edia **a**bsorption **s**pectroscopy (GASMAS) [14]. The technique utilises narrow-band tunable lasers, which makes it possible to scan the probing wavelength through the whole pressure broadened absorption profile of the gas. In particular, the wavelength tuning of compact, low-cost diode lasers can easily be achieved by changing the driving current or the temperature of such lasers.

In a porous material the light is scattered, which results in optical path lengths much longer than the distance of a straight line between the point of light injection and the point of light detection in the material. As an example, light travels several metres inside a few centimetre thick slab of polystyrene foam, which gives rise to large differential gas absorption signals even if the geometrical dimensions of the scattering sample are relatively small. Obviously, for absolute gas concentration measurements in materials where scattering dominates over absorption, the actual mean path length travelled by the light has to be measured [15]. However, for assessments of relative gas diffusion dynamics the actual mean path length is not required.

Although the optical path lengths can be long in a porous material, the differential absorption at transition lines of oxygen in the A-band around 760 nm, in a realistic porous sample, is in the best case just a few per cent. This calls for procedures to increase the detection sensitivity in the presence of noise. A common approach to increase the signal-to-noise ratio is to appropriately modulate the probing light at a specific frequency and to extract the corresponding frequency component, or a harmonic of it, in the detected signal by the use of lock-in techniques. In the present study, wavelength modulation spectroscopy (WMS) as discussed below was employed.

2.2. Set-up

A key component in the measurement set-up, see Fig. 1, is the diode laser, Sharp LT031MDO, with a nominal output power of 7 mW, which was used to generate the probing light. The wavelength of the light was scanned, with a repetition rate of 28 Hz, across the R7R7 oxygen line, with the vacuum wavelength 761.003 nm. Additionally, sinusoidal modulation of 55 kHz was superimposed on the diode laser injection current to achieve a modulation of the light that could be used to perform sensitive WMS detection. A Tefzel covered optical fibre with a core diameter of 600 μm was used to guide the light to the sample under study. Before entering the sample, the light was collimated by a collimating lens package, Thorlabs F230SMA-B.

After passage through the sample a photomultiplier tube, Hamamatsu 5070A, masked by a circular aperture with a diameter of 6 mm, detected the light. Ambient light was suppressed by the combination of the sensitivity fall-off towards longer wavelengths for the photomultiplier tube, and a coloured glass filter, RG715, that blocked shorter wavelengths. Additionally, the sample was surrounded by a black box to suppress the ambient light even further. The signal from the photomultiplier tube was split into two parts. One part, referred to as the direct signal, was sent directly to a digital oscilloscope, Tektronix TDS 520B. The other part was filtered by a home-made high-pass filter and phase-sensitive detection at twice the modulation frequency, i.e. 110 kHz, was achieved by the use of a lock-in amplifier, Signal

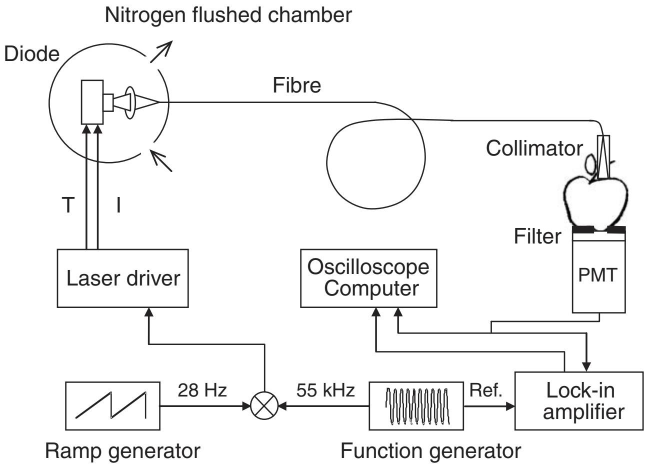

Fig. 1. Schematic layout of the GASMAS set-up used for molecular oxygen detection.

Recovery 7280 DSP. This lock-in signal, referred to as the 2f signal, was sent to the other channel of the oscilloscope, which was computer controlled through GPIB communication by a LabVIEW program.

2.3. Evaluation

The oxygen gas content was evaluated from the recorded wavelength scans by calculating the peak-to-peak value of the absorption signature in the 2f signal, as illustrated in Fig. 2 (left). The amplitude of the 2f signal is dependent both on the relative differential absorption due to the gas of interest, and the amount of light reaching the detector, i.e. it depends on the absolute size of the absorption dip. Thus, the peak-to-peak value of the 2f signal was normalised to the amount of light reaching the detector by dividing it with the interpolated direct signal, S_{Dir}, at the absorption line centre; see Fig. 2 (left). This normalised GASMAS measurement signal, GMS, is thus a measure of the absorption due to the gas of interest. As long

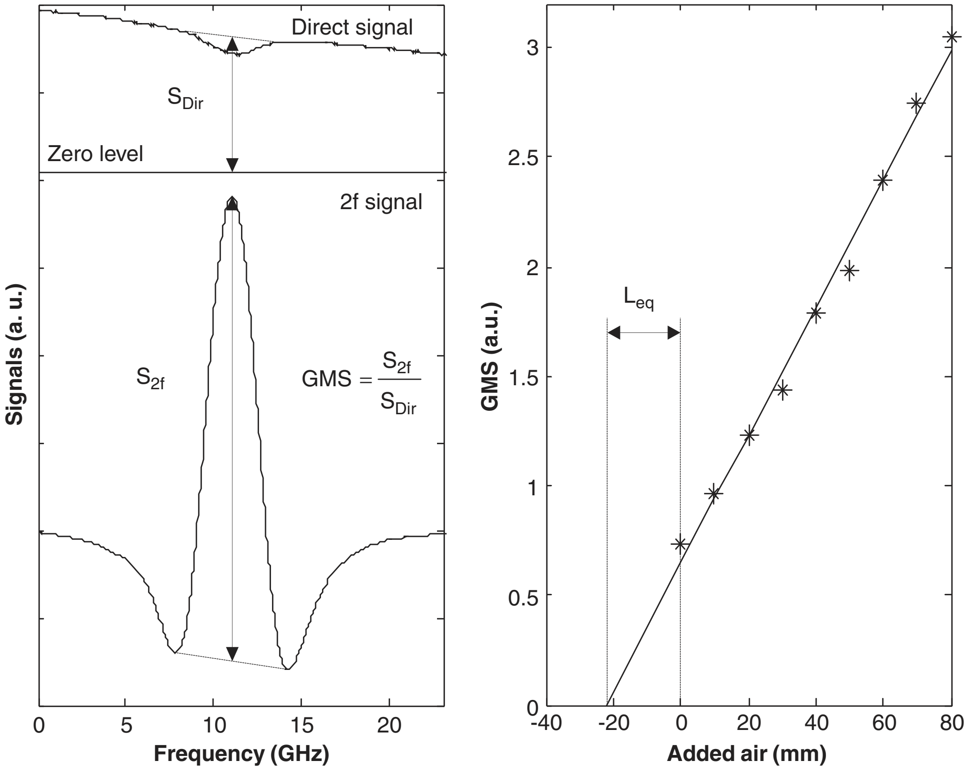

Fig. 2. (Left) Direct absorption and second-harmonic component of the absorption for the R7R7 line in the oxygen A-band measured along an approximately 10 m long path in air. (Right) Standard addition plot for molecular oxygen obtained with the GASMAS set-up showing the extrapolated equivalent mean path length for a 20 mm thick slab of Jonagold apple.

as the absorption is small, the GMS is proportional to the absorbance and thus to the product of the gas concentration and the path length travelled by the light.

One simple procedure to calibrate the arbitrary GMS and transform it into a more meaningful quantity is by using the method of standard addition, in which known amounts of the quantity of interest is added to the unknown quantity, which then can be determined. In the case of oxygen measurements, the light was sent through additional known path lengths of ambient air before entering the sample under investigation. The acquired GMS values were plotted as a function of the added distance of air as can be seen in Fig. 2 (right), where a standard addition measurement on a 20 mm thick slab of Jonagold apple is presented. The data points fall on a straight line as previously discussed and by determining the intercept of this fitted line with the added-distance axis, the equivalent distance in ambient air giving rise to a signal with the same magnitude as the unknown signal from the sample can be determined. In the case presented in Fig. 2 (right), the equivalent mean path length, L_{eq}, of molecular oxygen was found to be 22 mm. Since only a small fraction of the apple volume is gas, this means that the light has travelled a substantially longer distance through the apple than the geometrical dimensions of the apple.

3. Measurements and results

3.1. Introductory studies

In order to illustrate the general dynamics of gas in fruit samples a study of the equivalent mean path length, L_{eq}, of oxygen for fruit slabs of different thickness was performed. Five varieties of apples, Jonagold, Granny Smith, Red Delicious, Golden Delicious, and Royal Gala, bought in a local supermarket, were studied. The different apples were sliced in slabs with well-defined thicknesses (± 1 mm) and the equivalent mean path length was immediately measured, in order not to be affected by oxidation processes. Several different positions on each apple slab were sampled, since local variations in the slabs could be anticipated. Each measurement is an average of 500 single wavelength scans and ten such measurements were performed at each position in order to evaluate the influence of noise. The standard deviation of the ten measurements at each position was found to be at most 0.12 mm, and was not proportional to the equivalent mean path length measured, which is in accordance with the fact that optical fringes are limiting the sensitivity. The thicker the apple slab is cut, the more inhomogeneous the sampled tissue volume will be, which could be one reason for the, with increasing thickness, increasing standard deviation of the equivalent mean path length averages for the three different positions. The largest standard deviation was found to be 1 mm, which occurred for the Jonagold 18 mm slab. All these measurements made on the slabs were averaged into one value for each slab as can be seen in Fig. 3. It was observed that the equivalent mean path length for the apples studied follows a quadratic dependence on slab thickness in agreement with theoretical expectations for a medium where scattering dominates over absorption and the light transport can be treated as diffusing photons [15].

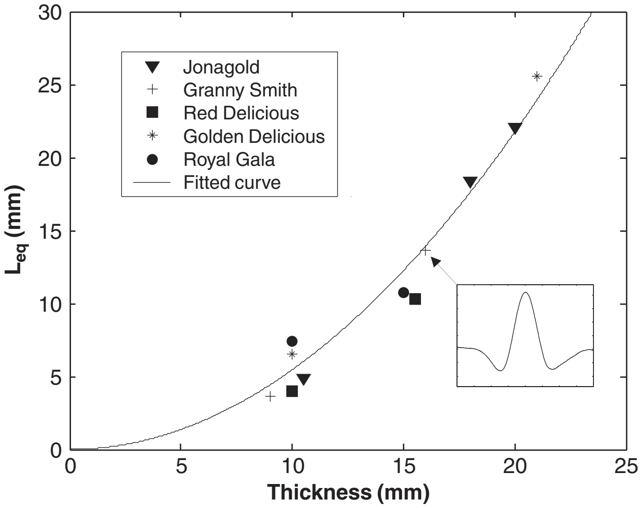

Fig. 3. Equivalent mean path length of oxygen, L_{eq}, for slabs of different apple varieties with various thickness. Ten measurements, each consisting of 500 single wavelength scans, were performed at three different places on the slab. Each data point is an average of these measurements. The WMS signal from the 16 mm thick Granny Smith slab is shown in the inset.

Since slabs of the same thickness of these different varieties of apples were found to have basically the same L_{eq}, all data points were fitted to a common quadratic function, with a root mean square error of 1.5 mm, see Fig. 3.

3.2. Gas transport studies

To elucidate the feasibility to study gas content inside an intact fruit and to follow diffusion processes in real-time, the influence of the skin on the oxygen content inside a Granny Smith apple was measured in ambient air. Furthermore, measurements were also made on an aubergine to illustrate the possibility of using the technique on produces with substantially lower light transmission.

The equivalent mean path length was measured as a function of time for differently treated apples; see Fig. 4. One untreated apple, with a thickness of 70 mm, was first measured. After that, the apple was immersed in nitrogen gas for about 24 h, by placing it in a plastic bag flushed with nitrogen gas before being sealed. Then it was brought out into ambient air and the re-invasion of oxygen containing ambient air was measured. The same apple was then pealed, immersed in nitrogen gas for 12 h before the measurement procedure was repeated. Finally, a new apple, with a thickness of 74 mm, was exposed to an atmosphere with a higher concentration of oxygen than in ambient air for about 12 h, before it was brought out into ambient air and the measurement procedure was again repeated. The data points that are shown in Fig. 4 are averages from 15 000 wavelength scans, corresponding to a sampling time of approximately 15 min.

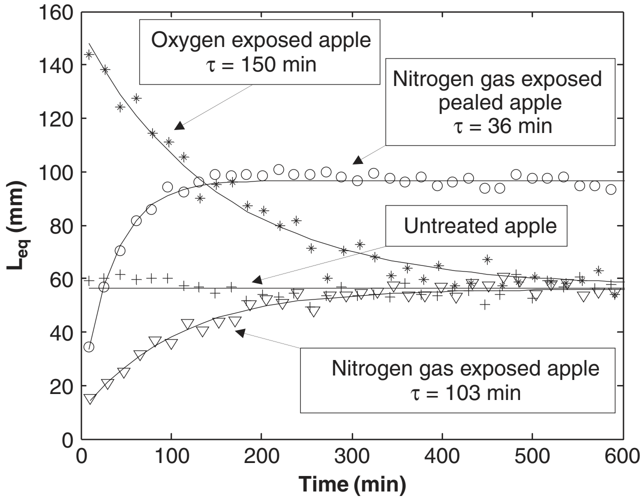

Fig. 4. Measurements of the gas exchange through differently treated Granny Smith apples in ambient air; untreated intact apple (+), intact apple pre-treated by immersion in nitrogen gas for 24 h (▽), pealed apple immersed in nitrogen gas for 12 h (○) and another apple pre-exposed to an atmosphere with higher concentration of oxygen than in ambient air for 12 h (∗). Exponential functions fitted to the data together with the estimated time constants are also included.

As was already observed in our first paper [14], the time evolution of the oxygen equivalent mean path length was found to follow a simple exponential curve, which is also expected with the experimental procedures utilized [16]. The time constant—the time the signal takes to change its separation from equilibrium by a factor of $1/e$ of its value at the starting time—was estimated by a fitting procedure.

As can be seen in Fig. 4, the time constant for the re-invasion of oxygen into the nitrogen-exposed apple with skin is around 100 min. It can also be seen that it takes the apple approximately 5 h to reach the same steady-state oxygen concentration as before the treatment. The figure also shows that in the pealed apple, the concentration equilibrium of oxygen becomes about two times higher than it was before the apple was pealed, and that the gas exchange goes about three times faster than in the presence of the intact skin, which is in accordance with the assumption that the major site of resistance to gas diffusion in fruits is most likely the skin [7]. The time constant for the oxygen-exposed apple was estimated to 150 min, which is slightly different from the time constant estimated for the nitrogen-exposed apple. However, any detailed conclusions about the physiological process should not be drawn from this difference since different apples were used.

These two measurements of re-invasion of ambient air after exposure to oxygen and nitrogen, respectively, were also performed on an aubergine, 57 mm thick, where both the time constants were estimated to approximately 30 min; see Fig. 5. In the figure it can also be seen that the equilibrium value for oxygen is about five times larger in the aubergine than in the Granny Smith apple. It is well known that this type of fruit contains considerable amounts of gas. However, it should be kept in

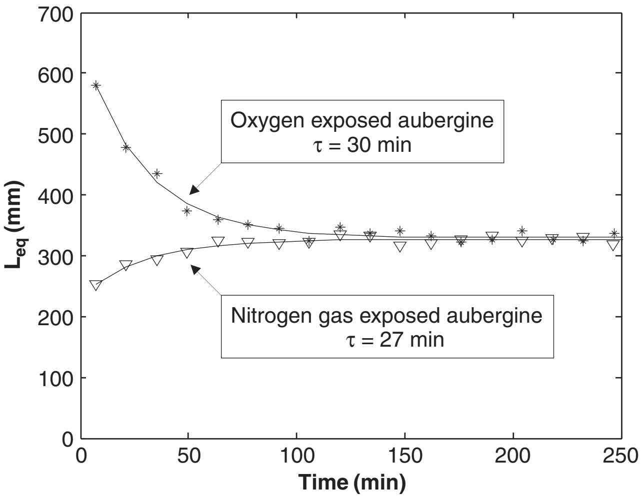

Fig. 5. The rate of gas exchange through an aubergine in ambient air after a previous immersion in nitrogen gas for 24 h (∇). The same aubergine was after the first measurement exposed to an atmosphere with higher concentration of oxygen than in ambient air for 12 h before being measured again (∗). Exponential functions fitted to the data together with the estimated time constants are also included.

mind that the oxygen equivalent mean path length is sensitive to the gas concentration as well as the scattering properties of the fruit.

3.3. Packaging measurements

In MAP different kinds of polymeric films are used with various permeabilities for oxygen and carbon dioxide to delay ripening of the fruit [7,17]. To illustrate the possibility of studying the protective action of cling film with the method presented, the rate of gas exchange in freshly cut fruit was studied. In Fig. 6 diffusion curves for slabs with similar thickness, around 15 mm, of Royal Gala apple are shown. The fruit was cut in slabs and immersed in nitrogen gas, as described above, for 24 h. Before they were released into ambient air and measured, one slab was wrapped in cling film inside the nitrogen environment while the other was not. The data that are shown in the figure are averages of 2500 wavelength scans, corresponding to a sampling time of approximately 3 min. An exponentially decaying function was fitted to the data and the time constant was found to be in the order of a few minutes for the unprotected slab, whereas the slab that was sealed with cling film had an approximately seven times longer time constant. An even more successful sealing was observed with a time constant around 8 h.

An experiment to show the possibility of studying the impact of packaging on the respiration rate was also done. A Granny Smith apple was placed in a sealed plastic bag with limited access to oxygen. In Fig. 7 the diffusion curve is shown, and again each data point is an average based on 15 000 wavelength scans. The time constant for this particular gas exchange was estimated to be around 300 min. However, the

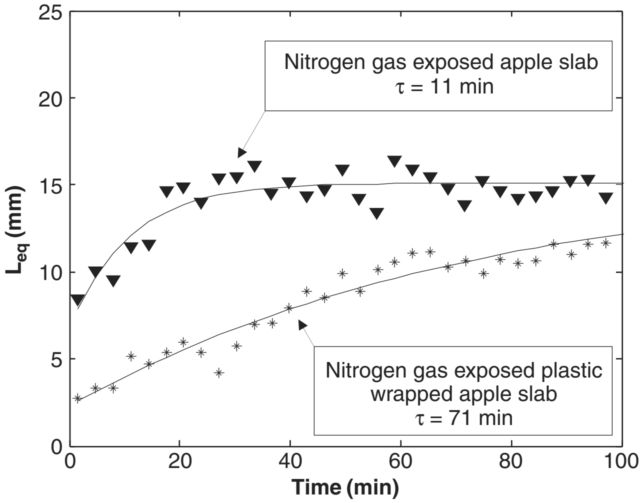

Fig. 6. The rate of gas exchange in freshly cut slices, 15 mm thickness, of Royal Gala apple in ambient air after a pre-immersion of the slices in nitrogen gas for 24 h are shown. One of the two slabs was wrapped in cling film before it was released into ambient air and measured (*) while the other one was not (▼). Exponential functions fitted to the data together with the estimated time constants are also included.

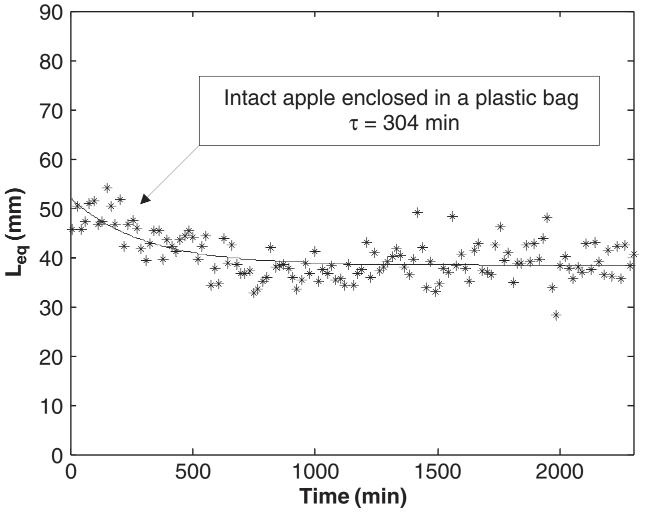

Fig. 7. The figure shows how an apple consumes oxygen in an enclosed atmosphere. A Granny Smith apple was placed in a sealed plastic bag with limited access to oxygen and measurements were performed. An exponential function fitted to the data together with the estimated time constant are also included.

time constant is strongly dependent on the amount of air in the bag when it was sealed, the respiration rate of the apple and the permeability of the plastic bag. The outcome of this experiment is not the time constant in itself, but rather the illustration of the suitability of the technique to study the time evolution of gas concentrations on their path to equilibrium inside modified atmosphere packaged fruits. This is interesting in assessments of the influence of different polymeric films on the produce inside modified atmosphere packages.

4. Discussion

Non-intrusive measurements of oxygen gas inside intact and sliced apple fruits were demonstrated using the newly introduced GASMAS technique. In contrast to other techniques the gas is measured non-intrusively inside the tissue rather than as gas extracted from the fruits. Gas exchange through the intact skin and through packaging films was demonstrated by observing the response of the oxygen equivalent mean path length to a transient change in the ambient gas concentration. The measurements suggest that the new technique might be developed into a valuable tool for gas studies in plant physiology, CA fruit storage and in MAP processes. Finally, this technique affords the prospect of real-time monitoring of gas exchange for a broad extension range of food storage and packaging.

Acknowledgements

This work was supported by the Swedish Research Council, the Asian-Swedish partnership programme of the Swedish International Development Cooperation Agency (SIDA), and the Knut and Alice Wallenberg Foundation.

References

[1] Hertog MLATM, Peppelenbos HW, Evelo RG, Tijskens LMM. A dynamic and generic model of gas exchange of respiring produce: the effects of oxygen, carbon dioxide and temperature. Postharvest Biol Technol 1998;14:335–49.

[2] Jurin V, Karel M. Studies on control of respiration of McIntosh apples by packaging methods. Food Technol 1963;17:782–6.

[3] Beaudry RM. Effect of O_2 and CO_2 partial pressure on selected phenomena affecting fruit and vegetable quality. Postharvest Biol Technol 1999;15:293–303.

[4] Mannapperuma JD, Singh RP. Modeling of gas exchange in polymeric packages of fresh fruits and vegetables. In: Singh RP, editor. Process optimization and minimal processing of foods. Boca Raton, FL, USA: CRC Press; 1994. p. 437.

[5] Fidler JC, North CJ. The effect of conditions of storage on the respiration of apples. I. The effect of temperature and concentrations of carbon dioxide and oxygen on the production of carbon dioxide and uptake of oxygen. J Hortic Sci 1967;42:189–206.

[6] Yearsley CW, Banks NH, Ganesh S. Temperature effect on internal lower oxygen limits of apple fruit. Postharvest Biol Technol 1997;11:73–83.

[7] Cameron AC, Talasila PC, Joles DW. Predicting film permeability needs for modified-atmosphere packaging of lightly processed fruits and vegetables. Hortic Sci 1995;30:25–34.

[8] Varoquaux P, Albagnac G, Gouble B. Physiology of minimally processed fresh vegetables. Austral Postharvest Hortic Conf 1995:437–43.

[9] Andrich G, Zinnai A, Silvestri S, Fiorentini R. Automatic control of aerobic and anaerobic respiration rates of fruits stored in refrigerated and controlled atmospheres. Automat Control Food Biol Processes 1994;36:281–7.
[10] Oomens J, Zuckermann H, Persijn S, Parker DH, Harren FJM. CO-laser-based photoacoustic trace-gas detection: applications in postharvest physiology. Appl Phys B 1996;67:459–66.
[11] Dadzie BD, Banks NH, Cleland DJ, Hewett EW. Changes in respiration and ethylene production of apple in response to internal and external oxygen partial pressures. Postharvest Biol Technol 1996;9:297–309.
[12] Konopacka D, Plocharski WJ. Effect of storage conditions on the relationship between apple firmness and texture acceptability. Postharvest Biol Technol 2004;32:205–11.
[13] Sigrist MW, editor. Air monitoring by spectroscopic techniques. New York: Wiley; 1994.
[14] Sjöholm M, Somesfalean G, Alnis J, Andersson-Engels S, Svanberg S. Analysis of gas dispersed in scattering media. Opt Lett 2001;26:16–8.
[15] Somesfalean G, Sjöholm M, Alnis J, af Klinteberg C, Andersson-Engels S, Svanberg S. Concentration measurement of gas embedded in scattering media by employing absorption and time-resolved laser spectroscopy. Appl Opt 2002;41:3538–44.
[16] Sjöholm M, et al. Determination of gas diffusion coefficients using the GASMAS technique. To appear.
[17] Renault P, Souty M, Chambroy Y. Gas exchange in modified atmosphere packaging. 1: A new theoretical approach for micro-perforated packs. Int J Food Sci Technol 1994;29:365–78.

PAPER VI

Studies of gas exchange in fruits using laser spectroscopic techniques

L. Persson, B. Anderson, M. Andersson, M. Sjöholm, and S. Svanberg.

Proceedings of FRUITIC 05, Information and Technology for Sustainable Fruit and Vegetable Production, 543–551, Montpellier (September 2005).

Information and Technology for Sustainable Fruit and Vegetable Production
FRUTIC 05, 12 – 16 September 2005, Montpellier France

Studies of Gas Exchange in Fruits Using Laser Spectroscopic Techniques

Linda Persson, Benjamin Anderson[1], Mats Andersson,
Mikael Sjöholm, and Sune Svanberg

Atomic Physics Division, Lund Institute of Technology, P.O. Box 118,
SE-221 00 Lund, Sweden

[1]Permanent address: LAFOC, University of Cape Coast, Ghana

Keywords: Diode laser spectroscopy, GASMAS, food packaging, gas exchange, oxygen, apple, avocado, orange

Abstract

Non-intrusive, *in-vivo*, real-time measurements of oxygen contents and oxygen diffusion in fruits using a laser spectroscopic technique are presented, where the narrow absorption features due to the free gas in pores in the fruits are observed. The technique is referred to as gas in scattering media absorption spectroscopy (GASMAS), and is performed using tunable diode lasers. In particular, assessment of oxygen transport in apples and oranges is demonstrated. To illustrate the possibility to use the technique for studies of modified atmosphere packaging processes, measurements on sealed horticultural produces were performed. Furthermore, preliminary studies of avocados concerning the possibility to non-intrusively determine the maturity of fruits are presented. This technique has substantial potential for the development of compact devices providing new types of information in postharvest fruit management.

INTRODUCTION

Assessment of free gas in porous materials is of considerable interest in several environmental, biological and medical processes. In the present paper a novel application of a laser spectroscopic technique to the study of gas exchange in porous agricultural products, in particular fruits, is discussed. Although any gas with absorption lines in reach of tunable diode laser sources can be probed by the technique, we here focus on biologically active molecular oxygen, whose concentration is of crucial importance for the ripening process and the quality of fruits. An overview of the influence of oxygen and carbon dioxide partial pressures on selected phenomena affecting fruit and vegetable quality has been given by, e.g., Beaudry (1999).

A common way to analyse gases *in situ* is to use absorption spectroscopy that employs a sufficiently narrow-band light source in combination with the Beer-Lambertian law. However, in porous materials the radiation is heavily scattered, which results in an enhanced average absorption path length compared to the geometrical dimensions of the sample. One approach to measure non-gaseous constituents in scattering media is to use time-resolved spectroscopy employing laser-produced white light; for a recent report, see Abrahamsson et al. (2005). This type of setup was recently used for studies on apples

(Cauchard et al., 2005). The spectral resolution needed in such systems is relatively low since solid materials and liquids have broad absorption features with linewidths normally not sharper than 10 nm, while free gases typically have a linewidth 10000 times sharper (Sigrist, 1994). Thus, the small and narrow absorption imprint in the emerging, multiply scattered diffuse light due to the gas can not be detected with such systems. However, by using single-mode continuous-wave lasers combined with modulation techniques the gas can be detected sensitively, without disturbance from the broader absorption features of the bulk material. In particular, diode lasers are highly suitable for sensitive absorption spectroscopy with high spectral resolution due to their availability in different wavelength ranges, uncomplicated wavelength tunability, and their relatively low cost compared to other laser sources. This methodology to study free gas embedded in scattering materials has been denoted GASMAS (gas in scattering media absorption spectroscopy) (Sjöholm et al., 2001; Somesfalean et al., 2002).

Measurements of molecular oxygen in wood have been performed in order to illustrate the influence of the density and anisotropy of the sample on the GASMAS signal (Alnis et al., 2003). Recently, studies of gas exchange in fruits, in particular apples, have been reported (Persson et al., 2005). The gas contents in the scattering medium gives rise to a signal of a certain strength, which is determined by the gas concentration as well as the average path length travelled by the light in the scattering medium. The latter quantity can be determined by time-resolved measurements allowing the true concentration to be determined (Somesfalean et al., 2002). In particular, transport of gas through the porous medium can be studied. Here, the sample is first exposed to a gas environmental anomaly; it may be placed for a few hours in a sealed plastic bag first flushed with pure nitrogen gas. Then, the sample is placed in the GASMAS setup and the time evolution of the atmospheric oxygen re-invasion is measured spectroscopically. Such gas transport in apples was first studied by Persson et al. (2005) in transillumination geometry, and is further investigated in the present paper in a more practical backscattering geometry. The technique presented may have powerful applications in the study of fruit physiology, controlled atmosphere (CA) storage and modified atmosphere packaging (MAP) performance.

EXPERIMENTAL PROCEDURE

Experimental arrangements for GASMAS measurements are shown in Figs 1 and 2a. The optics and electronics used are similar in the two arrangements and have been described more in detail by Persson et al. (2005). Two measurement geometries have been used; transillumination (Fig. 1) and backscattering (Fig. 2a). The spectroscopic light source used was a diode laser, Sharp LT031MDO, with a nominal output power of 7 mW. The wavelength of the diode laser was scanned by ramping the driving current at a repetition rate of 4 Hz across the R7R7 molecular oxygen line, which is situated at 761.003 nm (vacuum wavelength). Additionally, sinusoidal modulation of about 9 kHz was superimposed on the diode laser injection current to achieve a wavelength modulation of the light allowing sensitive wavelength modulation spectroscopy (WMS) using a lock-in amplifier. The laser radiation was guided to the sample by a 600 m core diameter optical fibre.

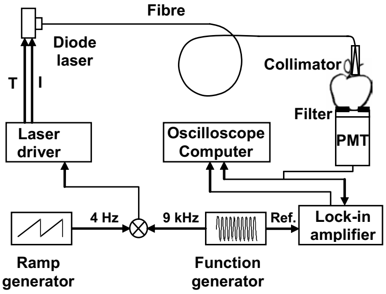

Fig. 1. Schematic layout of the GASMAS setup used for molecular oxygen detection in scattering porous materials such as fruits.

After light transport through the sample, a photomultiplier tube, Hamamatsu 5070A, detected the light. The ambient light was suppressed by a RG715 coloured glass filter used in combination with the sensitivity fall-off towards longer wavelengths for the photomultiplier tube. In the transmission geometry (Fig. 1) a circular aperture with a diameter of 6 mm was used to limit the detection area. The arrangement used in the backscattering geometry was slightly more complicated as can be seen in Fig. 2a. To launch the laser light into the scattering medium, a small right-angle prism providing total internal reflection was positioned in front of the fibre centrally located over the detector. The backscattered light that had travelled through the medium was collected in an annular aperture with an inner and an outer aperture diameter of 10 and 21 mm, respectively.

The DC and AC signals from the photomultiplier tube were detected separately. The DC signal, referred to as the direct signal, was sent to a digital oscilloscope, Tektronix TDS 520B. A high pass filter isolated the AC part and phase sensitive detection was performed with a lock-in amplifier. The component of the signal oscillating at the modulation frequency is similar to the first derivative of the direct signal, and, correspondingly, the component oscillating at twice the modulation frequency is similar to the 2nd derivative, etc. Since the direct signal is sloping, due to the simultaneous change in both wavelength and intensity as a function of injection current, the 1f signal is subject to a disadvantageous offset. This gives an advantage in using higher order components. However, the amplitude normally decreases by increasing the harmonic order. Thus, the component of the signal oscillating at twice the modulation frequency, i.e. 18 kHz, was selected as the output from the lock-in amplifier. This lock-in signal, referred to as the 2f signal, was sent to a second channel of the oscilloscope, which was computer controlled through GPIB communication by a LabVIEW program. An example of an oxygen signal recorded in backscattering geometry for the case of a 67-mm Granny Smith apple is shown in Fig. 2b.

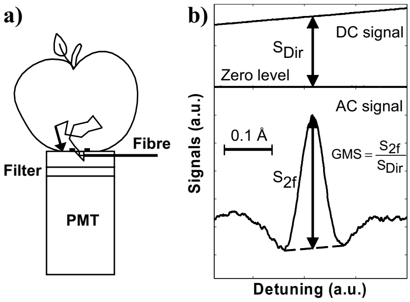

Fig. 2 (a). Modification of the GASMAS setup for backscattering (single-sided) measurements. (b). Direct absorption and second-harmonic component of the absorption for the R7R7 line in the oxygen A-band recorded from an Granny Smith apple in backscattering geometry.

As indicated in the figure the oxygen gas content can be evaluated from the peak-to-peak value of the absorption signature in the 2f signal. Clearly, the amplitude of the 2f signal is determined by the absolute size of the narrow gas absorption feature, i.e., to the fractional absorption due to the gas, and the amount of light reaching the detector. We are interested in the normalised GASMAS measurement signal, GMS, which is proportional to the fractional absorption. Thus, the AC signal (related to the oxygen content and the amount of light detected) was divided by the DC signal (related to the amount of light detected) as indicated in Fig. 2b. For small absorptions the GMS is proportional to the absorbance and thus to the product of the gas concentration and the path length travelled by the light. The standard addition method, just adding a path length of ambient air to be traversed by the laser light in addition to the scattering object under study, was adopted to calibrate a measured GMS and transform it into a more meaningful quantity. The acquired GMS values were plotted as a function of the added distance of air as discussed, e.g. by Persson et al (2005). The data points are expected to fall on a straight line, the zero intercept of which yields the equivalent distance, L_{eq}, in ambient air giving rise to a signal with the same magnitude as signal from the sample.

RESULTS AND DISCUSSION

Before presenting our new data, recorded mostly using backscattering geometry, we would like, in Fig. 3, to review some pertinent data obtained in our recent study (Persson et al., 2005). The recordings were performed in transillumination on Granny Smith apples using a setup of the type shown in Fig. 1. The gas content inside an intact fruit and the exchange of the gas was followed in real-time.

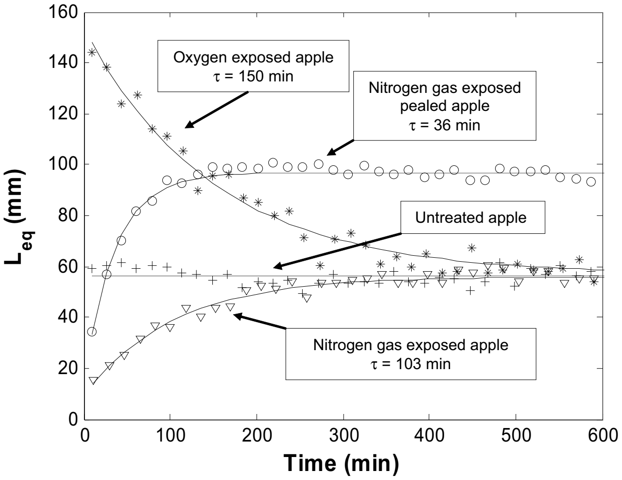

Fig. 3. Measurements of the gas exchange through differently treated Granny Smith apples in ambient air; untreated intact apple (+), intact apple pre-treated by immersion in nitrogen gas for 24 hours (□), pealed apple immersed in nitrogen gas for 12 hours (O) and another apple pre-exposed to an atmosphere with higher concentration of oxygen than in ambient air for 12 hours (). Exponential functions fitted to the data together with the estimated time constants are also included (Persson et al., 2005).

The equivalent mean path length, L_{eq}, was measured as a function of time for differently treated apples. A "flat" recording for an untreated apple, with a thickness of 70 mm, can be seen in the figure. The apple was then immersed in nitrogen gas for about 24 hours, by placing it in a plastic bag flushed with nitrogen gas before being sealed, as discussed above. Then it was brought out into ambient air and the re-invasion of oxygen containing ambient air was measured. The same apple was then pealed, immersed in nitrogen gas for 12 hours before the measurement procedure was repeated. Finally, a new apple, with a thickness of 74 mm, was exposed to an atmosphere with a higher concentration of oxygen than in ambient air for about 12 hours, before it was brought out into ambient air and the measurement procedure was again repeated. The time evolution of the oxygen equivalent mean path length was found to approximately follow a simple exponential curve, which also could be expected with the experimental procedures utilised (Sjöholm et al., 2005). The time constant for the re-invasion of oxygen into the nitrogen-exposed apple with skin was found to be around 100 min. It takes approximately 5 hours for the apple to reach the same steady-state oxygen concentration as before the treatment. It can also be seen that in the pealed apple, the concentration equilibrium of oxygen becomes twice as high as before the apple was pealed, and that the gas exchange is three times faster than in an intact apple.

Similar recordings obtained with our new more practical backscattering detection geometry (Fig. 2a) are shown for a 67-mm thick Granny Smith apple in Fig. 4. The same apple was also measured in transmission geometry, rendering a slightly slower change in the gas signal with time, which might be explained by the fact that the probed depth of the fruit is different in the two geometries (Sjöholm et al., 2005).

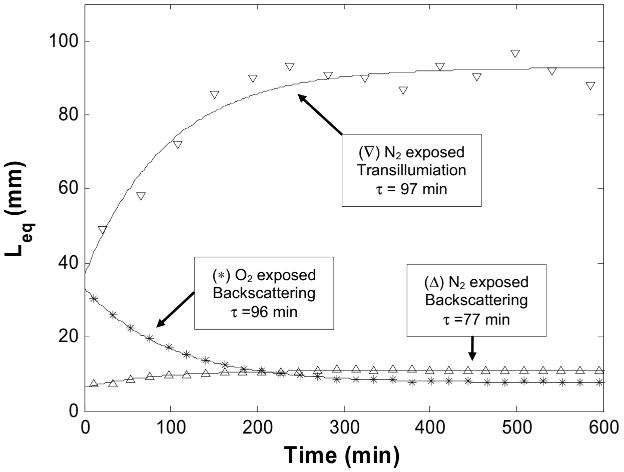

Fig. 4. Measurements of the gas exchange in transillumination and backscattering geometries in ambient air on a Granny Smith apple after different treatments; pre-treated by immersion in nitrogen gas for 24 hours in transillumination (□), pre-treated by immersion in nitrogen gas for 24 hours in backscattering geometry (□), and pre-exposed to an atmosphere with higher concentration of oxygen than in ambient air for 12 hours (). Exponential functions fitted to the data together with the estimated time constants are also included.

The same apple was also studied in backscattering geometry after oxygen exposure. As can be seen in the figure, the gas content equilibrium of oxygen becomes slightly lower, which might be due to the extreme levels of oxygen the apple has been exposed to, which might have harmed the apple. However, the reason can also be due to slightly different probed volumes of the apple.

To illustrate the possibility to use the GASMAS technique for modified atmosphere packaging issues, two different horticultural produces, apple and mushroom, with different expected respiration rates, were sealed in plastic bags and the consumption of oxygen was measured inside the produces in backscattering geometry. The results given in Fig. 5 show, as expected, that the change in the oxygen signal is faster for the mushroom than for the apple, which is a result of the faster respiration rate of the former compared to the latter (Gross et al., 2004).

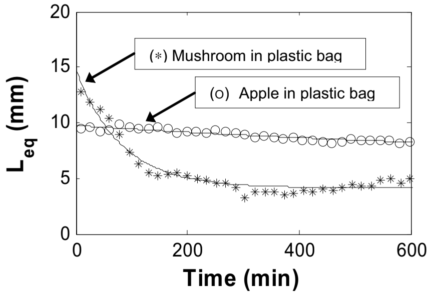

Fig. 5. The time evolution of the oxygen signal for two different horticultural produces with different respiration rates, apple (O) and mushroom (), while sealed in plastic bags, measured in backscattering geometry.

Finally, we illustrate some preliminary measurements in backscattering geometry on other types of horticultural produces such as avocado and orange. The GMS values from three avocados with different maturity are shown in Fig. 6. The hardness of the avocados was measured with a Stevens LFRA Texture Analyzer equipped with a circular probe with a diameter of 25 mm. Each avocado was compressed about 2 mm with a probe speed of 0.2 mm/s while the maximum force was measured. With increasing maturity it is noticed that the GMS values are reduced, probably related to both lower gas contents and less scattering. These aspects could be elucidated in time-resolved measurements (Somesfalean et al., 2002).

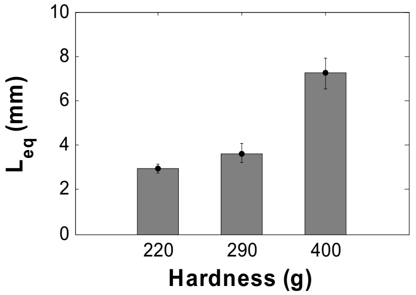

Fig. 6. The equivalent mean path length, Leq, measured for three avocados with different maturity, in backscattering geometry. Four measurements were performed on each avocado and the averages together with error bars corresponding to one standard deviation are shown.

Gas exchange into an orange, with and without peal, was measured after nitrogen exposure. In Fig. 7 the diffusion curve for the intact orange is shown, where the time constant was estimated to approximately 2.5 hours. No change in the GMS values with time could be observed for the equally treated pealed orange, which could be due to the low signal obtained compared to the background noise. However, the results indicate the possibility to study oxygen dynamics in the peal of an orange.

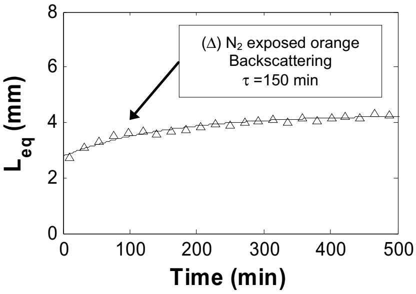

Fig. 7. Measurements of the gas exchange in backscattering geometry on an orange; intact orange pre-treated by immersion in nitrogen gas for 24 hours. Exponential function fitted to the data together with the estimated time constant is also included.

CONCLUSION

As illustrated by the preliminary work reported in the present paper and by Persson et al. (2005) the GASMAS technique has potential to non-intrusively and in real-time provide information on the conditions of horticultural produces. In contrast to other techniques, the gas is measured non-intrusively inside the tissue rather than as gas extracted from the fruits. Applications regarding basic plant physiology as well as in controlled atmosphere fruit storage and in modified atmosphere packaging processes can be foreseen. Also different stages of processing, including fermentation, could be studied. We presently aim at developing compact and realistic equipment for GASMAS studies also in the field.

ACKNOWLEDGEMENT

This work was supported by the Swedish Research Council, the Asian-Swedish partnership program of the Swedish International Development Cooperation Agency (SIDA), the International Science Programme (ISP), Uppsala, and the Knut and Alice Wallenberg Foundation. The authors gratefully acknowledge Professor Petr Dejmek at the Department of Food Engineering, Lund University Sweden, for the assistance in the measurements of fruit hardness.

References

Abrahamsson, Ch., Svensson, T., Svanberg, S., Andersson-Engels, S., Johansson, J. and Folestad., 2004 Time and wavelength resolved spectroscopy of turbid media using light continuum generated in a crystal fibre. Optics Express 12:4103-4112

Alnis, J., Anderson, Sjöholm, M., Somesfalean, G. and Svanberg, S. 2003. Laser spectroscopy of free molecular oxygen dispersed in wood material. Applied Physics B 77:691

Beaudry, R.M., 1999. Effect of O_2 and CO_2 partial pressure on selected phenomena affecting fruit and vegetable quality. Postharvest Biology and Technology 15:293-303.

Chauchard, F. et al (2005)

Gross, K.C., Wang, C.Y. Saltveit, M. 2004 Agriculture Handbook Number 66: The Commercial Storage of Fruits, Vegetables, and Florist and Nursery Stocks,

Persson, L., Gao, H., Sjöholm, M. and Svanberg, S. 2005. Diode laser absorption spectroscopy for studies of gas exchange in fruits. Lasers and Optics in Engineering, in press.

Sigrist, M.W., Ed. 1994. Air Monitoring by Spectroscopic Techniques. John Wiley and Sons, New York.

Sjöholm, M., Somesfalean, G., Alnis, J., Andersson-Engels, S. and Svanberg, S. 2001. Analysis of gas dispersed in scattering media. Optics Letters 26:16-18.

Sjöholm, M. *et al*. 2005. Determination of gas diffusion coefficients using the GASMAS technique. To appear.

Somesfalean, G., Sjöholm, M., Alnis, J., af Klinteberg, C., Andersson-Engels, S. and Svanberg, S. 2002. Concentration measurement of gas embedded in scattering media by employing absorption and time-resolved laser spectroscopy. Applied Optics 41:3538-3544.

Paper VII

Noninvasive characterization of pharmaceutical solids by diode laser oxygen spectroscopy

T. Svensson, L. Persson, M. Andersson, S. Svanberg,
S. Andersson-Engels, J. Johansson, and S. Folestad.

Applied Spectroscopy **61**, 784–786 (2007).

Noninvasive Characterization of Pharmaceutical Solids by Diode Laser Oxygen Spectroscopy

TOMAS SVENSSON,* LINDA PERSSON, MATS ANDERSSON, SUNE SVANBERG, STEFAN ANDERSSON-ENGELS, JONAS JOHANSSON, and STAFFAN FOLESTAD

Department of Physics, Lund University, Sweden (T.S., L.P., M.A., S.S., S.A.-E.); and Astra Zeneca R&D, Mölndal, Sweden

Index Headings: **Oxygen spectroscopy; Light scattering; Porosity.**

INTRODUCTION

Characterization of solid pharmaceuticals, ranging from monitoring of solid-state reactions to understanding tablet dissolution, is of great interest for pharmaceutical science.[1] The quality of the finished product highly depends on knowledge about the pharmaceutical materials used and the different unit operations involved in manufacturing of pharmaceuticals. Thus, availability of appropriate and reliable tools for measurements of physical and chemical properties of drug materials *in situ* during chemical and physical processing is a key for optimized processing. In early stages of pharmaceutical development a whole range of techniques for characterization of the solid state is available, addressing, for example, particle size and shape, density, porosity, calorimetry, thermo-mechanical properties, specific area, and crystallinity.[2] However, most of these techniques are slow and not well suited for fast laboratory-based or process applications. Process analytical technology (PAT) is a term describing a holistic approach to pharmaceutical manufacturing based on in-depth understanding through advanced process sensors and modeling tools.[3] In order to succeed with this, new tools are needed, e.g., with capability to directly measure physico-chemical attributes *in situ* of the mechanical process. In this context, tools based on spectroscopic techniques offer obvious advantages owing to their speed, compactness, versatility, and ability to perform noninvasive analysis.

By employing the spectroscopic technique referred to as gas in scattering media absorption spectroscopy (GASMAS), it is possible to extract information related to gas dispersed within highly scattering (turbid) materials.[4] In our case, the key is contrast between the sharp (GHz) absorption features of molecular oxygen located around 760 nm and the broad absorption features related to tablet bulk material. The technique is based on high-resolution diode laser absorption spectroscopy, and its main principle is illustrated in Fig. 1. Light is injected into a highly scattering sample, often utilizing optical fibers. The actual path length distribution of transmitted photons will depend on the scattering properties of the sample. Due to significant multiple scattering, the average photon path length greatly exceeds sample dimensions. For example, the average path length of photons that have traveled through a pharmaceutical tablet typically exceeds 10 cm.[5] During passages through air-filled pores, photons in resonance with an absorption line in the A-band of molecular oxygen can be absorbed. Oxygen absorption can be distinguished from bulk absorption due to the extremely narrow absorption features (GHz) exhibited by free gases. To resolve such narrow features, high-resolution spectroscopy must be employed. The resulting absorption signal depends on both the oxygen content and the scattering properties (photons path lengths) of the sample. Indirectly, it is thus related to mechanical properties such as porosity and particle size.

The GASMAS technique has previously been used to study the gas content in, for example, polystyrene foam, wheat flour, granulated salt, wood materials, fruit, and human sinuses.[4,6–9] Gas exchange dynamics has been studied by placing samples of wood and fruit in nitrogen atmospheres and monitoring the re-invasion of oxygen.[7,8]

In this paper we show the potential of using GASMAS for determination of physical and structural parameters of pharmaceutical solids. We present results from a study of pharmaceutical tablets made from two different sieve fractions (particle size distributions) and with different compression forces. In addition, the prospects of a broader use of this technique for pharmaceutical analysis are discussed.

EXPERIMENTAL

Instrumentation. A simplified schematic of the setup is given in Fig. 2. The instrumentation and corresponding data evaluation has been described in detail elsewhere.[10] Briefly, a temperature stabilized distributed feed-back (DFB) diode laser (NanoPlus, Germany) is repetitively wavelength tuned over one of the narrow absorption lines in the oxygen A-band (R11Q12, 760.445 nm vacuum wavelength). The DFB diode laser is pigtailed using a single-mode (SM) optical fiber, yielding an output of about 4 mW. Sensitivity was vastly increased by employing wavelength modulation spectroscopy (WMS), in this case implemented by imposing an $f = 9$ kHz harmonic modulation on the laser diode injection current. A 90/10% fiber splitter (Laser2000, Sweden) is used create a double-beam arrangement (reference and sample arm), allowing balanced detection. This maneuver is important in order to minimize the influence of optical interference fringes. The lower intensity optical fiber is immediately directed to a silicon photodiode (PIN-10DP/SB, UDT Sensors), producing a reference signal. The other fiber guides light to our sample (e.g., tablet).

Samples were placed in contact with a long-pass filter (Schott RG715), which in turn was placed directly on top of a photomultiplier tube (PMT, 5070A, Hamamatsu) detecting diffuse transmittance. The long-pass filter in combination with the PMT sensitivity fall-off effectively suppressed unwanted ambient light. Signals from the reference and sample detectors are sent to lock-in amplifiers detecting at the second harmonic ($2f$) of the modulation frequency f. The $2f$ signal is normalized

---

Received 17 January 2007; accepted 7 May 2007.

* Author to whom correspondence should be sent. E-mail: tomas.svensson@fysik.lth.se.

0003-7028/07/6107-000000$2.00/0

© 2007 Society for Applied Spectroscopy

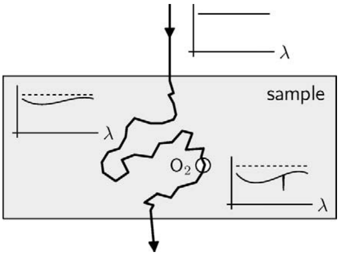

FIG. 1. The principle of GASMAS. The key is the contrast between the sharp absorption features of free gases (e.g., oxygen) and the broad absorption features related to bulk material. This is illustrated by the change in absorption spectra along a particular photon path. The gas absorption is typically much weaker than bulk absorption and is thus exaggerated in the graph.

using direct detector signals. Software-based balanced detection is employed to remove contributions originating from optical interference fringes. In addition, vibrators positioned close to the sample were used to further suppress such effects.

Data Evaluation. Acquired $2f$ signals are evaluated using curve fitting of an experimental long-path recording of the oxygen absorption feature. This recording was performed using the same setup as for tablet measurements. The oxygen imprint is measured in terms of mm of equivalent path length through air, L_{eq}. That is, if $L_{eq} = 10$ mm, the oxygen absorption exhibited by the turbid sample equals that of a 10 mm path length through ambient air. The absolute relation between the $2f$ signal and the equivalent path length is established experimentally by means of a standard addition calibration. In this particular case, the standard addition involves adding known path lengths of air to the sample arm. A detailed description of these procedures is found in a previous publication.[10]

Pharmaceutical Samples. Measurements were performed on 22 model tablets with microcrystalline cellulose as the main constituent, manufactured using a wet granulation process.[11] The influence of particle size distribution was studied by sieving the granulate, producing two different batches consisting of 11 tablets each (particle sizes: <150 µm and >400 µm). The tablets were compressed manually into various thicknesses (3–4 mm). The tablets were round, without score or engravings, and had a 10 mm diameter.

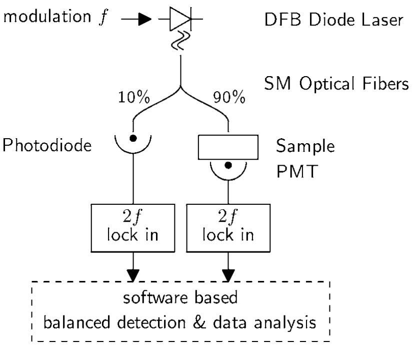

FIG. 2. Simplified schematic of the setup. A 90/10% optical fiber splitter is used to achieve the double-beam arrangement typical of applications requiring high sensitivity. Lock-in amplifiers detect at the second harmonic of the modulation frequency f. Software algorithms handle balanced detection and data evaluation.

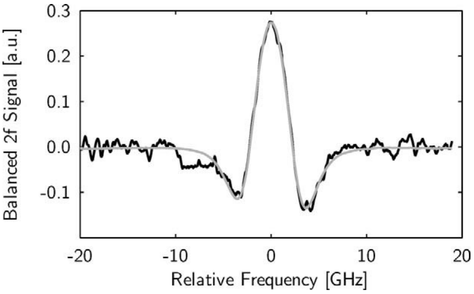

FIG. 3. Data obtained for a 3.38 mm thick tablet from PS > 400 µm. The $2f$ signal after balanced detection (black) is shown together with a fitted oxygen absorption signature (grey). The signal corresponds to an L_{eq} of 17.4 mm. The optical frequency is given relative to the oxygen absorption line (760.445 nm). The corresponding wavelength range is 760.41–760.48 nm, where the lower wavelength is to the right.

RESULTS

Examined tablets exhibited oxygen absorption corresponding to 5–50 mm propagation through ambient air. A typical example of the acquired $2f$ absorption signature is given in Fig. 3. To illustrate that obtained signals are related to oxygen absorption, additional nitrogen atmosphere experiments was performed. Tablets were then stored for several hours in plastic bags filled with nitrogen. When inserting them into the setup (while still in their plastic bags), obtained signals exhibited nothing but the ordinary 3 mm L_{eq} noise floor. When the plastic bags was opened and ventilated, the expected signal quickly appeared. This oxygen re-invasion could, however, not be temporally resolved.

The overall influence of tablet compression and particle size is shown in Fig. 4. Here, each tablet was measured four times consecutively, and the average derived L_{eq} is presented. The acquisition time was 25 s in each of the four measurements, and the standard deviation in these sets of four repetitions was on average 0.8 mm (<150 µm) and 1.0 mm (>400 µm). However, these measures of uncertainty do not include

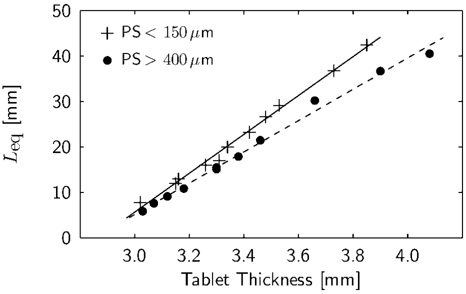

FIG. 4. Equivalent path length L_{eq} versus tablet thickness. Shown values are averages from four consecutive measurements. All tablets have the same weight (300 mg) and diameter (10 mm), but intentional variations in applied compression force yielded variations in tablet thickness.

systematic errors due to optical interference fringes that remain after balanced detection. The systematic errors due to such fringes can be estimated by looking at the amplitude of interference noise in spectral regions free from oxygen absorption (consider, for example, the 10–20 GHz range in Fig. 3). Furthermore, this noise was found to be stable between the four consecutive measurements. In the current configuration, optical noise remaining after balanced detection limits the accuracy to about 3 mm L_{eq}. This corresponds to an optical absorption fraction of 7.5×10^{-5}.

In the range of examined tablet thicknesses, there is a highly linear relation between tablet thickness and equivalent path length. It is also clear that in case of comparable thickness, tablets manufactured from the smaller granule particles (<150 μm) exhibited the largest oxygen absorption.

DISCUSSION

Our results clearly show that it is possible to detect oxygen dispersed within pharmaceutical tablets. Hence, a new tool is available for characterization of pharmaceutical solids. Using the GASMAS technique, parameters such as porosity and particle size may be determined in raw materials as well as finished tablets. This may in turn lead to a better optimization of pharmaceutical manufacturing processes. Required instrumentation involves standard components and is simple and fairly compact. Further development is expected to improve data quality.

The porosity of pharmaceutical tablets is normally estimated by employing mercury intrusion porosimetry.[12] This method has several limitations: it is a destructive technique, it includes hazardous handling of mercury, and it is not suitable for fast laboratory-based or on-line analysis. Furthermore, mercury porosimetry is only sensitive to open pores, while the presented technique is sensitive to all pores containing oxygen. It would thus be of interest to compare results from this technique with results from mercury porosimetry. Moreover, this will also provide opportunities for accessing functional properties such as tablet hardness. Preliminary data on such parameters has been shown before.[13,14]

In addition to the results reported here, we propose monitoring of gas diffusion dynamics. It would be attractive to study oxygen reinvasion in samples that have been placed in, for example, a pure nitrogen environment or a vacuum chamber. Such dynamic experiments have been successfully demonstrated in, for example, wood and fruit materials.[7,9] In addition, we propose GASMAS measurements on tablets in blister packages, allowing study of gas exchange through blister materials.

Although the oxygen absorption signal clearly correlates to relevant physical parameters, a detailed understanding of the interaction of near-infrared light with the turbid sample requires further studies. The signal is influenced by both oxygen concentration and photon path length, both being unknown quantities and adding to the total response. It would thus be of great interest to separate these effects in future research. Such a separation is possible by combining GASMAS with time- or frequency-domain photon migration techniques.[6] These techniques are frequently used in biomedical optics, but have also been applied to pharmaceutical solids.[5,15] More such work is forthcoming.

1. D. E. Bugay, Adv. Drug Delivery Rev. **48,** 43 (2001).
2. D. C. Lee and M. Webb, Eds., *Pharmaceutical Analysis* (Blackwell Publishing, Oxford, 2003), 1st ed.
3. J. Workman, M. Koch, and D. J. Veltcamp, Anal. Chem. **75,** 2859 (2003).
4. M. Sjöholm, G. Somesfalean, J. Alnis, S. Andersson-Engels, and S. Svanberg, Opt. Lett. **26,** 16 (2001).
5. J. Johansson, S. Folestad, M. Josefson, A. Sparén, C. Abrahamsson, S. Andersson-Engels, and S. Svanberg, Appl. Spectrosc. **56,** 725 (2002).
6. G. Somesfalean, M. Sjöholm, J. Alnis, C. af Klinteberg, S. Andersson-Engels, and S. Svanberg, Appl. Opt. **41,** 3538 (2002).
7. J. Alnis, B. Anderson, M. Sjöholm, G. Somesfalean, and S. Svanberg, Appl. Phys. B **77,** 691 (2003).
8. L. Persson, K. Svanberg, and S. Svanberg, Appl. Phys. B **82,** 313 (2006).
9. L. Persson, H. Gao, M. Sjöholm, and S. Svanberg, Opt. Laser. Eng. **44,** 687 (2006).
10. L. Persson, F. Andersson, M. Andersson, and S. Svanberg S, Appl. Phys. B DOI:10.1007/s00340-007-2593-y (2007).
11. A. Sparén, M. Malm, M. Josefson, S. Folestad, and J. Johansson, Appl. Spectrosc. **56,** 586 (2002).
12. J. M. Haynes and P. Rossi-Dori, Eds., *Principles and Applications of Pore Structural Characterization* (Arrowsmith, Bristol, 1985).
13. T. Svensson, J. Johansson, S. Andersson-Engels, S. Svanberg, and S. Folestad, "Non-invasive determination of porosity in solids by diode laser oxygen spectroscopy: application to pharmaceutical tablets", Poster \#562 at FACSS 2004 (Portland, OR, Oct 3–7, 2004).
14. J. Johansson, S. Folestad, S. Svanberg, M. Sjöholm, G. Somesfalean, C. Abrahamsson, and S. Andersson-Engels, "Method for analysing a pharmaceutical sample", international patent PCT no. WO 03/078983 (2003).
15. Z. G. Sun, S. Torrance, F. K. McNeil-Watson, and E. M. Sevick-Muraca, Anal. Chem. **75,** 1720 (2003).

Paper VIII

Spectroscopic studies of wood-drying processes

M. Andersson, L. Persson, M. Sjöholm, and S. Svanberg.

Optics Express **14**, 3641–3653 (2006).

Spectroscopic studies of wood-drying processes

Mats Andersson, Linda Persson, Mikael Sjöholm, and Sune Svanberg
Atomic Physics Division, Lund Institute of Technology,
P.O. Box 118, S-221 00 Lund, Sweden
sune.svanberg@fysik.lth.se

Abstract: By the use of wavelength-modulation diode laser spectroscopy, water vapor and oxygen are detected in scattering media nonintrusively, at 980 nm and 760 nm, respectively. The technique demonstrated is based on the fact that free gases have extremely sharp absorption structures in comparison with the broad features of bulk material. Water vapor and oxygen measurements have been performed during the drying process of wood. The results suggest that the demonstrated technique can give information about the drying process of wood to complement that of commercially available moisture meters. In particular, the time when all the free water has evaporated from the wood can be readily identified by a strong falloff in the water vapor signal accompanied by the reaching of a high-level plateau in the molecular oxygen signal. Furthermore, the same point is identified in the differential optical absorption signal for liquid water, with a sharp increase by an order of magnitude in the ratio of the signal intensities at 980 nm and 760 nm.

© 2006 Optical Society of America

OCIS codes: (000.2190) Experimental physics; (300.6260) Diode laser spectroscopy; (290.7050) Turbid media

---

References and links

1. J. M. Dinwoodie, "*Timber: Its nature and behaviour*," (E & FN, 2000).
2. B. Berglund, B. Brunekreef, H. Knöppel, T. Lindvall, M. Maroni, L. Mølhave, and P. Skov, "Effects of indoor air pollution on human health," Indoor Air **2**, 2–25 (1992).
3. S. Joseph Cohen and T C.S Yang, "Progress in food dehydration," Trends in Food Science & Technology **6**, (1995).
4. D. A. Skoog and M.D. West, "*Fundamentals of Analytical Chemistry*," 7th edition, (Saunders, 1995).
5. G.Müller, B. Chance, R. Alfano, S. Arridge, J. Beuthan, E. Gratton, M. Kaschke, B. Masters, S. Svanberg, and P. van der Zee, eds., "Medical optical tomography, functional imaging and monitoring," in *SPIE Institute Series*, Vol. **11**, (SPIE, 1993).
6. C. Abrahamsson, J. Johansson, S. Andersson-Engels, S. Svanberg, and S. Folestad, "Time-resolved NIR spectroscopy for quantitative analysis of intact pharmaceutical tablets," Anal. Chem. **77**, 1055–1059 (2005).
7. T. J. Farrell, M. S. Pattersson, and B. Wilson, "A diffusion theory model of spatially resolved, steady-state diffuse reflectance for noninvasive determination of tissue optical properties in vivo," Med. Phys. **19**, 879–888 (1992).
8. M. S. Pattersson, B. Chance, and B. C. Wilson, "Time-resolved reflectance and transmittance for the noninvasive measurement of tissue optical properties," Appl. Opt. **28**, 2331–2336 (1989).
9. C. af Klinteberg, A. Pifferi, S. Andersson-Engels, R. Cubeddu, and S. Svanberg, "In vivo absorption spectroscopy of tumor sensitizers using femtosecond white light," Appl. Opt. **44**, 2213–2220 (2005).
10. M. Sjöholm, G. Somesfalean, J. Alnis, S. Andersson-Engels, and S. Svanberg, "Analysis of gas dispersed in scattering media," Opt. Lett. **26,** 16–18 (2001).
11. J. Alnis, B. Anderson, M. Sjöholm, G. Somesfalean, and S. Svanberg, "Laser spectroscopy on free molecular oxygen dispersed in wood materials," Appl. Phys. B **77**, 691–695 (2003).

12. L. Persson, H. Gao, M. Sjöholm, and S. Svanberg, "Diode laser absorption spectroscopy for studies of gas exchange in fruits," Opt. Lasers Eng. **44**, 687–698 (2006).
13. L. Persson, B. Anderson, M. Andersson, M. Sjöholm, and S. Svanberg, "Studies of gas exchange in fruits using laser spectroscopic techniques," in Proceedings of Fruitic05 Symposium (Montpellier, France, September 12-16, 2005).
14. G. Somesfalean, M. Sjöholm, J. Alnis, C. af Klinteberg, S. Andersson-Engels, and S. Svanberg, "Concentration measurement of gas imbedded in scattering media employing time and spatially resolved techniques," Appl. Opt. **41**, 3538–3544 (2002).
15. L. Persson, K. Svanberg, and S. Svanberg, "On the potential of human sinus cavity diagnostics using diode laser gas spectroscopy," Appl. Phys. B **82,** 313–317 (2006).
16. L. Sandra, B. Roderick, and M. L. Roderick, "Plant-water relations and the fibre saturation point," New Phytol. **168**, 25–37 (2005).
17. P. Perré, "The role of wood anatomy in the drying of wood: Great Oaks from little acorns grow," 8th Int. IUFRO Wood Drying Conference (Brasov, Rumania, August 24–29, 2003).
18. M. Goyeneche, D. Lasseux, and D. Bruneau, "A film-flow model to describe free water transport during drying of a hydroscopic capillary porous medium," Transp. Porous Media **48**, 125-158 (2002).
19. L. James, "Electric moisture meters for wood," Gen. Tech. Rep. FPL-GTR-6. Madison, WI: U.S. Department of Agriculture, Forest Service, Forest Products Laboratory, 1988.
20. H. Forsén and V. Tarvainen, "Accuracy and functionality of hand held wood moisture content meters," VTT Publications 420 (2000).
21. P. J. Wilson, "Accuracy of a capacitance-type and three resistance-type pin meters for measuring wood moisture content," Forest Products Journal, **49**, 29–32 (1999).
22. C. Nordling and J. Österman, "*Physics Handbook*," 4th ed. (Studentlitteratur, 1987).
23. S. Matcher, M Cope, and D. Delpy, "Use of the water absorption spectrum to quantify tissue chromophore concentration changes in near infrared spectroscopy," Phys. Med. Biol. **39,** 177–196 (1994).
24. T. Svensson, J. Swartling, P. Taroni, A. Torricelli, P. Lindblom, C. Ingvar, and S. Andersson-Engels, "Characterization of normal breast tissue heterogeneity using time-resolved near-infrared spectroscopy," Phys. Med. Biol. **50,** 2559–2571 (2005).

---

1. Introduction

Drying processes, i.e., the removal of moisture from materials, are of utmost importance in many industrial contexts and everyday experiences. For instance, wood needs to be dried from its natural moisture before its use as a fuel or as a construction material [1]. An important issue is that moisture in building materials induces mold, especially if the ventilation is insufficient, which is of major concern in the building sector [2]. Grain and cereals need drying for storage and for further processing in the food industry [3]. Paper processing includes important drying steps as is the case also in many further industrial processes.

Many natural materials are porous and hydrophilic. The pores can be filled with air or other gases, but may also be partially or fully filled with water; a frequently undesired situation. Capillary action is an important passive process when porous materials take up water. Materials frequently swell (increase in volume) when wet. In nonporous media the process of osmosis is in action. If the material has some rigid scaffolding structure, such as wood and other building materials, the swelling is minor. Then the pores originally filled with air instead become water filled. By increasing the vapor pressure of water by heating in combination with securing an environment with reduced relative humidity, forced drying can be achieved.

The status of drying materials is often studied by handheld moisture meters that measure the water content by an indirect method relying on the fact that the electrical properties of the material is dependent on the water content. However, these instruments are not able to monitor the whole drying process and are in some cases intrusive. Recent developments in diode-laser-based spectroscopy pose an interesting alternative approach, which would be to monitor the water vapor as well as the liquid water by a more direct, noninstrusive spectroscopic approach.

The present paper deals with the study of drying of wood using high-resolution near-IR laser absorption spectroscopy. A tunable diode laser operating close to 980 nm is used to monitor gaseous water. Liquid water also exhibits a broad absorption peak in the same wavelength region. For reference, atmospheric oxygen gas in the pores is also monitored in its A band close to 760 nm. This wavelength also provides a convenient off-resonance wavelength in the liquid-water spectrum for assessment of liquid-water contents.

Absorption spectroscopy is a very common method for measuring concentrations of substances utilizing the Beer–Lambert law and a suitable calibration procedure (See, e.g., [4]). However, the application of this method is not straightforward for natural materials such as wood, since the fact that they are inhomogeneous and porous also means that they are highly scattering, making the optical pathlength through the sample undefined. This situation is common in medical optics, where scattering and absorption are intertwined [5], as is also the case in analytical spectroscopy of pharmaceutical preparations [6]. Different techniques for handling multiple scattering of light have been developed for assessing the concentration of liquid and solid absorbing constituents. Spatially separated measurements [7] and time-resolved techniques [8] constitute two main approaches for enabling concentration determinations. A recent example on the determination of tumor sensitizer concentration in vivo is given in Ref. [9].

Such techniques have been extended to free gases present in porous media through the introduction of the Gas in Scattering Media Absorption Spectroscopy (GASMAS) technique [10]. Normally a modest resolution is used in solid-state spectroscopy because of the broad absorbing structures. However, if single-mode diode laser spectroscopy using sensitive modulation techniques is employed, then structures appear that are typically 10,000 times narrower due to free gas. So far, the GASMAS technique was applied to the monitoring of free molecular oxygen in materials as diverse as wood, polystyrene foam, and fruits [10-13]. In particular, gas transport through the media could be studied by first subjecting the material to a pure nitrogen atmosphere and then observing the time constant for the reinvasion of normal ambient (oxygen-containing) air. Concentrations could be determined by combining GASMAS measurements with time-resolved measurement, revealing the time history of the photons inside the sample [14]. The GASMAS technique was also very recently applied to the monitoring of human sinus cavities [15].

The present paper focuses on spectroscopic monitoring of the drying of wood, and the GASMAS technique has in this context been extended to water-vapor monitoring. The structure of wood and the basics of wood-drying processes are presented in the next section. Conventional methods for measuring moisture in wood are discussed in Section 3. The experimental arrangements used in the present work are then presented in Section 4. Measurements and results are described in Section 5. A discussion of the results and conclusions from the study are presented in the final section.

2. Wood structure and its drying process

2.1. Wood structure

Wood has a complicated architecture, described in detailed, e.g., in Ref. [1]. In a tree the wood structure supports the treetop, stores nutritious substances, and transfers minerals and water, which have been absorbed by the root system. Thus, it needs to be strong, hydrophilic, and flexible since a tree grows and lives in a changing environment. Even though there exist hundreds of different types of wood material, they can be divided into two groups, hardwood (deciduous) and softwood (coniferous); see Fig. 1. Hardwood is the most complicated of the two and comprise wood such as balsa, white oak, ash, mahogany, etc. The density of hardwood may vary from about 0.1 to 1.2 g/cm^3, depending on type of wood. Hardwood is characterized by a combination of complicated cell types orientated both vertically, tangentially, and radially. Softwood, on the other hand, is distinguished by a much simpler combination of cells that runs mostly vertically in a tree. Typical examples of wood that belong to the softwood group are spruce, pine, and larch. The weight of softwood may vary from 0.3 to 0.7 g/cm^3.

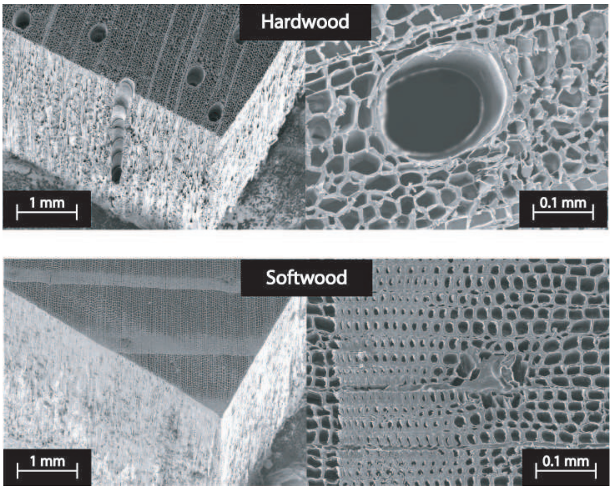

Fig. 1. Microscopic pictures of hardwood (balsa) and softwood (pine).

From a microscopic point of view wood consists of cellular structures that handle tasks carried out in a tree. Water and minerals are stored and transported vertically via cells, forming vessels, and horizontally via cell structures called rays. In total, wood cells can be classified into four different types; parenchyma (storage of nutritients), tracheids (support and conduction), fibers (support), and vessel cells (conduction).

In hardwood all four cell types are present, but tracheids are uncommon. Instead fibers and vessels are responsible for support and conduction of water and minerals. Fibers are usually 1-2 mm long and 10-20 μm wide, and their only function is support. However, vessel cells are about the same length as the fibers but up to 0.5 mm wide. Since the ends of the vessels are situated on top of each other they can make up a long tube. Thus, vessels act as an efficient water tube since the ends of the vessels are more or less dissolved.

In softwood only two cell types are present, namely parenchyma and tracheids. Tracheids are the most common cell type (about 90% of the softwood), and its main function is support and conduction of minerals and water. The size of the cell is about 2–4 mm long and about 30–50 μm wide. It is situated vertically in the tree and conducts water and minerals via small pits located on the cell surface. Parenchyma cells are small, 200 x 30 μm^2 in size, taking care of the storage of nutritients.

2.2. Wood drying processes

All types of wood consist of cellulose, hemicellulose, lignin, and extractives. The density of wood elements is about 1.5 g/cm^3, but since wood is based on a cell structure, with size that differs per type of wood, the density of wood may vary from 0.1 to 1.2 g/cm^3 if the content of water is kept low. However, since the wood cell structure is hydrophilic and full of air, wood is heavily affected by water and moisture.

The moisture content in wood is defined as the ratio between the weight of water in a piece of wood and the weight of the wood when no water is present. This means that the moisture content is higher than 100% in a living tree. During this state water is stored in cells and vessels (free water) but also in cell walls (bound water) that have expanded due to absorbed water.

If a tree is cut into pieces, the moisture content starts to decrease immediately; see Fig. 2.

At first free water is moved to the wood surface by capillary forces where it is evaporated into the atmosphere. Due to the evaporation process the surface temperature is decreased, and heat must be transferred from the environment in order to maintain the drying of the wood.

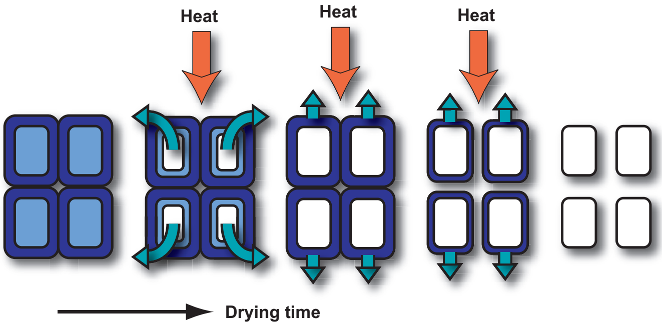

Fig. 2. Wood-drying process. At first the cells are filled with water, but in the end no free water exists, and the absorbed water in cell walls is dried out until an equilibrium state with the surrounding environment is reached.

When all free water has been evaporated the bound water starts to evaporate as well. This state of the wood is known as the fiber saturation point (FSP) and it corresponds to a moisture content of about 25–30%, depending of type of wood. Since bound water is situated inside the cell walls, more energy is needed to evaporate it. Thus, the drying rate decreases and the wood shrinks. In the end of the drying process, the wood reaches an equilibrium state with its environment. The moisture content inside wood depends on temperature and humidity level of the environment. A typical value of the moisture content for dried wood is 12–15% [16-18].

3. Commercially available moisture meters

Handheld electric moisture meters are commonly used to measure the moisture content in wood. The measurement technique was developed in the late 1930’s, and today there exists a number of manufacturers that develop and sell handheld moisture meters for measuring, e.g., moisture in wood and concrete. Mainly, two different measurement principles exist: resistance and dielectric type moisture meters [19-21].

The resistance type of moisture meter measures the electric resistance in wood between two pins that are connected at the wood surface or inserted into the wood, with typical distances of centimeters between the pins. If the wood is dry it acts as an isolator, and the resistance is in the order of 10^5 MΩ. However, since water in wood contains ions, the resistance in wood decreases down to about 0.5 MΩ when the moisture content is close to the saturation point.

In order to measure the moisture content using the resistance principal, one has to know the type of wood and from what region it comes. It turns out that all species of wood have different resistance curves even for one type of wood that has grown at two different locations. Today, resistance curves for many species of wood are stored in the device and controlled by a microprocessor.

Although the resistance type of moisture meter is easy to produce and operate, precautions should be considered. At first this measurement method is intrusive. Secondly, the resistance curve for wood is affected by temperature. Thus, a temperature sensor is included in some of the meters. Other disadvantages are the limited measurement range and that the result depends on whether the pins are inserted in parallel or perpendicular to the wood fibers. The upper

(C) 2006 OSA

limit is set by the fact that above the fiber saturation point (about 25–30% moisture content), the resistance measurement data are not reliable. The lower limit (about 7% moisture content) depends on the difficulties to measure resistance in the order of 10^5 MΩ and above.

The dielectric type of moisture meter uses a nonintrusive measurement technique that measures the dielectric constant of the combined wood and water material. Since the dielectric constant for water is much higher than that of wood (by a factor of 25), the moisture content may be estimated. Anyway, each type of wood has its specific dielectric constant. Specific wood calibration data are stored in the device and controlled by a microprocessor. The dielectric moisture meter is known to have poor performance compared to the resistance type. However, it is commonly used for relative measurements. The surface electrodes are sensitive to other materials close to the surface and density fluctuations of the wood. The measurement range varies from 5% to about 25% moisture content.

4. Setup for diode laser spectroscopy on wood

We will now describe our spectroscopic setup for moisture studies. While measurements using a light transmission or backscattered geometry can be made with the GASMAS method, the former one was chosen because of its simplicity in terms of the optical arrangement and also regarding the signal interpretation. However, a backscattering geometry is attractive in terms of optical access and is also the only possible one for thick samples. Our setup is based on two almost identical arrangements that are run simultaneously. One setup is used for oxygen measurement while the second is used to measure water vapor (moisture) contents in the same piece of wood. A schematic drawing is shown in Fig. 3. The oxygen measurement setup is explained in more detail in Refs. [12]. However, in the present setup the photo multiplier tube (PMT) sensor is replaced by a silicon detector (Photovoltaic PIN-10DP from UDT) with an active surface of 100 mm^2.

The major difference between the oxygen and the water-vapor setup is the wavelength of the diode lasers used. For the oxygen detection a diode laser (Sharp LT031MDO) with a maximum output power of 7 mW, operating at 2 mW at the sample, is used to scan across the R7R7 oxygen line at 761.003 nm (vacuum wavelength). The scan range was typically 20 GHz (0.04 nm). A near-IR Fabry–Pérot diode laser (Specdilas F760) with a maximum output of 200 mW at 980 nm, and efficiently operating at 40 mW at the sample, is used as a spectroscopic light source to detect the water-vapor line (vibration; (000)→ (121), rotation; J”=5→ J’=4, K_a”=0→ K_a’=0, K_c”=5→ K_c’=4) at 978.509 nm (vacuum wavelength). The scan range was typically 35 GHz (0.11 nm).

The basis for the measurement is that the wavelength of the laser light is scanned across the absorption lines by sweeping the operating current of the lasers by the use of a 4 Hz saw tooth ramp. To achieve wavelength modulation spectroscopy (WMS) with lock-in detection, the operating current is also modulated by a sinusoidal wave at 9 kHz with a modulation index of about 1 in both cases. The laser light is focused into a fiber that guides the light to the sample. The water vapor setup uses the same type of silicon detector as the one used for oxygen. The output from each detector is split into two signal branches. One, directly connected to an oscilloscope, is referred to as the direct signal, while the second part goes via the lock-in amplifier before being connected to another channel of the oscilloscope, and is referred to as the WMS signal. The data are stored and analyzed using a computer. Typical readings for oxygen and water vapor are shown in the lower part of Fig. 3. The peak-to-peak value of the WMS signal is measured and normalized by dividing with the direct signal value at the corresponding wavelength in order to determine the fractional absorption during the drying process.

As discussed for instance in [10], a method called standard addition, well known in analytical chemistry, is used in order to calibrate a measured normalized WMS signal and transfer it to a

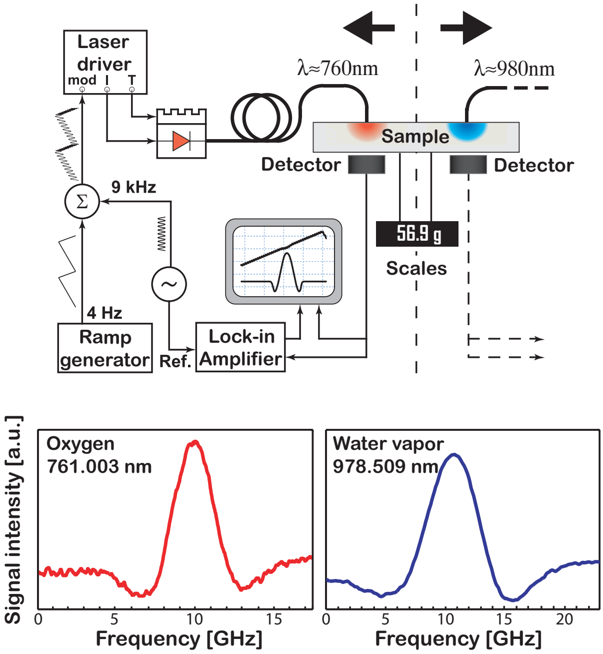

Fig. 3. Schematic drawing of the spectroscopic setup of similar diode laser spectrometers for oxygen (left) and water vapor (right). Typical readings of the WMS signals for oxygen and water vapor in wood are shown in the lower part. The half widths of the signals are of the order of a few GHz in both cases. The half widths at half maximum (HWHM) of the absorption lines are, according to HITRAN, 1.61 GHz for oxygen and 2.72 GHz for water vapor at standard conditions.

more meaningful quantity—a so-called equivalent mean path, L_{eq}. It is determined by adding free air path lengths in the collimated laser beam before it enters the test sample. The equivalent mean path length corresponds to the distance that the light has to travel in ambient air in order to obtain the same signal as in the sample $L_{eq} \cdot c_{air} = \langle L_{sample} \rangle \cdot c_{sample}$, where c_{air} corresponds to the gas concentration in air, $\langle L_{sample} \rangle$ to the mean path length in the sample, and c_{sample} to the gas concentration in the sample. The calibration procedure is carried out by removing the wood sample and placing an optical attenuation filter on top of the detector. A collimator lens was placed at the end of the fiber. The normalized WMS signal was measured for different added air distances between the collimator lens and the filter. A linear function between the normalized WMS signal and added air distance is obtained. This function can then be used to estimate the L_{eq}. The calibrations are done once for each laser, and these calibration curves are used for all experiments. Precautions were taken when the water-vapor WMS signal was calibrated. The room temperature and relative humidity were measured by a hygrometer (Testo 608-H1) sensor and the partial pressure of the water vapor was estimated.

An analog lab scale (Libror EB-280, Shimadzu) is used to measure the weight of the wood in order to calculate the average moisture content during the drying process. At the end of the drying process a commercial convection oven was used to dry the wood at 110^{o}C in order to determine the truly dry weight.

5. Measurements and results

Uniform balsa wood pieces of 10 cm width, 30 cm length, and 0.8 cm thickness derived from the same batch were used in the measurements. The figures of balsa wood shown in Fig. 1 are from the wood samples studied. The wood was kept under water for typically three days and was studied directly after being exposed to the ambient laboratory air. The drying could be followed by reading off the analog scales, onto which the piece of wood was attached.

The results of conventional measurements of the moisture contents during the drying process are shown in Fig. 4, with the instrument applied in a straightforward manner. The weight reading from the scale, expressed as moisture content, is plotted together with data from the resistance and the dielectric moisture meters. It can clearly be seen that the results from the meters poorly describe the real drying process monitored by the scale for moisture content above the FSP. Obviously there is a need for improved measurement techniques for moisture.

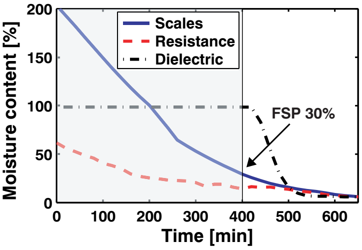

Fig. 4. Measured moisture contents during the drying process of the sample. Curves indicate moisture content (blue curve) when measured by logging the weight of the sample, (red dashed curve) when measured by using a resistance moisture meter (Protimeter Timbermaster), and (black dash-dotted curve) when measured with a dielelectric moisture meter (MC-300W, Exotek). The fiber saturation point (FSP) is indicated in the figure (moisture content=30%).

The temperature of the wood surface was also monitored with thermocouples. The measurements were performed on a different sample. In this case the sample had been soaked in water for a longer time than the case when recording the data in Fig. 4. Typical results are shown in Fig. 5(a), where the blue curve shows a weight loss to a stable value of about 33% of the original wet weight, the dry material plateau being reached after about 1200 min. The drying process is, as expected, accompanied by a lowering of the temperature. During the first 600 min the temperature was stable at 9°C below the ambient value (25°C), which was gradually reached after 1200 min. Local possible heating, due to laser beams, was found to be very small. This results in a marginal increase of water vapor pressure.

Since gaseous water (water vapor) is measured in our study it is interesting to consider the vapor pressure of water as a function of the temperature. The corresponding curve is given in Fig. 5(b). It shows the partial pressure of the vapor in a closed volume containing liquid water at the given temperature. We note that the vapor pressure is increasing by a factor 1.8 when the temperature rises from 16°C to 25°C. We also note that water vapor at ambient temperature only accounts for a small percentage of the mass in normal air. Frequently ambient air does not feature the full water vapor pressure corresponding to the ambient temperature. If there is no air movement and large amounts of distributed liquid water the relative humidity would be 100%, like in a sealed-off volume. Due to the exchange of dryer air, the effective humidity becomes less. Readings of 20–40% relative humidity (percentage of the fully saturated value at the given temperature) are common in indoor environments at wintertime in Sweden.

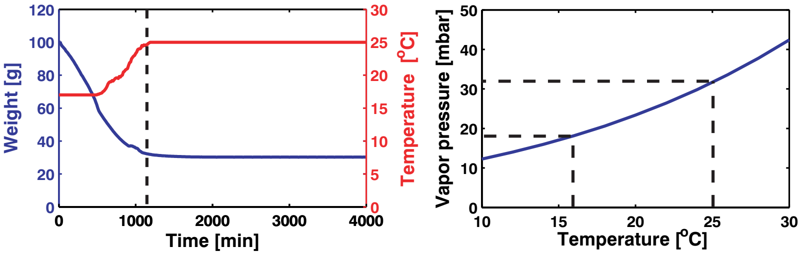

(a) (b)

Fig. 5. (a) Measured temperature at the surface of the sample and measured weight during the drying process. (b) Vapor pressure as a function of the temperature [22].

We will now present data from our near-IR laser spectroscopic measurements. We performed simultaneous (molecular) water vapor and molecular oxygen measurements at points separated by about 10 cm on the piece of wood, assuming the material to be laterally uniform. These data were recorded simultaneously as the temperature and weight data in Fig. 5(a). A small air space was left between the sample and the detectors to allow water to homogeneously diffuse out of the sample. The setup is shown in Fig. 3. Oxygen does not have a liquid phase in the temperature range studied (it liquifies at 90K). In contrast, water has a liquid phase as well as a gaseous phase, and the vapor pressure is, as just discussed, temperature dependent.

In understanding the dynamics of wood drying it is useful to first consider the behavior of the molecular oxygen L_{eq} during the drying, which as mentioned before is proportional to the normalized WMS signal. In Fig. 6(a) the fractional oxygen absorption is plotted in red. The signal is proportional to the oxygen concentration times the effective distance travelled through the gas-filled pores, the latter factor being strongly sensitive to the degree of light scattering in the material. The signal is plotted as an equivalent path length in normal air containing 21% oxygen, as previously discussed. It should be noted that the effective path length through the material, useful in a standard Beer–Lambert law view, can be expected to change during the drying process. One aspect is that while liquid water is an index-matching fluid reducing the scattering when the pores are water filled, the scattering should increase when the air-filled inhomogeneities develop during the drying process. We notice that the oxygen signal increases from a non-zero value (there are air-filled pores even in the very wet wood) by a factor of about 8 to then stay constant at the high value, reached at about 1300 min when all the liquid water is driven out and all the pores are instead gas filled.

The simultaneously measured gaseous water signal is included in blue in Fig. 6(a). Again, the curve starts at a non-zero level (corresponding to the presence of gas-filled pores with saturated water vapor also in the very wet wood). The signal increases to a maximum at about 1200 min, reached slightly before the oxygen signal maximum. At the same time as the oxygen signal stays constant the water vapor signal gradually falls off to a steady value of about 25% of the maximum value. This could be interpreted in the following way: Around 1200 min the pores are almost void of water, as indicated by the dashed line in Fig. 5(a), but there is still a sufficient amount of water to sustain the full saturated water vapor partial pressure. Shortly thereafter, this is no longer the case, and the pores with constant volumes and situated in a material with constant scattering properties gradually lose the saturated vapor pressure and gradually attain the relative humidity value of the laboratory, which for the measurement case with an ambient temperature of 25°C was separately measured to 24% with a hygrometer. This is in good agreement with the measured signal falloff to about 25% of the value with

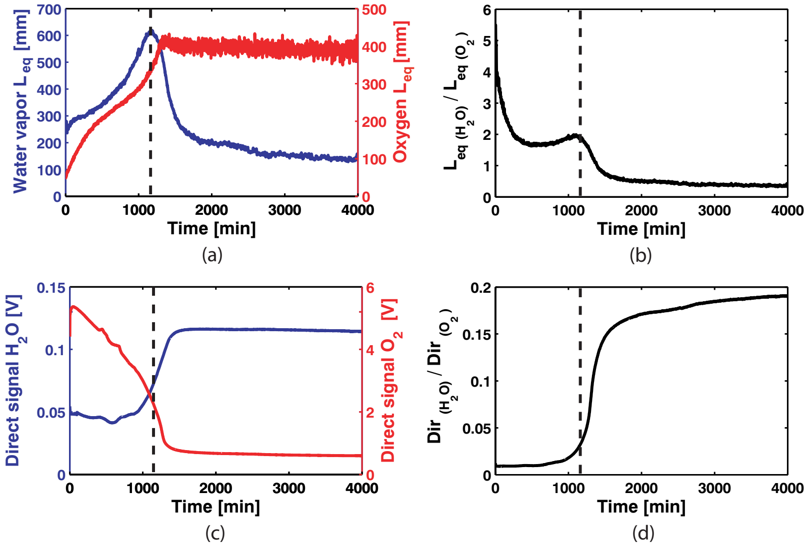

Fig. 6. (a) Equivalent mean path length for water vapor and oxygen during the drying process of balsa. (b) Ratio between detected equivalent mean path length for water vapor and oxygen. (c) Direct signals for water vapor and oxygen during the drying process of balsa. (d) Ratio between detected direct signal for water vapor and oxygen.

full saturation. The displacement of about 100 min between the reaching of the maximum for oxygen and water vapor is compatible with the typical times for air diffusion in balsa wood measured separately [11].

While the above observations are readily interpreted, the detailed behavior of the water vapor signal during the drying is due to many different influences. Let us first state that if two permanent gases such as nitrogen and oxygen had been studied, the same type of behavior (apart from small effects of different diffusivity), i.e., a constant ratio between the signals during the drying phase, would have been expected. This statement has as a prerequisite that the two gases absorb at close-lying wavelengths so that the scattering properties are similar. In contrast to this, the ratio between the water vapor signal and the oxygen signal is strongly varying during the drying process, as can be seen in Fig. 6(b). The temperature increase in the time span 400–1200 min (see Fig. 5, red curve) leads to an acceleration in the water-vapor signal level beyond that for oxygen, for which the concentration is marginally reduced (a few percent) by the temperature increase. This may explain the tendency of increase of the ratio curve toward the end of the drying period. The high initial value in the ratio curve may be related to the time constant for oxygen diffusion through the material also discussed with regard to the different times for the two gases to reach the maximum WMS signal. It should be noted that in the drying up of a pore, the walls of the cavity will be uniformly covered by liquid water due to the surface tension. This may impair the transport of oxygen through the film while the water vapor can freely build up in the central microbubble of the pore, see Fig. 2. Effects of this kind may also influence the balance between the two gases in the cavities during the drying process. As noted, when everything is dry, conditions are static with regard to scattering and the behavior of both curves is clearly understood as discussed above.

So far we have been discussing the fractional absorptive imprint of the gas (intensity on the absorption line compared to the intensity off the line), which is decisive for concentration measurements based on the Beer–Lambert law. However, it is also interesting to study the dynamics of the total light (off the narrow absorptive features) at the two wavelengths used (980 nm and 760 nm, respectively). Such measurements were performed and the results are shown in Figs. 6(c)–(d) and in Fig. 7. The curves in Fig. 6(c) show a very different behavior with the water signal increasing in the final phase of drying from an almost constant initial level to a final value about 2.5 times higher. On the contrary, the 760 nm signal starts at a high level and, with acceleration, reaches a steady value about 5 times lower when the wood is dry. The ratio of detected direct signal for water and oxygen is shown in Fig. 6(d). In explaining these phenomena it is important to note that liquid water has quite a strong broadband absorption around 980 nm, as detailed in Fig. 7(a) and already noted in the Introduction. We note that this absorption influences the on- and off-resonance frequencies for the narrowband water-vapor signals alike, and does not influence the fractional absorption determining the water-vapor concentration. However, the laser beam is clearly attenuated by the water contents. The initial flat response of the 980 nm curve for the drying wood can be interpreted to mean that the reduction of water during the initial drying is compensated by the increased light path length due to the developing gas-filled pores. Finally, the absorbing liquid water disappears and the detected light settles on a level determined by the attenuation of the light-scattering dry wood.

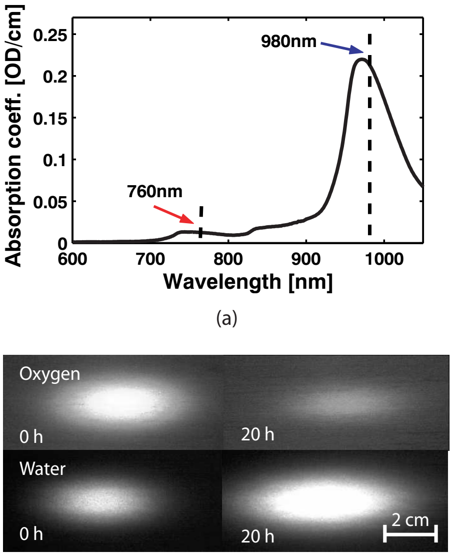

(b)

Fig. 7. (a) Absorption spectrum of 1 cm pure water reproduced from the measurements by Matcher *et al.* [23]. (b) Images of the sample on the detection side for oxygen (760 nm) and water vapor (980 nm) during its drying process.

The 760 nm light is off-resonance from the broad liquid water absorption as shown in Fig. 7(a), and bulk absorption due to the water is small, in strong contrast to the case for 980 nm. The high initial light level can be seen owing to the index-matching effect of the water in the pores, which reduces the lateral scattering and allows more light to reach the detector. As the wood dries the scattering increases and less and less light reaches the detector. Steady-state conditions then prevail in the dry wood. The significant change in the light levels, as well as the normalized WMS signals for both wavelengths when the wood is nearly dry can be interpreted as the final dry-up of the finest compartments long after the tube structure that contained most of the water has dried up. The scattering increases a lot due to the appearance of small pores of size comparable with the wavelength. This reduces the detected 760 nm light level. Also the 980 nm light level changes due to the continued loss of bulk water absorption.

The dynamics of the transmitted light levels at the two wavelengths could also be studied using near-IR imaging of the transmitted light using standard Web cameras (Q-Tec 100). The transmitted light blobs at 980 nm and 760 nm are shown in Fig. 7(b) for fully wet and fully dry (waiting 20 h = 1200 min) conditions. The intensity in the center of the blobs (where the detector is situated) is related to the intensities given in Fig. 6(c); the 760 nm signal is greatly reduced and the 980 nm is increased. The final levels (20 h) correspond to an attenuation by the sample of the incident light of about 80% for the 980 nm signal and 99.95% for the 760 nm signal. These attenuations suggest that the wood sample thicknesses accessible in transmission measurements cannot be considerably larger than 1 cm for most wood types. For thicker samples the backscattering geometry is still applicable. From recordings, such as the ones shown in Fig. 7(b), information of the spatial distribution can also be extracted and compared with theory [7]. However, a detailed analysis of the spatial distribution is outside the scope of the present paper.

6. Conclusions and discussion

Removing moisture from materials is of major importance in fields as diverse as industrial processing, handling of construction materials, and preparation of agricultural products. The origin of excess water is frequently connected to material porosity. Optical measurement techniques are attractive since they are nonintrusive and frequently deliver data in real time. However, quantitative absorption spectroscopy is hampered by the strong scattering in inhomogeneous materials, making the Beer–Lambert law not directly applicable. In the present paper we have demonstrated the application of the GASMAS technique applied in transmission for the monitoring of water vapor in wood, using corresponding molecular oxygen measurements as a reference. The wavelengths used for the free gas monitoring, 980 nm and 760 nm, are also on- and off-resonant for a broad liquid water absorption feature, and thus information of the bulk water is also obtained. The signal intensities observed can mostly be interpreted as the result of the interplay between specific absorption and scattering, both changing during the drying process. In particular, the time when all the free water has evaporated from the wood can be readily identified by a steep falloff in the water vapor signal accompanied by the reaching of a high-level plateau in the molecular oxygen signal. The ratio between these signals, being dimensionless and largely independent of scattering, shows in particular the arrival at a fully dry sample. This situation is also identified in the differential optical absorption signal for liquid water, with a sharp increase of an order of a magnitude in the ratio of the (broadband) signal intensities at 980 nm and 760 nm.

It is thus clear that optical spectroscopy can be a valuable tool for the practical monitoring of drying processes while also yielding additional information on specifics of drying. For the practical application of the method, measurements in back-scattering geometry (as already applied in our sinusitis monitoring [15]) is of great interest. In order to further elucidate the interplay between scattering and absorption, time-resolved measurements of the photon history in the wood for the two wavelengths would provide independent information on the scattering of the material and the liquid water contents. Such measurements can be performed using white light [6,9], capturing the full spectrum, or employing a number of pulsed diode lasers selected at appropriate wavelengths [24].

(C) 2006 OSA

Acknowledgement

The authors thank Rita Wallén from the Department of Cell and Organism Biology of Lund University for her help with the microscope pictures. We also acknowledge useful discussions with Lars-Olof Nilsson from the Division of Building Materials of the Lund Institute of Technology.

This work was supported by the Swedish Research Council and the Knut and Alice Wallenberg Foundation.

PAPER IX

Fluorescence monitoring of a topically applied liposomal Temoporfin formulation and photodynamic therapy of non-pigmented skin malignancies

N. Bendsoe, L. Persson, A. Johansson, J. Axelsson, J. Svensson, S. Gräfe, T. Trebst, S. Andersson-Engels, S. Svanberg, and K. Svanberg.

Journal of Environmental Pathology, Toxicology and Oncology **26**, 117–126 (2007).

Journal of Environmental Pathology, Toxicology, and Oncology, 26(2)117–126 (2007)

Fluorescence Monitoring of a Topically Applied Liposomal Temoporfin Formulation and Photodynamic Therapy of Nonpigmented Skin Malignancies

Niels Bendsoe,[1] Linda Persson,[2] Ann Johansson,[2]
Johan Axelsson,[2] Jenny Svensson,[2] Susanna Gräfe,[3]
Tilmann Trebst,[3] Stefan Andersson-Engels,[2]
*Sune Svanberg,[2] & Katarina Svanberg[4,]**

[1]Department of Dermatology, Lund University Hospital, Lund, Sweden; [2]Department of Physics, Lund University, Lund, Sweden; [3]Research & Development, Biolitec AG, Jena, Germany; [4]Department of Oncology, Lund University Hospital, SE-221 85 Lund, Sweden
****Corresponding author***. E-mail: Katarina.Svanberg@onk.lu.se

---

Meso-tetra(hydroxyphenyl)chlorin (mTHPC) (INN: Temoporfin) is a potent photodynamically active substance in clinical use today. Usually, the substance is given systemically and a known drawback with this administration route is a prolonged skin light sensitization. For the first time to our knowledge, a liposomal Temoporfin gel formulation for topical application was studied in connection with photodynamic therapy (PDT) of nonpigmented skin malignancies in humans. Intervals of 4 hr between drug administration and light irradiation were used. Sensitizer distribution within tumor and surrounding normal skin was investigated by means of point monitoring and imaging fluorescence spectroscopy before, during, and after PDT, showing high tumor selectivity. Furthermore, the bleaching of Temoporfin was studied during the PDT procedure by monitoring the fluorescence following excitation by using a therapeutic light. A 30–35% light-induced photometabolization was shown. No pain occurred during or after treatment. It was also observed that the treated area did not show any swollen tissue or reddening, as is often seen in PDT using topical δ-aminolevulinic acid. On controlling the patients one week after treatment, healing progress was observed in several patients and no complications were registered.

KEY WORDS: mTHPC, PDT, basal cell carcinoma, fluorescence, bleaching, spectroscopic monitoring, Temoporfin topically

0731-8898/06/$35.00 © 2007 by Begell House, Inc.

Introduction

This paper presents, to our knowledge, the first use of a new photosensitizer, a liposomal Temoporfin gel formulation, for topical application in humans. Photodynamic therapy (PDT) is a modality for local treatment of cancer and relies on a photosensitizing agent being activated by light at an appropriate wavelength, usually within the red wavelength region to optimize light penetration within tissue.[1] Many of the sensitizers are selectively located in malignant cells due to a variety of biological reasons[2] and therefore selectivity in the therapy is achieved. Provided the simultaneous presence of sensitizer and oxygen, a cytotoxic reaction can be photochemically induced, causing selective cell destruction. The PDT outcome is governed by a combination of the effect of direct cell kill and induction of apoptosis,[3] vascular damage,[4] and an elicited immune response.[5]

The majority of photosensitizers are administered systemically, which causes an unwanted side effect of skin sensitization. In PDT of certain types of skin abnormalities, topical application of a sensitizer is preferable in order not to cause general skin sensitization. Topical administration of δ-aminolevulinic acid (ALA) in combination with illumination from a laser or a light-emitting diode with light doses in the range of 35 and 200 J/cm^2 has been successfully used for treatment of nonmelanoma skin malignancies over the past decades.[6,7] ALA is often supplied in a cream at a concentration of 20%, and application times range between three and six hours.[8] During this time period, the ALA molecules diffuse into the tissue, followed by the synthesis of protoporphyrin IX (PPIX), which is the photodynamically active metabolite.[2] Because of an increased permeability of the ALA molecules through the damaged epidermis of many cutaneous tumors and differences in the enzymatic activity, the accumulation of PPIX often displays a significant selectivity between normal and malignant tissue for shorter application times up to about three to six hours.[2] The sensitizer distribution can easily be monitored via the characteristic PPIX fluorescence within the red wavelength region, thus making optical methods highly desirable as noninvasive tools for sensitizer monitoring.

For superficial basal cell carcinomas (sBCC), PDT following topical application of ALA has led to cure rates (CRs) of 79–100%.[6] Although, for nodular lesions, the reported CRs are often about 50–70%,[7] a fact that has been partly explained by the limited penetration (1–3mm) of the hydrophilic ALA molecules. A further drawback of ALA-mediated PDT is skin sensation, such as itching and sometimes pain reported in many trials.[9,10] ALA-PDT also induces immediate posttherapy tissue reactions with swollen, reddening, and oozing skin.

Due to the lipophilic character of ALA esters, these derivatives are expected to show better biological availability and tissue penetration than ALA. Peng et al. reported on a highly selective and homogeneous sensitizer distribution following topical administration of methyl δ-aminolaevulinate, Metvix®.[11] A high tumor selectivity was observed by means of PPIX fluorescence both in animal skin tumor models and in human basal cell carcinomas (BCCs).[12,13] On the other hand, as the PPIX molecule is activated at slightly shorter wavelengths than many other PDT agents, the light absorption of hemoglobin limits the light penetration and treatment depth to approximately a few millimeters.[14] Furthermore, the PPIX molecule itself presents some shortcomings in terms of the localization of the substance within the tissue,[15] and the relatively low extinction coefficient of this sensitizer.[16] These factors might limit the treatment outcome irrespective of which kind of ALA is used.[6,17]

Meso-tetra(hydroxyphenyl)chlorin (mTHPC) (INN: Temoporfin) has been reported as one of the most efficient sensitizers, since relatively small drug and light doses are required in order to achieve treatment response.[18] Another advantage with Temoporfin is the wavelength of the absorption maximum at 652 nm as compared to 635 nm for ALA, resulting in an enhanced light penetration. Systemically administered Temoporfin in ethanolic formulation, Foscan®, has been successfully used for PDT of head and neck malignancies,[19] prostate,[20] and for BCCs.[21] A major drawback utilizing systemic administration of Temoporfin is the prolonged photosensitivity, subjecting patients to subdued light conditions for several weeks following sensitizer administration. In addition, due to the hydrophobic character of the mTHPC molecules, it is practically insoluble in aqueous media. Following systemic administration of the ethanolic formulation, the sensitizer therefore forms aggregates, leading to limited transportation of the sensitizer within biological media as well as poor tumor selectivity and PDT efficacy.[22–24] The above factors can also lead to an intense inflammation at the injection site.[21]

To overcome the problem of the extended photosensitization associated with systemic administration of Temoporfin, Gupta et al. have reported on PDT combined with topical mTHPC administration for treatment of Bowen's disease and BCCs.[25] In this study, the CR was 32% at the two month follow-up. The authors suggested that the formulation of Temoporfin they used was a limiting factor for the treatment outcome.

Previously, our group has reported on sensitizer distribution studies following topical administration of a novel liposomal formulation of Temoporfin in a murine skin tumor model.[26] For Temoporfin gel application times of four and six hours, the chemical extraction from different organs revealed a selective accumulation of the substance within tumor tissue. The average sensitizer concentration within lesions was 6.0 ng/mg, whereas no detectable levels of generalized photosensitivity were shown. Within the study, the strongly fluorescing and absorbing characteristics of Temoporfin were also used for monitoring the drug distribution by fluorescence imaging and absorption spectroscopy. These noninvasive methods confirmed the selective sensitizer distribution and indicated sensitizer penetration depths of 3–4 mm within the investigated tumors.

Following these initial promising results on the animal skin tumor model, the same liposomal Temoporfin formulation is introduced for nonpigmented skin malignancies in patients. In this study, we include spectroscopic measurements in order to monitor the uptake of the liposomal Temoporfin formulation in connection with PDT using laser light at 652 nm. By incorporating Temoporfin in a liposomal formulation, the substance is made more suitable and transport within biological media is facilitated. The liposome encapsulated Temoporfin is supplied in a water-based heat-setting gel, rendering application times of several hours possible. Fluorescence spectroscopy data are presented as a tool to study sensitizer distribution and treatment-induced photobleaching. Clinical parameters, such as skin sensations during the treatment and other local skin reactions during the first week after treatment, are monitored.

Material and Methods

Sensitizer

The sensitizer compound is comprised of a liposomal formulation of mTHPC (Temoporfin) in a thermogel matrix with a sensitizer concentration of 0.5 mg mTHPC/ml gel (Biolitec AG, Jena, Germany). The liposome formulation is based on dipalmitoylphosphatidylcholine (DPPC), monosaccharide, water, and polyoxyehthylene polyoxypropylene block copolymers encapsulating mTHPC.[27] The mTHPC gel is in a liquid phase at the storage temperature of 4°C, but forms a highly viscous gel when heated by the skin to temperatures above 26°C. The thermothickening thus aids in increasing the retention time of the applied gel and transfer of the sensitizer into the tissue. No penetration enhancers are added to the Temoporfin gel.

Patients

The Temoporfin gel was used for topical PDT of 35 lesions in 10 consecutive patients in the ambulatory outpatient ward. The histopathology showed basal cell carcinoma for 29 and squamous cell carcinoma for the remaining 6 lesions. The gel was applied on the visible lesion and an additional margin of about 10 mm on the surrounding skin. Tegaderm® was used to cover the area (Fig. 1A). Four hours later, the gel was removed and the site was carefully cleaned with alcohol. PDT was performed by irradiating lesions with diode laser light at 652 nm (Ceralas, Bonn, Germany) at a light dose of 20 J/cm². Two tumors in one patient were treated with a different light doses; one with 40 J/cm² and one with 60 J/cm². The optical fiber used for light delivery was equipped with a microlens, giving a uniform irradiance adjusted to 100 mW/cm^2.

Optical Measurements

Point-monitoring fluorescence spectroscopy measurements were performed pre- and post-PDT to study both the Temoporfin-related signal and tissue autofluorescence. Several sites within and in close proximity to the lesions were studied. The point-monitoring fluorosensor utilizes a nitrogen laser pumping a dye laser emitting pulsed excitation light at 405 nm. The light is guided to the tissue through an optical fiber with a core diameter of 600 μm. The induced fluorescence light is transmitted through the same fiber back to a detection unit. This unit incorporates an RG435 cutoff filter, a spectrometer, and a cooled intensified CCD recording fluorescence spectra in the range from 450 to 800 nm.[28]

In addition, a fluorescence imaging system was used to monitor the whole treatment site, including the surrounding normal skin margin prior to, during, and after PDT. Fluorescence images were collected by a CCD camera (C4742-80-12AG, Hamamatsu) equipped with a liquid crystal tunable filter (LCTF VIS 20-35, Varispec) and a zoom objective lens (50 mm focal length and f/1.8, Nikon). For the measurements performed pre- and post-PDT, the excitation light source consisted of 12 light emitting diodes with optical output centered at 405 nm, and the fluorescence was imaged at 652 nm.

Measurements performed in order to study the sensitizer photobleaching during PDT utilized the treatment light at 652 nm to induce Temoporfin fluorescence, which was detected at 720 nm. In each treatment session, a total of 60 fluorescence images were collected at 3 s intervals in order to follow the photobleaching of the sensitizer. For evaluation of the Temoporfin bleaching kinetics, a subset of 12 images, separated by approximately 16 s, were extracted from the data set. In each image, four regions with an area of about 0.2 mm^2 were selected, and the mean of the intensity within these regions was calculated. This procedure was performed for the same four regions in the consecutive images. By normalizing the mean intensity for each image to the mean intensity at the start of the irradiation, a normalized temporal profile of the fluorescence intensity was calculated.

Results and Discussion

The use and handling of the novel liposomal Temoporfin gel was very convenient since the gel was fluid only at the low storage temperature in the refrigerator. As soon as the gel was applied on the skin of the patients, it became more viscous and was not as easily smeared off the surface. Despite this, a covering film was placed over the area in order to keep the gel in place during the four hours before PDT illumination (Fig. 1A). In contrast to the use of the PPIX-precursor ALA, this liposomal Temoporfin formulation is not dependent on an enzymatic transformation. The application time is only for the purpose of letting the substance diffuse into the tumor tissue. The use of a four hour drug-light interval was motivated by the results from a

FIGURE 1. (a) A picture of a Temoporfin vial together with Tegaderm® dressing and a light protecting cover. **(b)** and **(c)** Digital images from a tumor prior to the PDT procedure and one week after, respectively. Remaining scar structures are due to previous non-PDT treatments.

previous study in a murine skin tumor model.[26] Unlike ALA, mTHPC is a strongly fluorescing substance. Any Temoporfin gel remaining on the skin surface will thus cause a false non-tissue-uptake-related fluorescence signal. Within this study, a careful cleansing of the skin was of importance in order to avoid influence by superficially located Temoporfin gel.

Further comparison to ALA and its esters shows an advantage for Temoporfin-PDT in that it did not cause any discomfort to the patients. Previous work has reported that a majority of the patients experience painful sensations in the skin during ALA-PDT.[9] Our own clinical experience includes rare cases of patients feeling inclined to interrupt the ALA-PDT and not accepting another PDT treatment using the same type of sensitizer. Different methods, such as spraying water or using a fan on the area treated, have been reported to relieve the ALA-PDT-related pain. However, other studies show less discomfort where only 25% of the patients experienced some kind of skin sensation and very few patients felt any pain.[10] In the present Temoporfin study, none of the treated patients spontaneously complained about any pain. Also, on interviewing all 10 patients concerning their sensations during the treatment, no one reported on any pain, itching, or stinging, and all patients could finish the treatments without any complaints. As mentioned above, the PDT light dose was generally 20 J/cm^2 delivered at 100 mW/cm^2. This rendered the treatment time acceptably short (approximately 200 s), an attractive feature, especially for elderly patients. This light dose resulted in only a partial bleaching of the Temoporfin as monitored by the fluorescence levels. Due to this fact, we increased the light dosage up to 40–60 J/ cm^2 for a few treatment procedures, as mentioned above. This increased light dose also did not result in any inconvenience for the patient. All the patients, treated with the novel Temoporfin formulation and PDT, were reviewed in order to record immediate post-PDT reactions (Figs. 1B and 1C). In the case of ALA-PDT, it is normal to see swollen tissue and some reddening, oozing, and formation of small pustules in the area where ALA is applied. No such reactions were seen in the patients, who had undergone Temoporfin-PDT. It was also noted that tumor sites oozing or bleeding before the Temoporfin-PDT seemed to dry out during the first week following the treatment. Therefore, no posttreatment dressings or other medical procedures were necessary.

Fluorescence spectroscopy, both in point-monitoring and imaging mode, was used to study Temoporfin distribution within the PDT target area Point-monitoring fluorescence spectra recorded in a scan over a tumor, tumor border, and surrounding normal skin margin out to 10 mm before and after PDT are shown in Fig. 2, together with a digital photo of the tumor. In the region outside the tumor, the spectra shown are the average of data recorded at 2, 5, and 10 mm outside the visible boundary of the tumor. For the center of the tumor the spectra displayed are the average of three recorded spectra, whereas fluorescence spectra for the tumor border represent single acquisitions. The Temoporfin fluorescence emission is clearly seen in the red part of the wavelength region, peaking at about 653 nm, and also a second broader peak at approximately 720 nm. Beside the drug-related fluorescence, the autofluorescence from the tissue itself, characterized by broad emission in the blue/green part of the wavelength region, is also seen. As known from earlier studies, the autofluorescence shows very low intensity within the tumor area as well as in the tumor border zones.[8] It can be noted that in one of the areas outside the visible border of the tumor, the autofluorescence is very low and the Temoporfin signal high (the rightmost spectrum), which may well represent an outstretching part of the tumor. Even if it is not histopathologically proven, it is a clear indication to also include this part in the PDT-irradiated field to enhance the radicality of the treatment. After PDT, the substance-related emission is shown with a decreased intensity, which is a sign of photobleaching of the drug during the PDT procedure.

By using both the Temoporfin-related signal and the tissue autofluorescence, a diagnosis-related contrast function, C_{diag}, can be calculated (Fig. 3A) as

$$C_{\mathrm{diag}} = \frac{\mathrm{mTHPC}_{\lambda[640\text{-}690]} - \mathrm{Auto}_{\lambda[640\text{-}690]}}{\mathrm{Auto}_{\lambda[470\text{-}520]}}$$

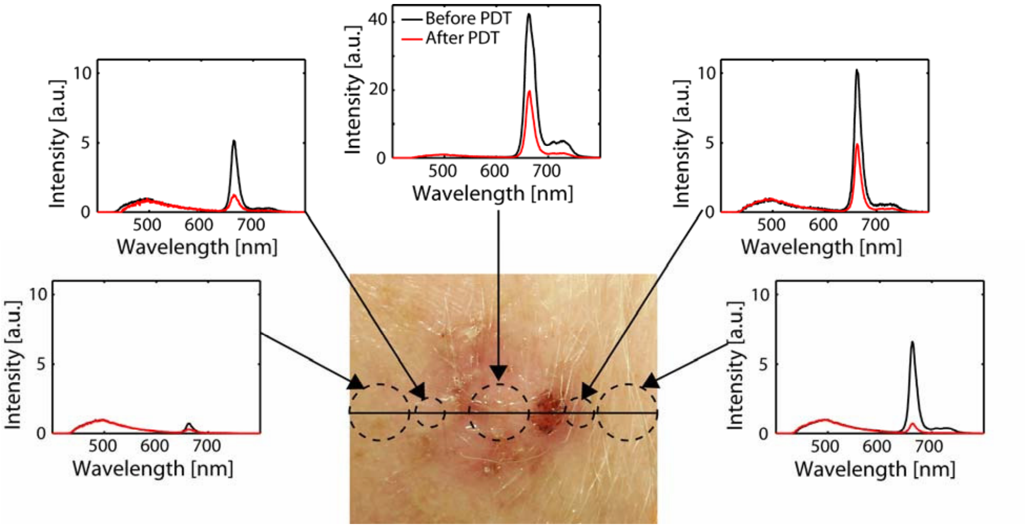

FIGURE 2. Fluorescence spectra induced by 405 nm excitation recorded from outside the lesion, border of the lesion, and center of the lesion before and after the PDT procedure.

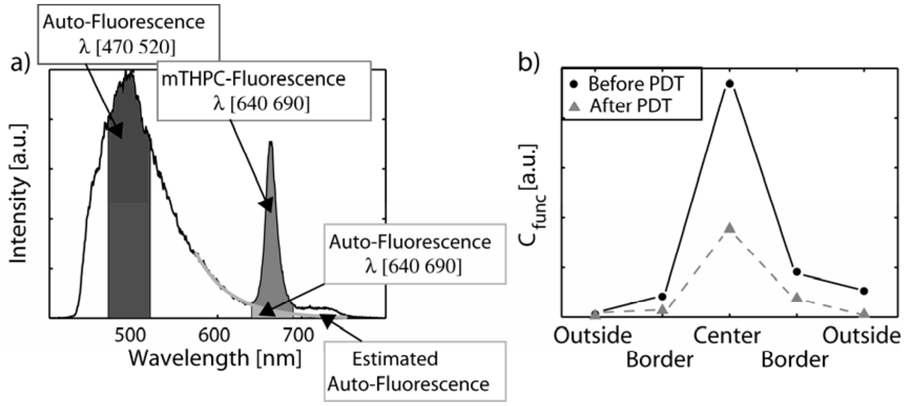

FIGURE 3. **(a)** Indications of the different areas used in the contrast function, C_{diag}. **(b)** The contrast function, C_{diag}, applied on spectra in Fig. 2 before and after PDT procedure. The data points are connected by lines for the guidance of the eye.

The function results in higher values in tumor, since the Temoporfin intensity is high and the autofluorescence is low compared to normal tissue (Fig. 2). This contrast function is slightly different from a contrast based only on the Temoporfin fluorescence amplitude without taking into account the tissue autofluorescence at this wavelength. Although the latter is perhaps more related to the sensitizer concentration and the PDT effect, C_{diag}, was employed in the present work. The values of this contrast function obtained before and after PDT for the tissue region in Fig. 2 are plotted in Fig. 3B. As can be seen, the contrast between tumor and manifest normal skin (the outermost left point) is very high. It can also be noted that the effect of bleaching due to PDT is substantial (about a factor of 2).

Typical fluorescence images of a tumor and surrounding skin following excitation at 405 nm with detection at 652 nm are shown in Fig. 4A. The images are monitored before and after the PDT procedure. The presented images are background subtracted, where the background was acquired without excitation light. For comparison, both images are normalized using the maximum intensity in the first image. It can be observed that the sensitizer distribution is heterogeneous within the tumor an effect that was observed in most of the tumors studied. Similar results were observed in the murine skin tumor model following administration of this liposome-encapsulated Temoprofin gel.[26] In that study, the increased penetration within lesions was ascribed to the absence of the *stratum corneum*, whereas an intact epidermis prevented normal skin from accumulating any detectable levels of the photosensitizer. Thus, the heterogeneous fluorescence signals observed within this study may reflect the status of the uppermost skin layers. A further explanation of the heterogeneous Temoporfin distribution might be the tumor growth pattern, since it is well known that BCCs grow in spots or patches with normal tissue intermixed within the tumor site, as illustrated in the photograph in Fig. 2.

Fluorescence spectra acquired with the point-monitoring setup are also presented before and after PDT (Fig. 4B). The spectra are normalized to the maximum of the autofluorescence from sur-

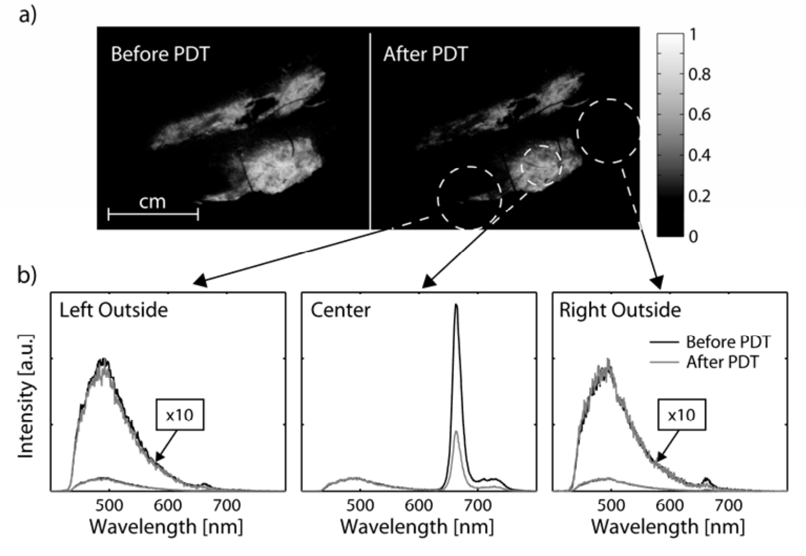

FIGURE 4. (a) Images of a tumor showing the fluorescence intensity at 652 nm for excitation at 405 nm before and after the PDT procedure, respectively. **(b)** The fluorescence spectra obtained in point monitoring for excitation at 405 nm from three different locations marked by circles; outside to the left and to the right of the visible tumor location, and inside the tumor area.

rounding skin between 470 and 520 nm. Since the Temoporfin signal shows a very low intensity in surrounding normal skin, the spectra are shown also with a tenfold magnification. A tumor demarcation based on the diagnosis-related contrast function, C_{diag}, of approximately 10:1 can be seen when comparing the tumor center spectrum with the two spectra from normal tissue outside the tumor. This is comparable to the contrast obtained for the majority of the tumors included in the study. Post-PDT, a decrease of the Temoporfin fluorescence in the center of the tumor as well as in the surrounding tissue can clearly be seen.

The laser light at 652 nm used for treatment also excites mTHPC fluorescence at 720 nm. Figure 5A shows the mean relative fluorescence intensity over time for ten representative tumors following excitation by the therapeutic laser light. The photodegradation of Temoporfin as monitored at 720 nm can clearly be seen. A photobleaching of about 30–35% is recorded after 200 s of therapeutic irradiation (20 J/cm^2), which concurs well with previously reported results for the photobleaching in mTHPC-sensitized spheroids.[29] Fluorescence images of a tumor are shown at three different time intervals during the PDT procedure (Fig. 5B); before, in the middle, and at the end of the session. These fluorescence images, detected at 720 nm following excitation by the therapeutic light at 652 nm, also illustrate the treatment-induced photobleaching. An apparent lower overall photobleaching can be observed following fluorescence excitation at 652 nm as compared to 405 nm excitation; see, for example, Figs. 4B and 5A. This effect might be explained by the different effective penetration depths of the two excitation wavelengths, i.e., violet light probes the superficial tissue regions where the therapeutic irradiation has efficiently bleached away most of the photosensitizer, whereas the red excitation wavelength also probes deeper into the tissue volume

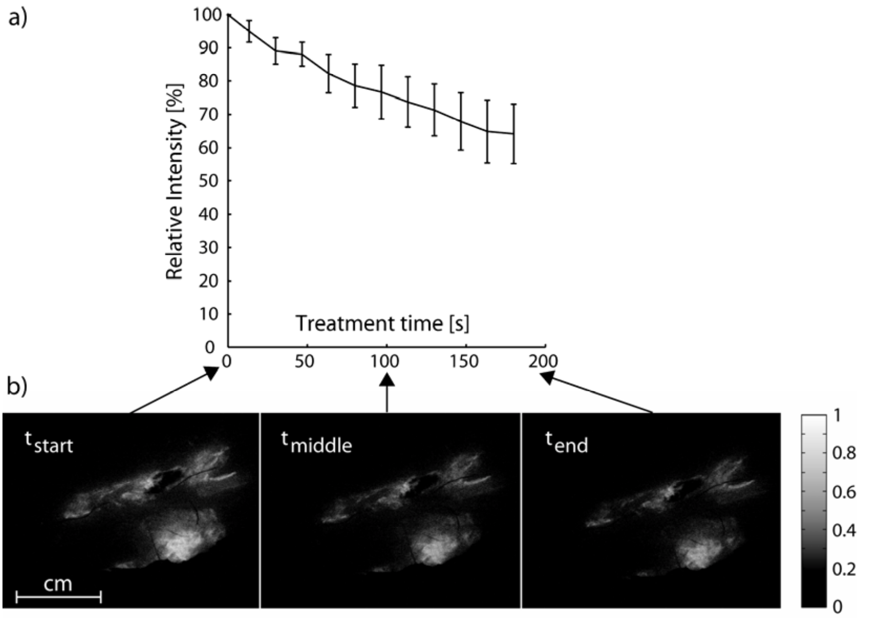

FIGURE 5. **(a)** Decrease of the normalized fluorescence intensity at 720 nm detected over time for ten tumors following excitation by the therapeutic radiation at 652 nm. Error bars represent ±1 SD. **(b)** Fluorescence images at 720 nm showing one of the tumors included in the data analysis after 0, 100, and 200 s of therapeutic irradiation, corresponding to 0, 10, and 20 J/cm^2.

where less bleaching has occurred due to the lower irradiance during treatment. These observations might suggest that sensitizer photobleaching as a parameter related to PDT outcome should be monitored utilizing the same excitation wavelength as for PDT induction whenever possible. Then a more representative tissue volume is probed.

Conclusions

In conclusion, we have reported a significant selectivity between tumor and surrounding skin at four hours following administration of liposome-encapsulated Temoporfin embedded into a thermosetting gel, constituting a novel Temoporfin formulation for topical use. The uptake of the substance was monitored by point-monitoring as well as imaging fluorescence spectroscopy. Fluorescence was induced either at 405 nm or by the treatment light at 652 nm. The bleaching of the sensitizer was estimated from the fluorescence levels by comparing the fluorescence images before, during, and after PDT. Furthermore, our initial results show that this new formulation is easily applicable due to its temperature-dependent viscosity, rendering the gel to firm after application onto the lesions. The light illumination is not connected with any treatment-related pain or other adverse reactions. As compared to ALA-PDT, no swollen tissue or oozing were noticed at the weekly follow-up. In cases where the tumor area was associated with a wound with or without bleeding, it was noted that these lesions seemed to dry up after a few days. After these promising initial results, further studies are needed in order to understand the penetration of the Temoporfin in skin following topical administration. Furthermore, studies for following long-term tumor response are being planned.

Acknowledgments

The economical support from the Swedish Research Council and the Knut and Alice Wallenberg Foundation is highly appreciated, as well as the valuable support from Stefan Spaniol at Biolitec, Bonn. The work was performed within the frameworks of the EU-BRIGHT Project No. IST-511-722-2003 and the EU project "Molecular imaging" LSHG-CT-2003-503259.

References

1. Dougherty TJ, Gomer CJ, Henderson BW, Jori G, Kessel D, Korbelik M, et al. Photodynamic therapy. J Natl Cancer Inst. 1998;90(12):889–905.
2. Peng Q, Berg K, Moan J, Kongshaug M, Nesland JM. 5-aminolevulinic acid-based photodynamic therapy: Principles and experimental research. Photochem Photobiol. 1997;65(2):235–51.
3. Almeida RD, Manadas BJ, Carvalho AP, Duarte CB. Intracellular signaling mechanisms in photodynamic therapy. Biochim Biophys Acta. 2004;1704(2):59–86.
4. Triesscheijn M, Ruevekamp M, Aalders M, Baas P, Stewart FA. Outcome of mTHPC mediated photodynamic therapy is primarily determined by the vascular response. Photochem Photobiol. 2005;81(5):1161–7.
5. van Duijnhoven FH, Aalbers RIJM, Rovers JP, Terpstra OT, Kuppen PJK. Immunological aspects of photodynamic therapy of liver tumors in a rat model for colorectal cancer. Photochem Photobiol. 2003;78(3):235–40.
6. Peng Q, Warloe T, Berg K, Moan J, Kongshaug M, Giercksky K-E, et al. 5-aminolevulinic acid-based photodynamic therapy: Clinical research and future challenges. Cancer. 1997;79:2282–308.
7. Svanberg K, Andersson T, Killander D, Wang I, Stenram U, Andersson-Engels S, et al. Photodynamic therapy of non-melanoma malignant tumours of the skin using topical δ-amino levulinic acid sensitization and laser irradiation. Br J Dermatol. 1994;130:743–51.
8. af Klinteberg C, Enejder AMK, Wang I, Andersson-Engels S, Svanberg S, Svanberg K. Kinetic fluorescence studies of 5-aminolaevulinic acid-induced protoporphyrin IX accumulation in basal cell carcinomas. J Photochem Photobiol B. 1999;49(2-3):120–8.
9. Holmes MV, Dawe RS, Ferguson J, Ibbotson SH. A randomized, double-blind, placebo-controlled study of the efficacy of tetracaine gel (Ametop®) for pain relief during topical photodynamic therapy. Br J Dermatol. 2004;150(2):337–40.
10. Wang I, Bendsoe N, af Klinteberg C, Enejder AMK, Andersson-Engels S, Svanberg S, et al.

Photodynamic therapy versus cryosurgery of basal cell carcinomas; results of a phase III randomized clinical trial. Br J Dermatol. 2001;144(4):832–40.

11. Peng Q, Soler AM, Warloe T, Nesland JM, Giercksky KE. Selective distribution of porphyrins in skin thick basal cell carcinoma after topical application of methyl 5-aminolevulinate. J Photochem Photobiol B. 2001;62(3):140–5.
12. Moan J, Ma LW, Iani V. On the pharmacokinetics of topically applied 5-aminolevulinic acid and two of its esters. Int J Cancer. 2001;92(1):139–43.
13. Juzenas P, Sharfaei S, Moan J, Bissonnette R. Protoporphyrin IX fluorescence kinetics in UV-induced tumours and normal skin of hairless mice after topical application of 5-aminolevulinic acid methyl ester. J Photochem Photobiol B. 2002; 67(1):11–7.
14. Mitra S, Foster TH. Carbogen breathing signifycantly enhances the penetration of red light in murine tumours in vivo. Phys Med Biol. 2004;-49(10):1891–904.
15. Ren QG, Wu SM, Peng Q, Chen YJ. Comparison of 5-aminolevulinic acid and its hexylester mediated photodynamic action on human hepatoma cells. Acta Biochim Biophys Sinica. 2002; 34(5):-650–4.
16. Balasubramaniam E, Natarajan P. Photophysical properties of protoporphyrin IX and thionine covalently attached to macromolecules. J Photochem Photobiol A. 1997;103(3):201–11.
17. Schleier P, Berndt A, Kolossa S, Wood M. Comparison between mALA- and ALA-PDT in the treatment of basal cell carcinomas. 50 Apr; 10th International Congress on Oral Cancer: Oral Onc Suppl. 2005;1(1):67–8.
18. Mitra S, Foster TH. Photophysical parameters, photosensitizer retention and tissue optical properties completely account for the higher photodynamic efficacy of meso-tetra-hydroxyphenyl-chlorin vs Photofrin. Photochem Photobiol. 2005;-81(4):849–59.
19. Lou PJ, Jager HR, Jones L, Theodossy T, Bown SG, Hopper C. Interstitial photodynamic therapy as salvage treatment for recurrent head and neck cancer. Br J Cancer. 2004;91(3):441–6.
20. Moore CM, Nathan TR, Lees WR, Mosse CA, Freeman A, Emberton M, et al. Photodynamic therapy using meso tetra hydroxy phenyl chlorin (mTHPC) in early prostate cancer. Lasers Surg Med. 2006;38(5):356–63.
21. Triesscheijn M, Ruevekamp M, Antonini N, Neering H, Stewart FA, Baas P. Optimizing meso-tetra-hydroxyphenyl-chlorin mediated photodynamic therapy for basal cell carcinoma. Photochem Photobiol. 2006;82(6):1686–90.
22. Sasnouski S, Zorin V, Khludeyev I, D'Hallewin MA, Guillemin F, Bezdetnaya L. Investigation of Foscan interactions with plasma proteins. Biochim Biophys Acta. 2005;1725(3):394–402.
23. Westerman P, Glanzmann T, Andrejevic S, Braichotte DR, Forrer M, Wagnieres GA, et al. Long circulating half-life and high tumor selectivity of the photosensitizer meta-tetrahydroxyphenyl-chlorin conjugated to polyethylene glycol in nude mice grafted with a human colon carcinoma. Int J Cancer. 1998;76(6):842–50.
24. Keene JP, Kessel D, Land EJ, Redmond RW, Truscott TG. Direct detection of singlet oxygen sensitized by haematoporphyrin and related compounds. Photochem Photobiol. 1986;43(2):117–20.
25. Gupta G, Morton CA, Whitehurst C, Moore JV, Mackie RM. Photodynamic therapy with meso-tetra(hydroxyphenyl) chlorin in the topical treatment of Bowen's disease and basal cell carcinoma. Br J Dermatol. 1999;141(2):385–6.
26. Johansson A, Svensson J, Andersson-Engels S, Svanberg K, Bendsoe N, Alexandratou E, et al. Fluorescence and absorption assessment of a lipid mTHPC formulation following topical application in a skin tumor model. J Biomed Opt. 2007;12(3): 034026.
27. Pegaz B, Debefve E, Ballini JP, Wagnieres G, Spaniol S, Albrecht V, et al. Photothrombic activity of m-THPC-loaded liposomal formulations: Pre-clinical assessment on chick chorioallantoic membrane model. Eur J Pharm Sci. 2006;28: 134–40.
28. af Klinteberg C, Andreasson M, Sandström O, Andersson-Engels S, Svanberg S. Compact medical fluorosensor for minimally invasive tissue characterisation. Rev Sci Instrum. 2005;76(3): 034303–6.
29. Coutier S, Mitra S, Bezdetnaya LN, Parache RM, Georgakoudi I, Foster TH, et al. Effects of fluence rate on cell survival and photobleaching in meta-tetra-(hydroxyphenyl)chlorin-photosensitized colo 26 multicell tumor spheroids. Photochem Photobiol. 2001;73(3):297–303.

Paper X

Monte Carlo simulations related to gas-based optical diagnosis of human sinusitis

L. Persson, E. Kristensson, L. Simonsson, and S. Svanberg.

Journal of Biomedical Optics **12**, Art. ID: 053002 (2007).

Journal of Biomedical Optics 12(5), 1 (September/October 2007)

Monte Carlo simulations related to gas-based optical diagnosis of human sinusitis

Linda Persson
Elias Kristensson
Lisa Simonsson
Sune Svanberg
Lund University Atomic Physics Division
P.O. Box 118
SE-221 00 Lund, Sweden

Abstract. We investigate the feasibility of using diode laser gas spectroscopy for sinusitis diagnostics. We simulate light propagation using the Monte Carlo concept, as implemented by the Advanced Systems Analysis Program (ASAP^{TM}) software. Simulations and experimental data are compared for a model based on two scattering bodies representing human tissue, with an air gap in-between representing the sinus cavity. Simulations are also performed to investigate the detection geometries used in the experiments, as well as the influence of the optical properties of the scattering bodies. Finally, we explore the possibility of performing imaging measurements of the sinuses. Results suggest that a diagnostic technique complementary to already existing ones could be developed. *© 2007 Society of Photo-Optical Instrumentation Engineers.* [DOI: 10.1117/1.2777179]

Keywords: simulations; infrared spectroscopy; diode lasers; scattering; molecular spectroscopy; medicine.

Paper 06166RRR received Jun. 22, 2006; revised manuscript received Apr. 11, 2007; accepted for publication May 17, 2007.

1 Introduction

Sinusitis is an inflammation of the paranasal sinus mucosa, which is treated with antibiotics and often followed by one week of sick leave. Every year, more than 37 million people in the U.S. are diagnosed with sinusitis. Today, the diagnosis of sinusitis is mostly based on the anamnestic history of the patient, and in some cases on paraclinical investigations such as x-ray, ultrasound, and low-dose computerized tomography. Unfortunately, unnecessary antibiotic treatment is very common due to the difficult diagnoses. Therefore, there is a great need for simple, nonintrusive alternatives or complementary methods to detect sinusitis.[1,2]

We describe computer simulations related to a new spectroscopic method for human sinusitis detection, which was demonstrated by Persson, Svanberg, and Svanberg.[3] This method is based on the sharp spectroscopic absorptive imprint of molecular oxygen characterizing an air-filled cavity traversed by diffusive light. Narrow-band diode laser radiation is launched through the facial skeleton and traverses the frontal sinus cavities in the forehead or the maxillary sinuses in the cheekbone (see Fig. 1 for sinuses location). The light is then diffusely scattered in the deeper lying tissues with part of the light again traversing the cavities and is again scattered in the facial tissue to reach an external detector. For the maxillary sinuses, an alternative light transmission geometry can be employed, where the laser light is transported through an optical fiber connected to the bucal mucosa, scattered through the sinus cavity, and detected externally.

In Ref. 3 we successfully demonstrated sinus cavity monitoring on a healthy human volunteer. The study was supported by extensive experimental trials on tissue-like plastic phantom materials separated by an air gap to simulate the human anatomy.

While all the results could phenomenologically be well understood, we have now performed detailed simulations of light propagation to further guide the development of the technique. For this study, we used the Advanced Systems Analysis Program (ASAP^{TM}) software, which operates on the Monte Carlo concept. We present simulation data in excellent numerical agreement with experimental data, as well as guidance for improved point monitoring and imaging applications of the technique.

In the next section, we describe the tools used in the study, which include the experimental setup, the computer simulations, and the sinus models investigated in the latter. Then we compare simulations with experimentally obtained data, and we investigate the influence of the scattering coefficient and the detection aperture and the possibility of imaging of the frontal sinuses using the present technique. Finally, conclusions are drawn.

2 Tools Employed in the Study

2.1 *Experimental Setup*

The experimental setup used in the measurements and previously reported[3] is based on a diode laser operating around 760 nm where the molecular oxygen A-band is located. The laser was tuned across a sharp individual line [typically a half width at half maximum (HWHM) of a few gigahertz] by applying a saw-tooth ramp to the driving current of the diode laser. To achieve sensitive lock-in detection, a sine-wave was superimposed to the saw-tooth ramp in a wavelength-modulation scheme.

The light was guided to the sample by a fiber. Two detection geometries were used, as shown in Fig. 2. In the backscattering geometry, a right-angled prism located in the center

---

1083-3668/2007/12(5)/1/0/$25.00 © 2007 SPIE

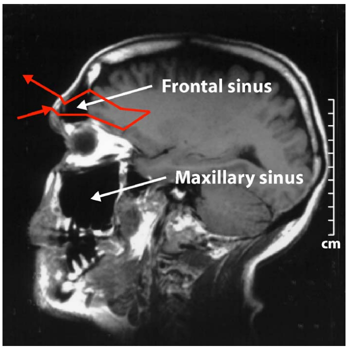

Fig. 1 (color online only) MRI image indicating the location of human maxillary and frontal sinuses. A light path illustrating the present technique is also included.

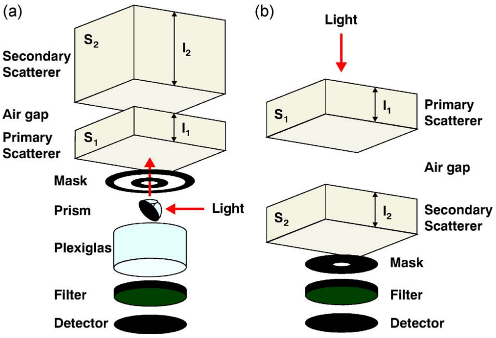

Fig. 2 (Color online.) Phantom models used in experiments and simulations representing (a) measurements on the human frontal sinuses with a backscattering detection geometry, and (b) measurements on the human maxillary sinuses with a transmission detection geometry.

of the detector was used to launch the light into the scattering medium. An annular aperture with a central block was used to collect photons backscattered from the sample. In the transmission geometry, the fiber was placed on the opposite side of the sample with respect to the detector. The detection was made by a photomultiplier to provide efficient photon collection. A blocking colored glass filter was placed in front of the detector to reduce ambient light.

The signal from the detector was split into two parts: one directly connected to an oscilloscope, and an other processed in a lock-in amplifier. The peak-to-peak value of the oxygen absorptive signal, recorded as the second derivative, was estimated and normalized to the amount of light reaching the detector. By applying a method called standard addition, a so-called equivalent mean path length, $\langle L_{eq} \rangle_{exp}$, could be estimated corresponding to the distance light has to travel in ambient air to obtain the same signal. This is described in Eq. (1), where c_{air} corresponds to the gas concentration in ambient air, $\langle L_{sample} \rangle$ to the mean path length in the sample, and c_{sample} to the gas concentration in the sample.

$$\langle L_{\mathrm{eq}} \rangle_{\mathrm{exp}} \cdot c_{\mathrm{air}} = \langle L_{\mathrm{sample}} \rangle \cdot c_{\mathrm{sample}} . \tag{1}$$

2.2 *Computer Simulations*

The Advanced Systems Analysis Program, ASAP$^{\mathrm{TM}}$, is a ray-tracing software that can be used to simulate light propagation in optical systems. Its implementation is based on the Monte Carlo method and the Henyey-Greenstein approach, which makes it well suitable for simulations in biological tissue and other light scattering materials.[4] The basic idea of Monte Carlo is to apply a probability view of light propagation, where an individual photon can be absorbed or laterally scattered by a certain angle according to relevant probability laws applying to the situation. After launching a large number of individual photons, the probability distributions are transformed into intensity distributions that can be compared to measured data. Basically, the physical experiment is repeated in the computer, considering a multitude of identical incident photons that later experience different fates.[5]

All simulated models considered in the present work incorporate scattering materials representing the human tissue and an air space representing the sinuses. By studying the rays reaching the detector in the simulations, the equivalent mean path length could be calculated for all models. For every ray, ASAP$^{\mathrm{TM}}$ computes information such as the flux at every surface it enters or is reflected off, as well as the distance it has traveled in all media. We then calculate the equivalent mean path length $\langle L_{eq} \rangle_{sim}$ by adding up, for all rays, the product of the distance L each individual ray has traveled in the air space and its corresponding flux ϕ when reaching the detector, and dividing it by the total flux reaching the detector. This is described in Eq. (2), where n is the total numbers of rays reaching the detector.

$$\langle L_{\mathrm{eq}} \rangle_{\mathrm{sim}} = \frac{\sum_{i=1}^{n} L_i \cdot \phi_i}{\sum_{i=1}^{n} \phi_i} . \tag{2}$$

It should be noted that rays reaching the detector that have not traveled in the air gap will have $L=0$, and only contribute to the simulated equivalent mean path length with a diluting factor. These rays are referred to as short-cut photons.

2.3 *Investigated Sinus Models*

The phantom model representing the human sinuses used in the experiments and the simulations contains two scattering slabs made of white Delrin-type plastic, with optical properties similar to human tissue (see Fig. 2). The scatterer closest to the light source is referred to as the primary scatterer S_1, and the other one is referred to as the secondary scatterer S_2. In the case of the transmission geometry, S_2 is the scatterer closest to the detector, and in the backscattering geometry it is the one located above S_1. The thicknesses of the scatterers are denoted l_1 and l_2. In-between the scatterers, a variable air gap was placed. The annular aperture determining the detection area was simulated by a variable absorptive mask.

To describe imaging of the frontal sinuses, a new model was created for simulations. In the case of imaging of the frontal sinuses, the sinuses were represented by two ellipsoids embedded in a scattering medium. The same backscattering detection geometry shown in Fig. 2(a) was used.

3 Results and Discussion

3.1 *Comparison between Experiments and Simulations*

To simulate the phantom experiments described in Ref. 3, which represent measurements on the human sinuses, we created a model in ASAP^{TM} consisting of two scattering materials S_1 and S_2, respectively, with a variable air gap in-between (see Fig. 2). The thicknesses l_1 and l_2 were varied, consistent with the experiment. The optical properties (the anisotropy factor g, the scattering coefficient μ_s, and the absorption coefficient μ_a) were measured for one of the Delrin plates used in the experiments by the integrating-sphere technique[6,7] to be $g \approx 0.87$, $\mu_s \approx 14\ \text{mm}^{-1}$, and $\mu_a \approx 0\ \text{mm}^{-1}$ at 760 nm. These values were used in the simulations. A small absorption $\mu_a = 0.0005\ \text{mm}^{-1}$ was added to better fit the experimental data. The index of refraction n for the Delrin plates was set to 1.48 and for the air gap to $n=1$.

Initial simulations, including all reflection and refraction phenomena according to the Fresnel and Snell formulas, were performed. It was noticed that the influence of the reflection was of minor importance for angles below the critical angle in our case. Thus it was suppressed in subsequent simulations, resulting in a manageable computer time. Above the critical angle, the total internal reflection was fully taken into account. The motivation to this approach has its roots in the fact that the solid angle for impinging photons corresponding to total internal reflection is much larger than that of shared reflection and refraction. Further, for photons impinging toward an optically denser medium, reflection has a small contribution as compared to penetration into the medium for the dominant fraction of the solid angle. For example, with two 10-mm-thick Delrin plates spaced by 10 mm, the underestimation of the true L_{eq} is about 8% and will, for larger spacings, become smaller (numerical values are provided in the Appendix.

In Fig. 3 the simulated and the experimental L_{eq} are shown for the backscattering detection geometry, representing measurements on the frontal sinuses [model according to Fig. 2(a)]. The inner detection radius r_i was about 6 mm, and the outer r_o about 10.5 mm in both simulations and experiments. Each simulated data point consists of launching 10^6 rays into the model.

As during the experimental trial,[3] it was observed in the simulation that an S_2 thicker than 30 mm did not influence the outcome. This can be understood because the photons being scattered deeper than 30 mm into S_2 have a very low probability to be detected. As can be seen in Fig. 3, the agreement between the simulations and the experiments is very good. It can be seen that introducing a thicker secondary scatterer results in L_{eq} increasing. This is because a thicker secondary scatterer results in a higher probability for the photons to be scattered back to the primary scatterer and be detected after passing through the air gap. On the contrary, a thicker primary scatterer results in a decrease of L_{eq}. The photons have now a lower probability of reaching the secondary scatterer, and even if they do, the backscattered photons from the secondary scatterer, are now more likely to be scattered outside the finite size of the detector. Because of the finite size of the detector, the signals first increase with increasing air gap until a certain distance, where they start to decrease. The maximum of the signal should be located at an air gap distance as large as possible to prevent two air gaps from giving rise to the same L_{eq} value, which could be critical in the case of real human measurements. The signal behavior is explained in more detail in Ref. 3.

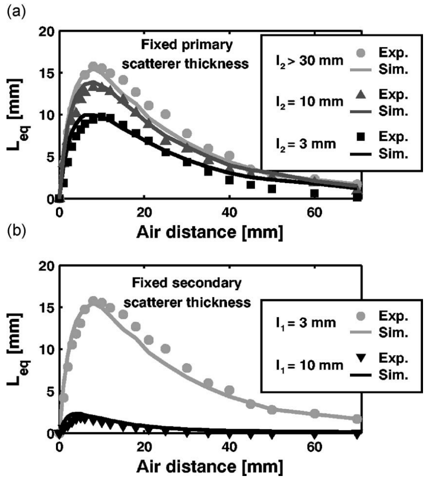

Fig. 3 The equivalent mean path length L_{eq} as a function of air-gap distance in phantom experiments and simulations for the backscattering detection model shown in Fig. 2(a), representing measurements on the human frontal sinuses. The optical properties of the primary and secondary scatterers are in the simulations set to $g=0.87$, $\mu_s=14\ \text{mm}^{-1}$, and $\mu_a=0.0005\ \text{mm}^{-1}$. (a) Fixed primary scatterer thickness $l_1=3$ mm. (b) Fixed secondary scatterer thickness $l_2=30$ mm.

The deviation between the experimental data and the simulated data can be due to many reasons. In the experiments, the thicknesses of the Delrin plates, the air gap, and the annular detection aperture could not be determined as precisely as they can be in the simulations. During the simulation it was also observed that a small change in one of the optical properties influenced the outcome. It should also be noted that the same optical properties were used for all the different Delrin plates in the simulations. This might not be the case, since the plates used in the experiments did not come from the same batch.

Experimentally it is impossible to explore the influence of multiple passes through the air gap. In contrast, this can easily be done in the simulations. Table 1 shows the number of times the detected photons pass over the air gap, for $l_1=10$ mm and $l_2=30$ mm, and for different air-gap distances. It should be noted that only even numbers of passes are possible, since the photons have to travel back and forth to be detected. Similar results were observed for the other thicknesses discussed in Fig. 3.[8]

Table 1 Distribution of the number of passes through the airgap for $l_1 = 10$ mm and $l_2 = 30$ mm and different air-gap distances in the backscattering detection geometry according to Fig. 2(a).

Air distance [mm]	1	5	10	30	70
2 passes [%]	31	42	51	74	98
4 passes [%]	20	22	23	19	2
6 passes [%]	14	13	11	5	0
8 passes [%]	10	8	6	1	0
10 passes [%]	7	4	3	1	0
12 passes [%]	5	4	2	0	0
14 passes [%]	3	2	2	0	0
Σ [%]	≈90	≈95	≈100	≈100	≈100

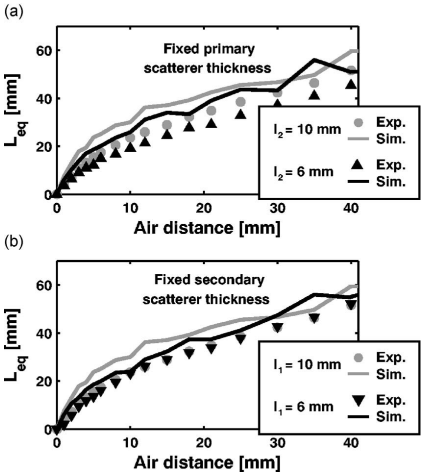

Fig. 4 The equivalent mean path length L_{eq} as a function of air-gap distance in phantom experiments and simulations for the transmission detection model shown in Fig. 2(b), representing measurements on the human maxillary sinuses. The optical properties of the primary and secondary scatterers in the simulations are in the simulations set to $g=0.87$, $\mu_s=14\ \mathrm{mm}^{-1}$, and $\mu_a=0.0005\ \mathrm{mm}^{-1}$. (a) Fixed primary scatterer thickness $l_1=10$ mm. (b) Fixed secondary scatterer thickness $l_2=10$ mm.

It can be seen that signals due to multiple passes can be significant, in contrast to what was intuitively assumed in Ref. 3. This illustrates the power of detailed Monte Carlo simulations, taking into account the actual regime of values of the optical constants.

It can also be seen from Table 1 that a larger air-gap distance results in fewer multiple passes. This phenomenon can be explained by the finite size of the detector. It was observed from the simulations that a thicker S_1 resulted in a increase of multiple passes. This can be understood because a thicker primary scatterer can collect oblique rays to be detected by the finite size detector that have been through more multiple passes. It was also observed that a thicker secondary scatterer increases the number of multiple passes, as a thicker secondary scatter allows more photons to be scattered back to the primary scatterer.[8]

In Fig. 4 the simulated and the experimental L_{eq} are shown for the transmission detection geometry, representing measurements on the maxillary sinuses [model according to Fig. 2(b)]. The mask radius was about 2.5 mm in both simulations and experiments. Each simulated data point consists of launching 10^6 rays into the model.

Again, very good agreement between the experimental and simulated data can be seen. The obtained L_{eq} for the different scatterer parameters increases with increasing air-gap distance. This can be understood, since in the case of the transmission detection geometry, all photons detected must have traveled over the air gap. This is in contrast to the backscattering detection geometry, where the short-cut photons (photons that have only been scattered in S_1 before being detected) dilute the observed L_{eq}. The signal behavior is explained in more detail in Ref. 3.

It can be seen that the photon statistics are not as good as for the backscattering detection geometry. For the transmission geometry, the percentage of detected photons in relation to the number of incident photons is much lower than for the backscattering case, despite the fact that all photons are carrying information of the sinuses. A much longer simulation time is needed to achieve good photon statistics. Again, the deviation between the experimental and the simulated data can be due to many reasons, as discussed before.

The number of multiple passes was also investigated in the transmission detection geometry for the models representing measurements on the human maxillary sinuses. Table 2 shows the number of times the detected photons pass the air gap, for $l_1=10$ mm and $l_2=10$ mm, and for different air distance. In this geometry, only odd number of passes are possible. Similar results were observed for the other thicknesses discussed in Fig. 4.[8]

Table 2 Distribution of the number of passes through the air gap for $l_1 = 10$ mm and $l_2 = 10$ mm and different air-gap distances in the transmission detection geometry according to Fig. 2(b).

Air distance [mm]	1	5	10	30	70
1 passes [%]	35	49	61	81	88
3 passes [%]	22	23	20	14	10
5 passes [%]	14	11	9	4	2
7 passes [%]	9	6	4	1	1
9 passes [%]	6	4	2	0	0
11 passes [%]	4	3	2	0	0
13 passes [%]	3	1	1	0	0
Σ [%]	≈93	≈97	≈100	≈100	≈100

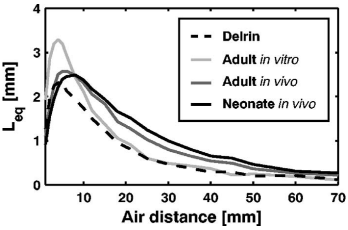

Fig. 5 Simulated equivalent mean path length L_{eq} as a function of air-gap distance, using backscattering detection geometry according to Fig. 2(a), with a primary scatterer thickness of 10 mm and a secondary scatterer thickness of 30 mm. An annular detection aperture with an inner radius r_i of 6 mm and another radius r_o of 10.5 mm, and optical properties of primary and secondary scatterer according to Table 3 were used in the simulations.

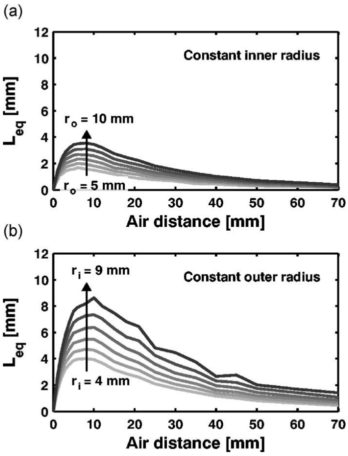

Fig. 6 Simulated equivalent mean path length L_{eq} as a function of the air-gap distance for different annular detection apertures in the case of backscattering detection geometry according to Fig. 2(a). The simulations were performed for a model with a primary scatterer thickness of 5 mm and a secondary scatterer thickness of 30 mm, and with optical properties corresponding to neonate (Table 3). (a) The inner radius of the annular detection aperture r_i is kept constant at 4 mm, while the outer radius r_o is varied between 5 and 10 mm. (b) The outer radius of the annular detection aperture r_o is kept constant at 10.5 mm, while the inner radius r_i is varied between 4 and 9 mm.

Again, as in the case of backscattering detection geometry, it can be seen that signals due to multiple passes can be significant. It can also be seen that for a larger air-gap distance, fewer multiple passes occur. As discussed before, this phenomenon can be understood from the finite size of the detector. It was also observed that a thicker S_2 results in more detected multiple pass rays. This can be understood, since more oblique rays will be collected by the finite size of the detector. The inverse argument is applicable to explain why a thicker S_1 results in less multiple passes.[8]

3.2 *Influence of the Scattering Coefficient*

The scattering coefficient and the thickness of the facial bone may vary between different humans, especially with age.[9] The scattering coefficient of bone is significantly smaller for children than for adults. In our model, a lower scattering coefficient has similar influence as a smaller thickness of the primary scatterer, i.e., a lower scattering coefficient of S_1 results in a higher probability for the photons to reach S_2 be scattered back and be detected by the finite size of the detector.

Figure 5 shows the influence of the scattering coefficient of S_1 and S_2. The simulations were performed for the backscattering detection geometry shown in Fig. 2(a), with an annular detection aperture of dimensions $r_i = 6$ mm and $r_o = 10.5$ mm. The optical properties used in the simulations are taken from different sources and presented in Table 3.[10–12] In all simulations, except for Delrin, $\mu_a \approx 0$ mm^{-1} was used. For each trial with a set of optical properties, simulations were performed with the same air-gap intervals as in Figs. 3 and 4, and by launching 10^6 rays into the model for each air-gap distance.

Table 3 Optical scattering properties used in the simulations taking from different sources.[10–12]

Optical properties	μ_s [mm^{-1}]	μ_s' [mm^{-1}]	μ_a [mm^{-1}]	g	λ [nm]
Delrin	14	1.8	0.0005	0.87	760
Adult skull *in vitro*	16	2.0	NA	0.87	800
Adult skull *in vivo*	13	0.9	NA	0.93	674–849
Neonate skull *in vivo*	9.3	0.65	NA	0.93	761

From the simulations it was observed that only the reduced scattering coefficients μ_s' and μ_a influence the result. The difference between optical properties corresponding to adult skull *in vivo* and neonate skull *in vivo* is only the reduced scattering coefficient. By comparing the curves obtained for these cases in Fig. 5, it can be seen that a lower μ_s' results in a larger air-gap distance needed to obtain the maximum signal. This is because a decrease in μ_s' can also be seen as a decrease in the thickness of the primary scatterer. This phenomenon can also be seen in Fig. 3(a). The influence of the absorption coefficient can be seen by comparing the simulated curves obtained for Delrin and adult skull *in vitro*. A lower μ_a gives rise to a higher integrated signal.

3.3 *Annular Detection Aperture*

In the experiments, the choice of annular detection aperture was done intuitively. Here we investigate the influence of the aperture geometry using the simulations.

In Fig. 6, L_{eq} is plotted as a function of the air-gap distance for different annular detection apertures in the case of the backscattering detection geometry. The thicknesses of S_1 and S_2 were set to 5 and 30 mm, respectively. The simulations were done with neonatal optical scattering properties (shown in Table 3). Again, the simulations were performed with the same air-gap intervals as in Figs. 3 and 4, and by launching 10^6 rays into the model for each air-gap distance.

In Fig. 6(a), it can be seen that increasing r_o while keeping r_i constant increases the signal. This is because a larger r_o allows more photons traveling over the air gap to reach the detector. This also gives rise to a larger photon flux reaching the detector. In Fig. 6(b), r_o is kept constant while r_i is varied. It can clearly be seen that increasing r_i results in a higher L_{eq}. This is equivalent to blocking out more of the short-cut photons that have only been scattered in the first medium, and thus only influence L_{eq} by diluting it. As can be seen in the figure, an increase in r_i also pushes the maximum of the signal toward larger air-gap distances. This might be very important for preventing two different air-gap distances giving rise to the same L_{eq} value.

The conclusion from these different curves obtained with different annular detection apertures is that an outer detection aperture as large as possible should be used. In the current setup, a photomultiplier (Hamamatsu 5070A) with a radius of 10.5 mm is used, which limits the outer radius. The simulations also show that an inner radius as large as possible should be used with an upper limit set by the experimental signal-to-noise ratio. Increasing the power of the diode laser used should thus be advantageous. Similar results were obtained and the same conclusion was drawn for scattering properties according to an adult, and are discussed in detail in Ref. 8.

A study of the influence of the detection aperture in the transmission detection geometry was also performed. In this detection geometry, the size of the aperture did not have the same influence on the signal as in the backscattering detection geometry. As mentioned before, all photons reaching the detector have traveled over the air gap distance, and short-cut photons need not to be blocked. This is discussed in more detail in Ref. 8.

3.4 *Frontal Imaging*

To investigate the feasibility of imaging the human frontal sinuses, a model according to Fig. 7(a) was studied. The two frontal sinuses were represented by two air-filled ellipsoids (25 mm high, 20 mm wide, 10 mm deep) separated by 5 mm and embedded at a depth of 10 mm in a scattering material, with optical properties corresponding to adult *in vitro* (Table 3). The backscattering detection geometry used in the simulations is shown in Fig. 2(a). Figure 7(b) shows the results of the simulations when using an annular aperture with $r_i = 5$ mm and $r_o = 10.5$ mm. The whole image consists of 1000 simulated data points with the light and detection arrangement scanned across the model. For each position, 0.5×10^6 rays were launched into the sample. The locations of the ellipsoids are also indicated. The figure clearly shows the possibility of spatially resolving the cavities.

Many factors might be considered to determine what constitutes a “good” image. It might be important to maintain the largest possible contrast between maximum and minimum signals, e.g., corresponding to the centers of the ellipsoids (the sinuses), and the center gap between them. To be able to resolve the two sinuses, it might also be critical to use a sufficiently small detection aperture to not blur the image.

In Fig. 8, the cross sections of the simulated backscattered image are shown for different detection apertures. In Fig. 8(a), r_i was kept constant at 4 mm, while r_o was varied between 5 and 10 mm. The real cross section is also included for the sake of clarity. It can be seen that selecting a larger outer detection radius results in a higher L_{eq} value. In Fig. 8(b), r_o was kept constant at 10.5 mm, while r_i was varied between 4 and 9 mm. It can be seen that the spatial resolution is rather independent of the chosen detection radii. Then it is important to obtain a sufficiently large L_{eq} value while maintaining a large photon flux.

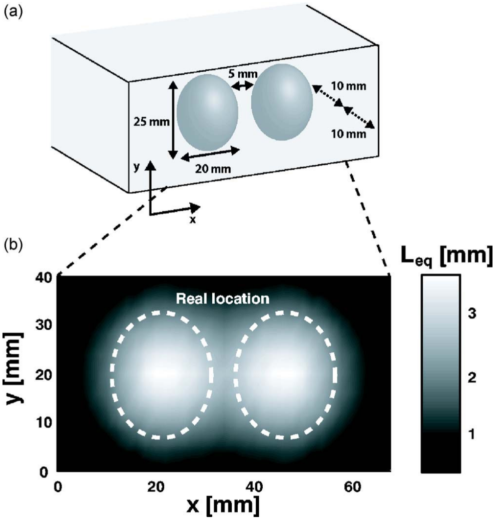

Fig. 7 (a) Model used in ASAP^{TM} to simulate imaging of the frontal sinuses. (b) Simulated equivalent mean path length L_{eq} obtained when scanning over the model using backscattering detection geometry according to Fig. 2(a) with an annular detection aperture with an inner radius r_i of 5 mm and another radius r_o of 10.5 mm. Optical properties according to adult *in vitro* in Table 3 were used.

4 Conclusion and Outlook

The power of Monte Carlo simulations in understanding and optimizing the experimental conditions for human sinus monitoring is demonstrated. The possibility of working with arbitrary geometries in the ASAP^{TM} approach is particularly valuable. The simulations agree well with experimental data for the limited setup conditions studied so far. This gives us confidence in using the simulations presented in the process of developing a new and clinically relevant modality for human sinus diagnostics.

In particular, realistic insight in the imaging capability for the frontal sinuses is obtained, showing that the main features of the cavities can be retrieved noninvasively. The geometry is complex and more difficult to test experimentally, but can be illuminated in the simulations. Since we deal with highly scattering media, only an equivalent air path is retrievable from the experiments, but this parameter seems to relate well to the factual geometry. Insight into how sensitive the oxygen signals are to the detailed probe positioning is obtained, which

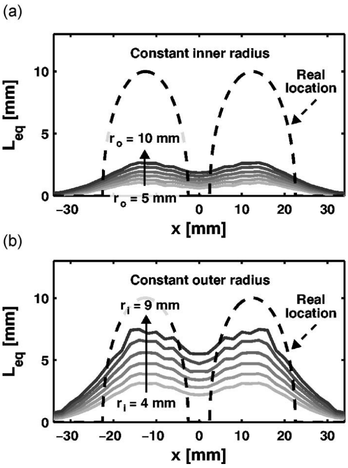

Fig. 8 Simulation of frontal sinus imaging using backscattering detection geometry according to Fig. 2(a) with different apertures. (a) The inner radius of the annular detection aperture r_i is kept constant at 4 mm, while the outer radius r_o is varied between 5 and 10 mm. (b) The outer radius of the annular detection aperture r_o is kept constant at 10.5 mm, while the inner radius r_i is varied between 4 and 9 mm.

is valuable in nonimaging applications. Among these, the measurement of gas-dynamic changes through the channels connecting the sinuses to the nasal cavity, and the measurement of concentration ratios between two gases, such as oxygen and water vapor, are of particular interest, since they yield information on the conductivity and absolute oxygen concentration, independent of the scattering properties.

Acknowledgments

The authors would like to thank Mats Andersson for technical assistance, and Breault Research for providing the ASAP™ software. We are also grateful to Katarina Svanberg for help with the medical aspects of this work, and to Stefan Andersson-Engels for valuable comments and advice. This research was supported by the Swedish Research Council, and the Knut and Alice Wallenberg Foundation.

Appendix

In the simulations presented, Fresnel reflection below the critical angle was not taken into account. It was observed that the influence was of minor impact in initial simulations, and therefore time consuming in the simulations and could be avoided. For example, 200 injected rays result in about 200 000 rays to track when simulating the backscattering detection geometry for the case of 10-mm-thick Delrin plates spaced by 10 mm, including Fresnel reflection. This is due to the fact that at each surface, the rays get divided up into one transmitted ray and one reflected ray with different weights according to Fresnel's laws. In Table 4, numerical values are given for the phantom simulations when employing the backscattering detection geometry. Data are presented for the case of 10-mm-thick Delrin plates (index of reflection equal to 1.48) spaced by 10 mm (index of reflection equal to 1). In the table, the total number of detected rays, the number of rays detected that have traveled over the air gap (oxygen rays), and the resulting simulated L_{eq} values are shown. Numerical values from three different cases are presented.

Table 4 Numerical values for the phantom simulations when employing the backscattering detection geometry ($l_1 = l_2 = d = 10$ mm). The different cases are explained in the text. For each case, $0.5 \cdot 10^6$ rays were launched into the sample. In case 3, the criterion that each ray was allowed no more than two divisions was set.

	Case 1	Case 2	Case 3
Total number of detected rays	8670	59163	67676
Detected oxygen rays	22	1788	3188
L_{eq} [mm]	0.074	1.46	1.59

Case 1. No Fresnel reflection is taken into account in the simulation, but refraction according to Snell's law is included.

Case 2. Total internal reflection is taken into account in the simulations, but Fresnel reflection is excluded below the critical angle. Snell's law refraction is included.

Case 3. All reflection and refraction phenomena according to the Fresnel and Snell formulas are taken into account in the simulations. For each case, 0.5×10^6 rays were launched into the sample.

It can clearly be seen that by not taking Fresnel reflection into account (Case 1), no detectable simulated L_{eq} is obtained. It can also clearly be seen that the important effect, which needs to be taken into account in the simulations, is total internal reflection (Case 2). By comparing Case 2 with a "correct" (and extremely time-consuming) calculation (Case 3), an error on the L_{eq} of only about 8% when excluding Fresnel reflection below the critical angle from the simulations is obtained.

References

1. *Health Matters, Sinusitis*, Nat. Inst. Allergy and Infectious Diseases, U.S. Dept. of Health and Human Services, Bethesda, MD (2005).
2. P. Stierna, G. Karlsson, I. Melén, and M. Jannert, "Aspect on sinusitis—diagnosis and treatment in adults," *Proc. Swedish Assoc. Otorhinolaryngol*, HNS, Stockholm (1995).
3. L. Persson, K. Svanberg, and S. Svanberg, "On the potential of human sinus cavity diagnostics using diode laser gas spectroscopy," *Appl. Phys. B* **82**, 313–317 (2006).
4. B. Michel and T. Beck, "Raytracing in medical applications," *Laser Photon.* **5**, 38–41 (2005).
5. L. Wang, S. L. Jacques, and L. Zheng, "MCML—Monte Carlo modeling of light transport in multi-layered tissues," *Comput. Methods Programs Biomed.* **47**, 131–146 (1995).
6. J. A. Jacquez and H. F. Kuppenheim, "Theory of the integrating sphere," *J. Opt. Soc. Am.* **45**, 460–470 (1955).
7. A. Nilsson, R. Borg, and S. Andersson-Engels, "Measurements of the optical properties of tissue in conjunction with photodynamic therapy," *Appl. Opt.* **34**, 4609–4619 (1995).
8. E. Kristensson and L. Simonsson, MSc Thesis, Lund Institute of Technology, Lund Reports on Atomic Physics LRAP-361, LTH, Sweden (2006).
9. N. Lynnerup et al., "Thickness of the human cranial dipole in relation to age, sex and general body build," *Head Face Med.* **1**, 1–13 (2005).
10. T. Vo-Dinh, *Biomedical Photonics Handbook*, CRC Press LLC, New York (2003).

11. S. Ijichi, T. Kusaka, K. Isobe, K. Okubo, K. Kawada, M. Namba, H. Okada, T. Nishida, T. Imai, and S. Itoh, "Developmental changes of optical properties in neonates determined by near-infrared time-resolved spectroscopy," *Pediatr. Res.* **58**(3), 568–573 (2005).
12. N. Ugryumova, S. J. Matcher, and D. P. Attenburrow, "Measurement of bone mineral density via light scattering," *Phys. Med. Biol.* **49**, 469–483 (2004).

Paper XI

Approach to optical interference fringes reduction in diode laser absorption spectroscopy

L. Persson, F. Andersson, M. Andersson, and S. Svanberg.

Applied Physics B **87**, 523–530 (2007).

Appl. Phys. B 87, 523–530 (2007)
DOI: 10.1007/s00340-007-2593-y

Applied Physics B
Lasers and Optics

L. PERSSON[1,✉]
F. ANDERSSON[2]
M. ANDERSSON[1]
S. SVANBERG [1]

Approach to optical interference fringes reduction in diode laser absorption spectroscopy

[1] Division of Atomic Physics, Lund University, P.O. Box 118, 22100 Lund, Sweden
[2] Centre for Mathematical Sciences, Lund University, P.O. Box 118, 22100 Lund, Sweden

Received: 6 October 2006/Revised version: 18 January 2007
Published online: 24 March 2007 • © Springer-Verlag 2007

ABSTRACT The advantage of a new scheme for balanced detection has been investigated to reduce the influence of optical interference fringes when performing diode laser gas absorption spectroscopy employing lock-in amplifiers and pigtailed lasers. The influence of the fringes has been reduced by comparing the lock-in 2 f signal due to the gas sample with that of a reference beam. The frequency regions outside the absorption feature have been used to obtain information on the interference fringe impact on the signal of interest. We have demonstrated an efficient way to reduce the influence of such fringes by employing this technique combined with non-linear signal processing methods. The different steps of the algorithm are presented. In the experimental arrangement presented, a reduction of the optical interference fringes by about 10 times is achieved, as demonstrated in measurements on molecular oxygen around 761 nm. The new technique is compared with an analog technique for balanced detection and certain advantages of the computer algorithm are pointed out. In particular, the emerging field of gas spectroscopy in scattering solid media strongly benefits from the technique presented.

PACS 42.55.Px; 39.30.+w; 42.25.Hz

1 Introduction

Diode laser absorption spectroscopy is increasingly used for monitoring gases in environmental, biological, and medical contexts [1, 2]. In many applications the gas concentration is in the sub-ppm (part-per-million) range, i.e. when dealing with trace-gas detection. As a result, measurements are heavily influenced by noise, interfering signals, and drifts. Different modulation techniques have been introduced to reduce the detrimental effects of noise. These techniques are based on imposing a high-frequency modulation signal to the injection current of the light source. The signal is then detected using phase-sensitive techniques at some harmonic of the modulation frequency [2, 3]. Even though such techniques may cancel out the effect of excess laser noise and reduce background fluctuations, they do not compensate for optical interference fringes. Seldom discussed in the literature, interference fringes constitute in practice the real limitation in low-level gas analysis. Interference fringes appear in light being partially reflected at optical surfaces. A light beam vertically impinging from air onto a common optical material of refraction index n undergoes a fractional reflection of $R = ((n-1)/(n+1))^2 \approx 4\%$. The reflected light from different surfaces can interfere causing a complex pattern intensity Fabry–Pérot fringes. Even if surfaces are anti-reflection coated or tilted, residual intensity variations easily occur on the per mille intensity scale. Clearly, this is of no concern for substantial absorption signals, but can become critical in the case of very weak absorptions, for which the sensitive modulation techniques have been developed.

Interference fringes can originate from various parts of the optical path between the laser and the detector. The fringes may obscure weak absorption signals if the free spectral range of the optical fringes is in the same order as the line width of the absorption signal, the half width of the fringes being also in this range due to the low finesse ($I_{\max}/I_{\min} = ((1+R)/(1-R))^2 \approx 1.2$ for $R = 4\%$) [4]. Several techniques have been introduced over the years to reduce the influence of optical interference fringes. Specific examples include signal averaging, mechanical vibration, and balanced detection [5–8]. Mechanical vibrations, however, are not applicable when using a fixed-optical-surface pigtailed laser, which is attractive for different reasons to be further discussed.

Balanced detection is commonly used to cancel out laser intensity fluctuations such as optical interference fringes. The general idea is to split the initial laser beam into two, where one beam, called the sample beam, passes through the sample, and the other beam, called the reference beam, goes directly to a detector. The analog balanced detection techniques can be divided into two groups. The first is based on subtraction of small currents (μA range) from photodiodes [9, 10], while the second is based on subtraction of voltage signals created by two identical transimpedance amplifiers [11–14]. Both techniques commonly use a feedback loop in order to minimize the difference between the detector signals. Subtraction of current signals should give better performance but requires careful design and closely mounted matched detectors. In practice this may be hard to implement and therefore solutions based on subtraction of signals from transimpedance amplifiers have been introduced. While these methods clearly improve the signal recovery they have certain drawbacks. The two detectors should be placed close to each other, in order to minimize additional noise and to optimize performance. The analog balanced detection method also frequently assumes

---

✉ Fax: +46-46-222-4250, E-mail: linda.persson@fysik.lth.se

that the reference beam power is larger than the sample beam power, as well as that matched detectors and matched transimpedance amplifiers are used. In many applications these conditions are not feasible, as discussed below.

Historically, diode laser spectroscopy has been performed on well-defined atmospheric beam paths, frequently in absorption cells, where the conditions with regard to the geometry and transmission are very stable (see [14] for an extensive review of molecular oxygen diode laser spectroscopy performed under such conditions). Then the cell can be evacuated allowing a subtraction of persistent fringes. In contrast, in applications recently developed in our group [15–19], the gas cell is replaced by a test sample that attenuates and scatters light differently during the measurements or on a day to day basis, which puts new demands on the detection- and signal-processing systems. In [17], wood-drying processes were studied by spectroscopic measurement of oxygen and water vapor. It turned out that the sample beam intensity varied by a factor of 10–100 depending on the water content. Spectroscopic measurements on pharmaceutical tablets put similar demands due to the differences of thickness and density of the tablets [18]. Further applications resulting in similar demands are measurements for medical diagnostics. In [19], spectroscopic measurements on human maxillary sinuses were described. It turned out that the intensity of the sample beam varied by a factor of 20 depending on the person that was studied even if the measurement procedure was the same. Thus, it is not enough to calibrate the system for a limited intensity range or use commonly known techniques to suppress non-linear disturbances, fringes, etc. The situations with sample beam intensity varying by several orders of magnitude depending on the state of the test sample is vastly different from the conventional trace-gas measurements in an absorption cell.

We largely use pigtailed lasers since it is not practical to measure on solid test samples with ordinary lasers. Backscattered light from the sample that enters the laser, fringes due to fibre coupling based on lenses, and handling laser heads close to a test sample at measurement all can be problematic. The present paper focuses on applications based on pigtailed lasers which are easy to implement in portable measurement systems for a variety of spectroscopic studies.

In the present paper, we describe a specific way of using software-based balanced detection to remove optical interference fringes in strongly varying measurement situations as described above. Our approach is based on using parts of the recorded signals falling in the frequency range outside the absorption region in order to estimate imperfections of the measurement system. In the reference beam, unaffected by gas absorption, fringe structures are also recorded in the frequency region of the gas absorption. The regions outside the absorption can be used to estimate the fringe contribution to the gas signal. In addition, the algorithm presented compensates for possible non-linear effects in the response of the two different detection arms as well as different offsets. This method can be applied to any system and be combined with other customary techniques such as mechanical vibrations to further reduce fringes not related to the common light path.

In Sect. 2 the experimental arrangements for this study are described. The different artifacts that occur in typical diode laser absorption spectroscopy experiments are then discussed together with an explanation of the presented software-based method and a previously discussed analog method for achieving balanced detection. The procedure to evaluate the gas content from the balanced-detection signals is then discussed. Results from both the software-based balanced detection and the balanced detection achieved by the electronic circuit are then shown and discussed. Finally, conclusions are drawn.

2 Experimental arrangements

Schematic drawings of the experimental arrangements used in the software-based and the analog balanced detection approaches are shown in Fig. 1. Common for both cases (Fig. 1a), a single-mode fibre-pigtailed thermoelectrically cooled DFB laser diode (Nanoplus, Germany) was used as a light source. The laser delivered about 4 mW at around 760 nm, where the molecular oxygen A-band is located. The wavelength of the light was tuned across the R11Q12 absorption line by supplying a 4 Hz saw-tooth ramp to the laser driver current. A 10 kHz sine wave was also superimposed on the laser driver current in a wavelength-modulation scheme to achieve sensitive detection.

The light was split 90%/10% with a single-mode fibre-coupled beam splitter (Laser2000, Sweden) with an insertion loss of about 5%. The fibre carrying about 10% of the light was directly guided to a silicon detector (UDT 10DP/SB) via an attenuation filter (×10). Thus, about 0.035 mW light enters the detector, which was connected to a transimpedance amplifier. The other fibre carrying about 90% of the output from the laser was connected to a collimating lens package (Thorlabs CFC-5-760). The light then travels over a certain air distance, or an absorbing and scattering medium, before being detected with a second identical silicon detector or a photomultiplier tube (PMT), which is connected to an identical transimpedance amplifier as the one used for the reference detector. An attenuation filter was mounted in between the fibre and the detector for the case of a non-scattering sample. The collimating package was mounted on a z-translator providing variable air distances. For the amplification, Hamamatsu C7319 units were available and used.

2.1 *Setup for software-based balanced detection*

In the left-hand part of Fig. 1b the arrangement to perform software-based balanced detection is shown. The reference signal was sent to an oscilloscope via a lock-in amplifier (EG&G Princeton Applied Research 5209), where the 2 f signal was recorded. This signal will be referred to as the reference signal. The signal from the sample detector was split into two parts; one part directly was connected to the oscilloscope (referred to as the direct signal) while the second part was sent via a second lock-in amplifier (EG&G Princeton Applied Research 5209) before being connected to the oscilloscope where the 2 f signal was recorded. This signal will be referred to as the sample signal.

2.2 *Setup for analog balanced detection*

In order to test the performance of an auto balanced detection approach, based on differential transimpedance am-

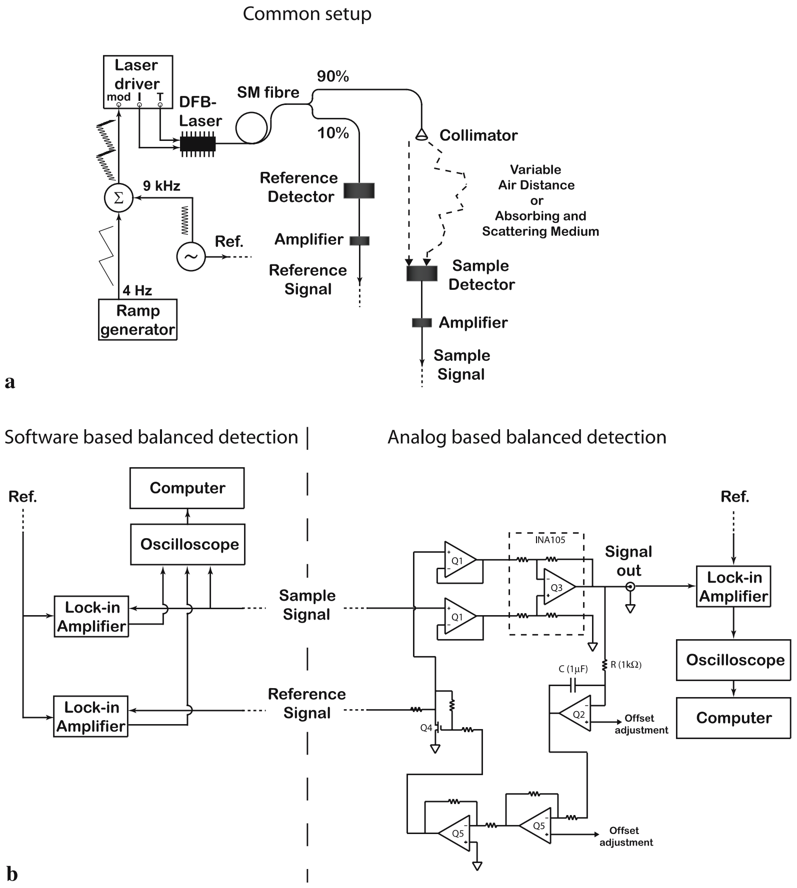

FIGURE 1 (**a**) Schematic drawing of experimental arrangement for diode laser gas absorption spectroscopy providing balanced detection. (**b**) In the *left-hand part* the arrangement for software-based balanced detection is shown and in the *right-hand part* the arrangement for analog balanced detection is shown [11]. The following components were used in the device: Q1 and Q5 – OP470 low-noise op-amp, Q2 – LF356 low-noise op-amp, Q3 – INA105 unity-gain differential amplifier, and Q4 – 2N5457 MOSFET

plification, we implemented an electronic cancellation device, according to [11], shown to the right in Fig. 1b. The sample signal is buffered by Q1 and fed into a unity-gain differential amplifier (INA105). The reference signal was connected to the unity-gain differential amplifier via a field-effect transistor (Q4). A feedback loop consisting of Q2 and Q5 controls the input level of Q4 (attenuation factor), trying to minimize the output of the differential amplifier. Thus, the output of the differential amplifier is proportional to $U_{\text{sample}} - U_{\text{reference}}$. The time constant of the feedback loop ($t = 0.001$ s) is set by the 1 kΩ resistor and the 1 μF capacitor mounted closely to Q2. The output of the noise cancellation circuit was led into a lock-in amplifier of the same type as used in the software-based balanced detection scheme, and the 2 f signal was recorded on an oscilloscope.

3 Data analysis

In order to achieve optimal signal retrieval for weak gas absorption signals we need to handle (a) interference fringes, (b) laser intensity noise, (c) non-linear detector response, and (d) different zero detector offsets.

Fringes mimicking real signals are most critical. They can be eliminated by studying spectral regions outside the expected absorption imprint. This could in principle be done in an exact way from the reference signal if the detection channels (detectors, amplifiers, and lock-ins) were identical, linear, and with a correct zero level. Since this might not be the case – Fig. 2 – the differential behavior between the two signals is described by a set of parameters corresponding to linear and non-linear phenomena, as discussed below.

3.1 *Software-based method for non-linear artifact suppression*

As mentioned above, two outputs from two detectors are measured; one detecting the light which has traveled over the gaseous sample to be analyzed and one measuring the reference light level. We will here denote the sample signal $p_{\text{samp}}(\nu)$ and the reference signal $p_{\text{ref}}(\nu)$. Ideally, $p_{\text{samp}}(\nu)$ and $p_{\text{ref}}(\nu)$ should be identical for ν-values outside the region of oxygen absorption. Hence, by considering the difference between the two signals we can determine the amount of oxygen in the measurement sample, since only effects of oxygen absorption should remain. The difference between the sample

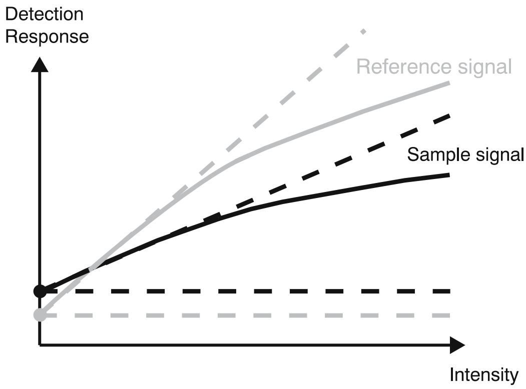

FIGURE 2 Schematic drawing of imperfections in detection arm response (heavily exaggerated)

signal and the reference signal will thus give us the balanced-detection signal, which we will denote $p_{\mathrm{bds}}(\nu)$. However, there are several practical measurement effects that need to be suppressed before constructing the balanced-detection signal.

Let $w(\nu)$ be a window function that vanishes in the neighborhood of the oxygen absorption region, and goes smoothly to 1 outside the region. We assume that data are sampled at points $\nu = \{\nu_j\}$, and introduce column vectors $\mathsf{p}_{\mathrm{samp}}$, $\mathsf{p}_{\mathrm{ref}}$, and $\mathsf{p}_{\mathrm{bds}}$, containing samplings of p_{samp}, p_{ref}, and p_{bds} at $\{\nu_j\}$, respectively. Furthermore, let W be a diagonal matrix with the values of $w(\nu_j)$ as entries. In the case of no difference in offset or in amplification, one would expect that

$$p_{\mathrm{samp}}(\nu)w(\nu) \approx p_{\mathrm{ref}}(\nu)w(\nu) . \tag{1}$$

However, due to imperfections of the measurement system, effects from various components bring degradation of the processing. This can be accounted for by considering non-linear effects and different background offsets in the two detectors and the downstream processing. We account for the effects by estimating their impact outside the oxygen absorption region. We expect deviations from (1) due to the effects mentioned above. Hence, we assume that

$$p_{\mathrm{samp}}(\nu)w(\nu) \approx \Big((l_0 + l_1\{\nu-\nu_0\})\, p_{\mathrm{ref}}(\nu) \\ + k_0 + k_1\{\nu-\nu_0\} + k_2\left\{(\nu-\nu_0)^2\right\} \Big) w(\nu) . \tag{2}$$

The constants introduced have the following interpretation:

- l_0: Amplification compensation
- l_1: Non-linear response compensation
- k_0: Background offset compensation
- k_1: Intensity-dependent laser stray-light compensation
- k_2: Residual non-linear intensity compensation

all of which are due to the differential behaviors of the two individual detectors and imperfections in the subsequent signal handling.

We can thus estimate the parameters

$$\boldsymbol{h} = \Big(l_0\ l_1\ k_0\ k_1\ k_2 \Big)^{\mathrm{T}}$$

by minimizing the residual of the matrix equation ($\mathsf{1}$ is the column vector containing 1 as elements)

$$\begin{aligned} \boldsymbol{W}\boldsymbol{p}_{\mathrm{samp}} &\approx \boldsymbol{W}\Big(\boldsymbol{p}_{\mathrm{ref}}\{\nu-\nu_0\} \circ \boldsymbol{p}_{\mathrm{ref}}\mathsf{1}\{\nu_j-\nu_0\}\left\{(\nu_j-\nu_0)^2\right\} \Big)\boldsymbol{h} \\ &= \boldsymbol{W}\,\boldsymbol{A}\,\boldsymbol{h} , \end{aligned} \tag{3}$$

where ν_0 is the center frequency and where $\circ$ denotes the Hadamard product [20]. Note that (3) is largely overdetermined.

We solve (3) in a (weighted) least-squares sense by forming and solving the normal equations:

$$\mathsf{h} = (\mathsf{A}^{\mathrm{T}}\boldsymbol{W}\mathsf{A})^{-1}\,\mathsf{A}^{\mathrm{T}}\,\boldsymbol{W}\,\mathsf{p}_{\mathrm{samp}} .$$

With these $\boldsymbol{h}$-parameters at hand, we define the balanced-detection signal as

$$\mathsf{p}_{\mathrm{bds}} = \mathsf{p}_{\mathrm{samp}} - \Big((l_0 + l_1\{\nu-\nu_0\})\mathsf{p}_{\mathrm{ref}} \\ + k_0 + k_1\{\nu-\nu_0\} + k_2\{(\nu-\nu_0)^2\} \Big) . \tag{4}$$

3.2 *Standard analog artifact suppression*

The analog balanced detection device, based on [11], is in principle a PI controller (integrator with a proportional gain) that adjusts the attenuation of the signal from the reference detector by changing the dynamic resistance of a field-effect transistor (FET). The aim is to minimize the output level of the device and thus suppress low-frequency noise caused by the laser, detector, and fringes. The time constant of the feedback loop is set by two components (C and R in Fig. 1b to the right) and is on the order of 1 ms. Thus, the feedback loop is not affected by the 2 f signal at 20 kHz that is transferred more or less without any distortion. An additional advantage is that the need for lock-in amplifiers with high dynamic range has decreased due to lower signal amplitudes in the low-frequency range.

3.3 *Gas content evaluation*

The gas concentration is evaluated using the Beer–Lambert law stating that

$$I(\lambda) = I_0(\lambda)\mathrm{e}^{-\sigma(\lambda)cL} ,$$

where $I_0(\lambda)$ is the initial intensity and $I(\lambda)$ is the intensity of the light that has traveled a distance L over a sample with the gas concentration c and the absorption cross section $\sigma(\lambda)$ [4]. Beer–Lambert's law also states that for low absorptions the fractional absorption is proportional to the concentration and the optical path length. Therefore, the balanced-detection signal must be normalized to the amount of light reaching the detector (direct signal). The amplitude of the balanced-detection signal is proportional to the gas content in the sample and is therefore the parameter of central interest in the gas analysis.

When starting a measurement, an ideal experimental absorption profile, $p_{\mathrm{i}}(\nu)$, is first measured where the noise is much smaller than the detected oxygen signal. This signal is obtained by measuring over an air distance of several meters. Once a clean balanced-detection signal is obtained, we can match it against our computed $p_{\mathrm{bds}}(\nu)$. In the matching process, we compensate for drifts in the frequency scale. Thus, we match the balanced-detection signal against the ideal function with regard to both location and amplitude. This is done by mimicking an autocorrelation function; we convolve $p_{\mathrm{bds}}(\nu)$ with $p_{\mathrm{i}}(\nu)$ and detect the resulting peak position, denoted ν_s. Once the peak position is known, we repeat a similar approach as for the construction of the balanced-detection signal with the algorithm; we form

$$\begin{aligned}(1-\boldsymbol{W})\,p_{\mathrm{i}} &= (1-\boldsymbol{W})\left(p_{\mathrm{bds}}\,1\right)m \\ &= \boldsymbol{W}\,B\,m\,, \qquad (5)\end{aligned}$$

and solve it for parameters m by forming and processing the corresponding normal equations. The global intensity parameter is then estimated (peak-to-peak value of the fit), which corresponds to the gas content after calibration.

4 Results and discussion

Several measurements were performed with different added air distances to investigate the performance of the implemented software-based balanced detection method. To investigate the influence of the different components in $\boldsymbol{h}$, (3) was solved with different $\boldsymbol{h}$-parameter combinations. Figure 3a shows signals obtained during measurements with an air distance of about 10 mm. This corresponds to an oxygen fractional absorption of 2.5×10^{-4} on the R11Q12 line at 760.445 nm (vacuum wavelength). Two identical photodiodes were used to detect the sample signal and the reference signal. In the left-hand part of Fig. 3a, the unprocessed sample signals together with the fitted reference signals are shown. The balanced-detection signals obtained according to (4) are shown in the right-hand part of the figure together with the fitted ideal experimental absorption profile. As can be seen in the figure, all components of $\boldsymbol{h}$ are needed to obtain a satisfactory balanced-detected signal. However, the influence of l_1 is very small, i.e. the non-linear amplification response compensation is not of great influence when using two identical detectors in our experimental setup.

The same procedure was carried out after changing the sample detector to a PMT. The reference signal was still recorded by a photodiode. The influence of the different $\boldsymbol{h}$-parameter combinations is shown in Fig. 3b. In this figure it can be observed that l_1 is of greater influence when employing detectors of different types to record the sample signal and the reference signal than when two identical detectors are used.

The observations in Fig. 3 and our general experience can be summarized in the following points:

- In the case with identical detectors it is sufficient to parameterize with fewer variables, while in the case of different types of detectors all parameters discussed are significant.
- In applications where the light intensity varies widely (large dynamic range) residual differences between similar detectors are more important and again call for more detailed parametrization. Thus, we retain all parameters for general purposes.

To compare the presented software-based method with the analog method [11], measurements with both approaches were performed with an air distance of about 6 mm (fractional absorption of 1.5×10^{-4}). An attenuation filter was placed in front of the sample detector to provide a reference beam power 100 times the sample beam power ($P_{\mathrm{ref}}/P_{\mathrm{samp}}\approx100$). This was done to optimize the performance of the analog device. In Fig. 4a obtained balanced-detection signals from both methods are shown when using two identical detectors. The measured unprocessed sample signal is also included. It can be seen that when performing analog balanced detection a large offset remains. Attempts were made to compensate for this by adjusting the offset in the device, but no difference could be seen. An 'ideal' experimental absorption profile was fitted to the software-based balanced-detection signal. The global intensity parameter, i.e. the peak-to-peak value of the fitted ideal experimental absorption profile, was estimated to be 0.44 scale units. This corresponds to an air distance of

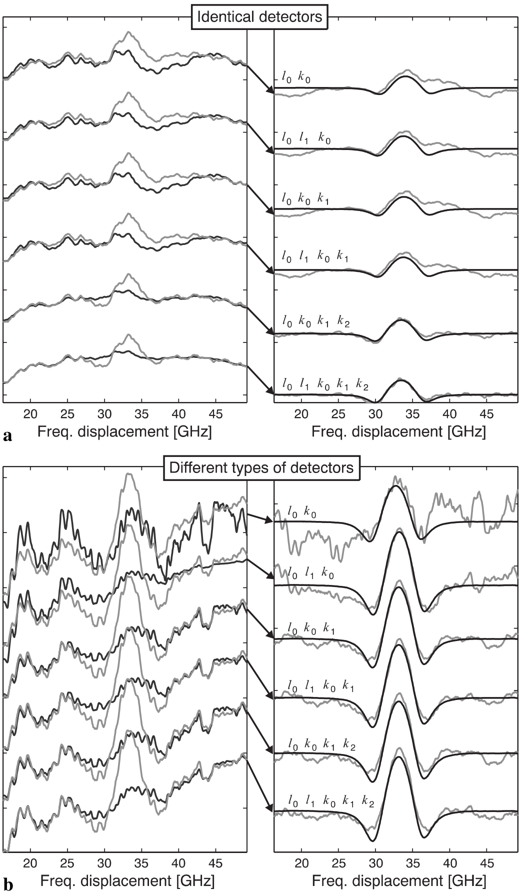

FIGURE 3 Typical curves obtained during software-based balanced detection with 10 mm of air distance. *To the left*: the *gray curves* show $\boldsymbol{p}_{\mathrm{samp}}$ and the *black curves* the fitted $\boldsymbol{p}_{\mathrm{ref}}$. *To the right*: the *gray curves* show the corresponding $\boldsymbol{p}_{\mathrm{bds}}$ and the *black curves* the fitted $\boldsymbol{p}_{\mathrm{i}}$. The influences of the different $\boldsymbol{h}$-parameter combinations are presented. (**a**) Two identical detectors have been used to detect the sample beam and the reference beam. (**b**) Two different types of detectors have been used to detect the sample signal and the reference signal

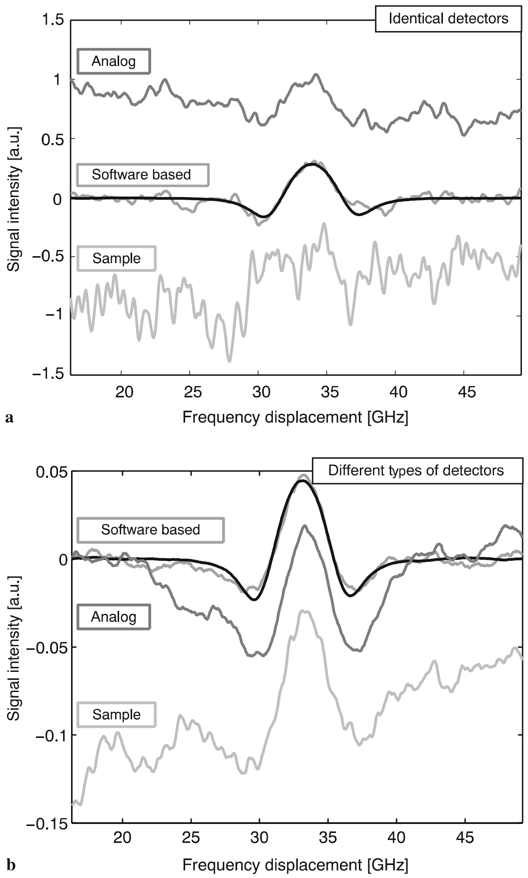

FIGURE 4 Achieved balanced-detection signals by using the software-based algorithm, $\boldsymbol{p}_{\mathrm{bds}}$, and the analog device. The unprocessed sample signal measured, $\boldsymbol{p}_{\mathrm{samp}}$, is also shown. No collimator package was used on the sample beam. (**a**) About 6 mm of added air distance. Two identical detectors were used to detect the sample signal and the reference signal ($P_{\mathrm{ref}}/P_{\mathrm{samp}} \approx 100$). (**b**) About 10 mm of added air distance. Two different types of detectors were used to detect the sample signal and the reference signal ($P_{\mathrm{ref}}/P_{\mathrm{samp}} \approx 4$). The curve with *darkest tone* is an 'ideal' experimental curve, $\boldsymbol{p}_{\mathrm{i}}$, fitted to the data

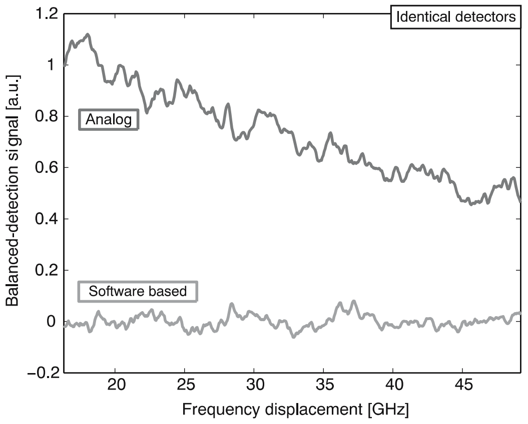

FIGURE 5 Achieved balanced-detection signals with no added air distance by using the software-based method, $\boldsymbol{p}_{\mathrm{bds}}$, and the analog device. Two identical detectors were used to detect the sample signal and the reference signal. No collimator package was used on the sample beam

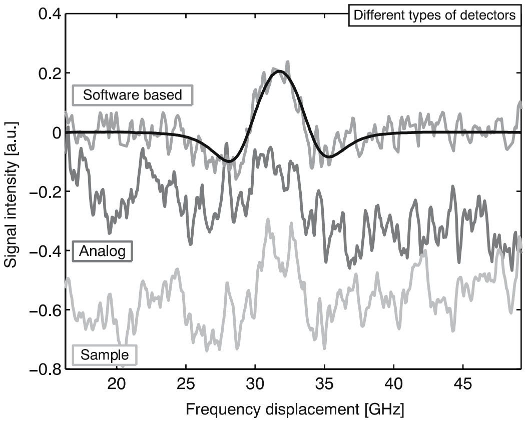

FIGURE 6 Achieved balanced-detection signals by using the software-based method, $\boldsymbol{p}_{\mathrm{bds}}$, and the analog device measured through the maxillary sinus on a human volunteer. The unprocessed sample signal measured, $\boldsymbol{p}_{\mathrm{samp}}$, is also shown. The curve with *darkest tone* is an 'ideal' experimental curve, $\boldsymbol{p}_{\mathrm{i}}$, fitted to the data

6.3 mm (calibration information is provided in Fig. 7 in the appendix).

Figure 4b shows signals obtained for a 10-mm air distance when using detectors of different types. The reference signal power was now only a factor of four larger than the sample signal power ($P_{\mathrm{ref}}/P_{\mathrm{samp}} \approx 4$). It can be seen that both methods are able to retrieve the oxygen signal; however, the software-based method is more successful. The peak-to-peak value of the fitted ideal experimental absorption profile was estimated to be 0.07 local scale units. This corresponds to an air distance of 10 mm. In Fig. 4a and b, an optical interference fringe reduction of about 10 times by the use of the algorithm approach can be seen compared to the sample signal. In the case of the analog method a baseline correction is needed, which would require a software approach. Then the full computational technique put forward in the present paper rather would come to mind.

To study the noise level remaining after performing balanced detection, and thereby the limitations of the experimental arrangement together with the algorithm, measurements were done with no air distance between the light source and the sample detector. Ideally, this should result in a zero signal, since the sample signal should not contain any oxygen imprint. Figure 5 shows the balanced-detection signals obtained with the software-based and the analog methods when using two identical detectors. In this figure it is again obvious that the analog noise reduction device does not fully compensate for offset differences between the sample signal and the reference signal. A noise level of about 0.15 scale units remains after the data are processed by the algorithm.

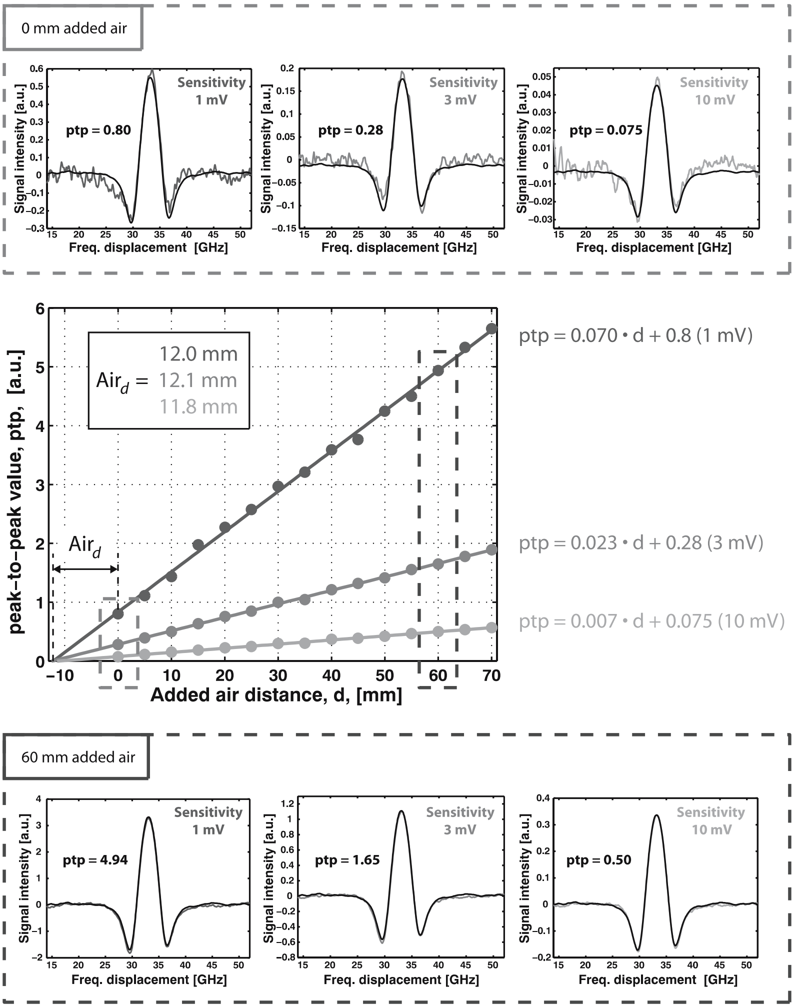

FIGURE 7 Results from measurements according to the standard addition method. Six obtained balanced-detection signals, $\boldsymbol{p}_{\mathrm{bds}}$, from 0 mm to 60 mm of added air distance measurements and the three different sensitivities used of the lock-in amplifier are included together with their estimated peak-to-peak values. The equations of the linear relationship between the peak-to-peak values and the added air distances for the three sensitivities are presented. The estimated unknown air distance, Air$_d$, of the collimator package was estimated to about 12 mm for all sensitivities

This corresponds to a signal of about 2 mm of air distance (a fractional absorption of 5×10^{-5}), which is a measure of the resolution of our experimental setup together with the algorithm.

As a final and most critical example we present data from a case where the sample is strongly scattering and attenuating. Here there is an unknown intensity relationship between the sample and the reference signals. Measurements on an air-filled human maxillary sinus cavity, located within the cranial skeleton below the orbital floor [19], are shown in Fig. 6. The fibre end is then placed inside the mouth on the palate and the multiply scattered light is detected externally on the cheekbone by a handheld probe containing the PMT. The achieved balanced-detection signal in the software-based approach corresponds to an air distance of about 10 mm. In the figure it can clearly be seen that a larger 'noise floor' of the balanced-detection signal remains in the analog approach compared to the software-based method even though correction of the baseline would be performed.

The calibration of the system is discussed in detail in the appendix.

5 Conclusion

In theory, intensity perturbations from laser and fibres, before the fibre coupler, should be canceled out by the analog noise cancellation device used in the study for comparison. However, due to detector channels' imperfections with regard to non-linearities and offsets, electronic cancellation of noise, based on the design described in Fig. 1b, is, in practice, imperfect. Figure 4 shows that the performance of the analog device was a factor of about two worse than achieved in the software-based approach as evaluated by comparing the remaining 'noise floor' in the absence of an absorption signal.

The new approach is, in contrast to the analog technique, forgiving in terms of signal levels, gain settings, and offsets, since the technique adjusts for all these factors. In particular, it was demonstrated (Fig. 3b) that quite different detectors can be used and still a very satisfactory balanced detection can be achieved. However, we note that two lock-in amplifiers were employed in the software-based method in contrast to only one in the analog approach. Since intensity drifts due to optical interference fringes can be expected to occur on a slow time scale, the use of one lock-in amplifier sequentially for recording the sample and the reference signals should be feasible. Then, signal averaging individually for the two signals could be performed as customarily done in, for example, differential absorption lidar (DIAL) [21].

Clearly, the techniques presented here only compensate for 'upstream' fringes generated in and close to the laser source, while differential fringe effects in the two detector paths remain untreated. This is also the case for the analog approach.

However, major sources of such differential fringe generation (e.g. absorption cells) are not present in most of our applications. Rather, we deal with cases of free-air propagation (long-path-absorption remote sensing) or gas pores or cavities embedded in scattering media [15–19].

Our experience shows that substantial and very valuable improved signals are observed in practical measurements. As already mentioned, the technique described is particularly useful when pigtailed lasers are employed and customary fringe elimination by shaking is not possible. Possible fringes between the two detectors can still be eliminated, for example by mechanical vibration.

ACKNOWLEDGEMENTS This research was supported by the Swedish Research Council, the Swedish Foundation for Strategic Research, and the Knut and Alice Wallenberg Foundation.

Appendix

Calibration measurements

The standard addition method (see e.g. [4]) was used in order to further investigate the algorithm presented, and to calibrate our measured signals and thereby be able to estimate the air distance from a recorded peak-to-peak value. The method is based on adding known path lengths of air and measuring the peak-to-peak value for each distance. The measured values are then plotted as a function of added air. These values should be linear with regard to the added air distance, since the absorption is so low that the fractional absorption is proportional to the concentration and the distance the light has traveled. A collimator package, described in Sect. 2, was placed on the fibre end of the sample part. Due to the design of the package, an unknown air distance was added between the fibre tip and the sample detector. The collimator package was moved away from the light source, in 5-mm steps, and the peak-to-peak values of the obtained processed signals were estimated for the different air distances. Three different sensitivities (1 mV, 3 mV, and 10 mV) of the lock-in amplifier were used at each added air distance. In Fig. 7 the results can be seen. In the figure, six obtained balanced-detection signals, from 0 mm to 60 mm of added air distances, are also shown together with their estimated peak-to-peak values. As can be seen, the values follow the expected linear relationship with regard to the added air distance. The slope of the curves was estimated and can then be used as a calibration factor (included in the figure). The relationship between the different sensitivities can also be seen. The peak-to-peak values from a fixed air distance for different sensitivities of the lock-in amplifier should scale with the sensitivity of the unit. Our estimated slopes of the curves agree with this to a high precision. The unknown air distance, Air_d, in the collimator package could be estimated to be about 12 mm. Measurements from all sensitivities gave approximately the same value (also included in the figure).

REFERENCES

1 M.W. Sigrist (ed.), *Air Monitoring by Spectroscopic Techniques* (Wiley, New York, 1994)
2 P. Werle, Spectrochim. Acta A **54**, 197 (1998)
3 E.I. Moses, C.L. Tang, Opt. Lett. **1**, 115 (1977)
4 S. Svanberg, *Atomic and Molecular Spectroscopy*, 4th edn. (Springer, Berlin, 2004)
5 P. Werle, R. Mücke, F. Slemr, Appl. Phys. B **57**, 131 (1993)
6 D.R. Hjelme, S. Neegård, E. Vartdal, Opt. Lett. **20**, 1731 (1995)
7 V. Liger, Spectrochim. Acta A **55**, 2021 (1999)
8 S. Wu, T. Kimishimai, Y. Yoshi, H. Kuze, N. Takeuch, Opt. Rev. **9**, 189 (2002)
9 P. Hobbs, Appl. Opt. **36**, 903 (1997)
10 V. Liger, A. Zybin, Y. Kuritsyn, K. Niemax, Spectrochim. Acta B **52**, 1125 (1997)
11 C. Lindsay, R. Rade, T. Oka, J. Mol. Spectrosc. **210**, 51 (2001)
12 X. Zhu, D.T. Cassidy, Appl. Opt. **34**, 8303 (1995)
13 R. Engelbrecht, Spectrochim. Acta A **60**, 3291 (2004)
14 P. Vogel, V. Ebert, Appl. Phys. B **72**, 127 (2001)
15 M. Sjöholm, G. Somesfalean, J. Alnis, S. Andersson-Engels, S. Svanberg, Opt. Lett. **26**, 16 (2001)
16 L. Persson, K. Svanberg, S. Svanberg, Appl. Phys. B **82**, 313 (2006)
17 M. Andersson, L. Persson, M. Sjöholm, S. Svanberg, Opt. Express **14**, 3641 (2006)
18 T. Svensson, L. Persson, M. Andersson, S. Andersson-Engels, S. Svanberg, J. Johansson, S. Folestad, Non-invasive characterization of pharmaceutical solids using diode laser oxygen spectroscopy, manuscript in preparation (2007)
19 L. Persson, M. Andersson, T. Svensson, K. Svanberg, S. Svanberg, Non-intrusive optical study of gas and its exchange in human maxillary sinuses, manuscript in preparation (2007)
20 R.A. Horn, C.R. Johnsson, *Topics in Matrix Analysis* (Cambridge University Press, New York, 1994)
21 S. Svanberg, Differential absorption lidar (DIAL), in *Air Monitoring by Spectroscopic Techniques*, ed. by M.W. Sigrist (Wiley, New York, 1994), Chap. 3

Paper XII

Flexible lock-in detection system based on synchronized computer plug-in boards applied in sensitive gas spectroscopy

M. Andersson, L. Persson, T. Svensson, and S. Svanberg.

Submitted, (2007).

Flexible lock-in detection system based on synchronized computer plug-in boards applied in sensitive gas spectroscopy

Mats Andersson, Linda Persson, Tomas Svensson, and Sune Svanberg*
Atomic Physics Division, Lund University,
P.O. Box 118, S-221 00 Lund, Sweden

(Dated: September 8, 2007)

We present a flexible and compact, digital, lock-in detection system and its use in high-resolution tunable diode laser spectroscopy. The system involves coherent sampling, and is based on the synchronization of two data acquisition cards running on a single standard computer. A software-controlled arbitrary waveform generator is used for laser modulation, and a four-channel A/D board records detector signals. Gas spectroscopy is performed in the wavelength modulation regime. The coherently detected signal is averaged a selected number of times before it is stored or analyzed by software-based, lock-in techniques. Multiple harmonics of the modulation signal (1f, 2f, 3f, 4f, etc.) are available in each single data set. The sensitivity is of the order of 10^{-5}, being limited by interference fringes in the measurement setup. The capabilities of the system are demonstrated by measurements of molecular oxygen in ambient air, as well as dispersed gas in scattering materials, such as plants and human tissue.

PACS numbers: 07.05.Bx,39.30.+w,42.55.Px,42.62.Fi,42.60.Fc

I. INTRODUCTION

Analog lock-in techniques for tunable diode laser spectroscopy have been used for decades to improve the performance in the detection of trace gases [1–4]. Originally, desk-top, lock-in amplifiers were used in combination with mechanically chopped light. Today, external signal generators are used to superimpose sinus modulation signals on the laser operation current. The modulation signal also acts as phase reference and is fed to an analog, lock-in amplifier. This lock-in amplifier is then capable of filtering out harmonic components generated when light passes an absorbing sample/gas cell. Absorption lines are scanned across by superimposing a low-frequency triangular or saw tooth ramp on the operating current of the laser. The major reason for using lock-in detection is to suppress noise by moving the detection frequency to a range that is normally less affected by noise (above 1 kHz) [5]. In the 1980s, modulation techniques such as wavelength- [6], frequency- [7], and two-tone frequency [8] modulation schemes were developed. Normally, direct absorption measurements (baseband detection) gives a detection limit of 10^{-3} to 10^{-4}, while modulation techniques such as wavelength and frequency modulation give a detection limit of 10^{-6} or better [9]. Over the past 10 years digital amplifiers have been used and currently small digital-signal-processing based lock-in solutions are being developed and used [10, 11].

Even if the use in spectroscopy of modulation techniques, based on phase-sensitive detection, is straight forward, it is normally not easy to analyze and probe the raw signal, due to sources of error that affect the gas imprint signal before the lock-in detection has been implemented. This is because the detected gas imprint signal is weak and markedly affected by noise. Thus, data from the lock-in amplifier need to be averaged for several seconds or minutes in order to achieve the needed signal-to-noise ratio (SNR). It is often not possible to average the raw signal without degradation. This is due to unavoidable trigger jitter. Moreover, since lock-in detection normally takes place in real-time, another drawback is that the influence of a change in lock-in settings (for example, the selection of harmonic) cannot be evaluated later on. In addition to the lock-in technique, methods to improve the signal include balanced detection [12], coherent sampling [13], waveform averaging [14] and high-pass filtering prior to lock-in detection [13].

Coherent sampling is a well-known technique, commonly used in spectrum analysis and signal processing for acoustics and telecom research and development. In coherent sampling, a master clock is used to create modulation waveforms and to control the sampling process of the detector signal. Coherent sampling requires that an integer number of wanted waveforms exist in the acquired data set and that the ratios between the sampling and the modulation frequencies (both laser scanning and laser modulation signals) are integers [15–17]. With this technique a number of scanned signals can be averaged before the lock-in detection is carried out. Periodic noise such as power supply ripple and external optical noise from fluorescent lamps, etc., which does not fulfill the requirements above, is averaged out (the coherent sampling process acts as a comb filter) together with non-periodic noise. It should be noted that coherent sampling facilitates complete post-data processing. For example, this means that applications which previously required several lock-in amplifiers, can now be realized using coherent data acquisition and subsequent harmonic demodu-

---

*Electronic address: `sune.svanberg@fysik.lth.se`

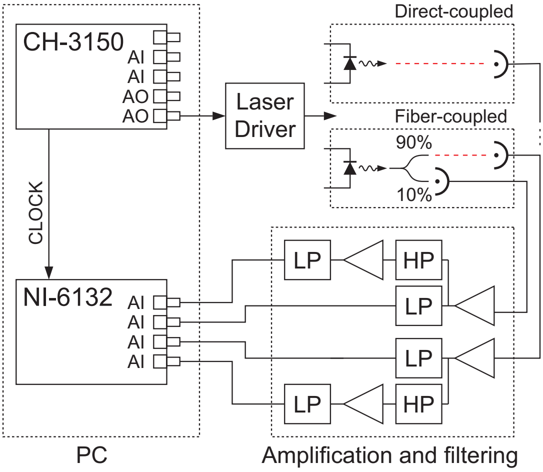

FIG. 1: The direct-coupled and the fiber-coupled experimental setups for measurement on ambient air by the use of VCSEL lasers. The lasers are modulated by an arbitrary waveform that is generated in a data acquisition board (CH-3150, Exacq Technologies). The amplified and high-pass filtered signals from the sample and the reference detectors are sampled coherently and synchronically by a four channel A/D board (NI-6132, National Instruments). See text for more details.

lation at desired harmonics (e.g. 1f and 2f). In addition, high-pass filtering can increase the dynamic range further, since it suppresses most of the low-frequency content (e.g., below the 1f frequency).

This paper describes the construction of a compact and flexible digital lock-in detection system based on two plug-in boards for a standard computer. By employing coherent sampling, raw data storage and post-data processing in the time- or frequency domain are made possible. The system can be used for both traditional trace gas analysis, and the more recently introduced high-speed combustion gas analysis requiring scan rates of 100 Hz or more. Experimental arrangements and data acquisition architecture are described in Sect. II. The required A/D resolution is also discussed. The calibration and applications of the system are presented in Sects III and IV. Finally, advantages of using a detection system based on coherent sampling and plug-in boards are discussed, and several examples of measurements are given.

II. MATERIALS AND METHODS

A. Optical Setup

An overview of the optical setup is shown in Fig. 1. Two different VCSELs (Vertical Cavity Surface Emitting Laser) are used alternatingly, and correspond to two different experimental configurations. The *direct-coupled setup* is based on a standard single-mode VCSEL (ULM763-03-TN-S46FOP, Ulm Photonics) with a maximal output of 0.3 mW, operating at 0.25 mW at the sample. The wavelength is scanned across the P11P11 oxygen line at 764.281 nm (vacuum wavelength). The second configuration is referred to as the *fiber-coupled setup*, and employs a pigtailed, single-mode VCSEL (L2K-P760-LD-SM, Laser2000, Sweden) with a maximum output power of 0.2 mW, operating at 0.085 mW at the sample. The wavelength is scanned across the R15Q16 oxygen line at 760.094 nm (vacuum wavelength). After the pigtailed laser, the light is split by a 10/90(%), single-mode fiber splitter (Laser2000, Sweden). The smaller fraction is guided to a reference detector, while the main part is either propagated through ambient air (for calibration purposes; see Sect. III), or guided to a scattering and absorbing sample. A collimating lens package (CFC-5-760, Thorlabs) is used in the case of measurements in ambient air.

The laser frequency is scanned over the absorption lines by ramping the operating current, which is provided by a standard VCSEL current controller (LDC200, Thorlabs). This is done by using a triangular waveform of 130 Hz. A temperature controller (TED200, Thorlabs) ensures general temperature stability. Wavelength modulation is achieved by superimposing a sinusoidal modulation of 133 kHz on the triangular ramping signal. The ramping and modulation signals are created in a PCI-based, 12-bit arbitrary waveform generator (CH-3150, Exacq Technologies). Its internal clock is used not only to clock out such waveforms, but also to externally clock the A/D converters (2.496 MHz), via a short coax cable, on a second computer board (NI-6132, National Instruments). It is this manoeuvre that implements coherent sampling.

In the fiber-coupled setup, the light beams enter two detectors with built-in transimpedance amplifiers (UDT-455LN, OSI Optoelectronics). In the direct-coupled setup only one of the above-mentioned detectors is used. In the present case, the gain of the amplifiers is set to 10^3 in order to fulfill a bandwidth of about 1 MHz. Both the sample and the reference signals are amplified by a factor of up to 1000 by an external amplifier in order to minimize external noise and for full utilization of the dynamic range of the AD converter. The reference and the sample signals are also filtered by a second-order, high-pass filter (50 kHz cutoff frequency), and amplified once more by a factor of 100. Measurements on scattering samples, such as bamboo or human tissue, require a large area detector due to the fact that incident light is scattered and absorbed by the sample. In this case, the default sample detector is replaced by a cooled, large-area (Ø=10 mm) avalanche photodiode module (SD 394-70-72-661, Advanced Photonix).

The advantage of using wavelength modulation techniques was estimated by measuring the relative intensity noise (RIN) of the direct-coupled laser and comparing the noise floor level at low frequency and at the laser modulation frequency. RIN is defined in a 1 Hz bandwidth,

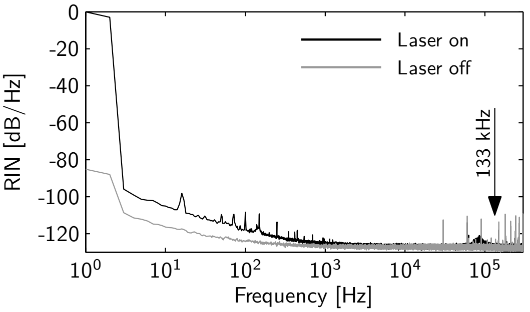

FIG. 2: Laser relative intensity noise (RIN) measurement with a spectral resolution of 1 Hz. Sensor data are recorded by a 14-bit data acquisition card at 600 kS/s over 100 seconds. The figure shows a power spectrum (RIN measurement) of the recorded detector data with and without unmodulated laser light turned on.

and expressed in decibel, as

$$RIN = 20 \times \log_{10} \frac{V_{noise}}{V_{average}},$$

where V_{noise} is the spectral noise root-mean-square (RMS) voltage and $V_{average}$ is the averaged RMS voltage corresponding to the averaged optical power recorded at the optical detector [18]. The RIN measurement was done by measuring the noise spectrum of the recorded detector signal with the laser turned on without any modulation or ramp signal. As shown in Fig. 2, the noise level at 133 kHz, is about 20 dB (10 times) lower than the low-frequency noise level and gives information on the expected improvement in performance when the wavelength modulation technique is used. The decrease in the performance of a tunable diode laser system based on direct detection is due to flicker noise from the laser. In Fig. 2 the dynamic range achieved is about 126 dB (2.0×10^6) at 133 kHz frequency. According to the data sheet of the laser the RIN value at 1 GHz is about -120 to -130 dB/Hz which sets the performance limit of a spectroscopy system based on this laser. As can be seen in the figure, any further improvement of the dynamic range is limited by the 14-bit data acquisition card since the noise floor is almost the same when the laser is turned off. Further, a detection limit of 10^{-6} requires the system to have a dynamic range of about 120 dB (1×10^6). To be able to resolve such a weak signal, a high-pass filter is mounted close to the detector to suppress any signal below the modulation frequency.

B. Data Acquisition

A software program, based on LabVIEW, controls the arbitrary waveform acquisition board (CH-3150). First the scanning and modulation signals to the laser are created and loaded to the board. During the run, the computer central processing unit (CPU) is free to carry out other tasks since the workload of the arbitrary waveform generator is handled by the board itself. All signals are sampled synchronously and coherently to the laser modulation waveforms by the externally-clocked, four channel, 14-bit A/D converter PCI board (NI-6132). Sample data blocks that correspond to one scan are added in a data vector created in LabVIEW. Normally 130 – 7800 scans (1 – 60 s) are carried out before averaged data, which are vector data divided by the number of scans, are stored on disc and/or are lock-in detected by a lock-in detection software module (Lock-in Toolkit for LabVIEW, National Instruments) executed in the computer. The phase reference, used by the lock-in detection module, is created by software. The first and the second channels record the signals from the sample detector (raw signal and high-pass filtered raw signal), while the third and the fourth channels record the signals from the reference detector (reference signal and high-pass filtered reference signal). These two last channels are used only in the fiber-coupled setup; see Fig. 1.

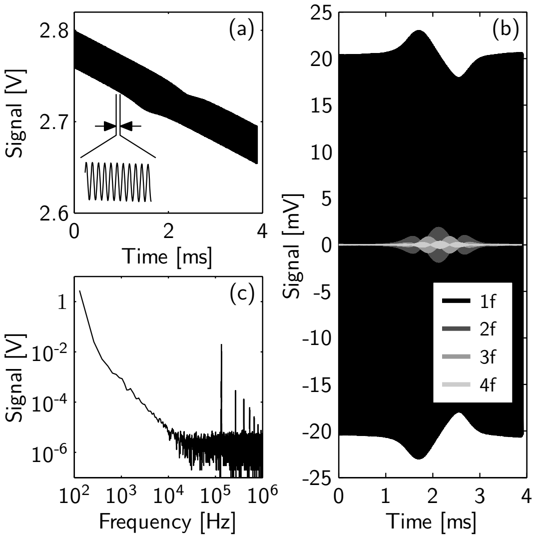

FIG. 3: Typical behavior of the recorded signal for a measurement of oxygen, based on wavelength modulation techniques, for 10 cm of air; 130 (1s) synchronous averages. Figure 3(a) shows the signal from the detector when the laser is scanned about 25 GHz, Fig. 3(b) shows the bandpass-filtered detector signals (3-pole Butterworth, 4 kHz bandwidth) of the detector signal, and Fig. 3(c) shows the spectral peak voltages based on an FFT of the detector signal presented in Figure 3(a). The spectral resolution of the FFT is 130 Hz. See text for more details.

To illustrate the potential of a digital lock-in detection system, based on wavelength modulation and coherent sampling, a measurement based on the direct-coupled setup was performed over a distance of 10 cm in ambient air. Fig. 3(a) presents the direct signal recorded, where the residual amplitude modulation (RAM) signal is clearly seen as a sinus signal that is present during a scan [20]. The RAM signal occurs because the change in frequency is caused by a change in diode driving current and so altering the output power of the diode laser. In the middle of the frequency scan, the absorption line (P11P11) is crossed, resulting in amplitude changes of the direct signal and overtones are created (2f, 3f, 4f...). The amplitude of the RAM signal (40 mV_{pp}) is about 1.5 percent of the DC level of the signal (2.7 V). The recorded, direct signal was filtered by four software-based, band-pass filters (center frequency at 1f, 2f, and 4f) and the data are presented in Fig. 3(b). This figure shows that the 2f signal (4 mV_{pp}) is weaker than the 1f signal (6 mV_{pp}) but still of similar amplitude compared to the dip in the direct signal since the amplitude of the 2f signal is about 0.1 percent of the amplitude of the direct signal. The amplitude of the harmonic signals is highly dependent on the modulation index that in this case is set to 2.2 [6]. The modulation index is the ratio between the modulation excursion in frequency and the half width at half maximum of absorption feature. The expected fractional absorption can be used to calculate the dynamic range of the system required. The absorption fraction for 10 cm of air corresponds to 2.45×10^{-3}. It is also shown that the 3f and 4f signals (1.8 mV_{pp} resp. 0.7 mV_{pp}) are weak and that the RAM signal is strong compared to the peak-to-peak of the 1f signal.

To get an overview of the signal spectrum recorded, an FFT of the data presented in Fig. 3(a) was carried out and is presented in Fig. 3(c). The figure shows that the 1f signal (20 mV_p at 133 kHz) is about a factor of 100 weaker than the averaged signal from the detector (2.7 V). It is also shown that the system SNR, for 130 averages, is about 3×10^5. The SNR is measured at 133 kHz and with a measurement bandwidth of 130 Hz. Normally, SNRs are expressed on a logarithmic (dB) scale according to

$$SNR = 20 \times \log_{10} \frac{V_{signal}}{V_{noise}},$$

where V_{signal} is the averaged detector RMS voltage level and V_{noise} is the RMS voltage level of measured noise. An SNR of 3×10^5 corresponds to an SNR of about 110 dB. If a high-pass filter is introduced, which suppresses signals below the 1f frequency, the A/D dynamic range required decreases by a factor of about 100, as shown in Fig. 3(c).

C. The Impact of the A/D Converter Resolution

The direct-coupled setup was used to study the impact the resolution of an A/D converter has on a coherent measurement system for spectroscopy. A number of streaming and scanning 2f detection measurements were performed for a distance in ambient air of 10 mm. This corresponds to a fractional absorption of 2.45×10^{-4}. Four measurements, each recording for 1 minute (7800 scans) were done. The sample signal and high-pass sample signal were streamed to a hard disc at 2.469 MS/s. Raw data were stored for each measurement, with different resolutions corresponding to 8, 10, 12, and 14 bits of the A/D converter. By default, the A/D board has a 14 bit resolution but this can be decreased by software during a streaming measurement (based on an application example provided by National Instruments). Thus, the impact of different A/D converter resolutions could be studied. The streamed data were read from the disc, averaged, and lock-in detected. In Fig. 4 the 2f signals for a resolution of 8 and 14 bits are presented.

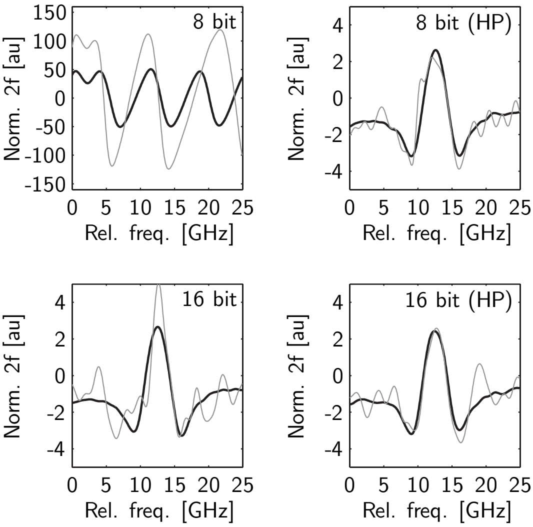

FIG. 4: Streaming measurements on 1 cm of ambient air (fractional absorption of 2.45×10^{-4}) with the direct-coupled setup based on different A/D resolutions and signal filtering. The 2f signal for the P11P11 oxygen line at about 764.3 nm is measured for two different average settings; 1 (grey line) and 100 averages (black line). On the left the 2f signal, based on 2f detection of the sample signal, is shown for different A/D resolutions and measurement times. On the right similar data based on 2f lock-in-detected, high-pass filtered, sample signals are shown.

As can be seen on the left-hand side of Fig. 4, an 8-bit A/D converter cannot resolve the oxygen absorption line even though 100 averages are performed. An absorption dip of 2.45×10^{-4} requires a dynamic range of the A/D converter of about 72 dB ($20 \times \log(1/2.45 \times 10^{-4})$) to reach an SNR of one. However, an 8-bit A/D converter has a dynamic range of only about 48 dB and this is too poor to resolve absorption lines in this test setup even though long time averaging is used. If more bits are used the absorption dip can be resolved, even with few or no data averages. 14 bits are enough to resolve an absorption dip of 2.45×10^{-4} since its theoretical dynamic range is about 86 dB. 100 averages increase the dynamic range by an additional factor of 10 (20 dB).

The performance can be increased by the use of dithering [21] or high-pass filtering [19] as shown on the right-hand side of Fig. 4. It can be seen that similar performance is reached regardless of whether an 8-bit or a 14-bit AD converter is used. If high pass filtering is used it should be possible to detect a weak absorption line (1×10^{-6} to 1×10^{-8}) by using a 14-bit or a 16-bit A/D converter. On the right-hand side of Fig. 4, it can also be seen that single scan data are not a priori improved by introducing more bits. This is due to the fact that data from one scan are greatly affected by mechanical vibrations introduced by vibration motors. Small vibration motors are mounted in the test setup in order to shake the laser and the detector to minimize persistent optical fringe generation, a well known detrimental factor in diode laser spectroscopy [22].

III. CALIBRATION OF THE SYSTEM

The standard addition method was used to calibrate and to test the linearity and noise behavior of the system. The method is based on adding a known distance through ambient air between the laser and the detector and monitoring the amplitude of the 2f signal, divided by the DC level of the direct signal [22]. The signal increases linearly as is also shown in Fig. 5. The estimated air offset of 4 mm, in the direct-coupled setup, is due to the fact that it is not possible to mount the detector directly connected to the laser in the direct-coupled setup. The estimated air offset of 14 mm in the fiber-coupled setup is due to air inside the collimator package used. It is possible to evaluate 1f – 4f signals from one measurement data file, since data are recorded synchronously almost 20 times for each period of the modulation signal. The figure also shows typical recorded signals of the 2f signal for a distance through air of about 35 mm for the fiber-coupled and the direct-coupled setups. As shown in Fig. 5(b), the 2f sample signal in the fiber-coupled setup is markedly distorted. The distortion is due to optical interference effects which occur frequently in pigtailed lasers. Periodic noise and fringes can be handled by using balanced detection [22]. By detecting both the sample and reference beams synchronously, a balanced 2f detection signal is evaluated, as shown in Fig. 5(b).

IV. APPLICATIONS

A. Gas Discharge Measurements on a Bamboo Stalk

To show the strength of using the digital lock-in detection system, we performed test measurements. The oxygen content inside a bamboo stalk was measured. Similar studies on wood have been carried out previously, using a traditional spectroscopy setup, based on desktop analog lock-in amplifiers [23, 24]. The purpose of our measurements was to show how the hollow compartment inside a bamboo stalk, interacts with ambient air. The stalk of a bamboo consists of hollow, jointed compartments. We performed measurements on a 23 cm long stalk with an inner diameter of 11 mm. The external diameter was approximately 18 mm. Before the measurement was started the bamboo stalk was exposed to a non-ambient gas by placing it for 72 hours in a bag containing nitrogen. Figure 6 shows the direct-coupled setup measurement arrangement and also experimental data, showing that the discharge of nitrogen has a time constant of about 30 minutes.

The light reaching the APD detector is in the range of only 0.3 µW or 0.1 percent of the emitted light from the laser. Initial measurements showed noisy signals, and no pure 2f signal could be detected for 20 s of averaging. This is due to interference fringes that appear between the laser, the bamboo stalk, and the detector. Small vibration motors were mounted on the laser and the detector in order to shake the test setup to minimize persistent fringe generation that otherwise overrides the 2f oxygen signal. Even though each measurement point in Fig. 6 is based on 20 s of averaging (2600 scans), mea-

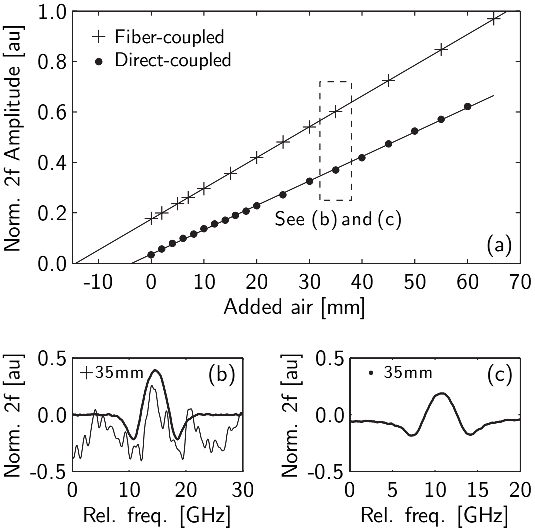

FIG. 5: a) Standard addition measurement results from the direct-coupled and fiber-coupled measurement setups. Ten measurements (20 s measurement time) were made at each air distance, ranging from 0 to 65 mm. b) Typical behavior of the 2f signal in the fiber-coupled setup for a distance through air of about 35 mm. The figure shows the 2f signal of the sample signal (thin line) and the evaluated balanced signal (bold line). c) Typical behavior of the 2f signal in the direct-coupled setup for a distance through air of about 35 mm.

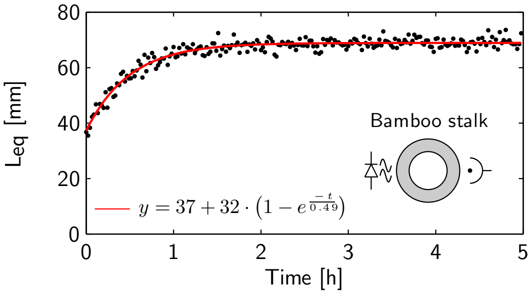

FIG. 6: Measurement on nitrogen discharge in a bamboo stalk with a diameter of 18 mm. As shown in the figure the 2f signal starts at an offset that corresponds to 37 mm of ambient air. This is partially because the stalk is mounted at a certain distance from the laser and the detector. Thus, light also passes through ambient air, not only through the stalk.

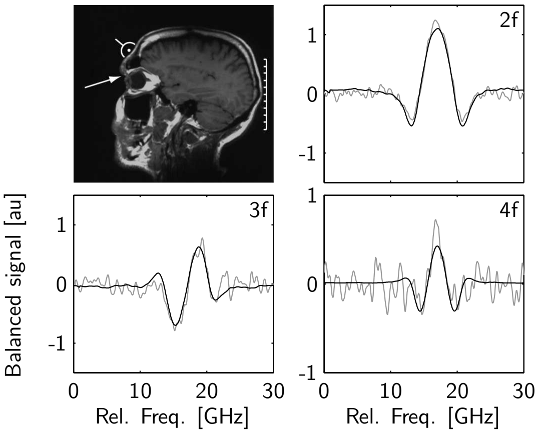

FIG. 7: Measurement on frontal sinuses on a healthy volunteer. The strength of the signal corresponds to a distance through ambient air of 13 mm. The figure shows the behavior of the 2f – 4f signals for one measurement (60 s averaging). See text for more details.

surement data still fluctuate. This could be the result of changing motor speed, backscattered light, interference fringes, etc., which add noise and intensity fluctuations.

B. Measurements on the Human Frontal Sinus

Human frontal sinuses are air-filled cavities in the frontal bone. Measurements on these sinuses, on a healthy volunteer, were performed with the fiber-coupled setup. This setup was chosen since the measurement requires a device that can be positioned at any point on the human body. The tip of the fiber was positioned onto the caudal part of the frontal bone while the APD detector was positioned on the forehead about 3 cm from the fiber. The light that reaches the APD detector, was in the range of only 0.15 µW or 0.2 percent of the emitted light from the laser. Measurements, based on 60 s of averaging, show a 2f signal that corresponds to an distance through ambient air of 13 mm. The result is in agreement to that reported in Ref. 25. As expected, the SNR of the 2f signal is higher than for the 3f, and 4f signals as shown in Fig. 7. A measurement time, to produce a signal of an acceptable signal, should be 10 – 30 s. Commonly, fringes dominate the noise floor and in some cases the 4f signal contains less such noise than the 2f signal [26]. Thus, the 4f signal may be a better choice for data analysis in the case of large interference fringes. However, the 4f analysis requires more light or less attenuation by the sample. This is due to the fact that the signal level of the 4f signal is lower than the 2f signal by a factor of 5, as shown in Fig. 3.

V. DISCUSSION

The CH-3150 board was chosen because it has a fast arbitrary generator onboard, which can be used to modulate the laser. Any modulation frequency from DC to several MHz can be created without loading the computer central processor unit (CPU). The two analog input channels onboard can be used to coherently sample the detector signals at the same time. Thus, this board would be adequate to develop a flexible, powerful, cheap, and compact system for trace gas analysis. This system can be used in general gas spectroscopy and in applications with fast changing environments such as in combustion, requiring a ramping frequency of the order of 1 kHz. However, since four input channels were required for balanced-detection to suppress fringes, a second board was introduced (NI-6132) that contains four synchronized A/D converters clocked by the CH-3150 board. The clock signal and the waveform sync signal were fed to the A/D board via two coaxial cables mounted inside the computer. This action was taken to suppress noise and prevent crosstalk between the clock and the detector signals.

Even though this system can be run incoherently, like an ordinary, PC-based, lock-in detection system, coherent sampling is used since this avoids the requirement that lock-in data are real-time data. Data can thus be averaged in real-time coherently and can be processed after the averaging is finished or stored for later analysis. The user is free to analyze the data in the time or the frequency domain. This provides the possibility of analyzing signals from several channels and performing baseband analysis and lock-in detection (1f – 4f) on the same data set. The current solution corresponds to the performance of standardized, digital lock-in amplifiers. However, with this setup, baseband detection, 1f – 4f detection, and fast ramp frequencies (4 Hz to 1 kHz) could be used by running different software applications without any changes having to be made in the hardware. The solution is compact and installed in an ordinary PC.

If higher performance is needed, high-pass filtering of the detector signal increases the dynamic range of the signal detection, since most of the low-frequency signals (below 1f) are thus suppressed. When this technique is used, the resolution requirement of the A/D converter is not critical. A 12 – 16 bit A/D converter should be adequate even for applications requiring a fractional absorbance of about 1×10^{-7}. The output resolution of the D/A converter is 12 bits, which adds quantization noise even though the CH-3150 board has analog reconstruction filters onboard. It is difficult to estimate how this limitation affects the resolution of the system since amplitude noise at the laser input is converted into amplitude and frequency variations in the laser at the same time.

Another way to improve the performance of the system is to replace the current DAQ boards with boards with higher resolution. As an example a second measurement was performed to measure the laser noise using a 24-bit data acquisition board (NI-4472, National Instruments). The use of this board resulted in lowering the noise floor at 10 kHz by an additional 30 dB. However, this board is too slow (about 100 kHz sampling frequency) for combustion measurements, for instance, and it is not possible to clock it externally. Thus, this board cannot be used in a coherent sampling system. It is also possible to add input channels by replacing the A/D board with a board with eight input channels, for example. If a cheaper solution is needed, standardized external sound cards can be used. Today, these devices have excellent performance with 24-bit resolution A/D and D/A converters. The only drawbacks are that the sampling clock is limited to 196 kHz and no DC level can be measured. However, this solution may be adequate for some applications.

VI. SUMMARY

By the use of plug-in boards for standardized computers, a powerful and flexible detection system for gas spectroscopy was developed. One of the greatest advantages of the system is that raw data, from a number of channels, can be streamed and stored on disc by the use of standardized software. There is no need for specially designed computers, field-programmable gate arrays, or embedded solutions. Coherent sampling allows the raw data to be analyzed in real-time or post-processed in the time- or frequency domain. In our experience the current system is limited by interference fringes in the optical setup.

VII. ACKNOWLEDGEMENT

This work was supported by the Swedish Research Council and the Knut and Alice Wallenberg Foundation. The authors are grateful for Lars Rippe for sharing his expertise in measurement technology.

[1] P. Werle, Spectrochim. Acta Part A **54**, 197 (1998).
[2] G. Galbács, Appl. Spectrosc. Rev. **41**, 259 (2006).
[3] M. Allen, Meas. Sci. Technol. **9**, 545 (1998).
[4] K. Song and E. C. Jung, Appl. Spectrosc. Rev. **38**, 395 (2003).
[5] D. T. Cassidy and J. Reid, Appl. Opt. **21**, 1185 (1982).
[6] J. Reid and D. Labrie, Appl. Phys. **26**, 203 (1981).
[7] G. C. Bjorklund, Opt. Lett. **5**, 15 (1980).
[8] D. T. Cassidy and J. Reid, Appl. Phys. B **29**, 279 (1982).
[9] J. Silver, Appl. Opt. **31**, 707 (1992).
[10] R. Alonso, F. Villuendas, J. Borja, L. A. Barragn, and I. Salinas, Meas. Sci. Technol. **14**, 551 (2003).
[11] Integrated lockin amplifier for sensor applications (European Solid-State Circuits Conference, 1999).
[12] P. Vogel and V. Ebert, Appl. Phys. B **72**, 127 (2001).
[13] T. Fernholz, H. Teichert, and V. Ebert, Appl. Phys. B **75**, 229 (2002).
[14] P. Werle, R. Miicke, and F. Slemr, Appl. Phys. B **57**, 131 (1993).
[15] R. Rosing, H. Kerkhoff, and R. Tangelder, J. Electron. Test. **14**, 67 (1999).
[16] P. Heinonen, T. Saramaki, J. Malmivuo, and Y. Neuvo, IEEE Trans. Circ. Syst. **31**, 438 (1984).
[17] M. E. Takanen, Ph.D. Thesis, Helsinki University of Technology Department of Electrical and Communications Engineering Laboratory of Acoustics and Audio Signal Processing (2005).
[18] C. Thibon, F. Dross, A. Marceaux, and N. Vodjdani, IEEE Photon. Technol. Lett. **17**, 1283 (2005).
[19] R. Engelbrecht, Spectrochim. Acta Part A **60**, 3291 (2004).
[20] X. Zhu and D. T. Cassidy, J. Opt. Soc. Am. B **14**, 1945 (1997).
[21] J. Reid, M. El-Sherbiny, B. K. Garside, and E. A. Ballik, Appl. Opt. **19**, 3349 (1980).
[22] L. Persson, F. Andersson, M. Andersson, and S. Svanberg, Appl. Phys. B **87**, 523 (2007).
[23] M. Sjöholm, G. Somesfalean, J. Alnis, S. Andersson-Engels, and S. Svanberg, Opt. Lett. **26**, 16 (2001).
[24] J. Alnis, B. Anderson, M. Sjholm, G. Somesfalean, and S. Svanberg, Appl. Phys. B **77**, 691 (2003).
[25] L. Persson, M. Andersson, M. Cassel-Engquist, K. Svanberg, and S. Svanberg, J. Biomed. Opt. **12**, Art. ID: 053001 (2007).
[26] P. Kluczynski and O. Axner, Appl. Opt. **38**, 5803 (1999).

Paper XIII

Temporal correlation scheme for spectroscopic gas analysis using multimode diode lasers

G. Somesfalean, M. Sjöholm, L. Persson, H. Gao, T. Svensson and S. Svanberg.

Applied Physics Letters **86**, Art. ID: 184102 (2005).

APPLIED PHYSICS LETTERS **86**, 184102 (2005)

Temporal correlation scheme for spectroscopic gas analysis using multimode diode lasers

G. Somesfalean, M. Sjöholm, L. Persson, H. Gao,[a] T. Svensson, and S. Svanberg[b]
Department of Physics, Lund Institute of Technology, P.O. Box 118, SE-221 00 Lund, Sweden

(Received 9 November 2004; accepted 15 March 2005; published online 26 April 2005)

The reliability of diode lasers used in spectroscopic applications is limited by their intrinsic multimode and mode-jump behavior when wavelength-tuned by current or temperature. We report on a scheme for gas analysis based on temporal correlation between absorption signals from an unknown external and a known reference gas concentration, simultaneously recorded when the diode laser wavelength is temperature-tuned across absorption features of the gas of interest. This procedure, which does not require any knowledge of the exact spectrum, also eliminates light intensity fluctuations due to mode competition. The method is illustrated for atmospheric oxygen absorption applied to diffusion measurements.

© *2005 American Institute of Physics*. [DOI: 10.1063/1.1921351]

Gas concentrations can be conveniently measured by high-resolution absorption spectroscopy employing single-mode tunable laser sources, especially diode lasers. The narrow-band laser radiation is scanned over an isolated absorption line, specific for the species to be studied, and the concentration is retrieved from the measured absorbance according to Beer–Lambert's law. The technique, commonly referred to as tunable diode laser absorption spectroscopy (TDLAS), has applications ranging from, e.g., long-path absorption measurements of environmental pollutants[1] to probing of gas confined in porous materials.[2]

However, semiconductor diode lasers have intrinsic properties that often impair their spectroscopic applicability.[3] For example, several longitudinal modes can oscillate simultaneously, since the width of the spectral gain profile is much broader than the separation between adjacent longitudinal modes. The mode competition leads to interfering gas absorption signals from the submodes. Additionally, the tuning range of diode lasers is often not continuous and mode-hops occur, which causes light intensity fluctuations that can be misinterpreted as absorption. To cope with these problems, essentially single-mode operation can be achieved by employing distributed feedback, distributed Bragg reflector, or external cavity arrangements. All these technologies increase the degree of complexity and the cost of the systems. Additionally, the wavelength characteristics of the laser can change over time due to aging. Diode laser system realizations are frequently subject to thermal drift and active stabilization may be needed. These inconveniences as well as the need of expert operators have been major obstacles for the widespread application of TDLAS.

Another approach is used in the gas filter correlation (GFC) technique,[4] in which, frequently passive, broadband radiation is either passed directly through the external gas that is analyzed, or is additionally filtered through an optically thick reference cell filled with the target gas. The direct recording is strongly dependent upon the presence of the target gas in the external path, whereas the signal from the reference cell is essentially the same, since the light at all characteristic wavelengths is anyway absorbed. The difference in spectral transmittance between the two paths is thus a sensitive indicator of the target gas concentration. Due to the inherent "holistic" property of the GFC technique, which matches out the unique spectral signature of the target gas, the presence of interfering gases does not affect the analysis. Notably, no knowledge of the gas spectrum is needed, which has been effectively used in, e.g., lidar gas monitoring[5] and gas imaging.[6,7]

In this letter a scheme for gas analysis, denoted temporal gas correlation spectroscopy (TEGACOS), is proposed. The technique combines the superior sensitivity and selectivity of the high-resolution TDLAS technique with the simplicity and robustness of a GFC spectrometer. The technique is particularly suited for analysis of gas with sharp absorption characteristics, and allows employment of multimode diode lasers. Similarly to the GFC technique, the radiation is split into one beam transmitted through the external gas, and another beam passed directly through a reference cell with a well-calibrated concentration of the target gas, as illustrated in the schematic setup shown in Fig. 1. Generally, the diode laser wavelength can be tuned across absorption structures of the target gas by changing the diode temperature or current. The simultaneously recorded signals from the two optical paths may contain gas absorption imprints, as well as intensity variations due to mode competition and mode hops, background fluctuations, and interference fringes. If the target gas is present in the external path, the gas signatures will correlate in time. Oppositely, mode-instability-induced fluctuations of the laser output will correlate differently, since they are independent of the presence of the gas. Thus, in order to discriminate between gas-related absorption and

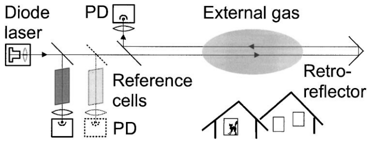

FIG. 1. Experimental setup for temporal gas correlation spectroscopy.

---

[a] Present address: Department of Applied Physics, Harbin Institute of Technology, P.O. Box 406, Harbin 150001, People's Republic of China.

[b] Electronic mail: sune.svanberg@fysik.lth.se

mode instability, at each point in time both the external and the reference signals are normalized to the laser output power, which is conveniently monitored using the integrated photodiode in the diode laser case.

In conclusion, if the diode laser operates in a single longitudinal mode when scanned through the gas absorption structures, the temporal recording obtained constitutes the actual absorption spectrum of the gas. This is the ideal case used in conventional TDLAS. Oppositely, if the laser mode is unstable, the detected signal no longer corresponds to the actual spectrum. By using the temporal correlation scheme, information about the gas absorption can still be retrieved. It should be noted that the influence of laser frequency fluctuations due to thermal drift are automatically eliminated with the temporal correlation scheme, due to the simultaneousness of the measurement. Note also that external background and internal optical variations, including changes in the optical system alignment, and interference fringes generated by external feedback from optical surfaces, should be minimized, as in conventional TDLAS. If the perturbation widths are comparable to the linewidth of the absorbing species under investigation, they can obscure the detection and reduce system performance. Increased sensitivity is achieved with the suggested method, as in conventional GFC, in wavelength regions with strong differential absorption, i.e., where the gas spectrum has high contrast.

To demonstrate the TEGACOS concept, preliminary proof-of-principle measurements were performed on atmospheric oxygen, which has close-lying and well-resolved absorption lines in the A-band around 760 nm. An AlGaAs Fabry–Pérot-type diode laser (Sharp LT031MDO) with a nominal wavelength of 757 nm at 25 °C and a free running output power of 7 mW was scanned across a wide wavelength range including several oxygen absorption lines, by changing the laser temperature about 12 °C. Although temperature scanning by a Peltier element in a standard laser mount was slow (~20 s per scan), a faster method based on photothermal heating of the diode laser by pulsed radiation from an external laser[8] was also investigated. Many commercially available diode lasers are notoriously emitting light at multiple longitudinal modes. Enhanced multimode behavior of the diode laser used in our experiments was obtained by operating it at an injection current close to the lasing threshold. The widely tunable but spectrally noisy diode laser source, not suitable to use in conventional TDLAS, was diagnosed using a spectrometer. The output spectrum obtained had discontinuities and mode hops, as illustrated in Fig. 2(b). The experimental setup, shown schematically in Fig. 1, consisted of an external path of variable length and several reference paths, corresponding to different absorbancies, utilized for calibration. Figure 2(a) shows the simultaneously recorded direct-absorption signals normalized to the monitor current and divided by a fitted third order polynomial for display purposes. The signals displayed correspond to 138, 304, and 830 g/m^2 path-integrated concentration of oxygen, respectively. The absorption features observed (counted from left to right) correspond to the P3P3, P3Q2, R13Q14, R15R15, R15Q16, and R17R17 lines of the oxygen A band. However, it should be stressed that such a detailed spectral knowledge is not required using the present technique, which functions for any combination of gas absorption signals obtained when the diode laser source exhibits arbitrary frequency shifts or mode competition.

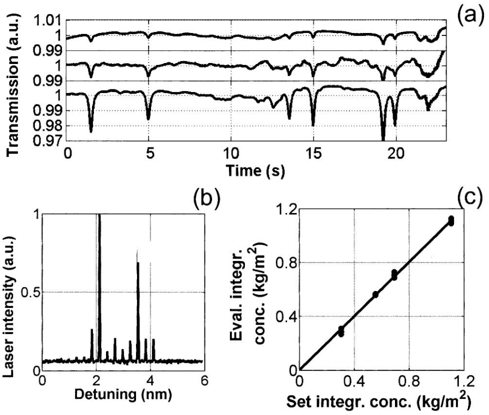

FIG. 2. (a) Simultaneously recorded single-scan time-correlated oxygen signals. The curves correspond to 138, 304, and 830 g/m^2 path-integrated concentrations of oxygen, equivalent to path lengths in air of 0.5, 1.1, and 3 m, respectively; (b) typical multimode diode laser spectrum around 760 nm; (c) evaluated vs set path-integrated oxygen concentrations in air, plotted with a linear fit.

Similarly to the broadband GFC technique, the reference cell provides an ultrasharp matching signature of the target gas. However, owing to the spectral sharpness of the laser source used in the temporal correlation scheme, the absorbed radiation is detected in a narrow wavelength interval at the time, and not integrated over all wavelengths as in the conventional case. Thus, in this scheme the reference cell is preferably not totally absorbing, and can also be used for calibration purposes. Since the reference gas concentration is well known, the external gas concentration can be related to it in a way that resembles the standard addition method. An important difference is that the standard addition calibration is usually not performed simultaneously, but in a time multiplexing procedure. To avoid line shape discrepancies of the absorption lines that would impair the correlation, the temperature and pressure in the reference path are kept as similar as possible to the conditions in the external gas. This can be achieved, e.g., by long-term temperature stabilization and pressure equilibrium in nonsealed reference cells.

The simple data processing consisted of initial subtraction of the background level, assessed by temporarily switching of the laser, followed by normalization of the signals to the laser output power. In order to remove the influence on the signals caused by path-differential variations due to, e.g., slowly wavelength-dependent transmission, a sliding pointwise-symmetric division was performed. The logarithms of the signals obtained were subject to a sliding correlation interval with a width corresponding to the expected width of the gas absorption features, resulting in a pointwise time-interval-integrated ratio between the signals. In a calibration procedure, a pair of reference signals of known concentration was used to single out points in time having the expected time-interval-integrated ratio, thus corresponding to the gas signature. Subsequently, the pointwise time-interval-integrated ratio between one of the reference signals and the external signal was used to determine the unknown gas concentration in the external path. The evaluated path-integrated concentrations obtained by the TEGACOS method versus

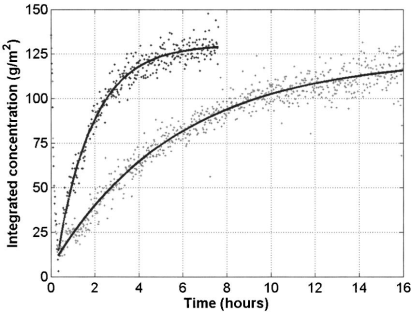

FIG. 3. Recording of the reinvasion of ambient air into a previously nitrogen-flushed glass container covered by polystyrene foam slabs of (a) 20 mm and (b) 10 mm thickness, respectively. An offset path-integrated concentration of 73 g/m^2, due to the air outside the container, was subtracted from the signals.

the corresponding set values from a multipath experiment are displayed in Fig. 2(c). The detection scheme was used to monitor gas exchange through differently thick slabs of polystyrene foam covering a glass container placed in ambient air after previously being flushed with pure nitrogen gas. The temporal variation of the path-integrated oxygen concentration in the container is shown in Fig. 3. Although the measurement lasted several hours, thermal drifts do not affect the measurement.

Improved signal-to-noise ratios can be achieved by averaging the concentrations evaluated from several wavelength scans. With the proposed temporal correlation scheme, as in conventional TDLAS, several orders of magnitude higher sensitivity compared to direct absorption could be obtained by employing modulation techniques. A large modulated signal proportional to the species concentration is generated, which can be temporally correlated in a similar way as in the case presented. Multivariate statistical methods, such as the powerful partial least-squares (PLS) technique,[9] are expected to further improve the accuracy and speed of data processing.

Although demonstrated for oxygen, it is evident that the TEGACOS technique works in any wavelength region and for any gas with close-lying and fairly sharp absorption lines. For example, in the mid-IR region, molecular band heads of several environmentally and biologically important gases could be monitored using the proposed scheme in combination with quantum cascade lasers. The requirements on the system are less stringent, facilitating use of cheaper, high-power multimode diode lasers without need for frequency stabilization. Although the detection sensitivity is lower than for conventional TDLAS, its robustness and relaxed stabilization requirements promise to make the technique very versatile.

This work was supported by the Swedish Research Council, the Asian-Swedish Research Partnership Programme of the Swedish International Development Cooperation Agency (SIDA), and the Knut and Alice Wallenberg Foundation.

[1] H. I. Schiff, G. I. Mackay, and J. Bechara, in *Air Monitoring by Spectroscopic Techniques*, edited by M. W. Sigrist (John Wiley, New York, 1994), pp. 239–333.
[2] M. Sjöholm, G. Somesfalean, J. Alnis, S. Andersson-Engels, and S. Svanberg, Opt. Lett. **26**, 16 (2001).
[3] P. Werle, Appl. Phys. B: Lasers Opt. **60**, 499 (1995).
[4] T. V. Ward and H. H. Zwick, Appl. Opt. **14**, 2896 (1975).
[5] H. Edner, S. Svanberg, L. Unéus, and W. Wendt, Opt. Lett. **9**, 493 (1984).
[6] J. Sandsten, P. Weibring, H. Edner, and S. Svanberg, Opt. Express **6**, 92 (2000).
[7] J. Sandsten, H. Edner, and S. Svanberg, Opt. Express **12**, 1443 (2004).
[8] C. Klimcak and J. Camparo, J. Opt. Soc. Am. B **5**, 211 (1988).
[9] P. Weibring, Ch. Abrahamsson, M. Sjöholm, J. N. Smith, H. Edner, and S. Svanberg, Appl. Phys. B: Lasers Opt. **79**, 525 (2004).

PAPER XIV

Laser spectroscopy of gas in scattering media at scales ranging from kilometers to millimeters

M. Andersson, R. Grönlund, L. Persson, M. Sjöholm, K. Svanberg and S. Svanberg.

Laser Physics **17**, 893–902 (2007).

ISSN 1054-660X, Laser Physics, 2007, Vol. 17, No. 7, pp. 893–902.
© MAIK "Nauka/Interperiodica" (Russia), 2007.
Original Text © Astro, Ltd., 2007.

Laser Spectroscopy of Gas in Scattering Media at Scales Ranging from Kilometers to Millimeters

M. Andersson[a], R. Grönlund[a], L. Persson[a], M. Sjöholm[a], K. Svanberg[b], and S. Svanberg[a, *]
[a] *Division of Atomic Physics, Lund University, P.O. Box 118, SE-221 00 Lund, Sweden*
[b] *Oncology Department, Lund University Hospital, SE-221 85 Lund, Sweden*
*e-mail: sune.svanberg@fysik.lth.se
Received January 10, 2007

Abstract—Free gases are characterized by their narrow line width, and they can conveniently be studied by laser spectroscopy. The present paper discusses the monitoring of such ambient pressure gases, which are dispersed in scattering media such as aerosol-laden atmospheres, solids, or liquids. Atmospheric work basically constitutes the well-known field of differential absorption lidar (DIAL), while the study of free gas in solids and liquids was initiated more recently under the name of GASMAS (GAs in Scattering Media Absorption Spectroscopy). We discuss the connections between the two techniques, which are extensively used in our laboratory. Thus, we span the field from trace-gas mapping of gases in the lower atmosphere to gas studies in construction materials, food products, and the human body. We show that the basic ideas are very similar, while the spatial and temporal scales vary greatly.

PACS numbers: 87.64.Je, 89.60.-k, 87.80.-y, 34.50.-s, 81.05.Rm

DOI: 10.1134/S1054660X07070018

1. INTRODUCTION

Media with strong optical scattering are extremely common in the real world, and are often encountered in everyday life. Examples of scattering media are clouds, fog, ice, snow, foams, food products, wood, and human tissue. Two major aspects pertain when light is propagating in such media. First, the light path traveled by the light becomes undefined with a distribution of path lengths, which results in the absence of a well-defined Beer–Lambertian law, directly applicable for determining the concentration of an absorbing species in the scattering material. Secondly, imaging through scattering media becomes blurred. Many techniques have been developed to alleviate the detrimental effects of scattering as discussed, e.g., in [1–3].

The influence of scattered light in imaging can be removed, e.g., by gated viewing and coherent gating, where the unique feature of the shortest traveling time, and the preserved coherence, respectively, for nonscattered light is taken advantage of [4, 5]. The problem of concentration evaluation can be addressed by using time-resolved measurements, where a histogram of the path lengths of individual photons is recorded, allowing a modified Beer–Lambertian law to be established [6]. In this way, it becomes possible to determine the concentration of molecular species, e.g., in tissue related to sensitizer concentration evaluation in photodynamic therapy [7], for breast tissue characterization in optical mammography [8], or for the concentration evaluation of active components in pharmaceutical tablets [9, 10].

These types of measurements were extended to the study of free gas in scattering media using a technique which was named GASMAS (GAs in Scattering Media Absorption Spectroscopy) [11]. The technique, although operating on samples on millimeter to centimeter scales, has a clear resemblance to laser radar (lidar, or light detection and ranging) measurements in the atmosphere, where the scales are up to several kilometers [12–14]. Single-scattering events strongly dominate in clear air, allowing a straight-forward evaluation of gas concentrations to be performed using the so-called differential absorption lidar (DIAL) technique [15, 16], which, for air pollution studies, was pioneered by Walther and collaborators [17] and Grant and collaborators [18]. However, in the presence of fog or clouds, multiple scattering frequently occurs, especially when operating at short wavelengths. The field of multiple-scattering lidar is extensive and has been covered in a series of international conferences (see, e.g., [19]). The situation in multiple-scattering lidar is very similar to GASMAS measurements, except that the spatial scale is different. In our group, DIAL as well as GASMAS studies are being pursued, and, in the present paper, we show their close connection. Laser spectroscopy applied to environmental and medical research has much in common [20], which is also illuminated, as is the power of multidisciplinary multispectral imaging [21].

The present paper is organized in the following way. Experimental arrangements for lidar and GASMAS measurements are presented in the next section. Then, some results from different types of experiments are presented. Finally, in a concluding section, the techniques are discussed and new fields of investigation are proposed.

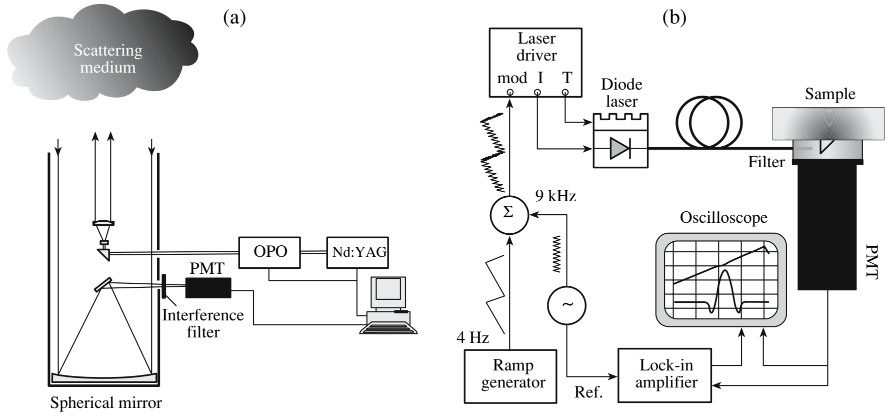

Fig. 1. (a) Schematic arrangement for lidar monitoring of atmospheric gases (left) and (b) the schematic arrangement for measurements of gases in solid or liquid scattering media (right) (from [3]).

2. EXPERIMENTAL ARRANGEMENTS

2.1. Lidar

A schematic diagram of the Lund lidar system used for range-resolved trace-gas element DIAL mapping in the atmosphere is shown in Fig. 1a. Short pulses from a tunable high-power laser are transmitted into the atmosphere, and the laser is switched between two different wavelengths—one on an absorption peak and one slightly off. The laser radiation is scattered by particles and molecules in the atmosphere and backscattered light is collected with a 40-cm-diameter Newtonian telescope and directed to a detector. The telescope has a very small viewing angle (about 1 mrad) defined by an aperture stop in the focal plane. The viewing angle matches the divergence of the laser beam, which is transmitted through a beam expander, and is mounted on the same optical axis as the receiving telescope. With this “tunnel-vision” arrangement, the probability of multiply scattered photons is strongly reduced—to the extent it is possible to be neglected in the absence of fog or clouds. The detected laser-radar signals will, for a uniform atmosphere, show a typical $1/r^2$ dependence, reflecting the diminishing solid angle of the receiving telescope presented to the scatterers along the propagating beam. This is true for the off-resonance wavelength, whereas the on-resonance signal will be additionally attenuated by absorption related to the gas of interest. Division of the on-resonance by the off-resonance curve will also eliminate the influence of nonuniform scattering particle distributions, and the slope of the ratio curve indicates the gas concentration.

The Lund lidar system [22] is housed in the cargo compartment of a Volvo truck and can easily be transported to measurement sites. The system is fully self-contained with an autonomous source of electricity. A 20 Hz Nd:YAG-pumped optical parametric oscillator (OPO) system (Spectra Physics MOPO-730), modified to make fast wavelength switching possible is used as the lidar transmitter. The OPO can be widely tuned, and, in combination with nonlinear frequency conversion techniques, the spectral range 220 nm to 3.4 μm can be covered. The vertically looking arrangement in Fig. 1a is normally complemented by a rooftop dome with a computer-controllable folding mirror to direct the radiation in any direction desired. Collected backscattered light is passed through a narrow-band interference filter, which transmits only the elastically scattered radiation onto a photomultiplier tube (PMT), while suppressing most of the ambient light.

Ultraviolet laser radiation is preferably used, since these wavelengths are essentially eye safe (below 400 nm) and a sufficiently strong backscattering is attained, which is not necessarily true in the infrared region, which otherwise is also eye safe beyond 1.4 μm.

Our group has performed measurements on several pollutants, including sulphur dioxide (SO_2), nitrogen dioxide (NO_2), nitric oxide (NO), and mercury (Hg), the last of which was recently studied in a major interdisciplinary project concerning chlor-alkali factories [23]. During these measurements, the absorption peak for Hg at 253.65 nm was used, where 5 mJ laser pulses with 4–5-ns length could be produced. The laser wavelength is switched on a shot-to-shot basis, such that there is not time for the atmosphere to change appreciably between the on- and off-resonance measurements.

2.2. GASMAS

A schematic setup for GASMAS is shown in Fig. 1b. It is employed to measure molecular gases inside scattering media by using tunable diode laser absorption spectroscopy. The laser is scanned across an absorption line of the gas to be studied by repetitively modifying the laser driver current by supplying a sawtooth ramp. Our work has been focused on molecular oxygen [11, 24–26], which has its conveniently located A-band around 760 nm. Furthermore, water vapor around 980 nm [27] has been studied for moisture assessment. In principle, any gas with absorption lines situated at a wavelength available with a suitable laser can be investigated, provided that the bulk material is sufficiently transparent. Thus, there is a practical limitation to the optical region below 1400 nm for samples containing large concentrations of liquid water (biological tissue, fruits, foods, etc.), and from 600–1400 nm for human tissue due to the additional absorption of hemoglobin at lower wavelength.

In order to achieve sensitive detection, lock-in detection techniques are used. The laser driver current is, then, modulated by a 10-kHz sine wave. The light is fiber optically guided to the sample, which, for oxygen monitoring, has the additional advantage of suppressing a strong background signal from ambient air. In the arrangement shown in Fig. 1b, a right-angle prism is positioned in front of the fiber, centrally located over a large area photomultiplier tube (PMT) detector. The backscattered light from the sample is collected through an annular aperture, which has the function of suppressing the strong light backscattered close to the injection point of the sample, allowing deeper levels of the sample to be probed. A high-pass filter with a cutoff wavelength at 715 nm is mounted on the detector in order to reduce the influence of background light. The sharp sensitivity cut off of the PMT towards the IR region provides the matching low-pass filter function. The signal from the detector is split into two parts. One part is directly connected to a digital oscilloscope, while the other part is fed to a lock-in amplifier, where the amplitude at twice the modulation frequency is phase sensitively detected and fed to a second channel of the oscilloscope. The lock-in signal normalized to the amount of light reaching the detector is used as a measure of the gas content. The standard-addition method, where known pathlengths of ambient air are added into the laser beam, is used to calibrate the system. By doing so, a so-called equivalent mean pathlength, L_{eq}, can be estimated for the sample, corresponding to the distance light has to travel in ambient air to obtain the same signal as in the sample, where multiple scattering produces a distribution of pathlengths. We note that L_{eq} depends on both the sample scattering properties and the concentration of the distributed gas.

2.3. Comparison

By comparing Figs. 1a and 1b, we notice the close resemblance between the lidar and GASMAS techniques, which typically operate at kilometer and millimeter ranges, respectively. In the second case, strong multiple scattering can cause the effective pathlengths to be centimeters up to meters in rare cases. Thus, while a lidar system operates at photon travel times on the order of microseconds, the latter system is characterized by pico- and nanosecond time scales. Both systems can, in principle, be operated in pulsed mode yielding time resolution, or in a continuous-wave (CW) mode. The former system is normally a pulsed one, while the latter is frequently a continuous one. In continuous operation, the overwhelming signal at short range must be suppressed by a ring-shaped aperture arrangement suppressing the on-axis signal. Pulsed operation in short-range applications (high temporal resolution) is not compatible with a high spectral resolution, due to Fourier broadening. However, the phase-shift method, where a CW laser is amplitude modulated, may be compatible with spectral as well as spatial resolution in a certain parameter range.

The CW detection scheme can also be seen as a long-path absorption arrangement where the range resolution is lost. Two scenarios are depicted in Figs. 2a and 2b. An arrangement for long-path absorption measurements of air pollutants is shown in Fig. 2a, where a retroreflecting mirror, placed at a distance far away is used to effectively throw the light back to the receiver. In Fig. 2b, a magnetic resonance image (MRI) indicating the frontal human sinus cavities is shown together with a light path for probing the gas content in the sinuses. This can be considered as equivalent to a long-path absorption measurement. Here, the very nonoptimal laser transmitting optics is the frontal bone, the retroreflector is the diffusely scattering underlying tissue (i.e., the brain), and the receiving optics, again, correspond to the inefficient "frontal-bone" telescope followed by the large-area detector. Still, it is possible to measure the pathlength traveled through air in the sinuses. As compared to the atmospheric monitoring case, a huge amount of light is wasted in the sinus case due to diffuse scattering.

3. MEASUREMENT EXAMPLES

Many different aspects of applied molecular spectroscopy are pursued in our research group. Different techniques are used; however, they are frequently closely related, as pointed out in this paper. Atmospheric long-path absorption measurements can be performed using single-mode diode lasers. Frequently, cheap and easily accessible diode lasers do not necessarily emit light at wavelengths corresponding to the strongest gas absorption lines, but rather, at weak overtone or combination spectral bands. To compensate for this, sensitive frequency-modulation techniques can be used, bringing down the sensitivity to the shot-noise limit. As an example, we performed road traffic measurements of nitrogen dioxide concentrations with a cheap laser emitting around 635 nm, rather than employing the commonly used blue spectral region [28]. The two-tone frequency modulation technique, which combines a large frequency modulation, matching the pressure-broadened lines, with convenient elec-

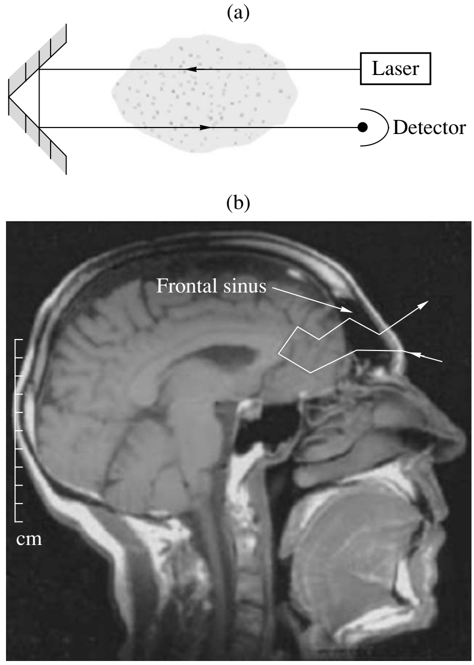

Fig. 2. The upper part (a) shows a schematic setup for a long-path absorption measurement employing a retroreflector. The lower part (b) shows an MRI image of the senior author indicating the location of the frontal sinuses. A light path illustrating the GASMAS technique measurement is also included (from [3]).

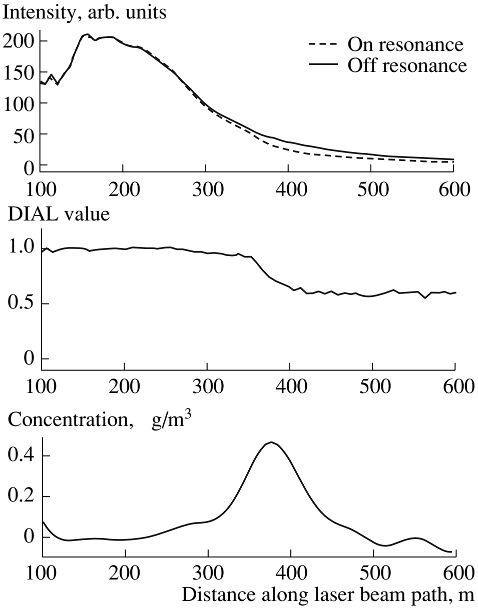

Fig. 3. Results from an atomic Hg lidar measurement: the top part shows the raw data for on- and off-resonance wavelengths, the middle part is the ratio between the two curves, and the bottom part is the evaluated range-resolved concentration (from [3]).

tronic detection around 10 MHz, was employed. A well-known problem with diode lasers is their tendency to mode hop if not accurately controlled. We have developed a new temporal correlation technique, where an uncontrolled multimode laser can be employed for gas concentration measurements. Observed intensity spikes related to modes hitting absorption lines of the atmospheric gas are correlated to the spikes observed from a laboratory cell containing the same gas [29].

As an example of a typical DIAL measurement, the signals received from a DIAL measurement on atmospheric mercury are shown in Fig. 3. The lidar beam was directed downwind from a chlor-alkali plant intersecting the atomic mercury plume. The upper part shows the on- and off-resonance lidar signals as a function of the range. We note that the signals are equal at short distances, indicating that no pollutant has been encountered. The curves run apart at about the 300-m range, indicating that the on-resonance light has been attenuated. The absolute intensity of the recorded signals depends on many different factors, including nonuniform distributions of scattering particles as discussed above, and range-modulated amplification of the detector. However, these factors are cancelled when forming the ratio between the on- and off-resonance signals, as can be seen in the middle part of Fig. 3. From the slope of the ratio curve, the range-resolved concentration shown in the bottom part of the figure can be calculated. Data from any measurement direction obtained in a fan-like scan through the plume can be merged into a cross-section image, such as the one shown in Fig. 4. Here, vertically and horizontally integrated values are also shown. By multiplying the area-integrated value by wind speed perpendicular to the cross section, the total flux of mercury from the plant can be evaluated. This was done in an extensive project at different European plants [23].

As a further DIAL example, we show data from ship-borne vertically sounding measurements of sulphur dioxide at the Italian volcano Mt. Etna in Fig. 5. Examples of on- and off-resonance lidar recordings around 300 nm are shown, and, also, the extension of the SO_2 plume from the volcano, recorded in a traverse under the plume. Passive measurements of the integrated SO_2 absorption using the blue-sky radiation as the light source were also performed. Due to the extended light source, passive measurement can be influenced by multiple scattering. Actually, the passive measurements were compared with nonaffected lidar

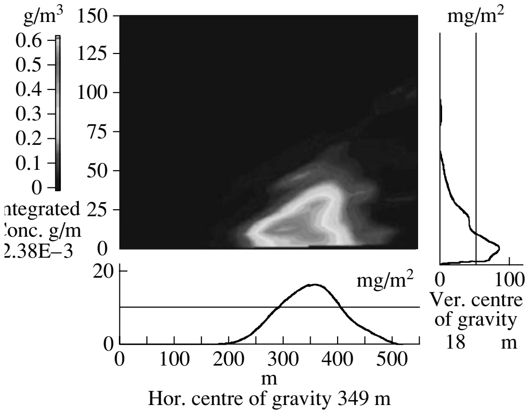

Fig. 4. Cross section of atomic mercury concentration through the emission plume from a chlor-alkali plant. Vertically and horizontally integrated values are also shown. By multiplying the total integrated value with the wind velocity perpendicular to the cross section, the total flux from the plant can be evaluated. Typical values for the case shown are around 70 g/h (from [23]).

data, and the scattering situation was also theoretically modeled [30].

The examples given constitute "conventional" single-scattering lidar cases. The data analysis is based on the time of the arrival of a photon, which is interpreted as a distance—that is, to and from its only scattering event. However, measurements through fog or clouds would be affected by multiple scattering. Multiple scattering lidar measurements—which, in fact, could be considered as large-scale GASMAS experiments—could be performed by spatially resolved measurements. In such a case, the lidar transmitter and receiver optical axes would not be aligned, but translated with respect to each other. Alternatively, the central part of the detector could be blocked with an annular aperture being left open as discussed above. In such a measurement arrangement, only the multiply scattered photons could be detected. If a DIAL measurement would be made on oxygen, the concentration is known and, thus, the optical pathlength could be calculated. Of particular interest would be to perform such measurements both at an A-band transition at about 760 nm, as mostly discussed in this paper, and at a transition around 254 nm, as encountered in [31]. Due to the strong wavelength dependence of both the dominant Mie scattering and the Rayleigh scattering, quite different behavior can be expected and the influence of multiple scattering could be further elucidated.

We will now discuss short-range lidar measurements of free gas, i.e., GASMAS experiments. The general principle is shown in Fig. 6, where transillumination and backscattering geometries are shown. Furthermore, the very narrow gas signal on a spectrally broad background absorption is highlighted. As a first example, a recording of molecular oxygen inside an apple is shown in Fig. 7 [25]. Here, an arrangement of the kind shown in Fig. 1b was used. The directly recorded backscattered light is shown, and the scanned absorption line around 760 nm is too weak to show up. However, the corresponding 2f-lock-in signal (resembling the second derivative of the true absorption line shape) is clearly seen.

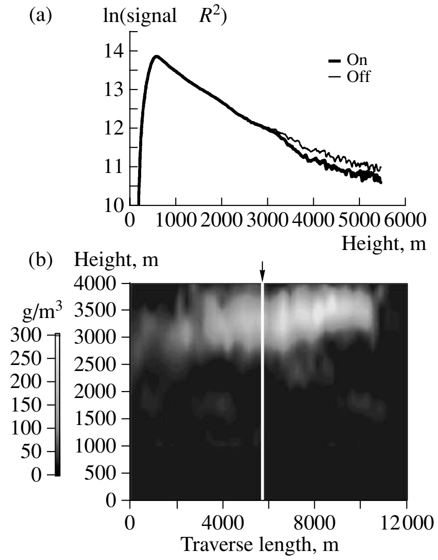

Fig. 5. Data from vertical lidar sounding of the sulphur dioxide flux from Mt. Etna, Italy. Examples of on- and off-resonance lidar curves are shown, illustrating the onset of SO_2 absorption at a height of about 3 km. The evaluated data from a ship-borne full scan under the volcanic plume are also shown (from [22, 30]).

Gas transport can be studied by first immersing the sample, in this case an apple, in an atmosphere of pure nitrogen (e.g., in a sealed-off plastic bag). The reinvasion of normal air (with oxygen) can then be studied as shown in Fig. 8 [25]. We note that the invasion is faster when the apple is pealed, and that the final concentration value, then, becomes almost double, illustrating the active functioning of the skin. Theoretical considerations regarding the GASMAS-based measurement of gas diffusion are given in [32].

Wood is a complex material with cellulose cells, which are partially water-filled and partially air-filled, depending of the state of drying (Fig. 9, upper part). We have studied wood-drying processes by measurements of gaseous water molecules and oxygen. In addition, liquid water, characterized by much broader absorption bands, was studied. Soaking wet balsa wood, placed on scales during the entire drying process, was used and GASMAS signals were recorded in transmission for

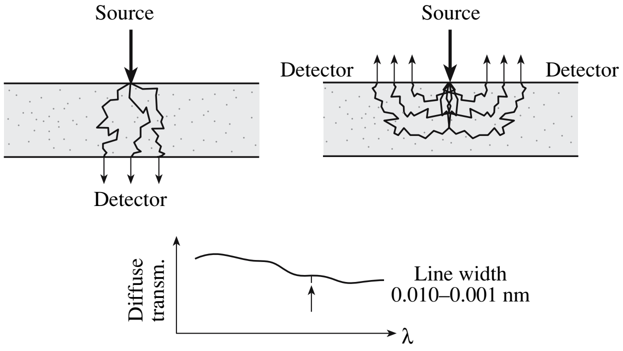

Fig. 6. The principles of GASMAS. The sharp absorptive features of free gas and the transmission and reflection measurement geometries are illustrated.

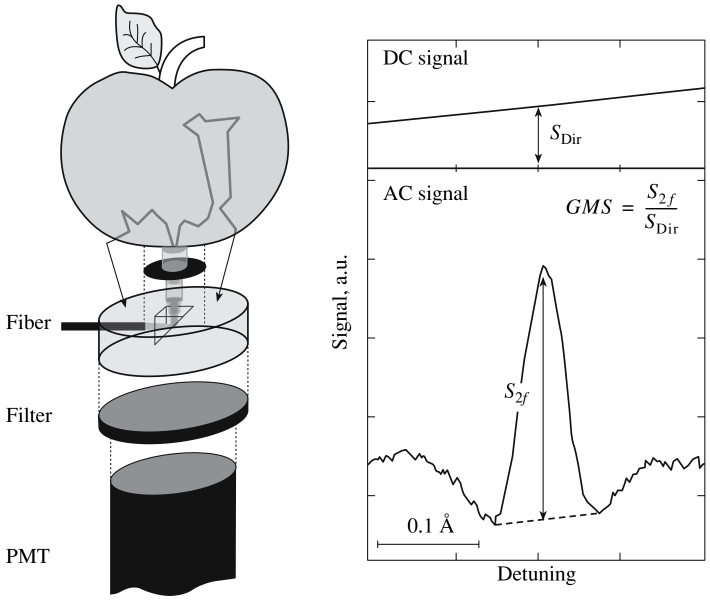

Fig. 7. GASMAS measurement of oxygen in an apple using backscattering geometry. Please note that the separations of the components are heavily exaggerated for clarity; in practice, they are touching each other. Direct transmission and 2f lock-in recordings of an oxygen line are also shown (from [25]).

both gases. The results are shown in the middle part of Fig. 9 [27]. The oxygen signal is seen to increase up to a maximum value reached when the wood is completely dry. The gaseous water signal is also increasing, because of the larger pore volumes where saturated water vapor builds up. However, when no more liquid water is available (the wood is dry), the saturation value cannot be maintained and the humidity gradually reaches that of the surrounding air. The ratio between the water and oxygen molecule signals is partly compensated for by the scattering effects and provides a useful drying diagnostic.

The lower part of the figure shows the total intensity curves for 980 and 760 nm, placed on- and off-resonance, respectively, of a broad liquid water peak. The

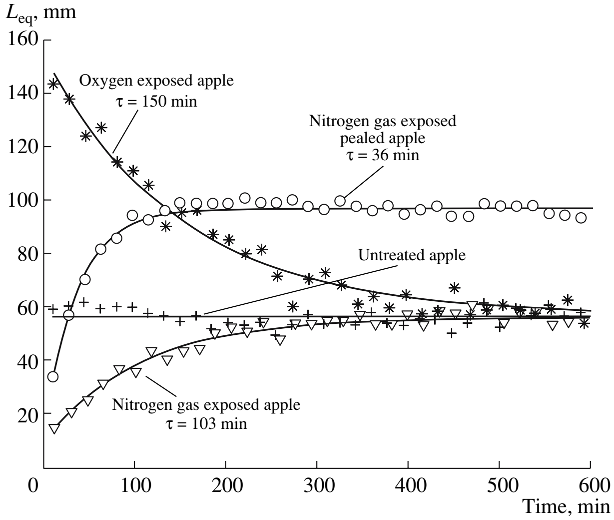

Fig. 8. Gas diffusion temporal curves are shown for apples previously exposed to pure nitrogen or oxygen (from [25]).

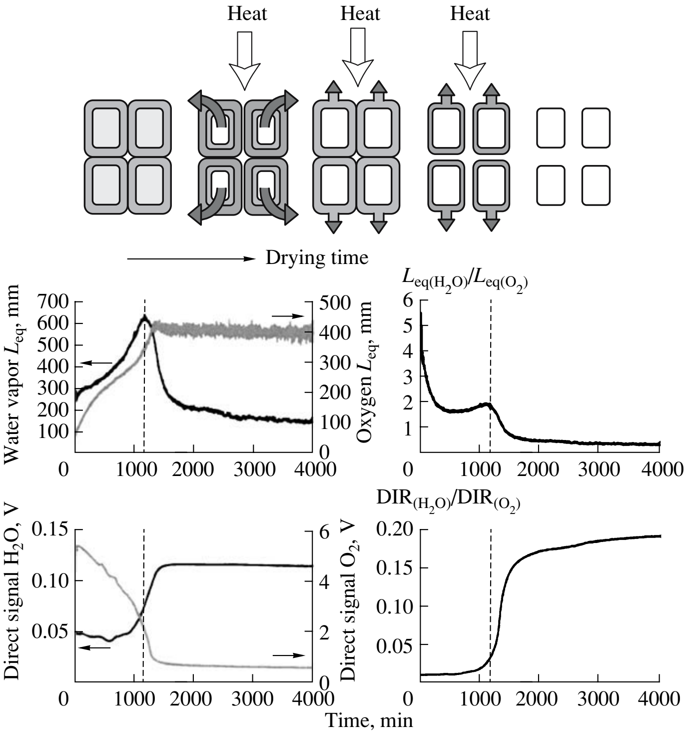

Fig. 9. Spectroscopic study of the drying of wood. Top: Schematic diagram of wood cells with different amounts of liquid water during the drying process. Middle: Recording of water vapor and oxygen GASMAS curves during drying and ratio curve (right). Bottom: Recording of total light transmission at 980 and 760 nm, corresponding to liquid water absorption and a reference wavelength, respectively. The ratio curve is also displayed (right) (from [27]).

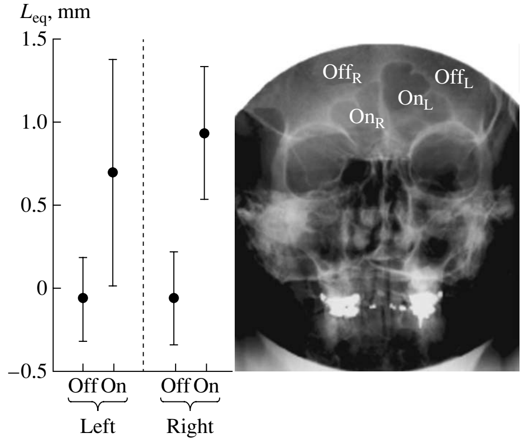

Fig. 10. Recording of molecular oxygen from the frontal sinuses of a healthy volunteer. The positions of the measurement points are indicated in the X-ray image (from [33]).

ratio curve is the differential absorption curve with partial compensation for scattering.

We will finish this section by showing how oxygen in the sinus cavities, as shown in Fig. 2b, can be detected. Here, the gas is not distributed in pores like it is in, e.g., wood, but rather a localized cavity, surrounded by strongly scattering tissue, is probed. A setup of the kind shown in Fig. 1b was used. Figure 10 shows an X-ray radiogram of the senior author with the frontal sinuses clearly visible. Recordings show the presence of oxygen in both cavities and a zero signal outside the sinus areas [33]. The case can be seen as a short-range lidar experiment, where, however, time resolution was not utilized. Instead, it was ensured that the signal was sampled from sufficient depth by blocking the close-range signal with the annular aperture.

Below the floor of the orbital cavity, the maxillary sinuses are located. They can be studied in backscattering, but also in transillumination, because of their locations. Thus, diode laser radiation can be launched through the mouth into the chin from a fiber held against the mucosa. Now, the PMT detector is placed on the outside against the cheek bone. Very distinct signals can be observed on a healthy volunteer as shown in Fig. 11 [34]. A stable amplitude is observed in repeated measurements. However, when the ipsilateral nostril is briefly flushed with nitrogen gas, a fast reduction of the signal is observed, showing that the sinus is connected to the nasal cavity by an open venting channel. When the nitrogen is taken away after 20 s, the sinus again "charges up" with oxygen. Clearly, an interesting new type of ear-nose-throat (ENT) diagnostic tool is in sight.

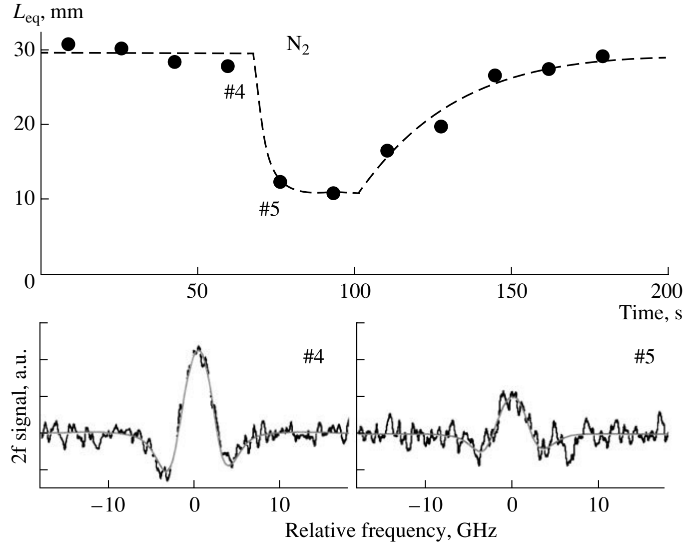

Fig. 11. Oxygen signal from the maxillary sinus of a healthy volunteer recorded in transmission. The laser light was launched fiber optically from the mouth, while the PMT detector was placed against the cheek bone. The signal change following a 20-s flushing of the nasal cavity with nitrogen is shown together with signal recordings (from [34]).

4. DISCUSSION AND OUTLOOK

Several examples showing the close connection between the lidar and GASMAS techniques were given. Multiple scattering differential absorption lidar (DIAL) measurements, i.e., large-scale GASMAS measurements, are of interest for many applications. For example, they could closely relate to studies of the Earth's radiation budget. As solar radiation passes through a cloud, it is multiply scattered. This leads to a larger gas absorptive imprint than otherwise expected. If a lidar beam is directed into a mass of distant snow or ice, the internally scattered radiation will emerge diffusely and can be picked up at a distant point, where the receiving telescope can be directed in a large-scale variety of the geometry shown in the right hand-side of Fig. 6. In particular, an annular detection geometry, such as that in the frontal sinus example, could be adopted. Gas composition in aged polar ice might be studied noninvasively. Furthermore, and more concretely, avalanche victims might be located from a helicopter-borne or stationary remote-sensing GASMAS system, detecting with high contrast exhaled carbon dioxide distributed in the strongly scattering snow.

Returning to small-scale GASMAS applications, the field of food packaging and food inspection appears interesting, in particular, since much of the considerations in this field regard the assurance that oxygen is kept away from foodstuffs. Modified atmosphere packaging is widespread. Gas penetration through plastic enclosures could readily be studied. Likewise, gas penetration through surface coatings, such as paints and veneers, could be studied for the characterization of products.

In the medical field, non-ENT applications might include nonintrusive monitoring of lung function in premature and neonatal infants. Pharmaceutical applications of GASMAS have already been demonstrated [35].

It could be noted that, by monitoring the ratio between the GASMAS signals for two gases, the influence of scattering may be eliminated and absolute concentration values for one gas may be given if the concentration of the other gas is known. Thus, water vapor might be normalized on oxygen in moisture measurements, and oxygen might be normalized on water vapor, having a known concentration in a naturally thermostated human sinus cavity.

As already pointed out in the introduction, the interplay between absorption and scattering, and gas analysis on different spatial scales, constitute an exceedingly rich field of phenomena of both basic and practical interest. In particular, environmental and biomedical applications are very closely related, and differences mainly pertain to the spatial scales and to the mindset of the investigator. Further research and developmental efforts within the field of study in the present paper should be worthwhile.

DEDICATION

This paper is dedicated to the memory of Professor Herbert Walther, who passed away on July 22, 2006. He served as the Faculty opponent at the senior author's dissertation in Göteborg in 1972. As one of the pioneers in laser spectroscopy, he provided great stimulus to the initiation of this field in Sweden in 1973, and, through his early work on laser radar, published in 1974, he also gave stimulus to the lidar work initiated in the senior author's group in 1975. Out of this program, laser applications in the fields of combustion diagnostics and medicine were also developed, and are now vigorously pursued at the Lund Laser Center.

ACKNOWLEDGMENTS

This work was supported by the Swedish Research Council and the Knut and Alice Wallenberg Foundation, and is based on the dedicated and extremely competent work of a large number of additional graduate students and collaborators.

REFERENCES

1. S. Svanberg, "Electromagnetic Radiation in Scattering Media–Spectroscopic Aspects," in *Progress in Nonlinear Science*, Ed. by A. G. Litvak (Univ. of Nizhny Novgorod, Nizhni Novgorod, 2002), Vol. 2, p. 429.
2. S. Svanberg, "Some Applications of Ultrashort Laser Pulses in Biology and Medicine," Meas. Sci. Technol. **12**, 1777 (2001).
3. R. Grönlund., L. Persson, M. Sjöholm, et al., "Studies of Free Gas in Scattering Media at Micro- and Macroscopic Scales," *Proceedings of the International Symposium on Biophotonics, Nanophotonics and Metamaterials, Hangzhou, China, 2006*, p. 51.
4. S. Andersson-Engels, R. Berg, S. Svanberg, and O. Jarlman, "Time-Resolved Transillumination for Medical Diagnostics," Opt. Lett. **15**, 1179 (1990).
5. R. Berg, S. Andersson-Engels, and S. Svanberg, "Time-Resolved Transillumination Imaging," in *Medical Optical Tomography, Functional Imaging and Monitoring*, Ed. by G. Müller et al. (SPIE, Bellingham, 1993), SPIE Institute Series, Vol. 11, p. 397.
6. M. S. Patterson, B. Chance, and B. C. Wilson, "Time Resolved Reflectance and Transmittance for the Non-Invasive Measurement of Optical Properties," Appl. Opt. **28**, 2331 (1989).
7. C. af Klinteberg, A. Pifferi, S. Andersson-Engels, et al., "In Vivo Absorption Spectroscopy of Tumor Sensitizers with Femtosecond White Light," Appl. Opt. **44**, 2213 (2005).
8. T. Svensson, J. Swartling, P. Taroni, et al., "Characterization of Normal Breast Tissue Heterogeneity Using Time-Resolved Near-Infrared Spectroscopy," Phys. Med. Biol. **50**, 2559 (2005).
9. J. Johansson, S. Folestad, M. Josefson, et al., "Time-Resolved NIR/VIS Spectroscopy for Analysis of Solids: Pharmaceutical Tablets," Appl. Spectrosc. **56**, 725 (2002).

10. Ch. Abrahamsson, T. Svensson, S. Svanberg, et al., "Time and Wavelength Resolved Spectroscopy of Turbid Media Using Light Continuum Generated in a Crystal Fibre," Opt. Express **12**, 4103 (2004).
11. M. Sjöholm, G. Somesfalean, J. Alnis, et al., "Analysis of Gas Dispersed in Scattering Media," Opt. Lett. **26**, 16 (2001).
12. G. Fioccio and L. D. Smullin, "Detection of Scattering Layers in the Upper Atmosphere (60–140 km) by Optical Radars," Nature **199**, 1275 (1963).
13. *Laser Remote Sensing*, Ed. by T. Fujii and T. Fukuchi (CRC, Fla, 2005).
14. S. Svanberg, "LIDAR," in *Springer Handbook of Lasers and Optics Springer*, Ed. by F. Träger (Springer, New York, 2007).
15. R. M. Shotland, "Some Observation of the Vertical Profile of Water Vapour by a Laser Optical Radar," *Proceedings of the 4th Symposium on Remote Sensitive Environment, Univ. Mich. Ann Arbor, 1966*, p. 273.
16. S. Svanberg, "Differential Absorption Lidar," in *Air Pollution Monitoring with Optical Techniques*, Ed. by M. Sigrist (Wiley, New York, 1993), Chap. 3.
17. K. W. Rothe, U. Brinkman, and H. Walther, "Applications of Tuneable Dye Lasers to Air Pollution Detection: Measurements of Atmospheric NO_2 Concentrations by Differential Absorption," Appl. Phys. **3**, 115 (1974); Appl. Phys. **4**, 181 (1974).
18. W. B. Grant, R. D. Hake, Jr., E. M. Liston, et al., "Calibrated Remote Measurements of NO_2 Using Differential Absorption Backscattering Technique," Appl. Phys. Lett. **24**, 550 (1974).
19. *12th International Workshop on Lidar Multiple Scattering Experiments*, Ed. by C. Werner, U. Oppel, and T. Rother (SPIE, Bellingham, WA, 2003).
20. S. Svanberg, "Environmental and Medical Applications of Photonic Interactions," Phys. Scr., T **110**, 39 (2004).
21. S. Svanberg, *Multi-Spectral Imaging—From Astronomy to Microscopy—from Radiowaves to Gammarays* (2007) (to appear).
22. P. Weibring, H. Edner, and S. Svanberg, "Versatile Mobile Lidar System for Environmental Monitoring," Appl. Opt. **42**, 3583 (2003).
23. R. Grönlund, M. Sjöholm, P. Weibring, et al., "Elemental Mercury Emissions from Chlor-Alkali Plants Measured by Lidar Techniques," Atmos. Environ. **39**, 7474 (2005).
24. G. Somesfalean, M. Sjöholm, J. Alnis, et al., "Concentration Measurement of Gas Embedded in Scattering Media by Employing Absorption and Time-Resolved Laser Spectroscopy," Appl. Opt. **41**, 3538 (2002).
25. L. Persson, B. Andersson, M. Sjöholm, and S. Svanberg, "Studies of Gas Exchange in Fruits Using Laser Spectroscopic Techniques," *Proceedings of FRUITIC 05, Information and Technology for Sustainable Fruit and Vegetable Production, Montpellier, France, 2005*, pp. 543–552.
26. L. Persson, H. Gao, M. Sjöholm, and S. Svanberg, "Diode Laser Absorption Spectroscopy for Studies of Gas Exchange in Fruits," Opt. Lasers Eng. **44**, 688 (2006).
27. M. Andersson, L. Persson, M. Sjöholm, and S. Svanberg, "Spectroscopic Studies of Wood-Drying Processes," Opt. Express **14**, 3641 (2006).
28. G. Somesfalean, J. Alnis, U. Gustafsson, and S. Svanberg, "Long-Path Monitoring of NO_2 with a 635 nm Diode Laser Using Frequency Modulation Spectroscopy," Appl. Opt. **44**, 5148 (2005).
29. G. Somesfalean, M. Sjöholm, L. Persson, et al., "Temporal Norrelation Scheme for Spectroscopic Gas Analysis Using Multimode Diode Lasers," Appl. Phys. Lett. **86**, 184102 (2005).
30. P. Weibring, J. Swartling, H. Edner, et al., "Optical Monitoring of Volcanic Sulphur Dioxide Emissions–Comparison between Four Different Remote Sensing Techniques," Opt. Lasers Eng. **37**, 267 (2002).
31. H. Edner, G.W. Faris, A. Sunesson, et al., "Lidar Search for Atomic Mercury in Icelandic Geothermal Fields," J. Geophys. Res. **96**, 2977 (1991).
32. M. Sjöholm, L. Persson and S. Svanberg, "Gas Diffusion Measurements in Porous Media by the Use of a Laser Spectroscopic Technique" (in preparation).
33. L. Persson, K. Svanberg, and S. Svanberg, "On the Potential of Human Sinus Cavity Diagnostics Using Diode Laser Gas Spectroscopy," Appl. Phys. B **82**, 313 (2006).
34. L. Persson, M. Andersson, T. Svensson, et al., "Non-Intrusive Optical Study of Gas and its Exchange in Human Maxillary Sinuses," Proc. ECBO, Paper Number: 6628-3 (2007).
35. T. Svensson, L. Persson, M. Andersson, et al., "Non-Invasive Characterization of Pharmaceutical Solids Using Diode Laser Oxygen Spectroscopy," Appl. Spectroscopy (in press).